

High Energy Resummation and Electroweak Corrections in Dijet Production at Hadronic Colliders



Jack J. Medley

A thesis submitted in fulfilment of the requirements
for the degree of Doctor of Philosophy
to the
University of Edinburgh

March 2016

Lay Summary

Coloured final states are ubiquitous at hadron colliders such as the Large Hadron Collider (LHC). Therefore understanding high energy perturbative quantum chromodynamics (QCD) at these experiments is essential not only as a test of the Standard Model, but also because these processes form the dominant background to many searches for new physics. One such ‘standard candle’ is the production of a dilepton pair in association with dijets. Here we present a new description of this final state (through the production of a Z^0 boson and virtual photon). This calculation adds to the fixed-order accuracy the dominant logarithms in the limit of large partonic centre-of-mass energy to all orders in the strong coupling α_s . This is achieved within the framework of High Energy Jets. This calculation is made possible by extending the high energy treatment to take into account the multiple t-channel exchanges arising from Z^0 and γ^* -emissions off several quark lines. The correct description of the interference effects from the various t-channel exchanges requires an extension of the subtraction terms in the all-order calculation. We describe this construction and compare the resulting predictions to a number of recent analyses of LHC data. The description of a wide range of observables is good, and, as expected, stands out from other approaches in particular in the regions of large dijet invariant mass and large dijet rapidity spans.

In addition we also present the application of the High Energy Jets framework to two new experimental scenarios. Firstly, we show a comparison of High Energy Jets matched to the ARIADNE parton shower to an ATLAS study of gap activity in dijet events. We see that our description agrees well with the data throughout and in many distributions gives the best theoretical description. This shows the extra logarithmic corrections are essential to describe data already in LHC Run I. Secondly, we present a study of Z^0/γ^* plus dijets at 100 TeV. We compare the behaviour of the high energy logarithmic enhancements to the QCD perturbative series at 7 TeV and 100 TeV and see that at any high energy hadronic Future Circular Collider (FCC) the effects described by our resummation become significantly more important.

Abstract

Coloured final states are ubiquitous at hadron colliders such as the Large Hadron Collider (LHC). Therefore understanding high energy perturbative quantum chromodynamics (QCD) at these experiments is essential not only as a test of the Standard Model, but also because these processes form the dominant background to many searches for new physics. One such ‘standard candle’ is the production of a dilepton pair in association with dijets. Here we present a new description of this final state (through the production of a Z^0 boson and γ^*). This calculation adds to the fixed-order accuracy the dominant logarithms in the limit of large partonic centre-of-mass energy to all orders in the strong coupling α_s . This is achieved within the framework of High Energy Jets. This calculation is made possible by extending the high energy treatment to take into account the multiple t-channel exchanges arising from Z^0 and gamma* -emissions off several quark lines. The correct description of the interference effects from the various t-channel exchanges requires an extension of the subtraction terms in the all-order calculation. We describe this construction and compare the resulting predictions to a number of recent analyses of LHC data. The description of a wide range of observables is good, and, as expected, stands out from other approaches in particular in the regions of large dijet invariant mass and large dijet rapidity spans.

In addition we also present the application of the High Energy Jets framework to two new experimental scenarios. Firstly, we show a comparison of High Energy Jets matched to the ARIADNE parton shower to an ATLAS study of gap activity in dijet events. We see that our description agrees well with the data throughout and in many distributions gives the best theoretical description. This shows the extra logarithmic corrections are essential to describe data already in LHC Run I. Secondly, we present a study of Z^0/γ^* plus dijets at 100 TeV. We compare the behaviour of the high energy logarithmic enhancements to the QCD perturbative series at 7 TeV and 100 Tev and see that at any high energy hadronic Future Circular Collider (FCC) the effects described by our resummation become significantly more important.

Declaration

Except where otherwise stated, the research undertaken in this thesis was the unaided work of the author. Where the work was done in collaboration with others, a significant contribution was made by the author.

In particular the work and results in chapter 4 was done in collaboration and appears in the following publication:

[59] J. Andersen, J. Medley, J. Smillie, Z/γ^* plus Multiple Hard Jets in High Energy Collisions [arXiv:1603.05460]

This has recently been accepted for publication in JHEP.

J. Medley

March 2016

Acknowledgements

Cheers guys!

At this point I feel it is necessary to apologise to those undergraduate physics students whose local computing use was disrupted by my scripts accidentally converting their computing labs into a server farm.

Contents

Abstract	i
Declaration	iii
Acknowledgements	iv
1 Introduction	1
1.1 A Little History	1
1.2 Thesis Outline	2
2 Quantum Chromodynamics at Hadronic Colliders	4
2.1 The QCD Lagrangian	4
2.2 The Partonic Cross-Section	6
2.3 Divergences and Regularisation	11
2.3.1 Ultraviolet divergences	11
2.3.2 Infrared and collinear divergences	12
2.3.3 Regularising divergences	13
2.4 The QCD Beta Function	15
2.5 QCD Factorisation at Hadronic Colliders	17
2.6 From Partons to Jets	18
2.7 Perturbative QCD and Resummation	20
2.7.1 Fixed-order Perturbation Theory	20
2.7.2 An Example Fixed-Order Calculation	22
2.7.3 Resumming Higher-Order Corrections	27
2.8 Spinor-Helicity Notation	31
2.8.1 Spinor-Helicity Calculations with Massive Partons	33
2.9 Monte Carlo Techniques	37
2.9.1 One Dimensional Integration	37
2.9.2 Higher Dimensional Integration	39
2.9.3 Variation Reduction Techniques	40
3 High Energy QCD	45
3.1 The ‘High Energy’ limit	45
3.2 Mandelstam Variables in the High Energy Limit	46
3.3 qQ -scattering at High Energy (at LO)	47

3.4	<i>qg</i> scattering at High Energy	49
3.4.1	<i>s</i> -channel	50
3.4.2	<i>t</i> -channel	52
3.4.3	<i>u</i> -channel	52
3.5	<i>qQ</i> -scattering at High Energy (at NLO)	53
3.6	<i>t</i> -channel Dominance	57
3.7	Effective Vertices For Real Emissions	59
3.8	Virtual Corrections To All Orders	64
3.9	High Energy Jets	65
3.9.1	The High Energy Jets Framework	65
3.9.2	Factorisation Into Currents	65
3.9.3	The High Energy Jets Monte Carlo	66
3.9.4	Matching to ARIADNE	69
3.9.5	Comparisons to data	70
4	<i>Z</i>/γ^*+Jets at the LHC	74
4.1	Introducing <i>Z</i> / γ^* +Jets at the LHC	74
4.2	Constructing <i>Z</i> / γ^* +jets	76
4.2.1	A Current for <i>Z</i> ⁰ +Jets	76
4.2.2	<i>Z</i> ⁰ Emission Interference	79
4.2.3	Photonic Interference	82
4.2.4	The $2 \rightarrow n$ Matrix Element	82
4.3	Regularising the <i>Z</i> / γ^* +Jets Matrix Element	84
4.3.1	Real Soft Emissions	84
4.3.2	Virtual Emissions	89
4.3.3	Cancellation of Infrared Divergences	90
4.3.4	An Explicit Check: $2 \rightarrow 3$ Scattering	93
4.4	Subtractions and the λ_{cut} scale	96
4.5	The Differential <i>Z</i> / γ Cross-Section	97
4.6	<i>Z</i> / γ^* +Jets: Computational Aspects	100
4.7	<i>Z</i> / γ^* +Jets at the LHC	103
4.7.1	<i>Z</i> / γ^* +Jets at the ATLAS Experiment	103
4.7.2	The <i>W</i> [±] +Jets to <i>Z</i> / γ^* +Jets Ratio at the ATLAS Experiment	109
4.7.3	<i>Z</i> / γ^* +Jets at the CMS Experiment	109
4.7.4	Differential Drell-Yan at the CMS Experiment	112
4.8	<i>Z</i> / γ^* +Jets Conclusions	115
5	Dijets and Gap Jets at ATLAS	117
6	<i>Z</i>/γ^*+Jets at 100TeV	126
7	Conclusions and Outlook	134
A	Next-to-leading order corrections for $\gamma^* \rightarrow q\bar{q}$	137
	Bibliography	148

List of Figures

2.1	The evolution of α_s over several orders of magnitude in the scale of the process Q^2 . The data points fitted are of varying degrees of formal accuracy ranging from next-to-leading order in α_s (NLO) to next-to-next-to-next-to-leading order in α_s (N^3LO). Fig. from [29].	17
2.2	Predictions for the average number of jets as a function of the sum of the transverse momenta in the event, H_T , for inclusive dijets at a 7 TeV LHC. Figure from [10].	22
2.3	Feynman diagrams for calculating the $O(\alpha_s)$ correction to $\gamma^* \rightarrow q\bar{q}$. Fig. (2.3a) is the leading order contribution, \mathcal{A}_0 . Figs. (2.3b)–(2.3d) are the virtual corrections \mathcal{A}_v , \mathcal{A}_{se1} and \mathcal{A}_{se2} respectively and figs. (2.3e)–(2.3f) are the real emission contributions \mathcal{A}_{r1} and \mathcal{A}_{r2} respectively.	23
2.4	The ratio of the inclusive Higgs plus three jet cross-section to inclusive Higgs plus two jet cross-section shown for centre-of-mass energies of 14TeV (similar to the current LHC), 33TeV and 100TeV (possible energy scales for a hadronic future circular collider).	29
2.5	The probability of a third jet emission in W^\pm plus inclusive dijets as a function of the rapidity gap between the two leading jets in rapidity at the D \emptyset experiment at the Tevatron experiment. The data are compared to a number of fixed-order generators plus the leading logarithmic accurate HEJ and the NLO accurate Blackhat+Sherpa	30
2.6	A simple importance sampling example (see eqn. (2.88)). The integrand, $f(x)$, is shown in blue, the importance sampling distribution is shown in green and, for comparison, the uniform probability density function used in the naïve case of no importance sampling is also shown (in red).	43
2.7	The absolute value squared of the Z^0 propagator for a range of values of the invariant mass squared of the Z^0 , p_Z^2 . We see that, as expected, it is strongly peaked at the Z^0 mass and, as such, is an ideal candidate for using importance sampling.	44
2.8	Recent parton distribution function fits from the HERA experiment. The observed variation in $f(x_{a/b}, Q^2)$, especially at high $x_{a/b}$, can be used to reduce the variance of a Monte Carlo approach to computing eqn (2.41) by using an importance sampling approach	44
3.1	The only diagram which contributes to $qQ \rightarrow qQ$ at leading order in α_s	49

3.2	The s , t and u channel diagrams contributing to $q^- g^+ \rightarrow q^- g^+$ at leading order in α_s in figs. (3.2a), (3.2b) and (3.2c) respectively.	50
3.3	The leading logarithmic contributions to $qg \rightarrow qg$ at NLO. The uncrossed diagram, $\mathcal{M}_{qQ \rightarrow qQ}^{\text{NLO},II}$, shown in (a) exchanges two gluons in the t channel and the crossed diagram, $\mathcal{M}_{qQ \rightarrow qQ}^{\text{NLO},X}$, case (b) exchanges two gluons in the u channel and is related to (a) (up to a colour factor) via a crossing symmetry	55
3.4	Three processes contributing to exclusive four jet production. (a) has the maximum number of gluons exchanged in the t -channels (three) and will dominate in the High Energy limit, (b) and (c) only have two and one gluon which can reggeise. As such as we move from (a) to (c) we will lose powers of large logarithms but maintain the same power of α_s and therefore we can reasonably approximate quad-jet production by neglecting (b) and (c) in the High Energy limit.	58
3.5	The limiting behaviour of $qg \rightarrow qg$ in the regions of phase space where either $y_g \gg y_q$ or $y_q \gg y_g$. The intermediate diagrams indicate the flow of colour through the process.	59
3.6	The 5 possible emission sites of extra QCD radiation in $qQ \rightarrow qQ$. Fig. from [20].	61
3.7	The average splitting function for HEJ and ARIADNE as a function of the transverse momentum, k_\perp . Emissions are required to be well separated from the emitting parton by enforcing a cut of $\Delta r \geq 0.5$ Figure from [19].	71
3.8	The average splitting function for HEJ and ARIADNE as a function of the collinearity, r . Emissions were kept from becoming soft by enforcing a cut on the transverse momentum of $k_\perp \geq 10$ GeV. Figure from [19].	72
3.9	The distribution of W^\pm plus inclusive dijets with at least 2 jets differential in the invariant mass of the leading dijets in p_\perp , m_{12} . Fig. from [5].	73
4.1	The possible emission sites for a neutral weak boson.	76
4.2	$\overline{ \mathcal{M}_{qg \rightarrow Zqg}^t ^2}$ shown for a slice through the final state phase-space defined by eqn. (4.5). We compare to the leading order result obtained from MadGraph_aMC@NLO	79
4.3	The matrix-element squared divided by the square of the partonic centre-of-mass energy for $qQ \rightarrow ZqQ$ with the Z^0 decaying to an electron-positron pair for the phase space slice described in eqn. (4.5). Increasing values of Δ represent increasing rapidity separation between the jets. The different lines show the contributions from different terms in the calculation: only emission from the forward or the backward quark line (black, dashed and green, dotted), their sum without the interference term (magenta, dotted) and their sum including interference (red, solid) which is seen to agree exactly with the LO result (blue, thick solid).	81

4.4	The matrix-element squared divided by the square of the partonic centre-of-mass energy for $qQ \rightarrow Z/\gamma^* qQ$ with the Z/γ^* decaying to an electron-positron pair. The $\mathcal{O}(\alpha_s^2 \alpha_W)$ tree-level contribution as described in HEJ (red, dashed) exactly matches that of <code>MadGraph_aMC@NLO</code> (blue, solid). The terms corresponding to the production of a Z^0 boson only (green, dotted) significantly undershoots the full result. The virtual photon terms are, therefore, clearly an important contribution to the matrix element away from the Z^0 Breit-Wigner peak.	83
4.5	A slice through phase space for the $Z/\gamma^* + 3$ jet final state. The slice defined is akin to that described for the 2 jet case in fig. (4.2) where as Δ increases we pull apart all three jets and the leptonic decay products are emitted increasingly far into the forward direction.	85
4.6	A slice through phase space for the $Z/\gamma^* + 3$ jet final state. The slice defined is akin to that described for the 2 and 3 jet case shown in fig. (4.2) and fig. (4.5) respectively.	86
4.7	Examples of both real and virtual diagrams contributing to $2 \rightarrow 3$ scattering. In fig. (4.7a) the p_2 has been drawn with a dashed line to denote it is not resolvable. In fig. (4.7b) the final state momenta have been labelled in a seemingly strange way - this was done to make clear the cancellation when working through the algebra.	94
4.8	The effect of varying λ_{cut} on the differential distribution in the rapidity gap between the two leading jets in p_\perp , $\Delta y_{j1,j2}$, with the $N_{jet} = 2, 3, 4$ exclusive selections shown from left to right. $\lambda_{cut} = 0.2$ (red), 0.5 (blue), 1.0 (green), 2.0 (purple). The bands represent the scale variation described in the text.	97
4.9	The effect of varying λ_{cut} on the differential distribution in the rapidity gap between the two extremal jets in rapidity, $\Delta y_{jf,jb}$, with the $N_{jet} = 2, 3, 4$ exclusive selections shown from left to right. $\lambda_{cut} = 0.2$ (red), 0.5 (blue), 1.0 (green), 2.0 (purple). The bands represent the scale variation described in the text.	97
4.10	These plots show the inclusive jet rates from (a) HEJ and (b) other theory descriptions and data [2]. HEJ events all contain at least two jets and do not contain matching for 5 jets and above, so these bins are not shown.	106
4.11	These plots show the invariant mass between the leading and second-leading jet in p_T . As in Fig. (4.10), predictions are shown from (a) HEJ and (b) other theory descriptions and data [2]. These studies will inform Higgs plus dijets analyses, where cuts are usually applied to select events with large m_{12}	106
4.12	The comparison of (a) HEJ and (b) other theoretical descriptions and data [2] to the distribution of the absolute rapidity difference between the two leading jets. HEJ and <code>Blackhat+Sherpa</code> give the best description.	107
4.13	These plots show the differential cross section in the ratio of the leading and second leading jet in p_T from (a) HEJ and (b) other theory descriptions and data [2].	107

4.14 The predictions of figs. (4.13a), (4.12a) and (4.11a) normalised to the total cross-section, with scale variation consistently applied to numerator and denominator.	108
4.15 The inclusive jet rates as given by (a) the HEJ description and (b) by other theoretical descriptions, both plots compared to the CMS data in [60].	111
4.16 The transverse momentum distribution of the second hardest jet in inclusive dijet events in [60], compared to (a) the predictions from HEJ and (b) the predictions from other theory descriptions.	111
4.17 The transverse momentum distribution of the third hardest jet in inclusive dijet events in [60], compared to (a) the predictions from HEJ and (b) the predictions from other theory descriptions.	112
4.18 Comparisons of HEJ and <code>MadGraph_aMC@NLO</code> to data from a CMS study of double-differential Drell-Yan production. Fig. (4.18a) shows the mass range focussed on the Z^0 peak (60-120 GeV), figs. (4.18b) and (4.18c) show the di-lepton invariant mass range from 30-60 GeV and lastly figs. (4.18d) and (4.18e) show the mass range from 120-1500 GeV. For figs. (2.9b-e) which probe regions away from the Breit-Wigner peak two HEJ lines are shown - figs. (4.18b) and (4.18d) use the naïve Breit-Wigner sampling while figs. (4.18b) and (4.18d) use a modified importance sampling scheme.	114
5.1 The gap fraction, $f(Q_0)$, as a function of (a) the rapidity gap, Δy in the 2010 data, and (b) the average p_T , $\bar{p_T}$, of the dijet system in the 2011 data.	121
5.2 The average number of jets, $\langle N_{\text{jets}} \text{ in the rapidity interval} \rangle$, in the rapidity gap bounded by the dijet system, as a function of (a) the rapidity gap, Δy , and (b) the average p_T , $\bar{p_T}$, of the dijet system.	122
5.3 The first azimuthal angular moment, $\langle \cos(\pi - \Delta\phi) \rangle$, as a function of (a) the rapidity gap, Δy and (b) the average p_T , $\bar{p_T}$, of the dijet system.	123
5.4 The ratio of the second azimuthal angular moment, $\langle \cos(2\Delta\phi) \rangle$, to the first azimuthal angular moment, $\langle \cos(\pi - \Delta\phi) \rangle$, as a function of (a) the rapidity gap, Δy , and (b) the average p_T , $\bar{p_T}$, of the dijet system.	124
5.5 The first azimuthal angular moment, $\langle \cos(\pi - \Delta\phi) \rangle$, for events passing the veto on gap activity above $Q_0 = 20\text{GeV}$ as a function of (a) the rapidity gap, Δy , and (b) the average transverse momentum, $\bar{p_T}$, of the dijet system.	124
5.6 The ratio of the second azimuthal angular moment, $\langle \cos(2\Delta\phi) \rangle$, to the first azimuthal angular moment, $\langle \cos(\pi - \Delta\phi) \rangle$, as a function of (a) the rapidity gap, Δy , and (b) the average p_T , $\bar{p_T}$, of the dijet system. A veto of $Q_0 = 20\text{GeV}$, for (a), and $Q_0 = 30\text{GeV}$, for (b), is applied on activity in the rapidity gap is applied.	125

6.1	Fig. (6.1a) - The differential cross-section for Z/γ^* plus inclusive dijets as a function of the azimuthal separation of the dijet system. Fig. (6.1b) - The cross-section for Z/γ^* plus inclusive dijets as a function of the number of jets, N_{jet}	128
6.2	Fig. (6.2a) - The differential cross-section for Z/γ^* plus inclusive dijets as a function of the absolute value of the rapidity gap between the dijets, $\Delta y^{j1,j2}$. Fig. (6.2b) - The differential cross-section for Z/γ^* plus inclusive dijets as a function of the invariant mass of the dijets, m^{jj}	130
6.3	The differential cross-section for Z/γ^* plus inclusive dijets as a function of the transverse momentum of the first, second and third leading jets in p_T shown in fig. (6.3a), (6.3b) and (6.3c) respectively.	132
6.4	The differential cross-section for Z/γ^* plus inclusive dijets as a function of the absolute value of the rapidity of the first, second and third leading jets in rapidity shown in fig. (6.4a), (6.4b) and (6.4c) respectively.	133

List of Tables

1.1	The fermion content of the standard model.	2
2.1	A graphical summary of the Feynman rules. The solid lines indicate a fermion (anti-fermion) propagator with momentum flowing parallel (anti-parallel) to the direction of the arrow. Similarly for the dashed lines which represent the ghost (anti-ghost) propagating and lastly the twisted lines depict a propagating gluon. As in the preceding equations i and j represent fundamental colour indices, a and b represent adjoint colour indices and, where present, f and f' represent fermion flavour. All Greek indices are Lorentz indices.	10
2.2	The Monte-Carlo approximation to eqn. (2.88) as we vary the number of sampled points, N , shown in the naïve sampling case and in the importance sampled case.	42
3.1	Some examples of $2 \rightarrow 2$ leading order matrix elements which contribute to the two jet exclusive cross-section.	60
4.1	The FKL-only cross sections for the 2-, 3- and 4-jet exclusive rates with associated statistical errors shown for different values of the regularisation parameter λ_{cut} . The scale choice was half the sum over all transverse scales in the event, $H_T/2$	96
4.2	The effect of matching on the total cross-section of the 2 jet final state FKL configurations.	100
4.3	The effect of matching on the total cross-section of the 3 and 4 jet final state FKL configurations.	101
4.4	The effect of matching on the total cross-section of the 2-, 3- and 4-jet final state non-FKL configurations.	102
4.5	Cuts applied to theory simulations in the ATLAS Z^0 -plus-jets analysis results shown in Figs. (4.10)–(4.13).	105
4.6	Cuts applied to theory simulations in the analysis of the ATLAS $W^\pm + \text{jets}/Z + \text{jets}$ ratio predictions shown in tabs. (4.7)–(4.8).	109
4.7	The HEJ prediction for inclusive R_{jet} rates at 2, 3 and 4 jets compared with ATLAS data.	109
4.8	The HEJ prediction for exclusive R_{jet} rates at 2, 3 and 4 jets compared with ATLAS data.	109

4.9	Cuts applied to theory simulations in the CMS Z^0 -plus-jets analysis results shown in Figs. (4.15)–(4.17)	110
4.10	Cuts applied to theory simulations in the CMS Drell-Yan analysis results shown in Figs. (4.18a)–(4.18e)	113
5.1	Cuts applied to theory simulations in the ATLAS dijets analyses. Q_0 is the gap jet veto scale. The results are shown in figs. (5.1)–(5.6).	117
6.1	Cuts applied to theory simulations for the 100 TeV Z -plus-jets analysis results shown in Figs. (6.1a)–(6.4c). We apply only one jet cut of 30 GeV to the jets in the 7 TeV analysis, shown in purple in the figures, but separately study the 100 TeV jets with cuts of 30 GeV, 60 GeV and 100 GeV shown in the figures in red, green and blue respectively.	127

Chapter 1

Introduction

1.1 A Little History

The Standard Model is a gauge quantum field theory describing three of the four observed fundamental forces - with the inclusion of gravity remaining elusive. Its local gauge structure is given by:

$$SU(3)_c \times SU(2)_L \times U(1)_Y. \quad (1.1)$$

The subscripts on the groups are simply a convenient notation. The ‘c’ on $SU(3)$ indicates that it is the strong ‘colour’ coupling being described. The ‘L’ on $SU(2)$ stands for left and indicates that all right-handed states are in the trivial representation of the group and the ‘Y’ on the $U(1)$ indicates that this is the hypercharge group and not the electromagnetic group.

The $SU(3)_c$ group describes the strong nuclear force (Quantum Chromodynamics or QCD) and its 8 gauge generators give us the massless spin-1 gluons, $G_a^\mu(x)$, $a = 1, \dots, 8$, present in the standard model. There are three weak boson states, $W_a^\mu(s)$, $a = 1, \dots, 3$, associated with the $SU(2)_L$ group and a further one, $B^\mu(x)$, which comes from the $U(1)_Y$ group.

The only remaining boson to complete the standard model arises from the complex scalar Higgs field whose ground state is not invariant under the action of $SU(2)_L \times U(1)_Y$. This field breaks the standard model gauge symmetry to

$$SU(3)_c \times U(1)_{em}, \quad (1.2)$$

where the $U(1)_{em}$ refers to the electromagnetic charge. After this ‘Spontaneous Symmetry Breaking’ occurs three of the four aforementioned bosons, $W_a^\mu(s)$ and $B^\mu(x)$ acquire mass and combinations of them are physically realised as the experimentally observed electroweak bosons; the massive states W^\pm, Z^0 and the massless photon, γ . The photon and the Z^0 bosons are of particular importance in the work that follows.

The fundamental particle content of the Standard Model also includes fermions. These are spin-1/2 particles which obey the spin-statistics theorem (and hence the Pauli exclusion principle) and comprise, along with the gluons which bind the nucleus together, all known visible matter in the universe. The fermions are structured in three so-called ‘generations’, shown in tab. (1.1) and can be further subdivided into quarks and leptons. Quarks are colour triplets under QCD but are also charged under the electroweak group. The up (u), charm (c) and top (t) quarks have electric charge $+\frac{2}{3}$ while the down (d), strange (s) and bottom (b) quarks have $-\frac{1}{3}$. Leptons are not charged under $SU(3)$ and so do not couple to the strong sector directly. The charged leptons e, μ and τ have electric charge -1 and the neutrinos are neutral.

	First Generation	Second Generation	Third Generation
Quarks	u, d	c, s	$t,$
Leptons	e, ν_e	μ, ν_μ	τ, ν_τ

Table 1.1: The fermion content of the standard model.

1.2 Thesis Outline

The aim of this thesis is to detail the importance of a certain class of perturbatively higher-order terms in events with QCD radiation in the final state. In particular we will consider high energy corrections to parton-parton collisions with a Z^0 or γ in association with high energy QCD radiation in the final state.

In chapter 2 I will begin by introducing quantum chromodynamics, the theory of the strong sector in the standard model, and detail how we might use this to calculate physical observables (such as cross-sections and differential distributions) at hadron colliders such as the Large Hadron Collider. I will discuss how these observables fall prey to divergences in QCD-like quantum field theories with massless states and talk briefly about how such divergences can be handled. I will then describe how the computationally expensive integrals derived in subsequent chapters may be efficiently evaluated using Monte-Carlo techniques.

In chapter 3 the details of QCD in the ‘High Energy’ limit are discussed. After completing a few instructive calculations we will see how, in this limit, the traditional fixed-order perturbation theory view of calculating cross-sections fades as another

subset of terms, namely the ‘Leading Logarithmic’ terms in $\frac{s}{t}$, become more important. I will discuss previous work in the High Energy limit of QCD and how this can be used to factorise complex parton-parton scattering amplitudes into contractions of ‘currents’ which, when combined with gauge-invariant effective gluon emission terms and the Lipatov ansatz for virtual corrections can be used to construct approximate high-multiplicity matrix elements.

In chapter 4 the work of the previous chapter is extended to the case where there is a massive Z^0 boson or an off-shell photon, γ^* , in the final state. A ‘current’ for this process is derived and the complexities arising from two separate sources of interference are explored. This new expression for the matrix element is seen to be in exact agreement when compared to the leading order in α_s generator **MadGraph5_aMC@NLO** (v5). The higher order corrections to this result must then be regularised to treat the divergences discussed in chapter 2 and this process is presented. The procedure for matching this regularised result to Leading Order results is shown and the importance of the inclusion of these non-resummation terms is discussed. Lastly, three comparisons of the High Energy Jets (often abbreviated to HEJ and pronounced “High”) Z+Jets Monte Carlo generator to recent experimental studies ATLAS and CMS at the LHC are shown and discussed.

In chapter 5 we discuss the results of a lengthy study of jet production from the ATLAS collaboration. This analysis was a thorough look at BFKL-like dynamics in proton-proton colliders and the HEJ predictions are seen to describe the data well in the regions of phase-space where we know the effects of our resummation become relevant. We compare the predictions from both partonic HEJ and HEJ interfaced with **ARIADNE**, a parton shower. Although the interface to **ARIADNE** increases the computational complexity significantly; we see that the corrections it contributes significantly improve the description of data.

In chapter 6 we show a study of Z/γ^*+ Jets at a centre-of-mass energy of 100 TeV relevant for the discussion of the next generation of high energy particle physics experiments (such as any Future Circular Collider) which are currently of great interest to the community at large. We see that the higher-order perturbative terms are much larger at 100 TeV relative to 7 TeV data and predictions. Moreover, the regions of phase-space relevant for this thesis; that of high energy wide-angle QCD radiation is especially enhanced and, therefore resumming these contributions will be essential for precision physics at any ‘Future Circular Collider’.

Finally, in chapter 7 I summarise the results of the above chapters and provide a short outlook for future work.

Chapter 2

Quantum Chromodynamics at Hadronic Colliders

2.1 The QCD Lagrangian

We obtain the QCD Lagrangian by considering the spin- $\frac{1}{2}$ Dirac Lagrangian for the case of a fermionic fields ψ each with mass m :

$$\mathcal{L}_D = \bar{\psi}_i (i\cancel{D} - m)_{ij} \psi_j, \quad (2.1)$$

where ψ_i is itself a vector of 3 fermion fields in the fundamental representation of $SU(3)$ with $i = 1, \dots, 3^1$. This is manifestly invariant under the *global* $SU(3)$ transformation

$$\psi_i \rightarrow e^{i\alpha^a T_{ij}^a} \psi_j \quad (2.2)$$

where $a = 1, \dots, 8$, α^a are constant and T^a are the generators of the $SU(3)$ group. We choose to promote this global symmetry to a *local* one by relaxing the constraint that α^a are constant and instead allow them to depend on a space-time coordinate i.e.

$$\alpha^a = \alpha^a(x^\mu). \quad (2.3)$$

¹The choice of 3 here is, again, well experimentally verified. Here we will work explicitly with the gauge group $SU(3)$ although many of the results which follow can be derived with a more general special unitary group $SU(N_c)$.

This breaks the $SU(3)$ symmetry but we can recover the required invariance by replacing the usual partial derivative term with a ‘covariant derivative’ defined by:

$$\mathcal{D}_{ij}^\mu = \partial_{ij}^\mu - ig_s A^{\mu a} T_{ij}^a, \quad (2.4)$$

where g_s is the QCD coupling constant and A_μ^a is the QCD gauge field associated with the gluon. With this replacement the local $SU(3)$ invariance of eqn. (2.1) is recovered. We must also include the effect of the kinetic term for the gluon field in our theory which we do by considering the field-strength tensor for A_μ^a , $F_{\mu\nu}^a$. This is given by:

$$F_{\mu\nu}^a = \partial_\mu A_\nu^a - \partial_\nu A_\mu^a + g_s f^{abc} A_\mu^b A_\nu^c \quad (2.5)$$

where f^{abc} are constants which define the algebra of the $SU(3)$ group and are given by

$$[T^a, T^b] = if^{abc} T^c. \quad (2.6)$$

Eqn. (2.6) is what makes QCD fundamentally different from Quantum Electrodynamics (QED): the simple fact that the generators of the underlying group *do not* commute makes performing calculations in QCD significantly more complicated than its Abelian cousin QED.

In summary then, the QCD Lagrangian is given by

$$\mathcal{L}_{\text{QCD (classical)}} = -\frac{1}{4} F_{\mu\nu}^a F^{a\mu\nu} + \sum_{f=1}^6 \bar{\psi}_i^{(f)} (i\cancel{D} - m_f)_{ij} \psi_j^{(f)}, \quad (2.7)$$

where we have now generalised to the experimentally proven case of 6 ‘flavours’ of quark in our model (outlined previously in tab. (1.1)). This is referred to as the ‘classical’ QCD Lagrangian since we have not included quantum effects such as loop corrections. The full ‘quantum’ Lagrangian is as follows [67]:

$$\mathcal{L}_{\text{QCD}} = \sum_{f=1}^6 \bar{\psi}_i^{(f)} (i\cancel{D}^{ij} - m_f)_{ij} \psi_j^{(f)} - \frac{1}{4} F_{\mu\nu}^a F^{a\mu\nu} - \frac{(\partial^\mu A_\mu^a)^2}{2\xi} + (\partial^\mu \bar{c}^a) \mathcal{D}_\mu^{ab} c^b, \quad (2.8)$$

where \mathcal{D}_μ is the covariant derivative in the adjoint representation given by

$$\mathcal{D}_\mu^{ab} = \delta^{ab}\partial_\mu - g_s f^{abc} A_\mu^c. \quad (2.9)$$

The final two terms arise from the treatment of a degeneracy in the QCD path integral which is caused by the gauge symmetry we enforced earlier - as a result we are only able to define a gluon propagator once we have “fixed the gauge” which is achieved by including by the penultimate term in eqn. (2.8). ξ is a free parameter in this process and, as we will see when we come to define the gluon propagator, it’s choice *defines* a specific gauge. The final term is a mathematical quirk of this process and c and \bar{c} represent the resulting QCD “ghost” and “anti-ghost” fields respectively. They are unphysical since they represent spin-0 anti-commuting fields.

2.2 The Partonic Cross-Section

Now we have a complete Lagrangian for QCD we can begin to move towards physical observables. The first step towards this is the Lehman-Symanzik-Zimmerman (LSZ) reduction formula. This gives us a relation between the scattering amplitude from some initial state into some final state, $\langle f|i\rangle \equiv \langle f|S|i\rangle$ where S is the scattering matrix, and a time-ordered vacuum expectation operator of a product of fields. Here we briefly present the argument behind the LSZ formula for the case of $2 \rightarrow 2$ scattering using scalar phi-cubed theory for simplicity. The Lagrangian for this theory is given by:

$$\mathcal{L}_{\text{phi-cubed}} = \frac{1}{2}\partial^\mu\phi\partial_\mu\phi + \frac{m^2}{2}\phi^2 - \frac{g}{6}\phi^3. \quad (2.10)$$

We can Fourier expand the field, $\phi(x)$, in terms of its annihilation and creating operators as follows:

$$\phi(x) = \int \frac{d^4k}{2E(2\pi)^3} \left(a(\vec{k})e^{ik\cdot x} + a^\dagger(\vec{k})e^{-ik\cdot x} \right), \quad (2.11)$$

and inverting this we find the following form for the creation operator $a^\dagger(\vec{k})$:

$$a^\dagger(\vec{k}) = i \int d^3x e^{-ix\cdot k} (\partial_0 - E)\phi(x). \quad (2.12)$$

We expect that as time flows forward to $+\infty$ (or backwards to $-\infty$) the field, $\phi(x)$, become asymptotically free and therefore we can neglect any interaction effects in these

extremes. From eqn. (2.12) it is straightforward to show that:

$$a^\dagger(\vec{k}, t = \infty) - a^\dagger(\vec{k}, t = -\infty) = i \int d^4x e^{-ix \cdot k} (\partial^2 + m^2) \phi(x). \quad (2.13)$$

Clearly this would be zero if we only consider the free theory where $g = 0$ in eqn. (2.10) - intuitively this is correct since once we remove any interaction terms a state we create at $t = -\infty$ should flow to $t = \infty$ unaltered. However, more generally for an interacting theory it will be non-zero and eqn. (2.13) gives us a relationship between asymptotically free initial and final states. Using eqn. (2.13) (and its hermitian conjugate) we can begin to look at the scattering from a 2 particle initial state $|i\rangle$ to some 2 particle final state $|f\rangle$, $k_1 + k_2 \rightarrow k'_1 + k'_2$, this is given by:

$$\langle i|j\rangle \equiv \langle 0|T \left(a(\vec{k}_1, \infty) a(\vec{k}_2, \infty) a^\dagger(\vec{k}_1, -\infty) a^\dagger(\vec{k}_2, -\infty) \right) |0\rangle, \quad (2.14)$$

where T denotes the time-ordered product of operators. After substituting for the a and a^\dagger operators and seeing that the time-ordering means that all of the remaining annihilation/creation operators end up acting on a vacuum state which they annihilate we are left with:

$$\begin{aligned} \langle i|j\rangle = i^4 \int d^4x'_1 d^4x'_2 d^4x_1 d^4x_2 & e^{ik'_1 \cdot x'_1} (\partial_{x'_1}^2 + m^2) e^{ik'_2 \cdot x'_2} (\partial_{x'_2}^2 + m^2) \times \\ & e^{ik_1 \cdot x_1} (\partial_{x_1}^2 + m^2) e^{ik_2 \cdot x_2} (\partial_{x_2}^2 + m^2) \times \\ & \langle 0|T (\phi(x'_1) \phi(x'_2) \phi(x_1) \phi(x_2)) |0\rangle. \end{aligned}$$

This is the LSZ reduction formula for $2 \rightarrow 2$ scattering in phi-cubed theory. It reduces the problem of finding scattering amplitudes to the calculation of time-ordered product of fields under the assumption that we may treat the fields at $t = \pm\infty$ as free.

The next step is to see how we can calculate these time-ordered products. This is most conveniently done by taking functional derivatives of the QCD path integral given by:

$$\mathcal{Z}[J, \eta, \bar{\eta}, \chi, \bar{\chi}] = \int \mathcal{D}A \mathcal{D}\psi \bar{\psi} \mathcal{D}c \bar{c} e^{i \int d^4x (\mathcal{L}_{QCD} + A^a \mu J_\mu^a + \bar{\psi}^a \eta^a + \bar{\eta}^a \psi^a + \bar{c}^a \chi^a + \bar{\chi}^a c^a)}, \quad (2.15)$$

where $J^{a\mu}$, η^a , $\bar{\eta}^a$, χ^a and $\bar{\chi}^a$ are ‘source’ terms which we target with functional derivatives and we have left the sum over quark flavours implicit. In order to proceed we

break down eqn. (2.1) into a free Lagrangian, $\mathcal{L}_{\text{QCD},0}$, and an interacting Lagrangian, $\mathcal{L}_{\text{QCD},I}$ as follows:

$$\begin{aligned}\mathcal{L}_{\text{QCD}} &= \mathcal{L}_{\text{QCD},0} + \mathcal{L}_{\text{QCD},I}, \\ \mathcal{L}_{\text{QCD},0} &= \bar{\psi}_i (i\cancel{D} - m)_{ij} \psi_j - \frac{1}{4} (\partial_\mu A_\nu^a - \partial_\nu A_\mu^a) (\partial^\mu A^\nu{}^a - \partial^\nu A^\mu{}^a) \\ &\quad - \frac{(\partial^\mu A_\mu^a)^2}{2\xi} + (\partial^\mu \bar{c}^a) (\partial_\mu c^a), \\ \mathcal{L}_{\text{QCD},I} &= g_s \bar{\psi}^i T_{ij}^a \gamma^\mu \psi^j - \frac{g_s}{2} f^{abc} (\partial_\mu A_\nu^a - \partial_\nu A_\mu^a) A^{b\mu} A^{c\nu} \\ &\quad - \frac{g_s^2}{4} f^{abe} f^{cde} A_\mu^a A_\nu^b A^{c\mu} A^{d\nu} - g_s f^{abc} \partial^\mu \bar{c}^a c^b A_\mu^c.\end{aligned}$$

We can then rewrite eqn. (2.15) as a combination of functional derivatives acting on the free QCD path integral, \mathcal{Z}_0 as:

$$\begin{aligned}\mathcal{Z}[J, \eta, \bar{\eta}, \chi, \bar{\chi}] &= \exp \left[i \int d^4x \mathcal{L}_{\text{QCD},I} \left(\frac{\delta}{i\delta J^{a\mu}}, \frac{\delta}{i\delta \eta^a}, \frac{\delta}{i\delta \bar{\eta}^a}, \frac{\delta}{i\delta \xi^a}, \frac{\delta}{i\delta \bar{\xi}^a} \right) \right] \\ &\quad \times \mathcal{Z}_0[J, \eta, \bar{\eta}, \chi, \bar{\chi}],\end{aligned}\tag{2.16}$$

where \mathcal{Z}_0 is identical to eqn. (2.15) but with the free Lagrangian in place of the full Lagrangian. We can solve \mathcal{Z}_0 exactly which yields the propagators for the gluons, quarks and ghosts, respectively:

$$\langle 0 | A_a^\mu(x) A_b^\nu(y) | 0 \rangle = \int \frac{d^4k}{(2\pi)^4} e^{-ik \cdot (x-y)} \delta_{ab} \frac{i}{k^2} \left(g^{\mu\nu} - (1-\xi) \frac{k^\mu k^\nu}{k^2} \right),\tag{2.17a}$$

$$\langle 0 | \bar{\psi}_i^{(f)}(x) \psi_j^{(f')}(y) | 0 \rangle = \int \frac{d^4k}{(2\pi)^4} e^{-ik \cdot (x-y)} \delta_{ij} \delta_{ff'} \frac{i(\not{k} + m)}{k^2 - m^2},\tag{2.17b}$$

$$\langle 0 | \bar{c}_a(x) c_b(y) | 0 \rangle = \int \frac{d^4k}{(2\pi)^4} e^{-ik \cdot (x-y)} \delta_{ab} \frac{i}{k^2}.\tag{2.17c}$$

We can read off the remaining QCD vertex factors directly from the interaction Lagrangian (or - more rigorously derive them by Taylor expanding eqn. (2.16) and disregarding any irrelevant diagrams such as those where no scattering occurs or those with bubble contributions). We will use $u(p)$ and $v(p)$ are Dirac spinors which solve the free Dirac equation for a plane-wave:

$$(i\gamma^\mu - m)u(p) = 0 \quad (i\gamma^\mu + m)v(p) = 0. \quad (2.18)$$

The full set of rules for the vertices and propagators are summarised in tab. (2.1) and the remaining *Feynman rules* may be summarised as:

1. Incoming external lines with spin s and momentum p are given a factor of $u_i^{(s)}(p)$ or $\bar{v}_i^{(s)}(p)$ for quarks or anti-quarks. Similarly outgoing external quark or anti-quark lines get a factor $\bar{u}_i^{(s)}(p)$ or $v_i^{(s)}(p)$. If the external particles are not coloured the procedure is the same but of course the spinors will no longer be $SU(3)$ fundamental vectors. External gluons with momentum p , polarisation ϵ and colour a are replaced by $\epsilon^a(p)$ or $\epsilon^{a*}(p)$ for either incoming or outgoing states.
2. For each vertex or propagator in the Feynman diagram insert the corresponding mathematical expression (see tab. (2.1)). The order of the Lorentz indices must be the same as that found by tracing the fermion lines in the diagram backwards,
3. A factor of (-1) must be included for each anti-fermion line flowing from the initial state to the final state,
4. A factor of (-1) must be included for each fermion, anti-fermion or ghost loop in the diagram
5. An integration over any unconstrained momenta in the diagram must be included with measure:

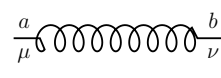
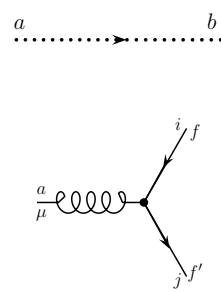
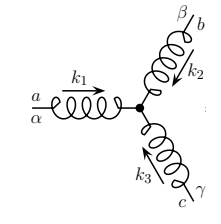
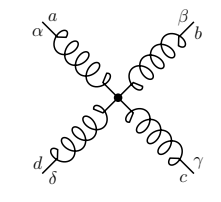
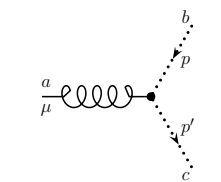
$$\int \frac{d^4k}{(2\pi)^4}, \quad (2.19)$$

where k is the momenta in question and the integral is understood to run over all four momentum components from zero up to infinity,

6. A diagram dependent symmetry factor must be included,
7. Lastly, for an unpolarised calculation we must sum over initial spin and colour and average over all possible final spins and colours.

The result of following these Feynman rules is what we refer to as the matrix element, $i\mathcal{M}$. We will now detail how we go from the matrix element of some scattering process to a useful physical observable: the *partonic cross-section*, $\hat{\sigma}$. The matrix element is related to the fully-differential cross-section by ‘Fermi’s golden rule’ which, for a scattering process $p_a + p_b \rightarrow p_1 + \dots + p_m$ is given by

Table 2.1: A graphical summary of the Feynman rules. The solid lines indicate a fermion (anti-fermion) propagator with momentum flowing parallel (anti-parallel) to the direction of the arrow. Similarly for the dashed lines which represent the ghost (anti-ghost) propagating and lastly the twisted lines depict a propagating gluon. As in the preceding equations i and j represent fundamental colour indices, a and b represent adjoint colour indices and, where present, f and f' represent fermion flavour. All Greek indices are Lorentz indices.

	$\frac{i\delta_i^j \delta_f^{f'}(\not{k} + m)}{k^2 - m^2}$
	$-\frac{i\delta_a^b}{k^2} \left(g^{\mu\nu} - (\xi - 1) \frac{k^\mu k^\nu}{k^2} \right)$
	$-ig_s \gamma^\mu \delta_f^{f'} T_{ij}^a$
	$-g_s f^{abc} \left(g^{\alpha\beta} (k_1 - k_2)^\gamma + g^{\beta\gamma} (k_2 - k_3)^\alpha + g^{\gamma\alpha} (k_3 - k_1)^\beta \right)$
	$-ig_s^2 \left(f^{abe} f^{cde} (g^{\alpha\gamma} g^{\beta\delta} - g^{\alpha\delta} g^{\beta\gamma}) + f^{ace} f^{bde} (g^{\alpha\beta} g^{\gamma\delta} - g^{\alpha\delta} g^{\gamma\beta}) + f^{ade} f^{bce} (g^{\alpha\beta} g^{\delta\gamma} - g^{\alpha\gamma} g^{\delta\beta}) \right)$
	$if^{abc} p_\mu'$

$$\begin{aligned}
 d\hat{\sigma} = & \frac{|\mathcal{M}(p_a + p_b \rightarrow p_1^{(f)}, \dots, p_m^{(f)})|^2}{F} \\
 & \times (2\pi)^4 \delta^{(4)}(p_a + p_b - p_1 - \dots - p_m) \\
 & \times \frac{d^3 \vec{p}_1}{2E_1(2\pi)^3} \cdots \frac{d^3 \vec{p}_m}{2E_m(2\pi)^3},
 \end{aligned} \tag{2.20}$$

where $F = 4\sqrt{(p_a p_b)^2 - m_a^2 m_b^2}$ is the flux of the incoming particles and the delta function enforces momentum conservation for the process.

We now have a procedure for going from a scattering process we wish to calculate to the partonic cross-section for that process (this discussion will be continued in subsequent chapters to include the considerations of parton distribution functions and jet clustering algorithms for the initial and final states respectively).

2.3 Divergences and Regularisation

In the preceding section we saw that any unconstrained momenta in a Feynman diagram must be integrated over to account for all possible ways the momenta in the process may flow. We refer to these contributions as loop-level corrections. When calculating these corrections we encounter divergences of various kinds which can be divided up into three classes based on how they arise.

2.3.1 Ultraviolet divergences

Ultraviolet divergences (UV) occur when all the components of a loop momenta grow large, $k \rightarrow \infty$, such that k^2 becomes the dominant term in propagator. Since these extremely high momentum modes correspond to physics at very short distance scales we choose to interpret these divergences as an indication that our theory is only an effective theory and we shouldn't attempt to apply it to all scales. We can quickly spot diagrams with these pathologies with a power counting argument. For example, one might have a diagram which results in a term such as the following:

$$\int \frac{d^4 k}{k^2(k^2 - m^2)}, \tag{2.21}$$

where m is some finite mass. In the UV region where $k \rightarrow \infty$ this is asymptotically

equal to:

$$\sim \int \frac{d^4 k}{k^4}, \quad (2.22)$$

which is clearly logarithmically divergent.

2.3.2 Infrared and collinear divergences

Infrared and collinear divergences (IRC) occur in theories with massless gauge bosons, such as the gluon in QCD, since a particle may emit any number of arbitrarily such bosons with infinitesimally small energy and we would never be able to resolve them. In contrast to the UV divergences the IR becomes important in the region of phase space where $k^2 \rightarrow 0$. A similar power counting analysis to that above can be applied here. For example if we consider the one-loop correction to the vertex diagram in massless phi-cubed from section (2.2) we would find an integral of the form [74]:

$$I = \int \frac{d^4 k}{(2\pi)^4} \frac{1}{k^2(p_1 - k)^2(p_2 + k)^2}, \quad (2.23)$$

where k is the loop momentum, $q = p_1 + p_2$ is the incoming momentum and p_i the outgoing momenta. Writing each momentum in light-cone coordinates with p_1 in the plus-direction, p_2 in the minus-direction, such that:

$$p_1 \sim (p_1^+, 0, \vec{0}) \quad p_2 \sim (0, p_2^-, \vec{0}). \quad (2.24)$$

and taking the Eikonal approximation, we have:

$$\begin{aligned} I &= \int \frac{dk^+ k^- k_T^2}{(2\pi)^4} \frac{1}{(2k^+ k^- - k_T^2)(-2p_1^+ k^-)(2p_2^- k^+)}, \\ &= \frac{1}{2q^2} \int \frac{dk^+ k^- k_T^2}{(2\pi)^4} \frac{1}{(2k^+ k^- - k_T^2)(-k^-)(k^+)}, \end{aligned} \quad (2.25)$$

where $q^2 = 2p_1 \cdot p_2$ since p_i are massless. Here we can further subdivide the divergences into a ‘soft’ sector and a collinear one.

Considering first the soft regime where we let all the components of our integration variable, k_μ become small at the same rate, that is, $k^\mu \sim \lambda\sqrt{q^2}$ where $\lambda \rightarrow 0$ then after a change of variables eqn. (2.25) becomes:

$$I \sim \int \frac{d^4\lambda}{\lambda^4}, \quad (2.26)$$

which diverges logarithmically for small lambda. The collinear sector follows similarly if we now look at the following scaling:

$$k^\pm \sim \sqrt{q^2} \quad k^\mp \sim \lambda^2 \sqrt{q^2} \quad k_T^2 \sim \lambda \sqrt{q^2}. \quad (2.27)$$

As we decrease λ we make k_μ increasingly collinear to either p_1 or p_2 . Using this scaling we exactly reproduce eqn. (2.26) and therefore we also have a collinear divergence.

2.3.3 Regularising divergences

If we are to extract any useful information from diagrams contributing above leading-order we must find ways to control these divergences. These methods are called ‘regularisation schemes’. The general approach with all regularisation schemes is to introduce a new parameter to the calculation which is used to get a handle on exactly how the integral diverges. Once we have performed the integration we take the limiting case where the effect of the regulator vanishes and we will see that the divergence now presents itself as some singular function of the regulator. There are many ways to regularise divergences each with their own advantages and disadvantages. Here we briefly describe three common approaches.

Given that the integrands seen so far only diverge in certain regions (very large or very small momenta) perhaps the most obvious thing to do is to manually alter the limits of our integration. This is the momentum cut-off scheme. We simply replace the upper (lower) bound with some finite large (small) value, Λ^2 . This will regulate any UV (soft) divergences and allow us to complete the calculation provided there are no collinear singularities which this approach cannot regulate. While this method has the advantage of being conceptually very simple it also has the disadvantage of breaking translational and gauge invariance. Worse still is that simply limiting the integration to avoid the extremities has no effect on the collinear sector.

An alternative which *does* keep both gauge and translational invariance is the Pauli-Villars regularisation scheme [69]. In this picture we introduce an extra field which has the opposite spin-statistics and therefore has the effect of suppressing the very high mass region in the integrand as follows

$$\int \frac{d^4 k}{(2\pi)^4} \frac{1}{p^2 - m^2} \rightarrow \int \frac{d^4 k}{(2\pi)^4} \left(\frac{1}{p^2 - m^2} - \frac{1}{p^2 - M^2} \right), \quad (2.28)$$

where M is the mass of the Pauli-Villars field with $m \ll M$. However, once again this does not treat any problems in the IRC sectors.

Lastly we have dimensional regularisation. Here we analytically continue the number of dimensions in our integral away from $d = 4$. We still want to be able to return to our physical four dimensional theory and so we choose

$$d = 4 - 2\epsilon \quad (2.29)$$

where ϵ is the regulator by which we control the divergence. Clearly then the limit $\epsilon \rightarrow 0$ would recover our original theory. It is worth noting that there are many conventions for defining epsilons but up to signs and factors of 2 they are equivalent. Dimensional regularisation treats both the UV and the IRC divergences and translational and gauge invariance are preserved. The disadvantage is that this modification changes the Dirac algebra relations which typically makes computing the integrals more involved.

When working in d dimensions the QCD coupling is no longer dimensionless. We can see this since the action is dimensionless and therefore we have

$$[\mathcal{L}] = d. \quad (2.30)$$

By considering the kinetic terms of the gluon and quark fields we can see that we must have

$$[g] + 2[\psi] + [A_\mu] = d, \quad (2.31)$$

and therefore

$$[g] = \frac{4-d}{2}. \quad (2.32)$$

In order to artificially fix this and restore the coupling to its dimensionless state we introduce a scale parameter, μ_r , as follows:

$$g = g_0 \mu_r^{\frac{4-d}{2}}. \quad (2.33)$$

The introduction of this scale has important consequences for our theory. Here we follow the instructive example from [70]. Say we have some dimensionless observable, R , which depends on one large scale, Q , which is much larger than all other scales in the problem (e.g. the quark masses). One would assume that R is approximately independent of this large scale but when we come to regulate and renormalise the divergences we have seen in this section the problem becomes one involving two scales and R develops a dependence on the ratio of these scales, $\frac{Q^2}{\mu_r^2}$. Since μ_r is completely arbitrary R must be independent of it for our theory to give meaningful predictions i.e if we now consider R as a function of both the QCD coupling strength, α_s , and the ratio of the scales we must have that

$$\mu_r^2 \frac{\partial R}{\partial \mu_r^2} + \mu_r^2 \frac{\partial \alpha_s}{\partial \mu_r^2} \frac{\partial R}{\partial \alpha_s} = 0. \quad (2.34)$$

For convenience we define $t = \ln \frac{Q^2}{\mu_r^2}$ and $\beta(\alpha_s) = \mu_r^2 \frac{\partial \alpha_s}{\partial \mu_r^2}$ and so we can write (2.34) as

$$\frac{\partial R(e^t, \alpha_s)}{\partial t} - \beta(\alpha_s) \frac{\partial R(e^t, \alpha_s)}{\partial \alpha_s} = 0. \quad (2.35)$$

This can be solved by defining the ‘running QCD coupling’, $\alpha = \alpha(Q^2)$

$$t = \int_{\alpha_s}^{\alpha(Q^2)} \frac{dx}{\beta(x)}, \quad (2.36)$$

where $\alpha = \alpha(Q^2)$ admits the boundary condition $\alpha(\mu_r^2) = \alpha_s$. Therefore the scale dependence of our observable R comes about through its dependence on α_s only.

2.4 The QCD Beta Function

QCD has two striking features which are not immediately apparent from the Lagrangian derived above. The first is asymptotic freedom. This is the fact that at *high* energies the QCD coupling strength becomes increasingly weak and it is this which allows us to perform a perturbative expansion of physical observables such as cross-sections. The

second feature is confinement. Confinement is the reason we do not observe bare quarks and gluons in nature, instead we only see colourless bound states of these fundamental QCD partons. This is because at very *low* energies the coupling strength becomes increasingly strong.

As we saw in section 2.3 when we renormalise QCD to remove the ultraviolet singularities we introduce a scale dependence in the coupling strength, $\alpha_s = \alpha_s(\mu_r)$. This can be interpreted as a measure of our ignorance of the true high-scale theory which governs nature, that is to say, we believe QCD is the right theory *only up to* some scale μ_r . The evolution of α_s with μ_r is given by the renormalisation group equation:

$$\mu_r^2 \frac{\partial \alpha_s}{\partial \mu_r^2} = \beta(\alpha_s(\mu_r^2)), \quad (2.37)$$

where $\beta(\alpha_s)$ is the beta function. It can be expanded perturbatively as a series in α_s as follows:

$$\beta(\alpha_s) = -\beta_0 \alpha_s (1 + \beta_1 \alpha_s + \beta_2 \alpha_s^2 + \dots), \quad (2.38)$$

where the perturbative coefficients, β_i , can be calculated using the methods of section (2.2). For example the leading order contribution, β_0 , is given by:

$$\beta_0 = 11 - \frac{2n_f}{3}. \quad (2.39)$$

If we truncate eqn. (2.38) at leading-order in α_s then we can solve eqn. (2.37) and we see that the coupling, $\alpha_s(\mu_r)$, ‘runs’ with the following form:

$$\alpha_s(Q^2) = \frac{\alpha_s(\mu_r^2)}{1 + \alpha(\mu_r^2) \frac{\beta_0}{4\pi} \ln \frac{Q^2}{\mu_r^2}}. \quad (2.40)$$

It is clear from this (since in the standard model we have $n_f \leq 6$ and therefore $\beta_0 > 0$)² that as Q^2 tends to zero the coupling strength becomes very large and at high values for Q^2 we see that $\alpha_s(Q^2) \rightarrow 0$. This latter limit is exactly the asymptotic freedom property of QCD and it holds even when we include the higher order terms we neglected in the

²The number of fermions we consider depends on the energy scale we are at. Clearly we must be at an energy larger than the mass of any given quark for it to be produced. This was experimentally observed in the famous R -ratio where the ratio of the $e^+e^- \rightarrow$ hadrons cross-section to the $e^+e^- \rightarrow \mu^+\mu^-$ cross-section was investigated

leading-order approximation used to arrive at eqn. (2.40) [29]. It is an essential result in that it allows us to perform perturbative expansions of observables and without this none of the following work would be possible. The evolution of the strong coupling with Q^2 is shown in fig. (2.1), it shows several extracted values of α_s based on six various types of experiment. For example, the hadronic collider predictions include studies of the ratio of the 3-jet inclusive cross-section to the 2-jet inclusive cross-section as a means of finding the strong coupling [38].

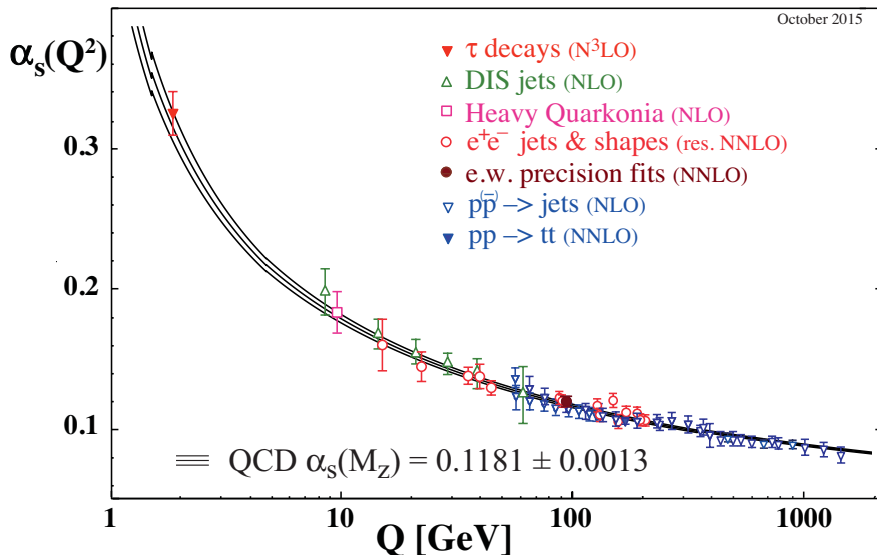


Figure 2.1: The evolution of α_s over several orders of magnitude in the scale of the process Q^2 . The data points fitted are of varying degrees of formal accuracy ranging from next-to-leading order in α_s (NLO) to next-to-next-to-next-to-leading order in α_s (N³LO). Fig. from [29].

2.5 QCD Factorisation at Hadronic Colliders

So far we have only talked about the very general idea of two particles interacting and scattering off one another into some final state which we are interested in. This is too simple a picture when we are considering hadronic colliders such as the Large Hadron Collider (proton-proton), the Tevatron (proton-antiproton), HERA (proton-lepton) or a potential Future Circular Collider (FCC) with a hadronic initial state.

At experiments we collide QCD bound states with one another but in practice when calculating cross-sections we perform a sum over the possible combinations of initial states we may encounter in the two incoming hadrons. In order to do this we must have a good understanding of the dynamics of the partons inside the onrushing hadrons;

this understanding is encoded in the Parton Distribution Functions (PDFs). A PDF, $f_{i/H}(x, Q^2)$ is a function which tells us how likely we are to find a parton of type i carrying a fraction, x , of the total hadron's momentum in a hadron, of type H , during a collision occurring at an energy scale Q . Because the PDFs contain non-perturbative information we cannot compute their properties in the same way as we calculate cross-sections, instead they are determined by fitting to data from a range of experiments (such as those mentioned above). Once we have the PDFs we can compute the physical hadronic cross-sections, σ , by convoluting two of them - one for each hadron - with the partonic cross-section for the scattering of partons of type i and j , $\hat{\sigma}_{ij}$, discussed in section (2.2) and summing over the possible initial partons as follows:

$$\sigma(Q^2) = \sum_{f_a, f_b} \int_0^1 dx_a dx_b f_{a/H_a}(x_a, Q^2) f_{b/H_b}(x_b, Q^2) \hat{\sigma}_{ij}(\alpha_s(\mu_r), \mu_r^2, \mu_f^2). \quad (2.41)$$

Eq. (2.41) can be intuitively understood as the separation of scales; the long distance physics of the PDFs is manifestly distinct from the short distance hard scatter contained in the partonic cross-section. The scale at which we separate the long and short range physics is called the *factorisation scale*, μ_f . As with the renormalisation scale it is not *a priori* clear what is the correct factorisation scale and results of perturbative calculations are often quoted with a ‘scale uncertainty’ band derived from varying this parameter.

2.6 From Partons to Jets

As alluded to in section (2.4) the computation of scattering amplitudes can only take us so far when comparing simulations to experiments. In particular, the final state quarks and gluons in our perturbative picture of QCD differ from the confined hadrons observed at hadronic colliders: It is well known that final state QCD partons fragment and emit showers of additional radiation before finally becoming colourless bound states in a process known as ‘hadronisation’. This process is not perturbatively well-understood since it occurs below a scale, Λ_{QCD} , at which QCD becomes non-perturbative, i.e. the coupling constant of the theory has become too large for us to legitimately truncate a perturbative expansion. There are models for both the ‘parton shower’ behaviour of the energetic final state partons, such as **Pythia** [73], **Herwig** [40] and **Sherpa** [57] as well as models for the hadronisation such as the ‘Lund string model’ [24] implemented in various physics software packages but most relevantly (for the remainder of this thesis) - in the **Ariadne** code [19, 64].

All high energy collider experiments see a great deal of QCD radiation in the final state. This radiation, produced through the mechanisms outlined above, appears in columnated structures called ‘jets’ and so it is at the jet level that we may compare our simulated results to actual measurements. The question of how we best map from the two or more parton level to the jet level is not a trivial one: a single high-energy (or ‘hard’) parton may split and form two final state jets but equally two low energy (or ‘soft’) partons may combine into a single jet.

There are several approaches to this problem include the **SISCone** algorithm [71] and Pythia’s own implementation **CellJet** [72]. However the most commonly used family of jet reconstruction algorithm are known as the ‘sequential recombination algorithms’. This group of approaches include the Cambridge-Aachen, k_T and anti- k_T algorithms. The general algorithm, as given in [35], is:

1. Given a list of final state partons calculate some generalised distance, d_{ij} , between all possible combinations of jets i and j as well as d_{iB} , for all i , where B is the beam-line,
2. We identify the smallest value of these. If, say d_{ab} is the smallest, we combine partons a and b . If however d_{aB} is the smallest then we call a a jet and remove it from the list of partons,
3. We then recompute all the generalised distances and repeat steps 1 and 2 until no further partons remain,

The generalised distances are defined as

$$d_{ij} = \min(k_{i\perp}^{2p}, k_{j\perp}^{2p}) \frac{\Delta R^2}{R^2}, \quad (2.42)$$

$$d_{iB} = k_{i\perp}^{2p},$$

where $k_{i\perp}$ is the transverse momentum of the i^{th} parton, R is a free parameter in the clustering which relates to the size of the jets and ΔR^2 is the distance in the detector metric between the two partons given by $\Delta R^2 = \Delta\phi^2 + \Delta y^2$ where $\Delta\phi$ and Δy are the angular distance (about the beam line) between the partons and the rapidity gap between the partons respectively. The parameter, p , specifies precisely which clustering algorithm we are using; $p = 0$ reduces eqn. (2.42) to the Cambridge-Aachen scheme while $p = \pm 1$ give the k_T and anti- k_T algorithms respectively. The question of which to use is outlined in detail in [35] but we give a brief summary here.

The choice of jet algorithm boils down to a handful of key properties the algorithm

must exhibit. Given a set of hard QCD final states we require that the result of the clustering algorithm, i.e. the jets and jet shapes, are not unduly sensitive to additional soft and collinear radiation. This is intuitively clear since, for example, a final state with a single high energy quark with momentum, k_{Ti} , may radiate infinitely a multitude of infinitely soft gluons, k_{Ts_i} , which may, or may not, be collinear to the original parton - but since $k_{Ts_i} \ll k_{Ti}$ the result must be a single jet, j_{Ti} , which has $j_{Ti} \sim k_{Ti}$. Any algorithm which satisfies this is said to be infra-red and collinear (IRC) safe. We also want an algorithm which is insensitive to the hadronisation model used, or any possible extra multiple-parton or experimental pile-up emissions since these things are, at present, poorly understood. It is also worth mentioning that since jet clustering algorithms are used in experimental triggers to quickly categorise events they should be as computationally cheap as possible.

Although the Cambridge-Aachen algorithm has advantages in some experimental searches such as studies where the substructure of jets is of particular interest [6,33], the most widely used sequential recombination algorithm is the anti- k_t algorithm ($p = -1$) and so all of the work which follows and all of the experimental comparisons made will use this as the method for mapping simulated parton level results to a more useful set of jet level results. The jet size parameter R varies between experiments but is typically either 0.4 for ATLAS analyses or 0.5 for CMS analyses.

2.7 Perturbative QCD and Resummation

In section 2.2 we saw that we could separate out the QCD Lagrangian into free and interacting components and that vacuum expectations of time ordered fields could be found by taking functional derivatives of the free partition function (eqn. (2.16)). Since terms which give rise to interactions in the Lagrangian come with a factor of the coupling strength, g , Taylor expanding the exponential in eqn. (2.16) will yield an infinite series of terms and, in principle, in order to compute any physical observable exactly we must calculate all of these. Of course in practice this is not possible. We must choose a subset of terms from this infinite array which we reason will give the best possible approximation to the full series.

2.7.1 Fixed-order Perturbation Theory

The fixed-order perturbative approach operates on the assumption that since, as we saw in section 2.4, the coupling strength α_s in the expansion becomes small at large energy scales we may simply truncate the series at some power of α_s . For example

given a cross-section of some scattering $X \rightarrow Y$ we wish to calculate, the fixed order picture of the expansion would be:

$$\sigma_{X \rightarrow Y} = \alpha_s^{i_0}(Q^2) \sum_{i=0}^N \alpha_s^i(Q^2) \mathcal{C}_{X \rightarrow Y}^{(i)} \quad (2.43)$$

where $\mathcal{C}_{X \rightarrow Y}^{(i)}$ are the coefficient terms which encode the kinematics of the diagrams contributing at each ‘order’ in the series. Since we expect that the more terms we can calculate the better our truncated series will approximate the full result we should choose N as large as possible though in principle it is determined by the complexity and the computational cost of the relevant calculation of the coefficient functions. Recent progress has allowed the automation of next-to-leading order QCD calculations ($N = 2$) in packages such as `MadGraph_aMC@NLO` (v5) [14], `BlackHat+Sherpa` [30], `MC@NLO` [49] and `Powheg` [48]. It is not known in general how to compute multi-loop ($N \geq 2$) calculations and while process specific calculations have been completed [34, 51, 53], it is still very much a hot topic in theoretical particle physics.

It is important to note the limitations of this fixed-order scheme. For example, if we were to consider NLO corrections to dijet production we would only be able to produce final states with two or three jets (since we can only have one extra real emission). Clearly this is a limitation since high energy partons can radiate arbitrarily many extra gluons into the final state. Fig. (2.2) shows precisely this phenomenon, the NLO calculations (shown in green and black) are limited to $\langle \text{jets} \rangle \leq 3$ while the predictions from `POWHEJ+PYTHIA` and `HEJ` which include higher-order corrections predict a higher average number of jets. Note that the higher-order corrections here are *not* the same in the case of `POWHEJ+PYTHIA` and `HEJ` (although the two predictions have been seen to both agree well with data in the past [10]). Also note that although the scale uncertainty band of the NLO calculation *does* exceed $\langle \text{jets} \rangle = 3$ this is not a result of the formalism but instead comes about as the result of the instability of NLO at large values of H_T . This scale dependence of observables will be discussed in more detail in chapter 3.

There are frameworks to allow the ‘merging’ of NLO calculations of different multiplicity. A comprehensive review of such methods may be found in [12].

We now summarise an instructive fixed-order calculation of the next-to-leading corrections to quark-antiquark pair production via an off-shell photon [45]. The full calculation can be found in appendix A.

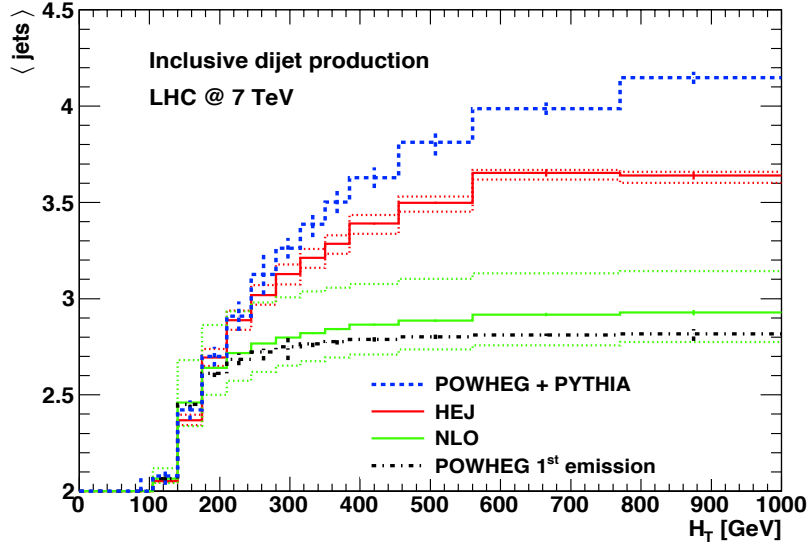


Figure 2.2: Predictions for the average number of jets as a function of the sum of the transverse momenta in the event, H_T , for inclusive dijets at a 7 TeV LHC. Figure from [10].

2.7.2 An Example Fixed-Order Calculation

The Feynman diagrams which need to be included for the leading order and next-to-leading order corrections to the $\gamma^* \rightarrow q\bar{q}$ process are shown in fig. (2.3). We refer to fig. (2.3a) as the tree level diagram, fig. (2.3b) as the vertex correction and figs. (2.3c) and (2.3d) as the self-energy corrections. Figs. (2.3e) and (2.3f) are the ‘real corrections’. Since the virtual corrections all have the same final state they must be summed and squared together. To make the order of each term in the perturbative expansion clear we extract the α_s factors from the \mathcal{A}_i here. Therefore:

$$\begin{aligned} |\mathcal{M}_{1 \rightarrow 2}|^2 &= |\mathcal{A}_0 + \alpha_s \mathcal{A}_v + \alpha_s \mathcal{A}_{se1} + \alpha_s \mathcal{A}_{se2}|^2 + \mathcal{O}(\alpha_s^2) \\ &= |\mathcal{A}_0|^2 + 2\alpha_s \Re\{\mathcal{A}_0^* \mathcal{A}_v\} + 2\alpha_s \Re\{\mathcal{A}_0^* \mathcal{A}_{se1}\} \\ &\quad + 2\alpha_s \Re\{\mathcal{A}_0^* \mathcal{A}_{se2}\} + \mathcal{O}(\alpha_s^2), \end{aligned} \quad (2.44)$$

We can see then that to $\mathcal{O}(\alpha_s)$ we have four contributions to consider, but the two self-energy contributions will have the same functional form so it would seem that in practice we only need to perform three calculations - it turns out this is not the case; we will find that the divergence associated with exchanging a soft gluon in fig. (2.3b) can only

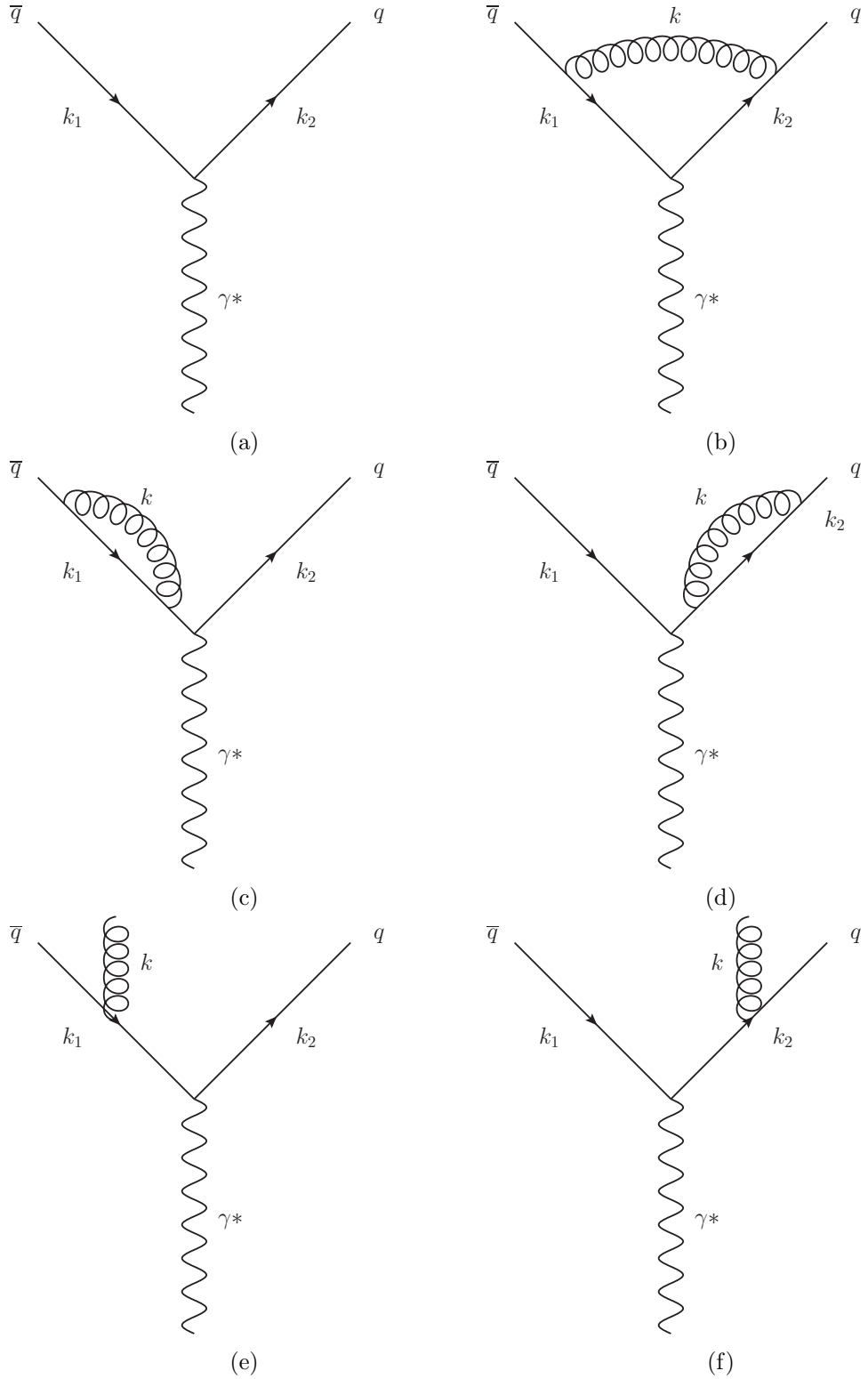


Figure 2.3: Feynman diagrams for calculating the $O(\alpha_s)$ correction to $\gamma^* \rightarrow q\bar{q}$. Fig. (2.3a) is the leading order contribution, \mathcal{A}_0 . Figs. (2.3b)–(2.3d) are the virtual corrections \mathcal{A}_v , \mathcal{A}_{se1} and \mathcal{A}_{se2} respectively and figs. (2.3e)–(2.3f) are the real emission contributions \mathcal{A}_{r1} and \mathcal{A}_{r2} respectively.

be cancelled if we also include the soft divergences that arise from figs. (2.3e) to (2.3f). At first glance this seems very peculiar since these diagrams have different final states and therefore should have no business contributing to this calculation. However, since the gluon can be emitted with vanishingly small momentum it would be experimentally impossible to detect and therefore the final states would look the same to an imperfect observer.

It is the cancellation of these divergences that will be shown in detail in the next two sections. Figs. (2.3a), (2.3b) and (2.3e) will be calculated in detail while the result for the self energy expressions will be omitted since it can be cancelled by choosing to work in the Landau gauge [45]. Since we expect both UV and IR divergences we choose to work in the dimensional regularisation scheme detailed previously.

The Leading Order Process

If we let the pair-produced quarks have charge $\pm Qe$ then we have:

$$\mathcal{A}_0 = -ieQ\bar{u}^{\lambda_2}(k_2)\gamma^\mu v^{\lambda_1}(k_1)\epsilon_\mu^r(p), \quad (2.45)$$

where we have used the QED Feynman rule for a quark-antiquark-photon vertex: $iQe\gamma^\mu$, the λ_i 's are the spins of the quarks, r is the polarisation of the incoming photon and $p = k_1 + k_2$ is the momentum carried by the incoming photon. Performing a sum over all polarisations, spins and colours and integrating of the two particle phase space in $d = 4 - 2\epsilon$ dimensions gives:

$$\sigma_0 = 3\alpha Q^2 \frac{\Gamma(\frac{d}{2})}{\Gamma(d-2)} \left(\frac{s}{4\pi\mu^2} \right)^{\frac{d}{2}-2}, \quad (2.46)$$

where we have neglected the quark mass terms since they are negligible in the High Energy limit. It is important to note that in the limit $\epsilon \rightarrow 0$ (i.e. $d \rightarrow 4$) the Born cross-section remains finite.

The Virtual $\mathcal{O}(\alpha_s)$ Corrections

The virtual correction graphs are shown in figs. (2.3b), (2.3c) and (2.3d). We will begin by calculating the second term in eqn. (2.44). Using the Feynman rules we have:

$$\mathcal{A}_v = \int \frac{d^d k}{(2\pi)^d} \bar{u}^{\lambda_2}(k_2) (-ig_s \mu^\epsilon \gamma^\alpha T_{ij}^a) \frac{i(\not{k}_1 + \not{k})}{(k_1 + k)^2} (-ieQ \gamma^\mu) \frac{i(\not{k}_2 - \not{k})}{(k_2 - k)^2}$$

$$(-g_s \mu^\epsilon \gamma^\beta T_{ij}^a) \epsilon_\mu^r(p) \frac{-i}{k^2} \left(g_{\alpha\beta} + (1 - \xi) \frac{k^\alpha k^\beta}{k^2} \right) v^{\lambda_1}(k_1).$$

$$\mathcal{A}_v = -ig_s^2 e Q \mu^{2\epsilon} \text{Tr}(T^a T^a) \bar{u}^{\lambda_2}(k_2) \int \frac{d^d k}{(2\pi)^d} \frac{\mathcal{N}_1(k_1, k_2, k)}{k^2 (k_1 + k)^2 (k_2 - k)^2} v^{\lambda_2}(k_2),$$

where the numerator of the fraction is given by:

$$\mathcal{N}_1(k_1, k_2, k) = \gamma^\alpha(\not{k}_1 + \not{k}) \gamma^\mu(\not{k}_2 - \not{k}) \gamma_\beta \left(g^{\alpha\beta} + (1 - \xi) \frac{k^\alpha k^\beta}{k^2} \right). \quad (2.48)$$

From eqn. (2.44) we see we need $\mathcal{A}_0^* \mathcal{A}_v$ and upon calculating that we are left with the cross-section contribution from the virtual diagrams in terms of the Born cross section:

$$\sigma_v = \frac{2\alpha_s}{3\pi} \sigma_0 \left[-\frac{8}{\epsilon^2} + \frac{1}{\epsilon} (6 - 4\gamma_E - 4L) + \gamma_E (3 - \gamma_E) - 8 + \frac{\pi^2}{6} + \pi^2 - L^2 - (2\gamma_E - 3)L \right], \quad (2.49)$$

where $L = \ln \left(\frac{s}{4\pi\mu^2} \right)$ and γ_E is Euler's constant. We can now see that the result for the vertex correction is gauge independent as the ξ dependence has completely cancelled. We also see that the parameter introduced to fix the coupling to be dimensionless, μ , appears in the final result; this is often the case when using dimensional regularisation and the modified minimal subtraction renormalisation scheme.

The Real $\mathcal{O}(\alpha_s)$ Corrections

The real gluon emission diagrams which contribute to the $\mathcal{O}(\alpha_s)$ corrections are figs. (2.3e) and (2.3f). These diagrams have an indistinguishable final state and so the real contribution, \mathcal{A}_r , will be of the form:

$$|\mathcal{A}_r|^2 = |\mathcal{A}_{left} + \mathcal{A}_{right}|^2 = |\mathcal{A}_{left}|^2 + |\mathcal{A}_{right}|^2 + 2\mathcal{A}_{left}\mathcal{A}_{right}^*, \quad (2.50)$$

where \mathcal{A}_{left} and \mathcal{A}_{right} refer to figs. (2.3e) and (2.3f) respectively and are given by:

$$\mathcal{A}_{left} = -Q e g_s T_{ij}^a \bar{u}(k_2) \gamma^\mu \frac{\not{k}_1 + \not{k}}{(k_1 + k)^2} \gamma^\nu v(k_1) \epsilon_\nu \eta_\mu, \quad (2.51a)$$

$$\mathcal{A}_{right} = -Q e g_s T_{ij}^a \bar{u}(k_2) \gamma^\nu \frac{\not{k}_2 + \not{k}}{(k_2 + k)^2} \gamma^\mu v(k_1) \epsilon_\nu \eta_\mu. \quad (2.51b)$$

In the calculation of the terms of eqn. (2.44) it will be useful to write the energy fractions for each particle as $x_i = \frac{2E_i}{\sqrt{s}}$ (where $i = 1$ is the external antiquark, $i = 2$ is the antiquark and $i = 3$ is the external gluon). In terms of these invariants the contraction of any two external particles simplifies to $p_i \cdot p_j = \frac{1}{2}s(1 - x_k)$ which (since we are still assuming our quarks can be taken to be massless) gives a simple expression for the Mandelstam variables. Evaluating the modulus squared terms gives:

$$|\mathcal{A}_{left}|^2 = \frac{Q^2 e^2 g_s^2}{(k_1 + k)^4} \text{Tr}(T^a T^a) \text{Tr}(\not{k}_2 \gamma^\mu (\not{k}_1 + \not{k}) \gamma^\nu \not{k}_1 \gamma_\nu (\not{k}_1 + \not{k}) \gamma_\mu), \quad (2.52a)$$

$$|\mathcal{A}_{right}|^2 = \frac{Q^2 e^2 g_s^2}{(k_2 + k)^4} \text{Tr}(T^a T^a) \text{Tr}(\not{k}_2 \gamma^\nu (\not{k}_2 + \not{k}) \gamma^\mu \not{k}_2 \gamma_\mu (\not{k}_2 + \not{k}) \gamma_\nu), \quad (2.52b)$$

$$\mathcal{A}_{left} \mathcal{A}_{right}^* = \frac{Q^2 e^2 g_s^2}{(k_2 + k)^2 (k_1 + k)^2} \text{Tr}(T^a T^a) \text{Tr}(\not{k}_2 \gamma^\mu (\not{k}_1 + \not{k}) \gamma^\nu \not{k}_1 \gamma_\mu (\not{k}_2 + \not{k}) \gamma_\nu). \quad (2.52c)$$

Summing these expressions and integrating over the three particle phase space yields:

$$\sigma_r = \frac{2\alpha_s}{3\pi} \sigma_0 \left[\frac{8}{\epsilon^2} + \frac{1}{\epsilon} (-6 + 4\gamma_E + 4L) - \gamma_E (3 - \gamma_E) - \frac{57}{6} + \frac{7\pi^2}{6} + L^2 + (2\gamma_E - 3)L \right].$$

for the real diagram contribution to the cross section. As in the case of the virtual corrections this is divergent in the limit $\epsilon \rightarrow 0$ and exhibits a residual dependence on μ .

Cancellation of divergences

Having now found the vertex corrections and the real corrections up to $\mathcal{O}(\epsilon^2)$ we can write the next-to-leading order cross-section by simply summing eqns. (2.49)

and (2.7.2):

$$\sigma_{NLO} = \sigma_r + \sigma_v = \frac{\alpha_s}{\pi} \sigma_0. \quad (2.53)$$

So the total cross-section to next-to-leading order accuracy is:

$$\sigma = \sigma_0 \left(1 + \frac{\alpha_s}{\pi} \right) + \mathcal{O}(\alpha_s^2). \quad (2.54)$$

The fact that the infrared divergences in both the real and virtual emission NLO diagrams cancel is an example of the KLN theorem [61] which states that the Standard Model is completely free of infrared divergences at all orders.

2.7.3 Resumming Higher-Order Corrections

As we have seen we can evaluate the truncated perturbative series and, provided we remember to include higher multiplicity diagrams which contribute in the soft limit, we will be left with a finite result which is invariant under gauge transformations.

It would seem then that this is the best way to proceed: we calculate as many corrections as we can and reason that all of the higher-order terms we have neglected are suppressed by powers of a small expansion parameter - the strong coupling, α_s . If this is indeed the case we should see that each time we go to a higher-order in perturbation theory our series begins to converge. For example the effect of the NLO terms should be small relative to the LO terms etc. It turns out that this is not true for all observables. To motivate this we give a schematic expansion of some variable we wish to calculate, \mathcal{O} :

$$\begin{aligned} \mathcal{O} = & \alpha_s (a_1 L^2 + b_1 L + c_1 1) + \\ & \alpha_s^2 (a_2 L^4 + b_2 L^3 + c_2 L^2 + d_2 L + e_2 1) + \\ & \alpha_s^3 (a_3 L^6 + b_3 L^5 + c_3 L^4 + d_3 L^3 + e_3 L^2 + f_3 L + g_3 1) + \dots, \end{aligned} \quad (2.55)$$

where L is some logarithm which may be large. A fixed-order scheme aims to exactly calculate as many of the rows of equation (2.55) as possible under the assumption that all remaining terms are sufficiently suppressed to ignore. The problem with this picture is that the logarithms may be large enough that the combination $\alpha_s^n L^{2n} \sim \mathcal{O}(1)$. In

this case it would appear that it would be better for us to calculate the first column of the terms (called the ‘leading logarithmic’ or LL approximation) than to find the first *row* of terms (the LO approximation).

Fig. (2.4) shows how the ratio of the inclusive Higgs-plus-three jet cross-section to inclusive Higgs-plus-two jet cross-section varies as a function of the rapidity gap between the two leading jets in p_T [16]. The HEJ prediction is formally leading logarithmic accurate (with leading order matching for final states with up to three jets) while MCFM [36] is formally next-to-leading order accurate. It is shown in chapter 3 that this rapidity gap is approximately equal to the logarithm, L . Hence, as we move to large $\Delta y(j_1, j_2)$ we increase the size of L in eqn. (2.55) and the terms neglected by the fixed-order scheme (but captured by a LL calculation) grow in size. The ratio of the inclusive $(n+1)$ -jet to n -jet cross-sections is an interesting probe of the convergence of the QCD perturbative expansion since we are directly comparing the size of the higher order contributions to the LO terms. Fig. (2.4a) shows that at a centre-of-mass energy of 14 TeV (the energy scales close to be being achieved at the LHC) even at *modest rapidity intervals* of around 4.0 we see that *half of all events* contain extra radiation and when we pull the leading jets apart further in rapidity this increases to three quarters of all events.

Furthermore, figs. (2.4b) and (2.4c) show that as we increase the centre-of-mass energy to that of a potential hadronic future circular collider, 33 TeV and 100 TeV respectively, these enhanced higher-order terms become even more important - in the case of dijets with a separation of $\Delta y(j_1, j_2) \approx 8.0$ at a 100 TeV collider *almost 90% of the cross-section* is coming from the next-to-leading term in the perturbative series: this is clear evidence that is not generally sufficient to think of the expansion as being controlled by only the strong coupling constant, α_s .

We can also test this against existing data; fig. (2.5) show the probability of extra jet activity in inclusive W^\pm -plus-dijets as a function of the rapidity gap between the two leading jets *in rapidity*, $\Delta y(j_F, j_B)$, taken from a very detailed study by the D \emptyset collaboration [7] at the Tevatron experiment. This is similar to the ratio of the inclusive $3j$ and inclusive $2j$ cross-sections described in fig. (2.4). We observe the same behaviour that as we pull apart the dijets we see a marked rise in the probability of extra emissions but, more importantly, we see that the data show this strongly increasing trend too.

The remaining chapters of this thesis will focus on deriving a formalism for calculating these higher-order corrections in order to describe Z/γ^* events at high energy hadronic colliders. However, we must first derive some technical methods for performing calculations.

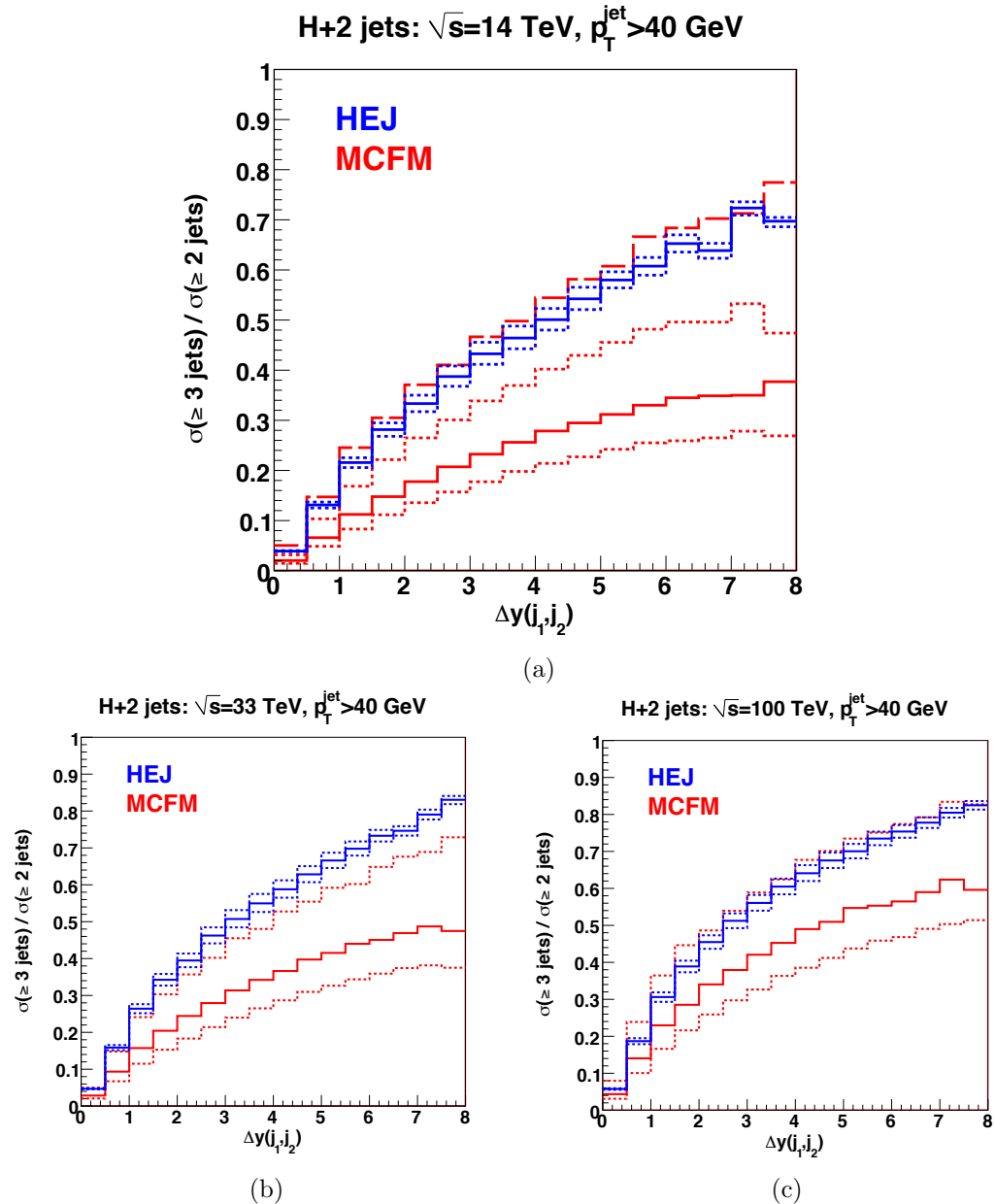


Figure 2.4: The ratio of the inclusive Higgs plus three jet cross-section to inclusive Higgs plus two jet cross-section shown for centre-of-mass energies of 14TeV (similar to the current LHC), 33TeV and 100TeV (possible energy scales for a hadronic future circular collider).

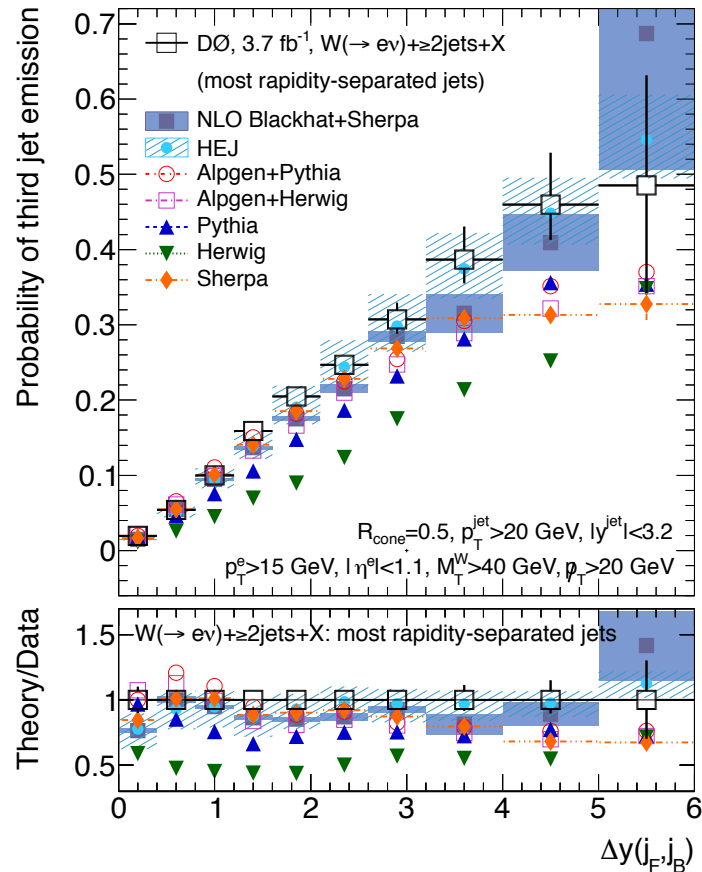


Figure 2.5: The probability of a third jet emission in W^\pm plus inclusive dijets as a function of the rapidity gap between the two leading jets in rapidity at the D \emptyset experiment at the Tevatron experiment. The data are compared to a number of fixed-order generators plus the leading logarithmic accurate HEJ and the NLO accurate Blackhat+Sherpa.

2.8 Spinor-Helicity Notation

We now move towards the more mechanical aspects of this thesis to discuss a technique which eases calculations. In chapters 3 and 4 we choose to work in the spinor-helicity formalism [42, 44]. This is a very convenient choice of notation which allows us to quickly evaluate complicated strings of products of Dirac spinors and Dirac matrices which would otherwise be troublesome to work with.

We begin by looking at the case of massless particles; this is relevant for high energy QCD since gluons are massless and the quark masses are negligible compared to the energy scale in a typical scattering process. The massless Dirac equation can be solved by using a plane-wave expansion with some momentum dependent coefficient functions, $u(p)$ and $v(p)$ where p is the momentum carried by the particle and must satisfy the on-shell condition $p^2 = 0$. This expansion gives the following equations:

$$\begin{aligned} (\not{p} + m)u(p) &= 0, \\ (\not{p} - m)v(p) &= 0. \end{aligned} \tag{2.56}$$

Each of these equations has two independent solutions which we identify as the helicity states, $u^\pm(p)$ and $v^\pm(p)$. We use the following notation for these spinors:

$$u^\pm(p) = | p\pm \rangle, \quad \overline{u^\pm(p)} = \langle p\pm | . \tag{2.57}$$

In the massless limit we also have the following relation $u^\pm(p) = v^\mp(p)$ which allows us to use the same notation for both quarks and anti-quarks. Often the helicity information will be suppressed in the interests of being concise. We also define the following spinor-brackets:

$$\langle pk \rangle = \langle p- | k+ \rangle, \quad [pk] = \langle p+ | k- \rangle. \tag{2.58}$$

In this language we have the following useful identities:

$$\begin{aligned}
 \langle ij \rangle [ij] &= s_{ij} & \langle i\pm | \gamma^\mu | i\pm \rangle &= 2k_i^\mu \\
 \langle ij \rangle &= -\langle ji \rangle & [ij] &= -[ji] \\
 \langle i\pm | \gamma^\mu | j\pm \rangle \langle k\pm | \gamma_\mu | l\pm \rangle &= 2[ik]\langle lj \rangle & \langle k\pm | \gamma^\mu | l\pm \rangle &= \langle l\mp | \gamma^\mu | k\mp \rangle \\
 \langle ij \rangle \langle kl \rangle &= \langle ik \rangle \langle lj \rangle + \langle il \rangle \langle kj \rangle & [ij][kl] &= [ik][jl] + [il][kj] \\
 \langle i+ | \not{k} | j+ \rangle &= [ik]\langle kj \rangle & \langle i- | \not{k} | j- \rangle &= \langle ik \rangle [kj]
 \end{aligned}$$

In the calculations here we use the following convention for spinors. We express the parton momenta in terms of light-cone coordinates where $p^\pm = E \pm p_z$ and $p_\perp = p_x + ip_y$. For outgoing positive (negative) helicity partons, $u^+(p)$ ($u^-(p)$) we have:

$$u^+(p) = \begin{pmatrix} \sqrt{p^+} \\ \sqrt{p^-} \frac{p_\perp}{|p_\perp|} \\ 0 \\ 0 \end{pmatrix} \quad u^-(p) = \begin{pmatrix} 0 \\ 0 \\ \sqrt{p^-} \frac{p_\perp^*}{|p_\perp|} \\ -\sqrt{p^+} \end{pmatrix} \quad (2.59)$$

respectively. While for incoming positive (negative) helicity partons moving in the positive z direction, $u^+(p)$ ($u^-(p)$) we have:

$$u^+(p) = \begin{pmatrix} \sqrt{p^+} \\ 0 \\ 0 \\ 0 \end{pmatrix} \quad u^-(p) = \begin{pmatrix} 0 \\ 0 \\ 0 \\ -\sqrt{p^+} \end{pmatrix} \quad (2.60)$$

respectively. Lastly for incoming positive (negative) helicity partons moving in the negative z direction, $u^+(p)$ ($u^-(p)$) we have:

$$u^+(p) = \begin{pmatrix} 0 \\ -\sqrt{p^-} \\ 0 \\ 0 \end{pmatrix} \quad u^-(p) = \begin{pmatrix} 0 \\ 0 \\ -\sqrt{p^-} \\ 0 \end{pmatrix}. \quad (2.61)$$

We also use following form for the Dirac matrices:

$$\gamma^0 = \begin{pmatrix} 0 & 0 & 1 & 0 \\ 0 & 0 & 0 & 1 \\ 1 & 0 & 0 & 0 \\ 0 & 1 & 0 & 0 \end{pmatrix} \quad \gamma^1 = \begin{pmatrix} 0 & 0 & 0 & -1 \\ 0 & 0 & -1 & 0 \\ 0 & 1 & 0 & 0 \\ 1 & 0 & 0 & 0 \end{pmatrix}, \quad (2.62)$$

$$\gamma^2 = \begin{pmatrix} 0 & 0 & 0 & i \\ 0 & 0 & -i & 0 \\ 0 & -i & 0 & 0 \\ i & 0 & 0 & 0 \end{pmatrix} \quad \gamma^3 = \begin{pmatrix} 0 & 0 & -1 & 0 \\ 0 & 0 & 0 & 1 \\ 1 & 0 & 0 & 0 \\ 0 & -1 & 0 & 0 \end{pmatrix}. \quad (2.63)$$

2.8.1 Spinor-Helicity Calculations with Massive Partons

To do calculations with massive partons using the spinor-helicity formalism we must be very careful since all of our favourite identities and tricks rely on the spinor brackets, $|i\rangle$, representing massless partons with $p_i^2 = 0$. We begin by defining ‘fundamental spinors’ [31] which we can use to build more general spinors and go from there. For some k_0, k_1 satisfying $k_0^2 = 0, k_1^2 = -1$ and $k_0 \cdot k_1 = 0$ we can define positive and negative helicity spinors as follows:

$$u_-(k_0)\bar{u}_-(k_0) \equiv \omega_- \not{k}_0 \quad (2.64a)$$

$$u_+(k_0) \equiv \not{k}_1 u_-(k_0), \quad (2.64b)$$

where $\omega_\lambda = \frac{1}{2}(1 + \lambda\gamma^5)$ is the helicity projection operator. In order for these to be valid spinors they must satisfy the following completeness relations:

$$\sum_\lambda u_\lambda(p)\bar{u}_\lambda(p) = \not{p} + m \quad (2.65a)$$

$$u_\lambda(p)\bar{u}_\lambda(p) = \omega_\lambda \not{p} \quad (2.65b)$$

The spinors in eqn. (2.64) can easily be shown to satisfy these as follows:

$$\begin{aligned}
 u_-(k_0)\bar{u}_-(k_0) + u_+(k_0)\bar{u}_+(k_0) &= \omega_- \not{k}_0 + \not{k}_1 u_-(k_0)\bar{u}_-(k_0)\not{k}_1, \\
 &= \omega_- \not{k}_0 + \not{k}_1 \omega_- \not{k}_0 \not{k}_1, \\
 &= \omega_- \not{k}_0 + \frac{1}{2} \gamma^\mu k_{1\mu} (1 - \gamma^5) \gamma^\nu k_{0\nu} \gamma^\sigma k_{1\sigma}, \\
 &= \omega_- \not{k}_0 + \frac{1}{2} k_{1\mu} k_{0\nu} k_{1\sigma} (\gamma^\mu \gamma^\nu \gamma^\sigma - \gamma^\mu \gamma^5 \gamma^\nu \gamma^\sigma), \\
 &= \omega_- \not{k}_0 + \frac{1}{2} k_{1\mu} k_{0\nu} k_{1\sigma} (2\gamma^\mu g^{\nu\sigma} \\
 &\quad - \gamma^\mu \gamma^\sigma \gamma^\nu + 2\gamma^5 \gamma^\mu g^{\nu\sigma} - \gamma^5 \gamma^\mu \gamma^\sigma \gamma^\nu), \\
 &= \omega_- \not{k}_0 + k_{1\mu} k_{0\nu} k_{1\sigma} \omega_+ \gamma^\mu (2g^{\nu\sigma} - \gamma^\sigma \gamma^\nu), \\
 &= \omega_- \not{k}_0 + 2\not{k}_1 k_0 \cdot k_1 - \omega_+ \not{k}_1 \not{k}_1 \not{k}_0, \\
 &= \omega_- \not{k}_0 + \omega_+ \not{k}_0,
 \end{aligned}$$

where we have used $\gamma^\mu, \gamma^\mu = 2g^{\mu\nu}$, $\gamma^\mu, \gamma^5 = 0$ and $\not{k}_1 \not{k}_1 = k_1^2 = 0$. This proves the property of eqn. (2.65a) and inserting the definition of ω_λ gives:

$$\begin{aligned}
 u_-(k_0)\bar{u}_-(k_0) + u_+(k_0)\bar{u}_+(k_0) &= \frac{1}{2} (1 - \gamma^5) \not{k}_0 + (1 + \gamma^5) \not{k}_0, \\
 &= \not{k}_0,
 \end{aligned}$$

which is eqn. (2.65b) for a massless particle.

We can use these fundamental spinors to form spinors for any given momenta, p (which has $p^2 = 0$), as follows:

$$u_\lambda(p) = \not{p} u_{-\lambda}(k_0) \frac{1}{\sqrt{2p \cdot k_0}}, \quad (2.68)$$

provided we don't have $p \cdot k_0 = 0$. Once again it is easy to show that this spinor satisfies

the necessary conditions, for example:

$$\begin{aligned}
 u_\lambda(p)\bar{u}_\lambda(p) &= \frac{1}{2p \cdot k_0} \not{p} u_{-\lambda}(k_0) \bar{u}_{-\lambda}(p) \not{p}, \\
 &= \frac{1}{2p \cdot k_0} \not{p} \omega_{-\lambda} \not{k}_0 \not{p}, \\
 &= \frac{1}{4p \cdot k_0} \not{p} (1 - \lambda \gamma^5) \not{k}_0 \not{p}, \\
 &= \frac{1}{2p \cdot k_0} p_\mu k_{0\nu} p_\sigma \omega_\lambda \gamma^\mu (2g^{\nu\sigma} - \gamma^\sigma \gamma^\nu), \\
 &= \frac{1}{2p \cdot k_0} \omega_\lambda (2\not{p} p \cdot k_0 - \not{p} \not{p} \not{k}), \\
 &= \omega_\lambda \not{p}.
 \end{aligned}$$

So far so good. This can also be generalised so that we can build massive spinors from our fundamental ones. We can use

$$u(q, s) = \frac{1}{\sqrt{2q \cdot k}} (\not{q} + m) u_-(k) \quad (2.70)$$

to describe a quark with spin 4-vector s , mass m and momentum q . To confirm this we go through the same procedure as above:

$$\begin{aligned}
 u_\lambda(p, s)\bar{u}_\lambda(p, s) &= \frac{1}{2q \cdot k_0} (\not{q} + m) u_-(k_0) \bar{u}_-(q) (\not{q} + m), \\
 &= \frac{1}{2q \cdot k_0} (\not{q} + m) \omega_- \not{k}_0 (\not{q} + m), \\
 &= \frac{1}{4q \cdot k_0} (\not{q} + m) (1 - \gamma^5) \not{k}_0 (\not{q} + m), \\
 &= \frac{1}{4q \cdot k_0} [(\not{q} \not{k}_0 \not{q} + m \not{k} \not{q} + m \not{q} \not{k}_0 + m^2 \not{k}) - \gamma^5 (\not{q} \not{k} \not{q} - m \not{k} \not{q} + m \not{q} \not{k}_0 - m^2 \not{k})], \\
 &= \frac{1}{2} \left(\not{q} + m - \gamma^5 \not{q} - m \gamma^5 + \frac{m \gamma^5 \not{k} \not{q}}{k \cdot q} + \frac{\gamma^5 m^2 \not{k}}{k \cdot q} \right), \\
 &= \frac{1}{2} \left(1 + \left(\frac{1}{m} \not{q} - \frac{m}{q \cdot k} \not{k} \right) \gamma^5 \right) (\not{q} + m), \\
 &= \frac{1}{2} (1 + \not{s} \gamma^5) (\not{q} + m),
 \end{aligned}$$

where the last line defines the spin vector $s = \frac{1}{m}q - \frac{m}{q \cdot k}k$. Conjecturing a similar form for an antiquark spinor with spin 4-vector s , mass m and momentum q :

$$v(q, s) = \frac{1}{\sqrt{2q \cdot k}}(\not{q} - m)u_-(k) \quad (2.72)$$

leads to:

$$\begin{aligned} v_\lambda(p, s)\bar{v}_\lambda(p, s) &= \frac{1}{2q \cdot k_0}(\not{q} - m)u_-(k_0)\bar{u}_-(q)(\not{q} - m), \\ &= \frac{1}{2}\left((\not{q} - m) + \left(-\not{q} + m + \frac{m^2}{q \cdot k_0}\not{k}_0 - \frac{m}{q \cdot k_0}\not{q}\not{k}_0\right)\gamma^5\right), \\ &= \frac{1}{2}(1 + \not{\gamma}^5)(\not{q} - m). \end{aligned}$$

One last check that is worth performing is that these spinors actually satisfy the Dirac equation for both the quark and antiquark case. For the quark:

$$\begin{aligned} \not{q}u(q, s) &= \frac{1}{2q \cdot k_0}\not{q}(\not{q} + m)u_-(k_0), \\ &= \frac{1}{2q \cdot k_0}(m^2 + m\not{q})u_-(k_0). \end{aligned}$$

We now define some momentum \tilde{q} through the relation $q = \tilde{q} + k_0$ such that $\tilde{q}^2 = 0$ and $q \cdot k_0 = \tilde{q} \cdot k_0$. Since $q^2 = 2\tilde{q} \cdot k_0 = m^2$ we may write

$$\begin{aligned} \not{q}u(q, s) &= \frac{1}{m}(m^2 + m\not{q})u_-(k_0), \\ &= (m + \not{q})u_-(k_0). \end{aligned}$$

We can now back substitute from the definition of $u(q, s)$ in eq. (2.70) to get:

$$\not{q}u(q, s) = \sqrt{2q \cdot k}u(q, s), \\ = mu(q, s),$$

which is the Dirac equation for a quark. The result for antiquarks follows similarly. Now we have forms for massive quarks and antiquarks in terms of massless spinors we can use all of the spinor-helicity machinery to make our computations more efficient. Slightly more useful forms of equations (2.70) and (2.72) can be found by decomposing q into massless components once again: $q = \tilde{q} + k$. Then from eq. (2.70):

$$u(q, s) = \frac{1}{m}(\not{\tilde{q}} + \not{k} + m)u_-(k), \\ = \frac{1}{m}(|\tilde{q}^+\rangle\langle\tilde{q}^+|k^-\rangle + |\tilde{q}^-\rangle\langle\tilde{q}^-|k^-\rangle + |k^-\rangle\langle k^-|k^-\rangle + |k^-\rangle\langle k^-|k^-\rangle + m|k^-\rangle), \\ = \frac{[\tilde{q}k]}{m}|\tilde{q}^+\rangle + |k^-\rangle,$$

and similarly for the other helicities and the antiquarks:

$$u(q, -s) = \frac{\langle\tilde{q}k\rangle}{m}|\tilde{q}^-\rangle + |k^+\rangle, \quad (2.78a)$$

$$v(q, s) = \frac{[\tilde{q}k]}{m}|\tilde{q}^+\rangle - |k^-\rangle, \quad (2.78b)$$

$$v(q, -s) = \frac{\langle\tilde{q}k\rangle}{m}|\tilde{q}^-\rangle - |k^+\rangle. \quad (2.78c)$$

2.9 Monte Carlo Techniques

2.9.1 One Dimensional Integration

Integrals are ubiquitous in every field of physics and particle physics is no different. We have already seen many examples where meaningful physical results can only be obtained after computing an integral, including: the convolution of the parton distribution functions with the partonic cross-section seen in section 2.5 and the more

complex multi-dimensional integrals seen in section 2.7.2 for the calculation of the one-loop correction to quark-antiquark production.

For some of the integrals derived here it is not always feasible (and sometimes not even possible) to calculate them analytically. In these situations we must use a numerical approach to approximate the exact result. Such approaches generally fall into one of two categories; quadrature or Monte Carlo random sampling approaches. The most appropriate solution depends on the integrand itself, and in particular our prior knowledge of the integrand, and the number of dimensions we are integrating over.

We begin by considering the one-dimensional case. Given an integral:

$$I = \int_a^b f(x) dx, \quad (2.79)$$

we can use well known results such as the Compound Simpson's Rule to approximate the integral by

$$I \approx \frac{h}{3} \sum_{i=0}^{N/2} (f(x_{2i-2}) + 4f(x_{2i-1}) + f(x_{2i})) + \mathcal{O}(N^{-4}), \quad (2.80)$$

where N is the number of subdivisions of the integral domain (a, b) and $x_i = a + \frac{i(b-a)}{N}$ are the points at which we sample the integrand. The error quoted on eqn. (2.80) only shows the dependence on the sampling rate and it should be noted that there are other factors arising from the size of the domain of integration and on derivatives of the integrand, $f(x)$. The $\mathcal{O}(N^{-4})$ scaling of the error in this method makes it a good choice for numerics in one-dimension.

The Monte-Carlo approach to approximating eqn. (2.79) would be to pseudo-randomly select a series of N points, x_i , from within the domain of integration and then compute the integral as follows:

$$I \approx I_{MC} = \frac{b-a}{N} \sum_{i=0}^N f(x_i) + \mathcal{O}(N^{-\frac{1}{2}}). \quad (2.81)$$

Convergence of this result is assured by the weak law of large numbers (also known as Bernoulli's Theorem) which states that for a series of independent and identically distributed random variables, $\{X_1, \dots, X_N\}$, each with $\mathbb{E}(X_i) = \mu$ the sample mean approaches the population mean as $N \rightarrow \infty$. That is,

$$\lim_{N \rightarrow \infty} \frac{X_1 + \cdots + X_N}{N} = \mu. \quad (2.82)$$

We can see this explicitly since the expectation of I_{MC} under the continuous probability density function p is:

$$\begin{aligned} \mathbb{E}_p[I_{MC}] &= \mathbb{E}_p \left[\frac{b-a}{N} \sum_{i=0}^N f(x_i) \right] \\ &= \frac{b-a}{N} \sum_{i=0}^N \mathbb{E}_p [f(x_i)] \\ &= \frac{b-a}{N} \sum_{i=0}^N \int_{-\infty}^{+\infty} f(x)p(x)dx \end{aligned}$$

where $p(x) = \frac{1}{b-a}$ is the uniform probability distribution for $x \in (a, b)$. Hence,

$$\begin{aligned} \mathbb{E}_p[I_{MC}] &= \frac{b-a}{N} \frac{1}{b-a} \sum_{i=0}^N \int_a^b f(x)dx \\ &= \int_a^b f(x)dx = I. \end{aligned}$$

Since the convergence of the Monte-Carlo approximation clearly scales significantly worse than the case for the quadrature approach it would seem that it is not worth considering and, indeed, for a single dimension it is not. However, the picture changes when we consider integrals in dimension $d \geq 2$.

2.9.2 Higher Dimensional Integration

In the case of higher dimensional integrals e.g.

$$I = \int_{[a,b]} f(\vec{x}) d\vec{x} = \int_{x_1=a_1}^{x_1=b_1} \cdots \int_{x_n=a_n}^{x_n=b_n} f(x_1, \dots, x_n) dx_1 \dots dx_n, \quad (2.83)$$

we can still look to generalisations of the quadrature methods touched on in the section above however the convergence of these methods is now less favourable. Quadrature methods have errors which scale with the number of dimensions we are integrating over, e.g. $\mathcal{O}(N^{-\frac{4}{d}})$ for the Compound Simpson's Rule. We can argue this intuitively since if we have N points in one dimension to get an error which scales as $\mathcal{O}(N^{-4})$ then

in two dimensions we would require N^2 to achieve the same density of samplings and hence $N^2 \sim \mathcal{O}(N^{-4}) \rightarrow N^2 \sim \mathcal{O}(N^{-\frac{4}{2}})$ and more generally $\mathcal{O}(N^{-\frac{4}{d}})$ for d dimensional integrals.

By comparison the error of a Monte Carlo approximation stays fixed at $\mathcal{O}(N^{-\frac{1}{2}})$ regardless of the number of dimensions in the integrals. We are spared from this so-called ‘curse of dimensionality’ by the Central Limit Theorem which states that for a sequence of independent and identically distributed random variables X_1, \dots, X_N each with variance σ^2 we have:

$$\frac{X_1 + \dots + X_N - N\mathbb{E}(X_1)}{\sqrt{N}\sigma} \xrightarrow{\lim N \rightarrow \infty} \mathcal{N}(0, 1), \quad (2.84)$$

where $\mathcal{N}(0, 1)$ is the normal distribution with mean zero and variance 1. Using the additive and multiplicative scaling of the normal distribution we get the more intuitive result:

$$\sum_{i=1}^N X_i \xrightarrow{\lim N \rightarrow \infty} \mathcal{N}\left(\mu, \frac{\sigma^2}{N}\right), \quad (2.85)$$

where μ is the mean of the variables X_i . The variance of a normal distribution is well known and we can use this to see that for a d -dimensional integral we can approximate our uncertainty as:

$$\int_{[a,b]} f(\vec{x}) d\vec{x} = V\langle f \rangle \pm V\sqrt{\frac{\langle f^2 \rangle - \langle f \rangle^2}{N}} \quad (2.86)$$

$$\equiv V\langle f \rangle \pm V\frac{\sigma_{MC}}{\sqrt{N}}, \quad (2.87)$$

where V is the volume of the domain of integration, $\langle f \rangle = \sum_i f(x_i)$ and $\langle f^2 \rangle = \sum_i f(x_i)^2$.

2.9.3 Variation Reduction Techniques

In eqn. (2.87) we saw that the error estimate of a Monte Carlo approximation depends not only on the number of points sampled, N , but also on σ_{MC} . We can try to reduce σ_{MC} by reducing how ‘variable’ the integrand is over the domain of integration, for instance in the trivial example where our integrand is $f(x) = f_0$, a constant, it is clear

that one Monte Carlo sample is sufficient to compute the integral exactly. Previously when computing $\mathbb{E}_p[I_{MC}]$ we used a uniform probability density function but in fact we are free to use any distribution we like to perform the integration. This can be seen through the change of variables:

$$\begin{aligned}\mathbb{E}_p[I_{MC}] &= \int f(x)p(x)dx, \\ &= \int \frac{f(x)p(x)q(x)}{q(x)}, \\ &= \mathbb{E}_q\left[\frac{I_{MC}p(x)}{q(x)}\right],\end{aligned}$$

where $q(x)$ is our ‘importance sampling’ distribution. For example let us consider the integral

$$I = 150 \int_0^{\frac{1}{2}} x^2 \arcsin x^2 dx. \quad (2.88)$$

The integrand of eqn. (2.88) is shown in fig. (2.6) along with two potential choices of importance sampling density functions. The uniform distribution (in red) will sample the integrand equally across the domain however it is clear from looking at the functional form of eqn. (2.88) and fig. (2.6) that it isn’t the most efficient approach since it is strongly peaked towards the right hand side of the domain. Hence that is where the largest contribution to the Monte Carlo sum will come from. However if we sample the modified integrand using pseudo-random numbers generated from a distribution proportional to x^4 (shown in green in fig. (2.6)) we can reduce the variance of our approximation significantly. Tab. (2.2) shows how the approximation improves as we vary the number of samples, N , for the two cases of $q \sim \mathcal{U}(0, 0.5)$ and $q \sim x^4$.

Tab. (2.2) clearly shows the value of an importance sampling approach; this result converges to the correct result much faster than when we sample uniformly. Of course this tactic relies on us having some prior knowledge of the behaviour of our integrand in order to select the correct probability density function to use which, in more complicated examples is not always possible³. A more realistic, and relevant, example of importance sampling comes from the cross-section for the production of a Z^0 boson in association

³More novel approaches whereby the sampling distribution is modified to improve convergence as the Monte-Carlo iterations are calculated, such as the **VEGAS** algorithm, exist but they will not be discussed here.

N	$q \sim \mathcal{U}(0.0, 0.5)$		$q \sim x^4$	
	Approximation	Error	Approximation	Error
10^1	0.5111428 ± 1.5932607	0.4318912	0.9424279 ± 1.6817093	0.0006061
10^2	0.9098668 ± 2.0212007	0.0331672	0.9429298 ± 2.6653523	0.0001042
10^3	0.9337252 ± 2.0040391	0.0093088	0.9431454 ± 0.8430513	8.936×10^{-5}
10^4	0.9456974 ± 2.0415918	0.0026633	0.9430386 ± 0.2665659	4.504×10^{-6}
10^5	0.9438040 ± 2.0222993	0.0007699	0.9430241 ± 0.0842942	2.848×10^{-6}

Table 2.2: The Monte-Carlo approximation to eqn. (2.88) as we vary the number of sampled points, N , shown in the naïve sampling case and in the importance sampled case.

with dijets. The matrix element squared for such a process will have following form:

$$|\mathcal{M}_{Z^0+jj}|^2 \sim \left| \frac{1}{p_Z^2 - M_Z + i\Gamma_Z M_Z} \right|^2 \times f(\text{QCD, EW}) \times g(\text{Kinematic}), \quad (2.89)$$

where p_Z is the momentum carried by the Z^0 boson, M_Z is its mass, Γ_Z is its width, $f(\text{QCD, EW})$ will contain all of the coupling information and $g(\text{Kinematic})$ encodes the remainder of the matrix element. When using a Monte-Carlo approach to generate events of this kind we can use the schematic form of eqn. (2.89) to *a priori* select an appropriate probability density function to sample from. Fig. (2.7) shows the squared Z^0 propagator. Obvious comparisons with fig. (2.6) can be drawn in the sense that were we to generate events with a uniform spread of values for p_Z^2 we would end with a very slow rate of convergence by oversampling areas where the integrand is very small and slowly varying.

Another good example of importance sampling is found in how we sample the incoming partons in our simulations. Simple momentum conservation considerations lead us to values for the Bjorken scaling variables of our incoming partons, x_a and x_b , and we can use these to intelligently sample the available partons. The naïve way to perform the sum over all possible incoming states would be to uniformly choose a random number corresponding to one of the light quarks, one the light anti-quarks or to a gluon⁴. We can, however, do better than this by using what we know about how the parton density functions vary with $x_{a/b}$ - fig. (2.8) shows this behaviour as measured by the HERA experiment. By choosing to randomly sample then incoming parton types according to the relative values for the parton density functions we can, once again, reduce the variance of our numerical integrations as much as possible. In chapter 4 we will see

⁴Here we mean all except the top and anti-top. The parton density functions for these are not available and, even if they were, they would be small enough that we could safely ignore their contribution to cross-sections.

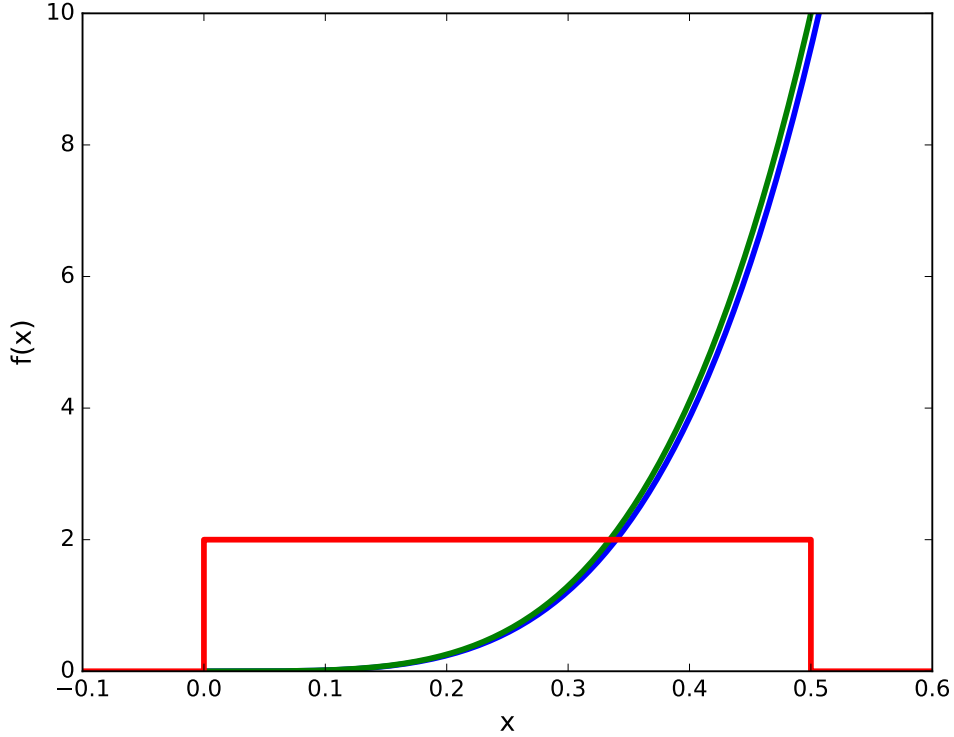


Figure 2.6: A simple importance sampling example (see eqn. (2.88)). The integrand, $f(x)$, is shown in blue, the importance sampling distribution is shown in green and, for comparison, the uniform probability density function used in the naïve case of no importance sampling is also shown (in red).

an example of the effect of picking an importance sampling distribution which is not relevant for the problem at hand - in this case it was necessary to change the way we sampled a Breit-Wigner because of specific experimental invariant mass cuts applied to the decay products of a Z/γ^* boson.

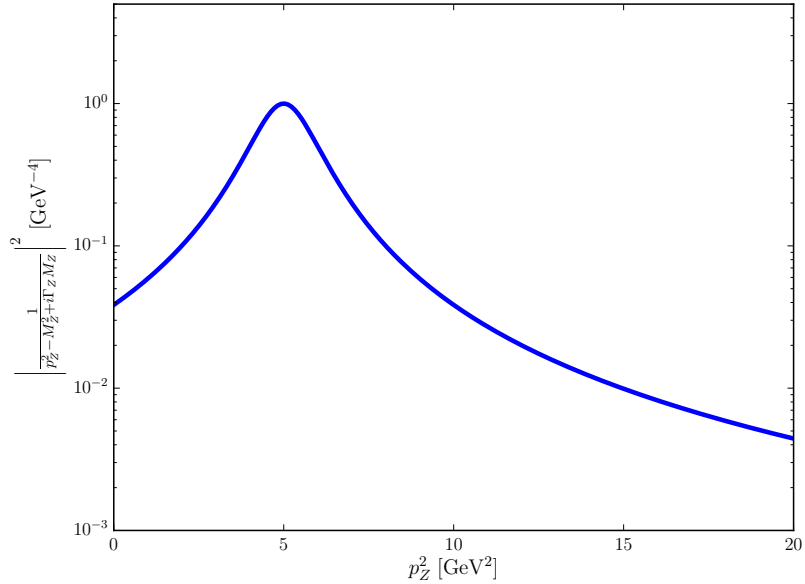


Figure 2.7: The absolute value squared of the Z^0 propagator for a range of values of the invariant mass squared of the Z^0 , p_Z^2 . We see that, as expected, it is strongly peaked at the Z^0 mass and, as such, is an ideal candidate for using importance sampling.

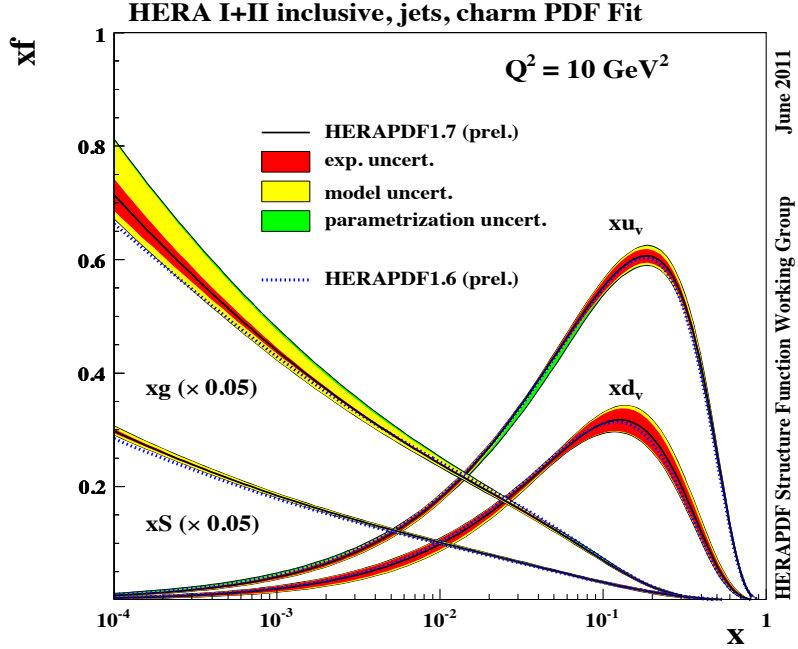


Figure 2.8: Recent parton distribution function fits from the HERA experiment. The observed variation in $f(x_{a/b}, Q^2)$, especially at high $x_{a/b}$, can be used to reduce the variance of a Monte Carlo approach to computing eqn (2.41) by using an importance sampling approach

Chapter 3

High Energy QCD

In this chapter we look in detail at the ‘High Energy’ limit of QCD. We begin by defining this limit and looking at how basic $2 \rightarrow 2$ scattering behaves at leading order and next-to-leading order in α_s before discussing how, in this limit, scattering amplitudes may be conveniently expressed as a contraction between two vector ‘current’ terms. Finally, we show how we may adorn $2 \rightarrow 2$ matrix elements with real and virtual corrections by way of an effective vertex for real emissions and the Lipatov ansatz respectively. In this way we construct an approximate description of $2 \rightarrow n$ scattering in the high energy limit.

3.1 The ‘High Energy’ limit

The ‘High Energy’ limit of QCD, also referred to as the Multi-Regge Kinematic (MRK) limit is defined in terms of the kinematics of the final state. We require a strong rapidity ordering of all outgoing radiation as well as all the emissions having similar transverse momenta. Mathematically:

$$y_1 \gg y_2 \gg \dots \gg y_n \text{ and } |p_{\perp 1}| \approx |p_{\perp 2}| \approx \dots \approx |p_{\perp(n-1)}|, \quad (3.1)$$

where we define the rapidity of a final state particle as

$$y = \frac{1}{2} \ln \left(\frac{E + p_z}{E - p_z} \right) \quad (3.2)$$

where E is the energy of particle and p_z is the z component of its momentum. We can

state the criteria in eqn. (3.1) equivalently as:

$$s_{ij} \rightarrow \infty \text{ for all } i, j \text{ with } |p_{i\perp}| \text{ fixed,} \quad (3.3)$$

where $s_{ij} = (p_i + p_j)^2$ is the invariant mass of a pair of outgoing partons. We sometimes parametrise the final states instead using pseudo-rapidity, η , rather than rapidity. Pseudo-rapidity is simply related to the angle of the outgoing state to the beam, θ :

$$\eta = -\ln \tan \frac{\theta}{2}. \quad (3.4)$$

For massless states eqn. (3.2) and eqn. (3.4) are equivalent.

3.2 Mandelstam Variables in the High Energy Limit

The $2 \rightarrow 2$ QCD scattering amplitudes can be expressed in terms of the well-known Mandelstam variables s , t and u , which, in terms of the momenta in the process, are given by:

$$\begin{aligned} s &= (p_a + p_b)^2, \\ t &= (p_a - p_1)^2, \\ u &= (p_b - p_2)^2, \end{aligned} \quad (3.5)$$

where p_a , p_b are the incoming parton momenta and p_1 , p_2 are the outgoing parton momenta. When working in the high energy limit it is convenient to re-express these in terms of the perpendicular momentum of the outgoing partons, p_{\perp} , and the difference in rapidity between the two final state partons, Δy . If we parametrise our outgoing states as

$$\begin{aligned} p_1 &= p_{\perp 1} (\cosh(y_1), \cos(\phi_1), \sin(\phi_1), \sinh(y_1)), \\ p_2 &= p_{\perp 2} (\cosh(y_2), \cos(\phi_2), \sin(\phi_2), \sinh(y_2)), \end{aligned} \quad (3.6)$$

then we can express eqs. (3.5) as follows:

$$\begin{aligned} s &= 4p_{\perp}^2 \cosh^2 \frac{\Delta y}{2}, \\ t &= -2p_{\perp}^2 \cosh \frac{\Delta y}{2} e^{-\frac{\Delta y}{2}}, \\ u &= -2p_{\perp}^2 \cosh \frac{\Delta y}{2} e^{\frac{\Delta y}{2}}. \end{aligned} \tag{3.7}$$

In the limit of hard jets well separated in rapidity, i.e. $\Delta y \rightarrow \infty$, these are approximated by

$$\begin{aligned} s &= p_{\perp}^2 e^{\Delta y}, \\ t &= -p_{\perp}^2, \\ u &= -p_{\perp}^2 e^{\Delta y}. \end{aligned} \tag{3.8}$$

From eqn. (3.8) it is clear that the ‘hard, wide-angle jet’ limit, i.e. $\Delta y \rightarrow \infty$, $p_{i\perp} \rightarrow \infty$, is equivalent to the High Energy limit since as Δy grows large s will grow exponentially large while t will stay fixed. Rearranging for Δy in the above equations yields:

$$\Delta y = \ln \left(\frac{s}{-t} \right). \tag{3.9}$$

This is a useful result because it directly relates the kinematics of an event to a (potentially) large logarithm. It is already apparent from eqn. (3.9) that a final state with large rapidity gaps between jets will carry with it a large logarithm as seen in eqn. (2.55), $L = \ln \left(\frac{s}{-t} \right)$, and therefore we may need a more careful inspection of our perturbative expansion than the fixed-order approach.

3.3 qQ -scattering at High Energy (at LO)

Here we consider the simplest example; the case of $qQ \rightarrow qQ$ for all negative helicity partons (the capital Q implies it is a different flavour to q). There is only one diagram which contributes shown in fig. (3.1). Using the Feynman rules detailed in section 2.2 we can write the matrix element as:

$$i\mathcal{M}_{q^-Q^- \rightarrow q^-Q^-}^{\text{LO}} = ig_s^2 T_{1a}^d T_{2b}^d \frac{\bar{u}^-(p_1) \gamma^\mu u^-(p_a) \bar{u}^-(p_2) \gamma_\mu u^-(p_b)}{t} \quad (3.10)$$

$$= ig_s^2 T_{1a}^d T_{2b}^d \frac{\langle 1|\mu|a\rangle \cdot \langle 2|\mu|b\rangle}{t}, \quad (3.11)$$

where $t = (p_a - p_1)^2$. Writing the contraction of these two ‘current’ terms in terms of light-cone coordinates we have:

$$i\mathcal{M}_{q^-Q^- \rightarrow q^-Q^-}^{\text{LO}} = ig_s^2 T_{1a}^d T_{2b}^d \frac{2\sqrt{p_a^- p_b^+}}{t} \left(\sqrt{p_1^+ p_2^-} e^{i\phi_2} + \sqrt{p_1^- p_2^+} e^{i\phi_1} \right), \quad (3.12)$$

where $e^{i\phi_i} = \frac{p_{\perp i}}{|p_{\perp i}|}$. We now approximate the kinematics in such a way that we may write eqn. (3.12) in a ‘factorised’ form once again. Specifically we consider that the scattering can be thought of as two incoming partons glancing off one another. That is, we assume that $p_1^+ \ll p_1^-$, $p_2^- \ll p_2^+$ with p_a (p_b) moving in the backwards (forward) direction. We can further assume that $p_1^- \approx p_a^-$ and $p_2^+ \approx p_b^+$ and with this we see that (3.12) becomes:

$$i\mathcal{M}_{q^-Q^- \rightarrow q^-Q^-}^{\text{LO}} = \frac{2s}{t} \left(g_s T_{1a}^d e^{i\phi_1} \right) \left(-ig_s T_{2b}^d \right), \quad (3.13)$$

which is ‘factorised’ in the sense that each scalar term in brackets depends only on one quark line; either on the $p_{a/1}$ line or the $p_{b/2}$ line. We see that the amplitude for $qQ \rightarrow qQ$ is dominated by the s kinematic variable. We can express this as:

$$\mathcal{M}_{q^-Q^- \rightarrow q^-Q^-}^{\text{LO}} \sim s^{\alpha(t)}, \quad (3.14)$$

This is exactly the behaviour expected when a particle exchanged in the t -channel has ‘reggeised’ [25, 41, 75]. $\alpha(t)$ is the Regge trajectory and is equal to the intrinsic spin of the state exchanged. In our example we have a gluon exchanged and accordingly we can see from eqn. (3.13) that $\alpha(t) = 1$ for $qQ \rightarrow qQ$ at leading order.

It is also interesting to consider the same process but with helicity structure $q^-Q^+ \rightarrow q^-Q^+$. The calculation proceeds similarly to the $q^-Q^- \rightarrow q^-Q^-$ and when we write the result in terms of two vector ‘currents’ we get:

$$i\mathcal{M}_{q^-Q^+ \rightarrow q^-Q^+}^{\text{LO}} = ig_s^2 T_{1a}^d T_{2b}^d \frac{\langle 1|\mu|a\rangle \cdot \langle b|\mu|2\rangle}{t}, \quad (3.15)$$

which is still manifestly expressible as a contraction of two vector currents. The contraction can be written approximately as $2[a2]\langle b1 \rangle \sim 2[a2]\langle 2a \rangle = -2u$. However when we continue on and take the High Energy limit of eqn. (3.15) we get:

$$\begin{aligned} i\mathcal{M}_{q^-Q^+ \rightarrow q^-Q^+}^{\text{LO}} &= ig_s^2 T_{1a}^d T_{2b}^d \frac{2}{t} \sqrt{p_a^- p_2^+} \sqrt{p_b^+ p_1^-} e^{i\phi_1} \\ &= ig_s^2 T_{1a}^d T_{2b}^d \frac{2s}{t} \end{aligned} \quad (3.16)$$

So we see that in the strict High Energy limit we have that $s = -u$ exactly. Whereas when we leave the amplitude in terms of vector currents we are able to keep more of the physics by keeping $s \sim -u$; at the LHC t and k_\perp^2 can often differ significantly and so the over-approximating the kinematics here would lead to a poor description of the data.

3.4 qg scattering at High Energy

We now explore the more involved case of $q^-g^+ \rightarrow q^-g^+$ scattering. At leading order this consists of the three diagrams shown in fig. (3.2). We use the following gauge choice for the gluon polarisations:

$$\epsilon_{2\sigma}^{+*} = \frac{\langle b|\sigma|2 \rangle}{\sqrt{2}\langle b2 \rangle} \quad \epsilon_{2\sigma}^{-*} = -\frac{\langle b|\sigma|2 \rangle}{\sqrt{2}[b2]} \quad (3.17)$$

$$\epsilon_{b\sigma}^+ = -\frac{\langle b|\sigma|2 \rangle}{\sqrt{2}[2b]} \quad \epsilon_{2\sigma}^{-*} = -\frac{\langle b|\sigma|2 \rangle}{\sqrt{2}\langle 2b \rangle} \quad (3.18)$$

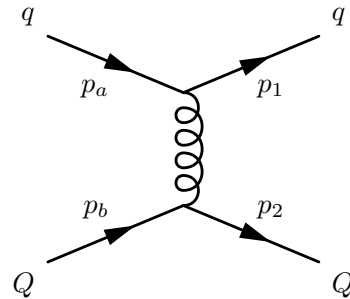


Figure 3.1: The only diagram which contributes to $qQ \rightarrow qQ$ at leading order in α_s .

For simplicity we choose to write everything in terms of negative helicity spinor-helicity brackets; to describe positive helicities we can use the transposition property of spinor-helicity brackets discussed in section 2.8.

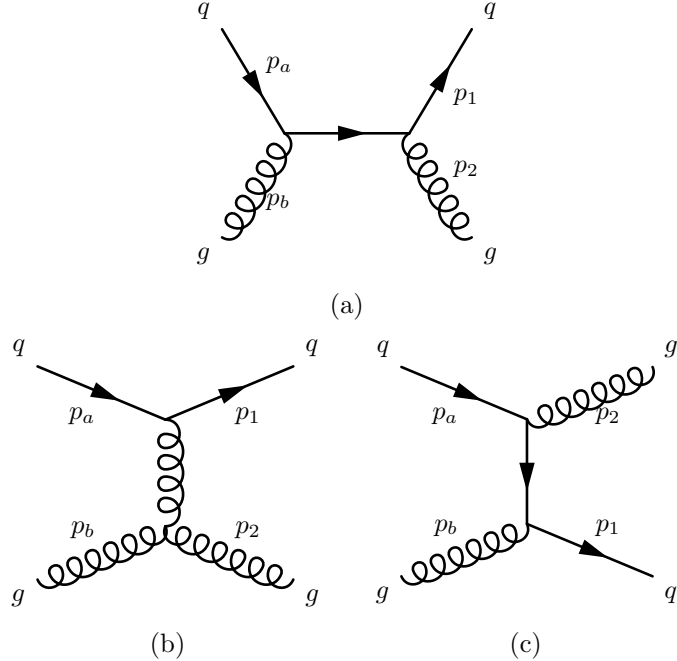


Figure 3.2: The s , t and u channel diagrams contributing to $q^- g^+ \rightarrow q^- g^+$ at leading order in α_s in figs. (3.2a), (3.2b) and (3.2c) respectively.

3.4.1 s -channel

The matrix element for the s -diagram, shown in fig. (3.2a), is:

$$\mathcal{M}_{q^- g^+ \rightarrow q^- g^+, s}^{\text{LO}} = T_{ae}^b T_{e1}^2 \bar{u}^-(p_1) \left(-\frac{i g_s}{2} \gamma^\mu \right) \epsilon_\mu^{*+}(p_2) \frac{i(\not{q} + m)}{q^2 - m^2} \left(-\frac{i g_s}{2} \gamma^\nu \right) \epsilon_\nu^+(p_b) u^-(p_a), \quad (3.19)$$

$$= -\frac{g_s^2}{4q^2} \epsilon_{2\mu}^{*+} \epsilon_{b\nu}^+ \bar{u}_1^- \gamma^\mu \not{q} \gamma^\nu u_a^-, \quad (3.20)$$

where we have neglected the quark mass term since we are in the High Energy limit. The propagator has momentum $q = p_a + p_b = p_1 + p_2$ and therefore:

$$\mathcal{M}_{q^-g^+ \rightarrow q^-g^+, s}^{\text{LO}} = -T_{ae}^b T_{e1}^2 \frac{g_s^2}{4q^2} \frac{\langle b|\mu|2\rangle}{\sqrt{2}\langle b2\rangle} \frac{\langle b|\nu|2\rangle}{\sqrt{2}[2b]} \bar{u}_1^- \gamma^\mu (\not{p}_a + \not{p}_b) \gamma^\nu u_a^-. \quad (3.21)$$

We use the completeness relations for $\not{p}_{a/b}$ and see that:

$$\mathcal{M}_{q^-g^+ \rightarrow q^-g^+, s}^{\text{LO}} = -T_{ae}^b T_{e1}^2 \frac{g_s^2}{4q^2 t} [2a] \langle ab \rangle \langle b|\mu|2\rangle \langle 1|\mu|a \rangle \quad (3.22)$$

Using $q^2 = s_{ab} = \langle ab \rangle [ba]$ and $t = \langle 2b \rangle [b2]$ we have:

$$\mathcal{M}_{q^-g^+ \rightarrow q^-g^+, s}^{\text{LO}} = -T_{ae}^b T_{e1}^2 \frac{g_s^2}{4} \frac{[2a]\langle ab \rangle}{\langle ab \rangle [ba] \langle 2b \rangle [b2]} \langle b|\mu|2\rangle \langle 1|\mu|a \rangle. \quad (3.23)$$

We must now calculate explicitly the spinor product brackets using the conventions for spinors outlined in the previous chapter, for example:

$$[2a] = \bar{u}_2^+ u_a^- = -\frac{\sqrt{p_a^+ p_2^-} p_2^\perp}{|p_2^\perp|}. \quad (3.24)$$

After calculating the other brackets in eqn. (3.23) we see:

$$\mathcal{M}_{q^-g^+ \rightarrow q^-g^+, s}^{\text{LO}} = -T_{ae}^b T_{e1}^2 \frac{g_s^2}{4} \sqrt{\frac{p_2^-}{p_b^+}} \frac{1}{p_2^+ p_b^-} \frac{p_{2\perp}^*}{|p_{2\perp}|} \langle b|\mu|2\rangle \langle 1|\mu|a \rangle \quad (3.25)$$

Which can be simplified to give the final result:

$$\mathcal{M}_{q^-g^+ \rightarrow q^-g^+, s}^{\text{LO}} = -T_{ae}^b T_{e1}^2 \frac{g_s^2}{2t} \sqrt{\frac{p_2^-}{p_b^+}} \frac{p_{2\perp}^*}{|p_{2\perp}|} \langle b|\mu|2\rangle \langle 1|\mu|a \rangle \quad (3.26)$$

3.4.2 *t*-channel

The matrix element for the *t*-channel diagram, shown in fig. (3.2b), is:

$$-i\mathcal{M}_{q^-g^+ \rightarrow q^-g^+,t}^{\text{LO}} = -T_{a1}^e f^{b2e} \bar{u}_1^- \left(-\frac{ig_s}{2} \gamma^\mu \right) \left(-\frac{ig_{\mu\nu}}{q^2} \right) u_a^- g_s \left(g_{\sigma\nu}(p_b - q)_\rho + g_{\nu\rho}(q + p_b)_\sigma - g_{\rho\sigma}(p_b + p_2)_\nu \right) \epsilon_{2+}^{\rho*} \epsilon_{b+}^\sigma \quad (3.27)$$

Now using $q = p_2 - p_b$ and $p_2 \cdot \epsilon_2 = p_b \cdot \epsilon_b = 0$:

$$-i\mathcal{M}_{q^-g^+ \rightarrow q^-g^+,t}^{\text{LO}} = -T_{a1}^e f^{b2e} \frac{g_s^2}{2q^2 s_{2b}} (\bar{u}_1^- \gamma^\nu u_a^-) (\bar{u}_b^- \gamma^\rho u_2^-) (\bar{u}_b^- \gamma^\sigma u_2^-) \left(2g_{\sigma\nu} p_{b\rho} + 2g_{\nu\rho} p_{2\sigma} - g_{\rho\sigma}(p_b + p_2)_\nu \right), \quad (3.28)$$

which cancels completely and therefore:

$$\mathcal{M}_{q^-g^+ \rightarrow q^-g^+,t}^{\text{LO}} = 0, \quad (3.29)$$

in this gauge.

3.4.3 *u*-channel

The matrix element for the *u*-diagram, shown in fig. (3.2c), is:

$$\begin{aligned} -i\mathcal{M}_{q^-g^+ \rightarrow q^-g^+,u}^{\text{LO}} &= T_{ae}^2 T_{e1}^b \bar{u}^-(p_1) \left(-\frac{ig_s}{2} \gamma^\mu \right) \frac{i(\not{q} + mc)}{q^2 - m^2 c^2} \left(-\frac{ig_s}{2} \gamma^\nu \right) u^-(p_a) \epsilon_\mu^{*+}(p_b) \epsilon_\nu^+(p_2) \\ \mathcal{A}_u &= \frac{g_s^2}{4q^2} \bar{u}_1^- \gamma^\mu \not{q} \gamma^\nu u_a^- \epsilon_{b\mu}^{*+} \epsilon_{2\nu}^* \\ &= \frac{g_s^2}{8q^2 s_{2b}} \langle b|\mu|2\rangle \langle b|\nu|1\rangle \bar{u}_1^- \gamma^\mu (\not{p}_a - \not{p}_2) \gamma^\nu u_a^- \end{aligned} \quad (3.30)$$

Where we have used $q = p_a - p_2$. By direct comparison with the procedure used for the *s*-channel we can see the result will be:

$$\mathcal{M}_{q^-g^+ \rightarrow q^-g^+, u}^{\text{LO}} = T_{ae}^2 T_{e1}^b \frac{g_s^2}{2t} \sqrt{\frac{p_b^-}{p_2^-}} \frac{p_{2\perp}^*}{|p_{2\perp}|} \langle b|\mu|2\rangle \langle 1|\mu|a\rangle. \quad (3.31)$$

The total total matrix element is given by the sum of eqs. (3.26), (3.29) and (3.31) which is:

$$\mathcal{M}_{q^-g^+ \rightarrow q^-g^+}^{\text{LO}} = \frac{g_s^2}{2} \frac{p_{2\perp}^*}{|p_{2\perp}|} \left(T_{ae}^2 T_{e1}^b \sqrt{\frac{p_b^-}{p_2^-}} - T_{ae}^b T_{e1}^2 \sqrt{\frac{p_2^-}{p_b^-}} \right) \frac{\langle b|\mu|2\rangle \langle 1|\mu|a\rangle}{t}, \quad (3.32)$$

We also see that eqn. (3.32) has the same spinor-helicity brackets contracted as eqn. (3.11) and so the dominant behaviour of $q^-g^+ \rightarrow q^-g^+$ in the high energy limit is $\frac{s}{t}$ as predicted by Regge theory. In the High Energy limit we have $p_b^- \sim p_2^-$ and so eqn. (3.32) could be simplified further to:

$$\mathcal{M}_{q^-g^+ \rightarrow q^-g^+}^{\text{LO}} = i \frac{g_s^2}{2} \frac{p_{2\perp}^*}{|p_{2\perp}|} f^{2bc} T_{a1}^c \frac{\langle b|\mu|2\rangle \langle 1|\mu|a\rangle}{t}. \quad (3.33)$$

which is identical to the result found in the previous $qQ \rightarrow qQ$ calculation (save for a phase which cancels at the amplitude squared level and a different colour factor). The kinematics of eqn. (3.32) are exactly in the form of two ‘currents’ contracted as seen in section 3.3. We have:

$$|\mathcal{M}_{qg \rightarrow qg}^{\text{LO}}|^2 = \frac{C_A}{C_f} |\mathcal{M}_{qQ \rightarrow qQ}^{\text{LO}}|^2, \quad (3.34)$$

in the High Energy limit. In practice we actually choose *not* to take the High Energy limit to obtain eqn. (3.33) so as to approximate as little as possible. Even without this extra approximation eqn. (3.32) is still exactly the form of a t -channel gluon exchange as seen in eqn. (3.11).

In section 3.9 we will return to this result and the results of section 3.3 and discuss how, despite their simplicity, they act as a basis and can be used to construct very general approximate forms for matrix elements which could now otherwise be evaluated

3.5 qQ -scattering at High Energy (at NLO)

Before we continue on to look at how we might add extra real emissions to high energy matrix elements we briefly look at higher order (in α_s) corrections to the process we

studied in section 3.3. So far we have seen the leading order processes with a t -channel exchange are enhanced but in eqn. (2.55) we sketched out a form for the perturbative expansion which also had enhanced contributions at higher order.

Here we continue on from section 3.3 and calculate the virtual diagrams which contribute a leading logarithm for $qQ \rightarrow qQ$ at next-to-leading in α_s [41, 75].

We might expect that the next-to-leading order diagrams with the maximal number of t -channel exchanges will give the greatest enhancement and, indeed, this turns out to be the case. These diagrams are shown for the case of $qQ \rightarrow qQ$ in fig. (3.3). We can rule out the other virtual diagrams which contribute at this order since they will contain (anti-)quark propagators along the $p_{a/1}$ or $p_{b/2}$ lines and in the high energy limit these will be suppressed.

The diagrams in fig. (3.3) can be elegantly computed by using the ‘Cutkosky rules’ which are used to relate two sub-diagrams to the imaginary part of a higher order diagram through the Optical theorem. This can be seen very quickly since the scattering matrix, S , must be unitary i.e. $S^\dagger S = 1$. If we write this instead in terms of the transition matrix, T , defined by $S = 1 + iT$ then we immediately have that

$$-i(T - T^\dagger) = T^\dagger T. \quad (3.35)$$

The left hand side of which can be written as twice the imaginary part of T . If we now let T represent the transition from some initial state $|i\rangle$ to some final state $|f\rangle$ then we can write this as:

$$2i\text{Im}(\langle i|T|f\rangle) = \sum_p \langle i|T^\dagger|p\rangle \langle p|T|f\rangle, \quad (3.36)$$

where we have inserted a sum over a complete set of states $|p\rangle$. Pictorially we ‘cut’ propagators by forcing them on-shell with delta functions and inserting a complete set of states.

For example the uncrossed amplitude in fig. (3.3a), $\mathcal{M}_{qQ \rightarrow qQ}^{\text{NLO, II}}$, may be expressed as a combination of two copies of the amplitude arising from fig. (3.1):

$$\mathcal{M}_{q^-Q^- \rightarrow q^-Q^-}^{\text{LO}} = -g_s^2 T_{1a}^d T_{2b}^d \frac{\langle 1|\mu|a\rangle \cdot \langle 2|\mu|b\rangle}{t}, \quad (3.37)$$

as follows:

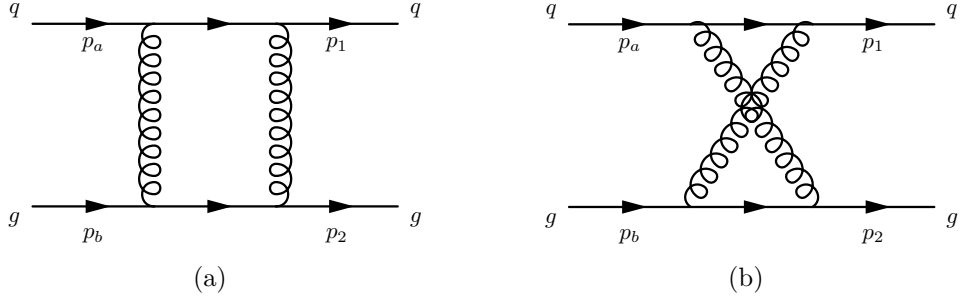


Figure 3.3: The leading logarithmic contributions to $qg \rightarrow qg$ at NLO. The uncrossed diagram, $\mathcal{M}_{qQ \rightarrow qQ}^{\text{NLO}, II}$, shown in (a) exchanges two gluons in the t channel and the crossed diagram, $\mathcal{M}_{qQ \rightarrow qQ}^{\text{NLO}, X}$, case (b) exchanges two gluons in the u channel and is related to (a) (up to a colour factor) via a crossing symmetry

$$2\text{Im}\left(\mathcal{M}_{qQ \rightarrow qQ}^{\text{NLO}, II}\right) = \frac{1}{(2\pi)^2} \int d^4 k \delta((p_a - k)^2) \delta((p_b + k)^2) \quad (3.38)$$

$$\mathcal{M}_{q^- Q^- \rightarrow q^- Q^-}^{\text{LO}}(k) \mathcal{M}_{q^- Q^- \rightarrow q^- Q^-}^{\dagger \text{LO}}(k - q), \quad (3.39)$$

where $\text{Im}(\cdot)$ denotes the imaginary part, k is the loop momentum, q is the momentum transfer and \dagger denotes Hermitian conjugation. The sum over a complete of states here corresponds to integrating over all possible momenta flowing around the loop. In the High Energy limit we can perform the integration to give:

$$\text{Im}\left(\mathcal{M}_{qQ \rightarrow qQ}^{\text{NLO}, II}\right) = 4\alpha_s^2 s \mathcal{C}_1(T^a, T^b) \int \frac{dk_\perp}{k_\perp(k_\perp - q_\perp)}, \quad (3.40)$$

where $\mathcal{C}_1(T^a, T^b)$ is the colour factor for the diagram in fig. (3.3a) and k_\perp is the transverse component of k . We can now relate the imaginary part of the amplitude to the full amplitude by conjecturing that the amplitude will be logarithmically enhanced as follows:

$$\mathcal{M}_{qQ \rightarrow qQ}^{\text{NLO}, II} = \text{Re}(\mathcal{M}_{qQ \rightarrow qQ}^{\text{NLO}, II}) + i\text{Im}(\mathcal{M}_{qQ \rightarrow qQ}^{\text{NLO}, II}), \quad (3.41)$$

and defining $\widetilde{\mathcal{M}}_{qQ \rightarrow qQ}^{\text{NLO}, II}$ as the leading logarithmic coefficient of the matrix element:

$$\begin{aligned}\mathcal{M}_{qQ \rightarrow qQ}^{\text{NLO, II}} &= \widetilde{\mathcal{M}}_{qQ \rightarrow qQ}^{\text{NLO, II}} \ln \frac{s}{t} + \text{sub-leading} \\ &= \widetilde{\mathcal{M}}_{qQ \rightarrow qQ}^{\text{NLO, II}} \left(\ln \left| \frac{s}{t} \right| - i\pi \right) + \text{sub-leading},\end{aligned}\tag{3.42}$$

where we have used that $\frac{s}{t} < 0$. Comparing real and imaginary parts of eqn. (3.42) and assuming that $\widetilde{\mathcal{M}}_{qQ \rightarrow qQ}^{\text{NLO, II}}$ is real we see that:

$$\text{Re}(\mathcal{M}_{qQ \rightarrow qQ}^{\text{NLO, II}}) = -\frac{1}{\pi} \text{Im}(\mathcal{M}_{qQ \rightarrow qQ}^{\text{NLO, II}}) \ln \left| \frac{s}{t} \right| \tag{3.43}$$

and we can therefore reconstruct the real part of the amplitude as:

$$\text{Re}(\mathcal{M}_{qQ \rightarrow qQ}^{\text{NLO, II}}) = -\frac{4\alpha_s^2 s}{\pi} \mathcal{C}_1(T^a, T^b) \ln \left| \frac{s}{t} \right| \int \frac{dk_\perp}{k_\perp(k_\perp - q_\perp)}. \tag{3.44}$$

The crossed-diagram, (3.3b), also contributes a leading logarithmic piece and is related to eqn. (3.3a) by a crossing symmetry and so we simply replace s with u in eqn. (3.44) and calculate a new colour factor, $\mathcal{C}_2(T^a, T^b)$:

$$\text{Re}(\mathcal{M}_{qQ \rightarrow qQ}^{\text{NLO, X}}) = -\frac{4\alpha_s^2 u}{\pi} \mathcal{C}_2(T^a, T^b) \ln \left| \frac{u}{t} \right| \int \frac{dk_\perp}{k_\perp(k_\perp - q_\perp)}. \tag{3.45}$$

But in the high energy limit $s \sim -u$ (this is clear from eqn. (3.8)) and so we can combine these terms and express the leading logarithmic part of the NLO correction in terms of the leading order result:

$$\mathcal{M}_{qQ \rightarrow qQ}^{\text{NLO}} = \frac{3\alpha_s}{\pi^2} \hat{\alpha}(q) \ln \left| \frac{s}{t} \right| \mathcal{M}_{qQ \rightarrow qQ}^{\text{LO}}, \tag{3.46}$$

where:

$$\hat{\alpha}(q) = \int dk_\perp \frac{q_\perp^2}{k_\perp(k_\perp - q_\perp)}. \tag{3.47}$$

From eqn. (3.46) we can see the logarithmic enhancement explicitly; there is still a suppression from the inclusion of an extra factor of α_s with respect to the leading order term but as we have seen previously the logarithm is related to the kinematics of the final state - namely - the rapidity gap between the outgoing quarks p_1 and p_2 and this can be large enough to compensate for the smallness of α_s . Eqn. (3.47) will clearly

diverge when we come to integrate over the soft region (where k_\perp is very small). This divergence will be treated, i.e. regularised and explicitly shown to cancel, in chapter 4.

3.6 *t*-channel Dominance

In what follows we construct high multiplicity matrix elements by approximating the full result by the contraction of two currents and a number of effective vertices. This choice allows us to construct all the matrix elements which contain the leading logarithms.

As a simple example we consider the production of 4 exclusive jets in the High Energy limit. We present a brief argument for precisely which diagrams contribute these leading logarithms. Although heuristic it is sufficient to motivate the construction of high multiplicity amplitudes from *t*-channel gluon exchanges with the understanding that any other diagrams will be formally sub-leading. Fig. (3.4) shows three diagrams which all contribute at leading order in α_s ; fig. (3.4a) has three gluons exchanged in the *t*-channel and so its amplitude will have propagator terms which goes like:

$$\mathcal{M}_{(a)} \sim \frac{1}{(p_a - p_1)^2 (p_a - p_1 - p_2)^2 (p_a - p_1 - p_2 - p_3)^2}, \quad (3.48)$$

By contrast figs. (3.4b) and (3.4c) will have, in place of (3.48):

$$\mathcal{M}_{(b)} \sim \frac{\not{p}_a - \not{p}_1}{(p_a - p_1)^2 (p_a - p_1 - p_2)^2 (p_a - p_1 - p_2 - p_3)^2}, \quad (3.49)$$

and,

$$\mathcal{M}_{(c)} \sim \frac{(\not{p}_a - \not{p}_1)(\not{p}_4 - \not{p}_b)}{(p_a - p_1)^2 (p_a - p_1 - p_2)^2 (p_a - p_1 - p_2 - p_3)^2}, \quad (3.50)$$

respectively. Since in the High Energy limit we have $p_a \sim p_1$ and $p_b \sim p_4$ it is clear that $\mathcal{M}_{(b)}$ and $\mathcal{M}_{(c)}$ will be suppressed with respect to $\mathcal{M}_{(a)}$. We call the configurations with a maximal number of gluons exchanged in the *t*-channels an ‘FKL’ configuration; For example fig. (3.4a) is an FKL configuration while fig. (3.4b) and fig. (3.4c) are ‘non-FKL’ configurations.

A formal argument for which processes dominate in this limit was given by Fadin and Lipatov [27, 63]. They found that, in the High Energy limit, scattering amplitudes

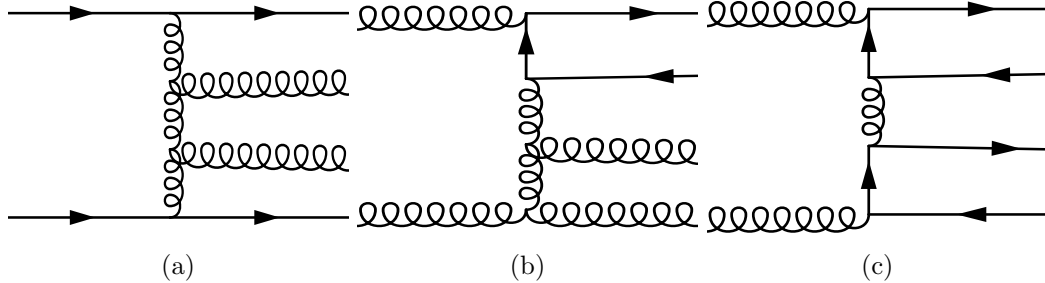


Figure 3.4: Three processes contributing to exclusive four jet production. (a) has the maximum number of gluons exchanged in the *t*-channels (three) and will dominate in the High Energy limit, (b) and (c) only have two and one gluon which can reggeise. As such as we move from (a) to (c) we will lose powers of large logarithms but maintain the same power of α_s and therefore we can reasonably approximate quad-jet production by neglecting (b) and (c) in the High Energy limit.

scaled in the same way as was predicted by Regge theory. This states that in the large invariant mass region a $2 \rightarrow n$ matrix element has a limiting behaviour determined by the maximum spin of any particle which could be exchanged in the *t*-channels between final state partons neighbouring in rapidity. We can then find the scaling of a process, for example $qg \rightarrow qg$, in particular regions of phase space where either $y_g \gg y_q$ or $y_q \gg y_g$ simply by drawing the associated colour connection diagrams for it. This is shown in fig. (3.5). Since when we have $y_g \gg y_q$ it is only possible to exchange a colour singlet (with spin one half) the cross-section will be dominated by the region where $y_q \gg y_g$. The case for $2 \rightarrow n$ is similar with the limiting behaviour of the matrix element given by

$$\mathcal{M}_{2 \rightarrow n}^{\text{HE}} \sim s_{12}^{\omega_1} \cdots s_{(n-1)n}^{\omega_{(n-1)}}. \quad (3.51)$$

Eqn. (3.51) now makes the previous discussion regarding figs. (3.4) formally clear since fig. (3.4a) will scale like:

$$\mathcal{M}_{2 \rightarrow 4}^{\text{HE}} \sim s_{12}s_{23}s_{34}, \quad (3.52)$$

in the High Energy limit while figs. (3.4b) and (3.4c) will scale like:

$$\mathcal{M}_{2 \rightarrow 4}^{\text{HE}} \sim s_{12}^{1/2}s_{23}s_{34}, \quad (3.53)$$

and,

$$\mathcal{M}_{2 \rightarrow 4}^{\text{HE}} \sim s_{12}^{1/2} s_{23} s_{34}^{1/2}, \quad (3.54)$$

respectively. Since s_{ij} are all large here, the processes with a (anti)quark exchanged in the t -channel will be highly suppressed relative to fig. (3.4a).

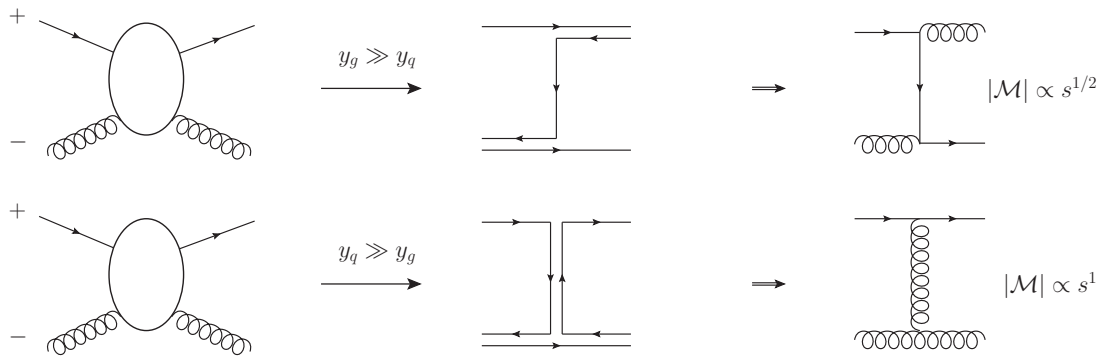


Figure 3.5: The limiting behaviour of $qg \rightarrow qg$ in the regions of phase space where either $y_g \gg y_q$ or $y_q \gg y_g$. The intermediate diagrams indicate the flow of colour through the process.

To further illustrate this we can look at the various processes contributing to the exclusive two jet cross-section. Tab. (3.1) shows several examples of parton level processes and their exact leading order matrix elements [70]. We can see clearly from this that any process which can proceed via a t -channel gluon exchange has a term proportional to s^2/t^2 which will dominate in the High Energy limit; for example $q\bar{Q} \rightarrow q\bar{Q}$ can only go via a t -channel diagram. Conversely, processes in which a t -channel gluon diagram can not contribute are suppressed in this limit. For example $q\bar{q} \rightarrow Q\bar{Q}$ can only proceed via an s -channel gluon and we can see that in the limit $s \rightarrow \infty$ and keeping t finite it's matrix element tends to u^2/s^2 which is $\mathcal{O}(1)$ since $s \sim -u$ in the High Energy limit). Processes like $gg \rightarrow gg$ have diagrams with and without the exchange we are interested in and, as such, only some of the terms from the exact leading order matrix element contribute - but they do still contribute.

3.7 Effective Vertices For Real Emissions

In order to generalise what we have done so far to higher multiplicity scattering events we begin by considering $qQ \rightarrow qQg$ in the high energy limit. The five diagrams which

Process	$1/g^4 \bar{\mathcal{M}} ^2$
$qQ \rightarrow qQ$	$\frac{4}{9} \frac{s^2+u^2}{t^2}$
$q\bar{Q} \rightarrow q\bar{Q}$	$\frac{4}{9} \frac{s^2+u^2}{t^2}$
$qq \rightarrow qq$	$\frac{4}{9} \left(\frac{s^2+u^2}{t^2} + \frac{s^2+t^2}{u^2} \right) - \frac{8}{27} \frac{s^2}{ut}$
$q\bar{q} \rightarrow Q\bar{Q}$	$\frac{4}{9} \frac{t^2+u^2}{s^2}$
$gg \rightarrow gg$	$\frac{9}{2} \left(3 - \frac{tu}{s^2} - \frac{su}{t^2} - \frac{st}{u^2} \right)$

Table 3.1: Some examples of $2 \rightarrow 2$ leading order matrix elements which contribute to the two jet exclusive cross-section.

contribute at leading order are illustrated in fig. (3.6). The diagram where the extra gluon is emitted from the t -channel gluon is given by:

$$\begin{aligned} \mathcal{M}_{t\text{-channel}} = & - \frac{g_s^3}{t_{a1} t_{b2}} f^{i2j} T_{1a}^i T_{3b}^j \langle 1 | \rho | a \rangle \langle 3 | \mu | b \rangle \epsilon_{2\nu}^* \\ & (2p_2^\mu g^{\nu\rho} - 2p_2^\rho g^{\mu\nu} - (q_1 + q_2)^\nu g^{\mu\rho}), \end{aligned} \quad (3.55)$$

and the remaining four diagrams are:

$$\begin{aligned} \mathcal{M}_{\text{Eik.}} = & (ig_s)^3 \epsilon_{2\nu} \left(T_{1i}^2 T_{ia}^d T_{3b}^d \frac{2p_1^\nu \langle 1 | \mu | a \rangle + \langle 1 | \nu | 2 \rangle \langle 2 | \mu | a \rangle}{s_{12} t_{b3}} \langle 3 | \mu | b \rangle \right. \\ & + T_{1i}^d T_{ia}^2 T_{3b}^d \frac{2p_a^\nu \langle 1 | \mu | a \rangle - \langle 1 | \mu | 2 \rangle \langle 2 | \nu | a \rangle}{t_{a2} t_{b3}} \langle 3 | \mu | b \rangle \\ & + T_{3i}^2 T_{ib}^d T_{1a}^d \frac{2p_3^\nu \langle 3 | \mu | b \rangle + \langle 3 | \nu | 2 \rangle \langle 2 | \mu | b \rangle}{s_{32} t_{a1}} \langle 1 | \mu | a \rangle \\ & \left. + T_{3i}^d T_{ib}^2 T_{1a}^d \frac{2p_b^\nu \langle 3 | \mu | b \rangle - \langle 3 | \mu | 2 \rangle \langle 2 | \nu | b \rangle}{t_{b2} t_{a1}} \langle 1 | \mu | a \rangle \right). \end{aligned} \quad (3.56)$$

In the High Energy limit the second term in each of the lines is suppressed with respect to the first and can therefore be disregarded. This turns out to be equivalent to considering p_2 as a soft emission using the Eikonal approximation. The resulting amplitude for the sum of all four may be written as:

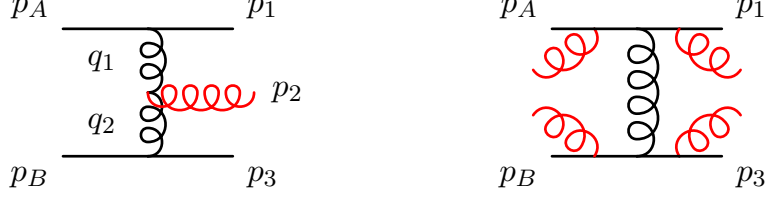


Figure 3.6: The 5 possible emission sites of extra QCD radiation in $qQ \rightarrow qQ$. Fig. from [20].

$$\begin{aligned} \mathcal{M}_{\text{Eik.}} = (ig_s)^3 \epsilon_{2\nu} \langle 1|\mu|a\rangle \langle 3|\mu|b\rangle & \left(T_{1i}^2 T_{ia}^d T_{3b}^d \frac{2p_1^\nu}{s_{12}t_{b3}} + T_{1i}^d T_{ia}^2 T_{3b}^d \frac{2p_a^\nu}{t_{a2}t_{b3}} \right. \\ & \left. + T_{3i}^2 T_{ib}^d T_{1a}^d \frac{2p_3^\nu}{s_{32}t_{a1}} + T_{3i}^d T_{ib}^2 T_{1a}^d \frac{2p_b^\nu}{t_{b2}t_{a1}} \right). \end{aligned} \quad (3.57)$$

Now using that $p_a \sim p_1 = p_+$ and $p_b \sim p_3 = p_-$ in the High Energy limit:

$$\begin{aligned} \mathcal{M}_{\text{Eik.}} = (ig_s)^3 \epsilon_{2\nu} \langle 1|\mu|a\rangle \langle 3|\mu|b\rangle & \left(\frac{2p_+^\nu}{p_+ \cdot p_2 t_{b3}} (T_{1i}^2 T_{ia}^d - T_{1i}^d T_{ia}^2) T_{3b}^d \right. \\ & \left. + \frac{2p_-^\nu}{p_- \cdot p_2 t_{a1}} (T_{3i}^2 T_{ib}^d - T_{3i}^d T_{ib}^2) T_{1a}^d \right). \end{aligned} \quad (3.58)$$

and tidying up the colour factors:

$$\mathcal{M}_{\text{Eik.}} = (ig_s)^3 \epsilon_{2\nu} \langle 1|\mu|a\rangle \langle 3|\mu|b\rangle f^{2de} T_{3b}^b T_{1a}^e \frac{1}{t_{a1} t_{b3}} \left(\frac{2p_+^\nu}{p_+ \cdot p_2} t_{a1} - \frac{2p_-^\nu}{p_- \cdot p_2} t_{b3} \right), \quad (3.59)$$

which has a colour factor similar to that found for the diagrams with a gluon emitted from the t -channel gluon. We choose to ‘symmetrise’ eqn. (3.59) by returning to $p_{a/1}$ and $p_{b/3}$ explicitly in place of p_+ and p_- respectively:

$$\begin{aligned} \mathcal{M}_{\text{Eik.}} = & (ig_s)^3 \epsilon_{2\nu} \langle 1|\mu|a\rangle \langle 3|\mu|b\rangle f^{2de} T_{3b}^b T_{1a}^e \frac{1}{t_{a1} t_{b3}} \\ & \frac{1}{2} \left(\frac{2p_a^\nu}{p_a \cdot p_2} t_{a1} + \frac{2p_1^\nu}{p_1 \cdot p_2} t_{a1} - \frac{2p_b^\nu}{p_b \cdot p_2} t_{b3} - \frac{2p_3^\nu}{p_3 \cdot p_2} t_{b3} \right). \end{aligned} \quad (3.60)$$

We now consider (3.55). The final term contracts the two currents and so it is only the first two terms which need to be massaged into the right form. Once again we approximate using $p_a \sim p_1 = p_+$ and $p_b \sim p_3 = p_-$ to write the currents as momenta. Upon doing this we find:

$$\begin{aligned} \mathcal{M}_{t\text{-channel}} = & - \frac{g_s^3}{t_{a1} t_{b2}} f^{i2j} T_{1a}^i T_{3b}^j \epsilon_{2\nu}^* \\ & \left(8e^{i\phi_-} (p_+^\nu p_- \cdot p_2 - p_-^\nu p_+ \cdot p_2) - (q_1 + q_2)^\nu \langle 1|\mu|a\rangle \langle 3|\mu|b\rangle \right), \end{aligned} \quad (3.61)$$

where ϕ_- is a phase resulting from the spinor conventions detailed in chapter 2. Now using that $s \sim 2p_+ \cdot p_- = \frac{1}{2} \langle 1|\mu|a\rangle \langle 3|\mu|b\rangle e^{-i\phi_-}$ we can write all three terms as something proportional to the desired current structure:

$$\begin{aligned} \mathcal{M}_{t\text{-channel}} = & - \frac{g_s^3}{t_{a1} t_{b2}} f^{i2j} T_{1a}^i T_{3b}^j \epsilon_{2\nu}^* \langle 1|\mu|a\rangle \langle 3|\mu|b\rangle \\ & \left(4 \left(p_+^\nu \frac{p_- \cdot p_2}{s} - p_-^\nu \frac{p_+ \cdot p_2}{s} \right) - (q_1 + q_2)^\nu \right). \end{aligned} \quad (3.62)$$

Similarly to before with $\mathcal{M}_{\text{Eik.}}$ we choose to include as much of the actual kinematic information as possible by symmetrising (3.62) to get:

$$\begin{aligned} \mathcal{M}_{t\text{-channel}} = & - \frac{g_s^3}{t_{a1} t_{b2}} f^{i2j} T_{1a}^i T_{3b}^j \epsilon_{2\nu}^* \langle 1|\mu|a\rangle \langle 3|\mu|b\rangle \\ & \left(-(q_1 + q_2)^\nu + \frac{1}{2} \left(p_a^\nu \frac{p_2 \cdot p_b}{p_a \cdot p_b} + p_a^\nu \frac{p_2 \cdot p_3}{p_a \cdot p_3} + p_1^\nu \frac{p_2 \cdot p_b}{p_1 \cdot p_b} + p_1^\nu \frac{p_2 \cdot p_3}{p_1 \cdot p_3} \right. \right. \\ & \left. \left. - p_b^\nu \frac{p_2 \cdot p_a}{p_a \cdot p_b} - p_b^\nu \frac{p_1 \cdot p_2}{p_b \cdot p_1} - p_2^\nu \frac{p_2 \cdot p_a}{p_a \cdot p_3} - p_2^\nu \frac{p_1 \cdot p_2}{p_1 \cdot p_3} \right) \right). \end{aligned} \quad (3.63)$$

Since eqns. (3.63) and (3.60) have the same colour factor we can simply sum them to

get:

$$\mathcal{M}_{qQ \rightarrow qQg} = \frac{S_{qQ \rightarrow qQ}}{t_{a1} t_{b2}} f^{2de} T_{3b}^b T_{1a}^e g_s^3 \epsilon_\rho^* V_\rho(q_1, q_2), \quad (3.64)$$

where:

$$V^\rho(q_1, q_2) = -(q_1 + q_2)^\rho + \frac{p_a^\rho}{2} \left(\frac{q_1^2}{p_a \cdot p_2} + \frac{p_2 \cdot p_b}{p_a \cdot p_b} + \frac{p_2 \cdot p_3}{p_a \cdot p_3} \right) + (p_a \leftrightarrow p_1) - \frac{p_b^\rho}{2} \left(\frac{q_2^2}{p_b \cdot p_2} + \frac{p_2 \cdot p_a}{p_b \cdot p_b} + \frac{p_2 \cdot p_1}{p_b \cdot p_1} \right) - (p_b \leftrightarrow p_3), \quad (3.65)$$

and $S_{qQ \rightarrow qQ}$ contains the current contraction. Eqn. (3.65) is manifestly gauge invariant which can be checked explicitly by calculating $p_g \cdot V$. It is, however clearly divergent: if any of p_a , p_b , p_1 , p_2 or p_3 becomes soft then the momenta contractions in the denominators of eqn. (3.65) will become zero. We organise the cancellation of divergences in the following chapter.

Armed with eqn. (3.65) and the quark and gluon currents we can calculate high multiplicity matrix elements by generalising eqn. (3.71) to include contractions of this effective vertex expression. For example the $2 \rightarrow 3$ matrix element squared for qQ scattering is therefore given by:

$$|\overline{\mathcal{M}}_{qQ \rightarrow qgQ}^t|^2 = \frac{1}{4(N_c^2 - 1)} \frac{g^2 C_F}{t_1} \frac{g^2 C_F}{t_2} \sum_{h_a, h_b, h_1, h_2} |S_{qQ \rightarrow qQ}^{h_a h_b \rightarrow h_1 h_2}|^2 \times \left(\frac{-g_s C_A}{t_1 t_2} V^\mu(q_1, q_2) V_\mu(q_1, q_2) \right). \quad (3.66)$$

This can be generalised to the $2 \rightarrow n$ matrix element by simply including more contractions of effective vertices

$$|\overline{\mathcal{M}}_{qQ \rightarrow qg \dots gQ}^t|^2 = \frac{1}{4(N_c^2 - 1)} \frac{g^2 C_F}{t_1} \frac{g^2 C_F}{t_2} \sum_{h_a, h_b, h_1, h_2} |S_{qQ \rightarrow qQ}^{h_a h_b \rightarrow h_1 h_2}|^2 \times \prod_{i=1}^{n-1} \left(\frac{-g_s C_A}{t_i t_{i+1}} V^\mu(q_i, q_{i+1}) V_\mu(q_i, q_{i+1}) \right). \quad (3.67)$$

Using eqn. (3.67) we can describe the real emission higher order corrections but this expression is manifestly divergent.

3.8 Virtual Corrections To All Orders

Thus far we have a prescription for approximating high energy scattering amplitudes with additional real radiation added through the effective vertices described in section (3.7). However, to complete our picture we must also include the virtual corrections to the process in a similar way to the example shown in section (2.7.2). This is important not only since these processes obviously contribute to the process but also because, as we saw in the one loop $\gamma^* \rightarrow q\bar{q}$ calculation, the soft divergences in eqn. (3.65) need to be cancelled. Both the cancellation in section (2.7.2) and the cancellation we will see here are examples of the KLN theorem [67] which states that the soft and virtual divergences in QCD must cancel for inclusive processes.

In the High Energy limit we may include the virtual corrections to all orders in α_s by using the Lipatov ansatz [63]. This is a prescription where t -channel gluon propagators are replaced with a ‘dressed’ version:

$$\frac{1}{q_i^2} \rightarrow \frac{1}{q_i^2} e^{\hat{\alpha}(q_i)\Delta_{i,i-1}}, \quad (3.68)$$

where:

$$\hat{\alpha}(q_i) = \alpha_s C_A q_i^2 \int \frac{d^{2+2\epsilon} k_\perp}{(2\pi)^{2+2\epsilon}} \frac{1}{k_\perp^2 (k_\perp - q_{i\perp})^2} \mu^{-2\epsilon}, \quad (3.69)$$

and $\Delta_{i,i-1}$ is the rapidity gap between the external gluon legs emitted from the dressed gluon. Similarly to eqn. (3.65) in the preceding section this new expression for the propagator contains divergences arising from the soft limit of the integral in the expression for $\hat{\alpha}(q_i)$. In the following chapter we show in some detail that these divergences cancel with those mentioned in section 3.7.

The keen reader will have noticed that eqn. (3.69) is exactly what we found in our next-to-leading order calculation in eqn. (3.47) expressed in $2 + 2\epsilon$ dimensions rather than 2 (save for a few numerical factors). This is no coincidence and, indeed, is the source of the ansatz. Higher order (in α_s) calculations [41, 46] have shown that to two loops the leading logarithmic virtual part of the full $2 \rightarrow 2$ amplitude agrees exactly with what we get when we Taylor expand the exponential term in eqn. (3.68).

3.9 High Energy Jets

3.9.1 The High Energy Jets Framework

The High Energy Jets framework is the basis of the later chapters of this thesis. Details of this framework beyond the brief summary presented here may be found in [18, 20–22, 59].

3.9.2 Factorisation Into Currents

The High Energy Jets framework is based, in part, on the observations of sections (3.3) and (3.4). In these sections we saw that in the High Energy limit we can write down matrix elements in the form of two vector ‘currents’ contracted over a t -channel pole. While one could argue that the fact that the $qQ \rightarrow qQ$ matrix element would factorise into a contraction of two vector currents with a t -channel pole was obvious (since the only contribution was from a t -channel diagram), it was not at all obvious that this would also be the case for the $qg \rightarrow qg$ amplitude. It can also be shown that the same structure is found even in the case of gluon-gluon scattering [22].

It turns out that this factorisation into a form with only a t -channel pole holds for all the helicity configurations where the helicities of the incoming-outgoing parton lines remain unchanged (aside from those in the Colour Accelerated Multiplier or ‘CAM’, factor [21]). For those diagrams where the helicity *is* flipped we find poles in s and u and so these contributions are heavily suppressed in the High Energy limit. The fact that all of the approximate helicity averaged matrix elements squared for any combination of incoming partons, a and b , can be written as:

$$|\bar{\mathcal{M}}_{2 \rightarrow 2}| \propto \sum_{h_a, h_b, h_1, h_2} \left| \frac{j_a^\mu(p_a, p_1) j_{b,\mu}(p_b, p_2)}{t} \right|^2, \quad (3.70)$$

is exploited in High Energy Jets to express more general matrix elements (those with higher multiplicity or more complicated final states) approximately.

Here is a convenient place to define the ‘ t -channel factorised’ form for matrix elements, $\overline{\mathcal{M}}_{qQ \rightarrow qQ}^t$, in which we extract the t poles from the rest of the matrix element [20]. We write the square of eqn. (3.11) as:

$$|\overline{\mathcal{M}}_{qQ \rightarrow qQ}^t|^2 = \frac{1}{4(N_c^2 - 1)} \frac{g^2 C_F}{t_1} \frac{g^2 C_F}{t_2} \sum_{h_a, h_b, h_1, h_2} |S_{qQ \rightarrow qQ}^{h_a h_b \rightarrow h_1 h_2}|^2, \quad (3.71)$$

where $N_c = 3$ and $C_F = 4/3$ for QCD, S is the matrix element for a $2 \rightarrow 2$ process in the form of a contraction of two currents, and t_i are the squared t -channel momenta - in this case $t_1 = (p_a - p_1)^2$ and $t_2 = (p_2 - p_b)^2$.

While for the $2 \rightarrow 2$ examples in section (3.3) and section (3.4) eqn. (3.71) is just an exact rewriting of a previous result, we will use the form shown here to generalise to describing extra final state radiation in the next section at which point the t -channel factorisation weakens to an approximation of the full result (but one which contains enough of the underlying physics to be useful nonetheless).

Extending eqn. (3.71) to higher multiplicity final states within the High Energy Jets framework is then done by using chains of products of effective vertices discussed in section (3.7) (for the real emissions) and the Lipatov ansatz described in section (3.8) (for the virtual emissions):

$$\begin{aligned} |\overline{\mathcal{M}}_{qQ \rightarrow qg \dots gQ}^t|^2 &= \frac{1}{4(N_c^2 - 1)} \frac{g^2 C_F}{t_1} \frac{g^2 C_F}{t_2} \sum_{h_a, h_b, h_1, h_2} |S_{qQ \rightarrow qQ}^{h_a h_b \rightarrow h_1 h_2}|^2 \\ &\times \prod_{i=1}^{n-1} \left(\frac{-g_s C_A}{t_i t_{i+1}} V^\mu(q_i, q_{i+1}) V_\mu(q_i, q_{i+1}) e^{\hat{\alpha}(q_i^2) \Delta y_{i,i+1}} \right). \end{aligned} \quad (3.72)$$

Eqn. (3.71) can also be easily generalised to describing different final states by using different current expressions in the contraction in S . For example by constructing a current describing a W^\pm boson being emitted from an incoming-outgoing quark line we can then write down the matrix element for the process $q'q \rightarrow (W^\pm \rightarrow) \nu e^\pm q'Q$ using eqn. (3.71) with $S_{qQ \rightarrow qQ}^{h_a h_b \rightarrow h_1 h_2}$ replaced with:

$$S_{q'q \rightarrow (W^\pm \rightarrow) e^\pm \nu_e q'Q}^{h_a h_b \rightarrow h_{e^\pm} h_{\nu_e} h_1 h_2} = j_{W^\pm}^\mu(p_a, p_1, p_{e^\pm}, p_\nu) j_\mu(p_b, p_2). \quad (3.73)$$

3.9.3 The High Energy Jets Monte Carlo

The High Energy Jets framework is implemented in a general purpose Monte Carlo, referred to as HEJ, and publicly available at <http://hej.web.cern.ch/HEJ/>. This C++ package is under continual development to test and improve it and the work of chapter 4 was a major contribution of the author to it (among many other changes and improvements).

Here we briefly summarise the main aspects of the software aspects of High Energy

Jets. A general HEJ run consists of three main stages.

1. **Setup:** at which point a user defined input file is parsed and, based on the specifics of the input, one of several class hierarchies is initialised after which essential components for the physics stage are constructed including: an interface to a PDF package (either `MSTW` or `LHAPDF` (v6)), a (pseudo-)random number generator and a physics analysis class structure.

HEJ comes with a stand-alone analysis class which implements many standard operations and is therefore sufficient in most cases. It may also be interfaced with the `Rivet` analysis package; this is particularly useful when comparing Monte Carlo results to data since many experimental analyses are implemented in `Rivet` routines and it is, in principle, just a matter of plugging in the right analysis name.

2. **Monte Carlo Generation:** In the Monte Carlo stage of a HEJ run we proceed iteratively over a (typically very large) number of events. For each event we must generate a point in phase space; a number of outgoing partons and their momentum. With this information we can use our knowledge of x_a and x_b and the importance sampling ideas discussed in chapter 2 to randomly generate parton types for our incoming partons - there are, of course, additional constraints which are process dependent to consider. For example, we will never select a gluon-gluon incoming pairing if we wish to calculate the matrix element for $Z/\gamma^* + \text{jets}$ in an FKL configuration since there is no such contribution.

Once we have a definite phase space and the incoming types have been specified we can calculate the matrix element using some generalisation of eqn. (3.71) - the exact matrix element used will depend on the final state multiplicity and the process chosen by the user in stage (1). Virtual corrections are also included at this stage. Lastly we perform a multiplicative matching to the exact leading order matrix element provided by `MadGraph_aMC@NLO` (v5), the details of which will be discussed further in chapter 4.

We include the 2-, 3- and 4-jet non-FKL contributions as exclusive sums to correct the total cross section. This is done separately to the resummation Monte Carlo calls, it can either be computed as a stand-alone run and then summed with the FKL matched resummation events upon completion or both FKL and non-FKL configurations can be calculated as a single run. In practise the majority of the computer time is spent on these non-FKL terms as processes such as $gg \rightarrow (Z/\gamma^* \rightarrow) e^+ e^- ggggg$ are complex matrix elements and therefore are slow to evaluate even at leading order.

3. Analysis: In the analysis stage the event is passed to either the **HEJ** analysis framework or to **Rivet**. Here we enforce kinematic constraints on our final state to study the regions of phase space we are interested in - or those regions probed by a particular experimental analysis whose results we wish to compare to. In **HEJ** it is possible perform a complete run ‘un-cut’ whereby the generated events are outputted before the analysis phase into a given format (**ROOT** N-tuples, **LH** events and **HepMC** (v2) records are all supported). This is preferable when the same generation can be reused multiple times however for very long runs outputting all of the events becomes unfeasible due to storage requirements (this was the case for the work presented in chapter 5) and we must take the second option of performing **HEJ** analyses on-the-fly i.e. cutting as we iterate through events, binning into histograms and discarding event details.

While this breakdown is a good broad strokes overview of **HEJ** there are hundreds of intricacies which must be treated along the way. One worth mentioning is the calculation of scale uncertainty bands for predictions. In section (2.3) we discussed how some given observable, R , will depend on the renormalisation scale, μ_r , or more specifically - how it must not. Our theory is, after all, meaningless if its predictions are effected by a choice of an unphysical scale. However, when we do our perturbative expansion (through a resummation or fixed-order approach) we develop a dependence on this scale. It is important to understand the size of this dependence and so when generating Monte Carlo predictions we must produce not only a ‘central’ prediction for each value but also an associated ‘scale uncertainty’ band. For fixed-order calculations this is simply a case of varying α_s through the value of μ_r but since the High Energy Jets matrix element contains scale dependence through the QCD coupling *and* the Lipatov ansatz we must evaluate entire matrix elements at a variety of scales to properly understand our dependence and to provide meaningful predictions. The factorisation scale must also be varied (in tandem with varying μ_r) to get a complete scale uncertainty band and this is run by default as part of **HEJ**.

In a standard partonic **HEJ** run we evaluate the matrix element for each event at 76 different scale choices. 76 because we give four choices for the ‘central’ scale and for each central scale we take 5 values for μ_r and μ_f (the central value multiplicatively scaled by $1/2$, $1/\sqrt{2}$, 1 , $\sqrt{2}$ and 2) but exclude the combinations where the relative ratio is greater than 2 - leaving 19 for each central choice. The remaining combinations form an ‘envelope’ of predictions for each bin in each plot which indicate our dependence on the renormalisation and factorisation scales. Scale bands are shown in all integrated distributions in chapters 4–6.

3.9.4 Matching to ARIADNE

The HEJ scheme for describing all-order corrections to jet rates at hadronic colliders is based on the limit in which emissions are both hard and well separated. Of course, some radiation at hadronic colliders is soft or produced collinear to other radiation (or both) and such emissions also lead to large logarithmic enhancements similar to those discussed in this work and so it is obviously advantageous to describe both. These effects can be included through a parton shower description.

HEJ has been matched to the ARIADNE parton shower [19]. ARIADNE [64] is based on the Lund colour dipole model [55] which attempts to describe final state QCD radiation resulting from a hard scatter: it considers the splitting of colour dipoles into more colour dipoles rather than partons splitting to more partons. It calculates the probability of an emission from the splitting function, $\mathcal{D}(p_\perp^2, y)$, as being approximately given by:

$$\mathcal{D}(p_\perp^2, y) \approx \frac{z}{16\pi^2} \frac{|\mathcal{M}_{n+1}|^2}{|\mathcal{M}_n|^2}, \quad (3.74)$$

where z is the energy fraction carried by the emission. From this one defines ‘no-emission’ probabilities, $\Delta(p_{1\perp}^2, p_{2\perp}^2)$, which give us the probability that no extra radiation is emitted as we evolve the squared transverse momentum of a parton between two scales $p_{1\perp}^2$ and $p_{2\perp}^2$:

$$\Delta(p_{1\perp}^2, p_{2\perp}^2) = \exp \left(- \int_{p_{1\perp}^2}^{p_{2\perp}^2} dp_\perp^2 \int dy \mathcal{D}(p_\perp^2, y) \right). \quad (3.75)$$

Matching HEJ to ARIADNE is very different to the usual hard-scatter matching to a parton shower. As we will see in chapter 4, HEJ includes radiation down to a very soft scale and so were we to perform a naïve matching to a parton shower we would be double-counting all of the soft non-collinear radiation. Fig. (3.7) shows the average ARIADNE splitting function, \mathcal{D}/z , compared to the equivalent expression in HEJ for 30 GeV jets. The extra emissions were required to be at least $\Delta r = 0.5$ away from the emitting parton in order to probe only the soft contributions coming from the shower. HEJ includes soft emissions and therefore we expect to see that the majority of the emissions from ARIADNE are already being described by the partonic description. Indeed fig. (3.7) shows that, aside from extremely soft radiation, the average splitting function of HEJ is indeed greater than that of ARIADNE. Fig. (3.8) shows a similar comparison where the extra emissions were required to have transverse momentum of 10 GeV but no cut on Δr was applied so that we are now investigating the effect

of the collinearity of the extra emission on the splitting function. This time we see a much bigger difference in the splitting functions at low values of r , i.e. collinear emissions. This is expected since one of the key approximations required to derive our matrix element expressions is that emissions are well separated in rapidity. At values of r greater than the jet definition of 0.6 we see that as in the soft radiation case the HEJ splitting function is greater than the shower splitting function. When generating showered events with HEJ+ARIADNE we must be careful not to double count terms; it is clear from figs. (3.7) and (3.8) that soft and wide-angle emissions are taken care of by HEJ and so it would be a mistake to allow ARIADNE to also generate these.

An outline of the algorithm for matching ARIADNE to HEJ is as follows:

- HEJ generates a partonic state. The extremal partons are required to form jets while the gluon emissions from the effective vertices are allowed to be soft (but still above some very soft scale, λ_{cut} (e.g. 0.2 GeV).
- ARIADNE then begins its dipole cascade. Each additional dipole generated by ARIADNE is checked to see if it is an emission that could have been generated by HEJ. If it could be a High Energy Jets emission then the emission is rejected with probability $r_{HEJ}/r_{ARIADNE}$, where:

$$r_{HEJ} = \frac{|\mathcal{M}_{n+1}^t|^2}{|\mathcal{M}_n^t|^2}, \quad (3.76)$$

and,

$$r_{ARIADNE} = \frac{|\mathcal{M}_{n+1}|^2}{|\mathcal{M}_n|^2}. \quad (3.77)$$

Any emission which could not have been generated by HEJ is automatically kept, e.g. gluons splitting to quark-antiquark pairs, gluon emissions outside of the extremal partons in rapidity or emissions between the High Energy Jets soft cut-off, λ_{cut} .

- Upon completion of the cascade the final state is passed to PYTHIA to perform hadronisation.

3.9.5 Comparisons to data

The High Energy Jets framework has been thoroughly tested for a number of the currently available final states (jets, W^\pm +jets and Z/γ^* +jets) against other theoretical descriptions and experimental data in analyses by the ATLAS, CMS and D \emptyset collaborations [1, 3–5, 7, 37, 59].

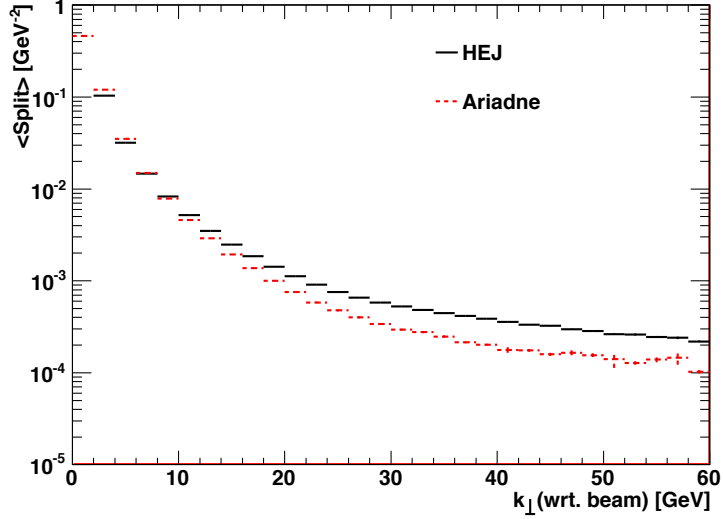


Figure 3.7: The average splitting function for HEJ and ARIADNE as a function of the transverse momentum, k_{\perp} . Emissions are required to be well separated from the emitting parton by enforcing a cut of $\Delta r \geq 0.5$ Figure from [19].

These studies probe wide ranges of experimental observables with a variety of cuts designed to probe specific regions of phase space. High Energy Jets is seen to provide an excellent description of data in all of these studies in the regions of phase space close to the High Energy limit. Interestingly there are cases where HEJ is seen to be competitive with other state-of-the-art theoretical descriptions even when we are far from this strict limit. We now discuss a few specific examples of comparisons to data.

In fig. (2.5) we see that the probability of a third emission from a dijet system (constructed from the most forward and backward jets in the event) in addition to a W^{\pm} boson. As we pull apart the dijet system there is increasingly more phase space into which we can radiate extra emissions and so the probability of emission increases. We see that HEJ and BlackHat describe the data well across the full range of the dijet rapidity, $\Delta y_{j_F, j_B}$, while the other generators considerably underestimate the dijet activity.

Fig. (3.9) describes the differential distribution for W^{\pm} plus dijets in terms of the invariant mass of the dijet system defined by the two leading jets in p_{\perp} , m_{12} . The logarithms resummed by High Energy Jets become significant for large values of m_{12} and so we expect that HEJ should describe this distribution well while fixed-order schemes who cannot capture these large logarithmic corrections may not. In fact, HEJ gives the best description of data across almost the entire range of m_{jj} with the other theoretical predictions only agreeing with data below an invariant mass of approximately 300 GeV, deviating badly by 2 TeV. This high invariant mass region is

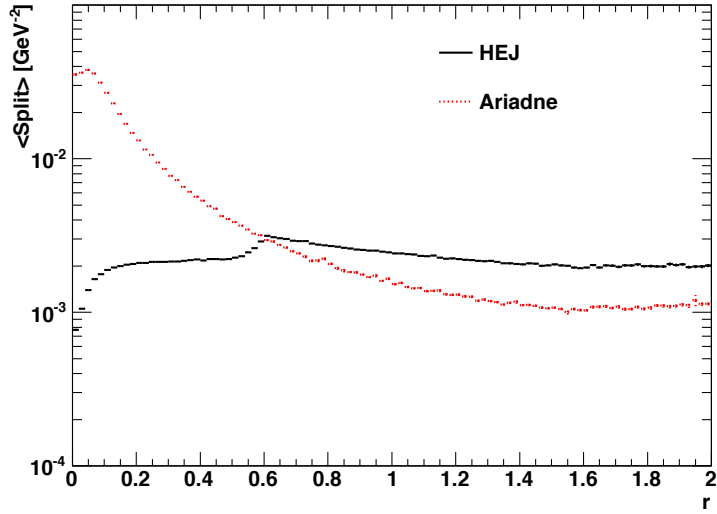


Figure 3.8: The average splitting function for HEJ and ARIADNE as a function of the collinearity, r . Emissions were kept from becoming soft by enforcing a cut on the transverse momentum of $k_T \geq 10$ GeV. Figure from [19].

an important region for VBF studies and so it is important that we are able to describe QCD emissions here. The failure of fixed order calculations show that perturbative stability already begins to breakdown in 7 TeV LHC data. This is a challenge we must face in LHC run II and as we will see in chapter 6 this is a challenge we must face at a potential high energy Future Circular Collider.

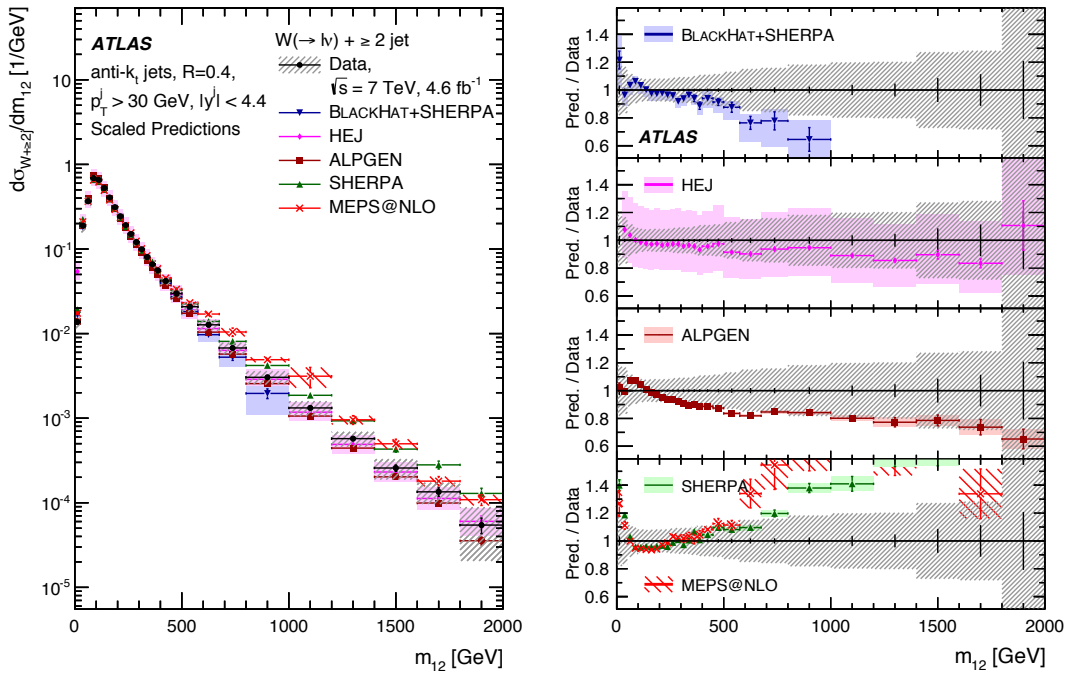


Figure 3.9: The distribution of W^\pm plus inclusive dijets with at least 2 jets differential in the invariant mass of the leading dijets in p_\perp , m_{12} . Fig. from [5].

Chapter 4

$Z/\gamma^* + \text{Jets}$ at the LHC

Except where otherwise referenced the work in this chapter and the subsequent chapters refers to work undertaken by the author as part of the High Energy Jets collaboration. This work is the theoretical foundation for the full-flexible parton level Monte Carlo generator soon to be publicly available from

<http://hej.web.cern.ch/HEJ/>

and is published in [59].

4.1 Introducing $Z/\gamma^* + \text{Jets}$ at the LHC

The Large Hadron Collider (LHC) has opened up a new range of energies for hadronic collisions. It has already been a resounding success with the discovery of the scalar Higgs boson completing the particle content of the Standard Model (SM). Hadronic colliders, by their very nature, lead to final states with large amounts of QCD radiation and being able to accurately describe this is essential. Both the SM and many ‘Beyond the Standard Model’ theories predict events with multiple hard jets in the final state and as seen in the previous chapter this can pose a serious problem for fixed-order descriptions.

The current best approach for describing QCD radiation is through the use of a Monte Carlo (MC) generators using the principles outlined in section 2.9. A wide range of such MC generators are available implementing everything from fixed-order perturbative schemes such as those described in [26, 65] to parton shower models which resum the logarithms arising from soft and collinear logarithms [40, 52, 73]. This soft and collinear radiation is experimentally observed to cascade from outgoing high energy

quarks and gluons in chaotic patterns we refer to as jets. While parton showers do a good job of describing the composition of jets they cannot be expected to give the correct description of the p_T spectrum of events with a high multiplicity of jets. It is also possible to combine the theoretical ideas behind fixed order and parton shower predictions. These schemes typically produce resummed results and then match to either leading order or next-to-leading results giving a formal accuracy of LO+LL [66] and NLO+LL [9] respectively. This approach gives a better description of multi-jet states however the current state-of-the-art for the fixed order component is still limited to next-to-leading order in α_s (with the exception of the recent N³LO result [15]).

In the High Energy Jets framework we aim to resum the large logarithmic corrections arising from well separated (in rapidity), hard final state jets. We capture these important terms by calculating those diagrams which contribute a ‘leading logarithm’ in the High Energy limit at all orders in α_s .

In the remainder of this chapter we discuss how we can describe the production of di-leptons plus multiple hard jets through the emission of an electroweak Z^0 boson and an off-shell photon, γ^* . We do this by constructing a current describing Z/γ^* emission from one of the incoming quark or anti-quark lines and then combine this with a ‘passive’ quark or gluon current as was described in section 3.9.2. The effective vertex derived in section 3.7 can then be used to generalise the resulting matrix element to give an approximate description of the $(Z/\gamma^* \rightarrow e^+e^- + n \text{ jets})$ final state valid in the High Energy limit of QCD discussed in chapter 3. The interference present from the multiple possible emission sites of the Z/γ^* is described exactly by a generalisation of the t -channel picture which allows for multiple ‘chains’ of momenta flowing through the reggeised gluons in the t -channel. This approach requires a new regularisation procedure to carefully render the resulting matrix element finite when we consider the cancellation of poles from the Lipatov propagator terms and the effective vertices. We also treat the interference arising from the two distinct emissions (Z^0 and γ^*) exactly.

The formal accuracy of the description given here is LO+LL. The leading order accuracy is achieved by performing a multiplicative matching to exact matrix elements generated using `MadGraph_aMC@NLO`. As discussed in section 3.9 this required a completely new matching set-up and this too is described later in this chapter along with some of the other computational challenges encountered along the way.

Finally we present a comparison of results from High Energy Jets Z/γ^* plus jets to several recent experimental studies at the LHC; both from the ATLAS collaboration and from the CMS experiment. We see that we describe the data well in these studies and, in particular, in the regions of phase-space with large rapidity gaps and high

invariant mass High Energy Jets gives a better description of the data than the other fixed-order and fixed-order plus parton shower predictions included.

4.2 Constructing $Z/\gamma^* + \text{jets}$

We now consider the construction of a current and an all orders inclusive cross-section for the Z/γ^* . We start by looking at just the Z^0 emission from a single fermion line.

4.2.1 A Current for $Z^0 + \text{Jets}$

For any given initial state (excluding the case of gluon-gluon scattering which will not contribute an FKL configuration) there are two possible emission sites for the Z^0 per fermion i.e. two for qg and $\bar{q}g$ scattering and four for qq , $\bar{q}q$ and $\bar{q}\bar{q}$ scattering. The emission sites on a single fermion line are illustrated in fig. (4.1). In the language of currents discussed previously we call the left hand side of fig. (4.1) j_μ^Z . It is given by:

$$j_\mu^Z = \frac{C_{Zq}C_{Ze}}{p_Z^2 - M_Z^2 + i\Gamma_Z M_Z} \left(\frac{\langle 1 | \gamma^\sigma (\not{p}_{out} + \not{p}_{e+} + \not{p}_{e-}) \gamma_\mu | a \rangle}{(p_{out} + p_Z)^2} + \frac{\langle 1 | \gamma^\mu (\not{p}_{in} - \not{p}_{e+} - \not{p}_{e-}) \gamma_\sigma | a \rangle}{(p_{in} - p_Z)^2} \right) \langle e^+ | \gamma_\sigma | e^- \rangle, \quad (4.1)$$

where M_Z is the mass of the Z^0 boson, Γ_Z is its width, C_{Zx} is the coupling of the Z^0 to x , $x = e, q, \nu_e, \dots$ and μ is the Lorentz index for the t -channel gluon propagator.

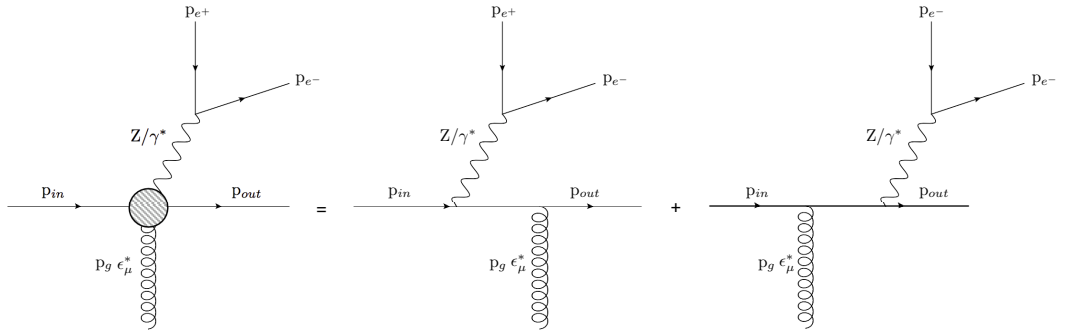


Figure 4.1: The possible emission sites for a neutral weak boson.

We can expand the quark and lepton momenta using their completeness relations which, in terms of spinor-helicity brackets, is given by:

$$\not{p}_i = |i_+\rangle\langle i_+| + |i_-\rangle\langle i_-|. \quad (4.2)$$

This fixes the helicity of the incoming quark, h_{in} , and the outgoing quark, h_{out} , to be identical, and we are left with a current which only has four possible helicity configurations depending on $h_q = h_{\text{in}} = h_{\text{out}}$ and the electron helicity, h_e :

$$\begin{aligned} j_\mu^Z(h_q, h_e) &= C_{Zq}^{h_q} C_{Ze}^{h_e} \frac{\langle e_{h_e}^+ | \gamma_\sigma | e_{h_e}^- \rangle}{p_Z^2 - M_Z^2 + i\Gamma_Z M_Z} \\ &\times \left(\frac{2p_1^\sigma \langle 1_{h_q} | \gamma^\mu | a_{h_q} \rangle + \langle 1_{h_q} | \gamma^\sigma | e_{h_q}^+ \rangle \langle e_{h_q}^+ | \gamma^\mu | a_{h_q} \rangle + \langle 1_{h_q} | \gamma^\sigma | e_{h_q}^- \rangle \langle e_{h_q}^- | \gamma^\mu | a_{h_q} \rangle}{(p_{\text{out}} + p_Z)^2} \right. \\ &\quad \left. + \frac{2p_a^\sigma \langle 1_{h_q} | \gamma^\mu | a_{h_q} \rangle - \langle 1_{h_q} | \gamma^\mu | e_{h_q}^+ \rangle \langle e_{h_q}^+ | \gamma^\sigma | a_{h_q} \rangle - \langle 1_{h_q} | \gamma^\mu | e_{h_q}^- \rangle \langle e_{h_q}^- | \gamma^\sigma | a_{h_q} \rangle}{(p_{\text{in}} - p_Z)^2} \right). \end{aligned} \quad (4.3)$$

We can then express amplitudes for Z^0 plus jets in terms of contractions of a Z^0 emitting current with either a quark or gluon current discussed previously. Taking the concrete example of $qg \rightarrow Zqg$ we can write the matrix element as follows:

$$|\bar{\mathcal{M}}_{qg \rightarrow Zqg}^t|^2 = \frac{g_s^2}{8} \frac{1}{(p_a - p_1 - p_{e^+} - p_{e^-})^2 (p_b - p_n)^2} \sum_{h_q, h_e, h_g} |j_\mu^Z(h_q, h_e) j^{g\mu}(h_g)|^2. \quad (4.4)$$

We will investigate the behaviour of eqn. (4.4) for a ‘slice’ through the final state phase-space where each particles momenta is parametrised by:

$$p_i = k_{i\perp} \left(\cosh(y_i); \cos(\phi_i), \sin(\phi_i), \sinh(y_i) \right)$$

and,

$$\begin{aligned}
 k_{1\perp} = k_{e^+\perp} &= 40 \text{ GeV} & k_{e^-\perp} &= \frac{m_Z^2}{2k_{e^+\perp}(\cosh(y_{e^+} - y_{e^-}) - \cos(\varphi_{e^+} - \varphi_{e^-}))), \\
 \varphi_1 &= \pi & \varphi_{e^+} &= \pi + 0.2 & \varphi_{e^-} &= -(\pi + 0.2), \\
 y_1 &= \Delta & y_2 &= -\Delta & y_{e^+} &= \Delta & y_{e^-} &= \Delta - 1.5,
 \end{aligned} \tag{4.5}$$

So as Δ increases we pull the two jets apart in rapidity. In this phase space slice the lepton pair are emitted in the forward region and so the physical picture is that the incoming quark with $p_a \sim p_1 = p_+$ emits a Z^0 and then a t -channel gluon (or a t -channel gluon and *then* a Z^0).

We then observe the behaviour shown in fig. (4.2): as we pull the jets apart in rapidity (i.e. as we go to large Δ) we see that the matrix element approaches a constant; this is the result which would be obtained by using the BFKL formalism in which all jets are taken to be infinitely well separated in rapidity.

As we expect for the case of $2 \rightarrow 2$ scattering we see exact agreement between our expression and the leading order result obtained from `MadGraph_aMC@NLO` [13]. It is clear that the BFKL limit is not reached until relatively large values for Δ , therefore it would be a poor approximation were we to just take the infinite rapidity limit of this as our expression for the Z^0 matrix element.

The picture becomes more complicated when considering the $qQ \rightarrow ZqQ$ scattering since there are now four possible places where the (anti-)quark may emit the Z^0 . In previous work by the High Energy Jets collaboration the case of W^\pm plus multiple hard jets was treated by attaching the boson to a single external quark line probabilistically [18]. In the case of W^\pm the interference terms arising from multiple boson emission sites is small and can be neglected, the reason for this is two fold. Firstly, the emission of the W^\pm changes the flavour of the emitting quark line and so the final state will differ in almost all diagrams depending on where you emit (and hence there is no interference allowed), the exceptions to this are processes such as $uu \rightarrow (W^\pm \rightarrow) e + \nu_e ud$ where either line could have been the emitter and so these are PDF suppressed. Secondly, in order to have interference the W boson must be able to be emitted from multiple legs *and* have the same charge wherever you attach it - again this is because the W^\pm will decay to a distinct final state and no interference can occur. With these constraints in mind there are far fewer diagrams which contribute to the interference effects in W^\pm -plus-jets. However as we will see later in the case of Z/γ^* this leads to an approximate matrix element which differs significantly from the leading-order result and so here we will include not only the contributions to the matrix

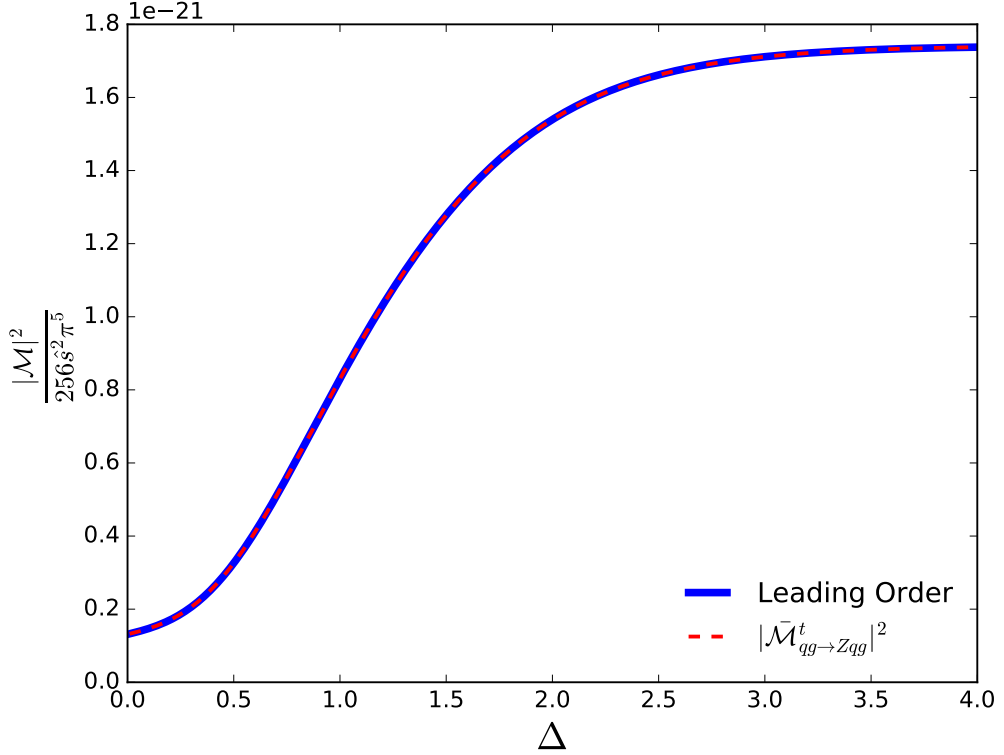


Figure 4.2: $\overline{|\mathcal{M}_{qg \rightarrow Zqg}^t|^2}$ shown for a slice through the final state phase-space defined by eqn. (4.5). We compare to the leading order result obtained from `MadGraph_aMC@NLO`.

element arising from the Z^0 being emitted from both (anti-)quark legs separately but also the resulting interference term.

4.2.2 Z^0 Emission Interference

Our high-energy description of the matrix elements relies on the correct description of the t -channel momenta, and this obviously depends on which of the quark lines the Z^0 was emitted from. We therefore need to modify the simple framework outlined above. We will use the subscript a (b) to label the current at the lowest (highest) end of the rapidity chain. We then define t_a (t_b) to be the t -channel momentum exchanged when the bosons are emitted at the lowest (highest) end of the rapidity chain. Then the amplitude squared for $qQ \rightarrow qQ(Z^0 \rightarrow e^+e^-)$ is given by:

$$\begin{aligned}
 |\bar{\mathcal{M}}_{qQ \rightarrow ZqQ}^t|^2 &= g_s^2 \frac{C_F}{8N_c} \left| \frac{j_a^{Z^0} \cdot j_b}{t_a} + \frac{j_a \cdot j_b^{Z^0}}{t_b} \right|^2 \\
 &= g_s^2 \frac{C_F}{8N_c} \left(\left| \frac{j_a^{Z^0} \cdot j_b}{t_a} \right|^2 + \left| \frac{j_a \cdot j_b^{Z^0}}{t_b} \right|^2 + 2\Re \left\{ \left(\frac{j_a^{Z^0} \cdot j_b}{t_a} \right) \left(\frac{j_a \cdot j_b^{Z^0}}{t_b} \right)^* \right\} \right),
 \end{aligned} \tag{4.6}$$

where $j_{a,b}$ are the pure quark currents defined previously. The coupling constants of the Z^0 to the relevant quarks and leptons are contained within $j^{Z^0}(h_q, h_e)$, as in eqn. (4.1).

Fig. (4.3) shows the value of this matrix element squared scaled by the squared partonic centre-of-mass energy for increasing rapidity separation of the two jets. Once again the result is compared with that obtained from the full, tree-level matrix elements from `MadGraph_aMC@NLO`. The slice through phase space here is the same as that used in the previous section given by eqn. (4.5). Fig. (4.3) also shows the separate contributions to the total matrix element squared coming from the Z/γ^* emission from the forward moving quark line (black, dashed) and emission from the backward moving quark line (green, dotted). In this phase space slice, the leptons also have an increasing positive rapidity and so the forward emission matrix element describes the full matrix element most closely, with the contribution from backward-emission falling at large values of Δy . The sum of the forward and backward emission matrix elements neglecting interference (magenta, dotted) significantly overestimates the final result. Once the destructive interference effects have been taken into account, the full sum (red, solid) correctly reproduces the LO matrix element (blue, thick solid). It is therefore clear that at low rapidities the inclusion of the interference effect plays an important rôle in the accuracy of the matrix element.

Fig. (4.3) shows that in the region of very high rapidity separation the full matrix element squared (scaled by s^2 and an irrelevant phase space factor) approaches a constant. We could have predicted this behaviour by considering eqn. (3.16); in the strict High Energy limit all the absolute rapidity information becomes lost and we only have dependence on s and the transverse momenta of the outgoing partons (we still have information about the rapidity gap through s using eqn. (3.8)). In this case we also have the Z^0 propagator and its couplings to the partons and leptons to consider but the kinematics of the t -channel gluon still dominates. The limit approached can be easily evaluated by applying the high energy limit, since in the $\Delta y \rightarrow \infty$ limit only the forward emission term contributes we have:

$$\frac{|\bar{\mathcal{M}}_{qQ \rightarrow ZqQ}^{HE}|^2}{256\pi^5 s^2} = \frac{\alpha_s^2 C_F^2}{64\pi^3(N_c^2 - 1)} \sum_{h_a, h_e} \frac{|C_{Za}^{h_a} C_{Ze}^{h_e}|^2}{|p_{1\perp}|^2 |p_{2\perp}|^2}. \quad (4.7)$$

Once we have scaled out the invariant mass squared divergence (as well as the usual phase space factor) out we have the limiting behaviour shown in fig (4.3).

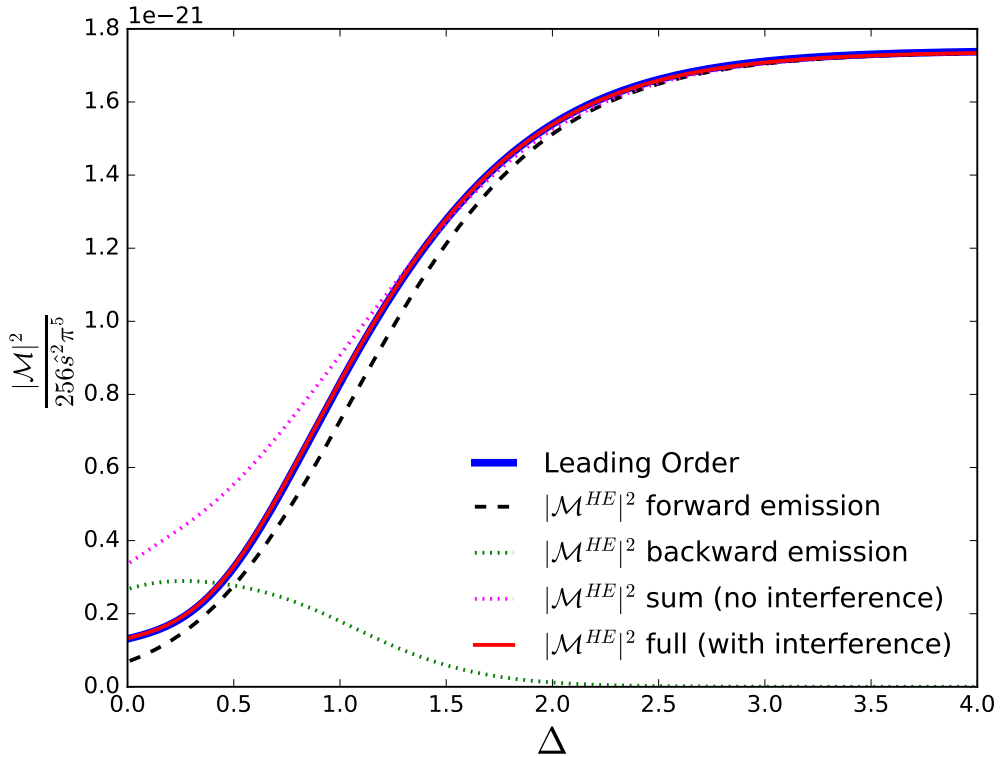


Figure 4.3: The matrix-element squared divided by the square of the partonic centre-of-mass energy for $qQ \rightarrow ZqQ$ with the Z^0 decaying to an electron-positron pair for the phase space slice described in eqn. (4.5). Increasing values of Δ represent increasing rapidity separation between the jets. The different lines show the contributions from different terms in the calculation: only emission from the forward or the backward quark line (black, dashed and green, dotted), their sum without the interference term (magenta, dotted) and their sum including interference (red, solid) which is seen to agree exactly with the LO result (blue, thick solid).

4.2.3 Photonic Interference

Since any virtual Z^0 decaying to an e^+e^- pair could also have proceeded via an off-shell virtual photon, γ^* , we must also include these processes and the resulting interference between the Z^0 and γ^* .

The γ^* emission matrix element is similar to that of the Z^0 -only matrix element shown in eqn. (4.4) and the same story applies with the possible emission sites causing interference. All that needs to be changed is the propagator term and the couplings of the boson to the emitting (anti-)quark and the decay products. The full current for Z/γ^* emission is then obtained by summing the two separate currents as follows:

$$j_\mu^{Z/\gamma^*}(h_q, h_e) = j_\mu^Z(h_q, h_e) + j_\mu^\gamma(h_q, h_e). \quad (4.8)$$

Then upon squaring eqn. (4.8) we will automatically include the interference terms from the cross-terms. The inclusion of the virtual photon terms is particularly important when studying a combined lepton invariant mass, $(p_{e^+} + p_{e^-})^2$, far from the Z^0 Breit-Wigner mass peak. This can be seen in fig. (4.4), where slices through phase space are shown similarly to fig. (4.3), but now for an (a) lower and (b) higher value of the di-lepton mass. In both cases, the contribution of the virtual photon processes is above 25%.

4.2.4 The $2 \rightarrow n$ Matrix Element

Armed with eqn. (4.8) we can extend eqn. (4.4) in the obvious way to form a complete matrix element for the emission of a Z/γ^* boson. We can also describe the various possibilities (qq , qg and gg) simply by substituting the currents which apply in any given situation. Of course, in practice we use the importance sampling techniques discussed in chapter 3 to randomly sample the possible incoming parton types and so all combinations of currents are included.

Following in the vein of the previous chapter we now look to extend our description to higher multiplicity final states. Since our expression for the effective vertices are independent of the currents at either end of the t -chain we can write the squared matrix element for $qQ \rightarrow (Z/\gamma^* \rightarrow) e^+e^- q(n-2)gQ$ as:

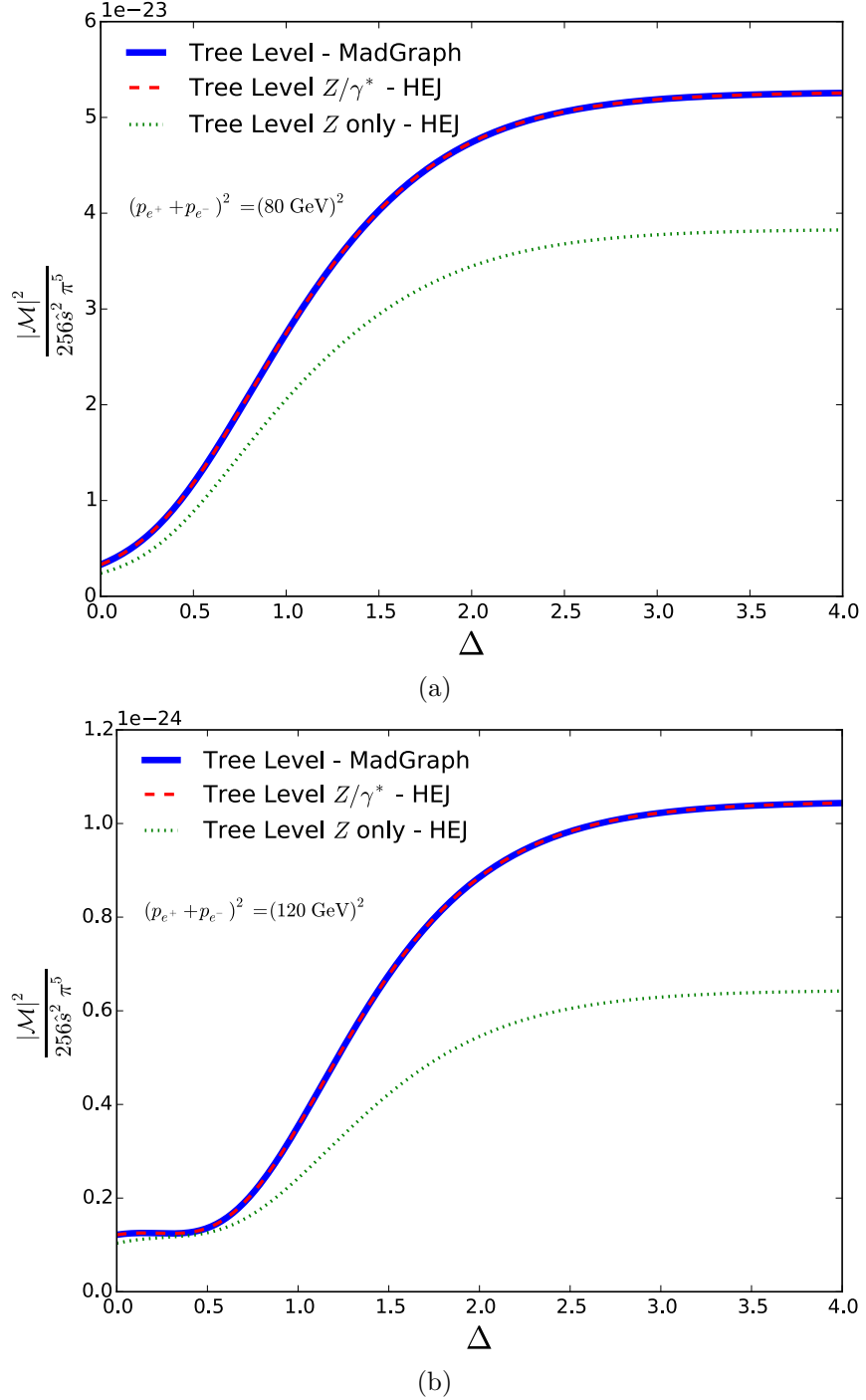


Figure 4.4: The matrix-element squared divided by the square of the partonic centre-of-mass energy for $qQ \rightarrow Z/\gamma^* qQ$ with the Z/γ^* decaying to an electron-positron pair. The $\mathcal{O}(\alpha_s^2 \alpha_W)$ tree-level contribution as described in HEJ (red, dashed) exactly matches that of `MadGraph_aMC@NLO` (blue, solid). The terms corresponding to the production of a Z^0 boson only (green, dotted) significantly undershoots the full result. The virtual photon terms are, therefore, clearly an important contribution to the matrix element away from the Z^0 Breit-Wigner peak.

$$\begin{aligned}
 & |\mathcal{M}_{qQ \rightarrow Z/\gamma^* q(n-2)gQ}^t|^2 = \\
 & \frac{g_s^{2n} C_F}{8N_c} \times \left(\frac{|j_a^{Z/\gamma^*} \cdot j_b|^2}{t_{a1} t_{a(n-1)}} \prod_{i=1}^{n-2} \frac{-C_A V^2(q_{ai}, q_{a(i+1)})}{t_{ait} t_{a(i+1)}} \right. \\
 & + \frac{|j_a \cdot j_b^{Z/\gamma^*}|^2}{t_{b1} t_{b(n-1)}} \prod_{i=1}^{n-2} \frac{-C_A V^2(q_{bi}, q_{b(i+1)})}{t_{bit} t_{b(i+1)}} \\
 & \left. - \frac{2\Re\{(j_a^{Z/\gamma^*} \cdot j_b)(j_a \cdot j_b^{Z/\gamma^*})^*\}}{\sqrt{t_{a1} t_{b1}} \sqrt{t_{a(n-1)} t_{b(n-1)}}} \prod_{i=1}^{n-2} \frac{C_A V(q_{ai}, q_{a(i+1)}) \cdot V(q_{bi}, q_{b(i+1)})}{\sqrt{t_{ait} t_{bi}} \sqrt{t_{a(i+1)} t_{b(i+1)}}} \right). \tag{4.9}
 \end{aligned}$$

In the case of $n = 2$, this reduces back to eqn. (4.6). If either a or b is an incoming gluon then there are only two possible emission sites for the Z/γ^* once again and therefore we only need calculate one t -channel momenta chain and one can set the relevant j_a^{Z/γ^*} or j_b^{Z/γ^*} to zero in eqn. (4.6).

Fig.s (4.5) and (4.6) show the phase space slices for $qQ \rightarrow (Z/\gamma^* \rightarrow) e^+ e^- qgQ$ and $qQ \rightarrow (Z/\gamma^* \rightarrow) e^+ e^- qggQ$ respectively, we see the same behaviour as observed for the 2 jet final state described in fig. (4.2). For these higher multiplicity final states we only approximate the leading order matrix element however we see that at large rapidity separations our approximation converges to the exact result as indeed it must in the High Energy limit.

Eqn. (4.9) gives us the all-orders real corrections to Z/γ^* plus jets which we wish to sum for all n . However, before proceeding to calculate the cross-section we must carefully render eqn. (4.9) finite by including the corresponding virtual corrections whose divergences will cancel the pathologies in the effective vertices.

4.3 Regularising the $Z/\gamma^* + \text{Jets}$ Matrix Element

4.3.1 Real Soft Emissions

To calculate useful quantities such as cross sections etc. we must integrate equation eqn. (4.9) over all of phase space. However, as discussed in chapter 2 problems arise when we attempt to integrate over the soft regions of phase space. It is well understood that the divergences coming from soft real emissions cancel with those coming from virtual emissions and so we must explicitly show this cancellation and calculate the remaining finite contribution multiplying the $(n-1)$ -final state parton matrix element.

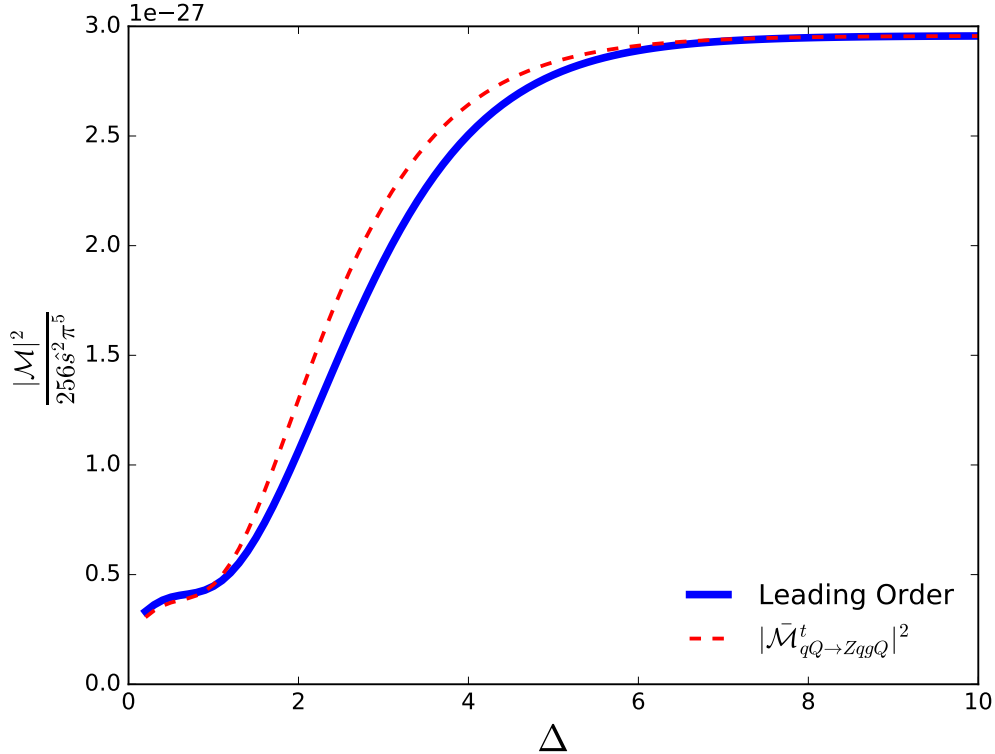


Figure 4.5: A slice through phase space for the $Z/\gamma^* + 3$ jet final state. The slice defined is akin to that described for the 2 jet case in fig. (4.2) where as Δ increases we pull apart all three jets and the leptonic decay products are emitted increasingly far into the forward direction.

In the previous work on W^\pm emission the finite remainder from this cancellation was found to be [17, 20]:

$$\frac{\alpha_s C_a \Delta_{j-1,j+1}}{\pi} \ln \frac{\lambda_{cut}^2}{|\vec{q}_{j\perp}|^2}, \quad (4.10)$$

where $\Delta_{i-1,i+1}$ is the rapidity span of the final state partons either side of our soft emission and $|\vec{q}_{j\perp}|^2$ is the sum of squares of the transverse components of the j^{th} t -channel gluon momenta. λ_{cut} is a parameter we choose which *defines* the soft region. That is, any real emission satisfying $p^2 \geq \lambda_{cut}^2$ we consider a hard perturbative emission while any emission with $p^2 < \lambda_{cut}^2$ we consider too soft to be resolved.

Here we investigate the cancellation of these divergences for Z^0 emission and most importantly whether the finite term is of the same form for the interference term which was previously excluded.

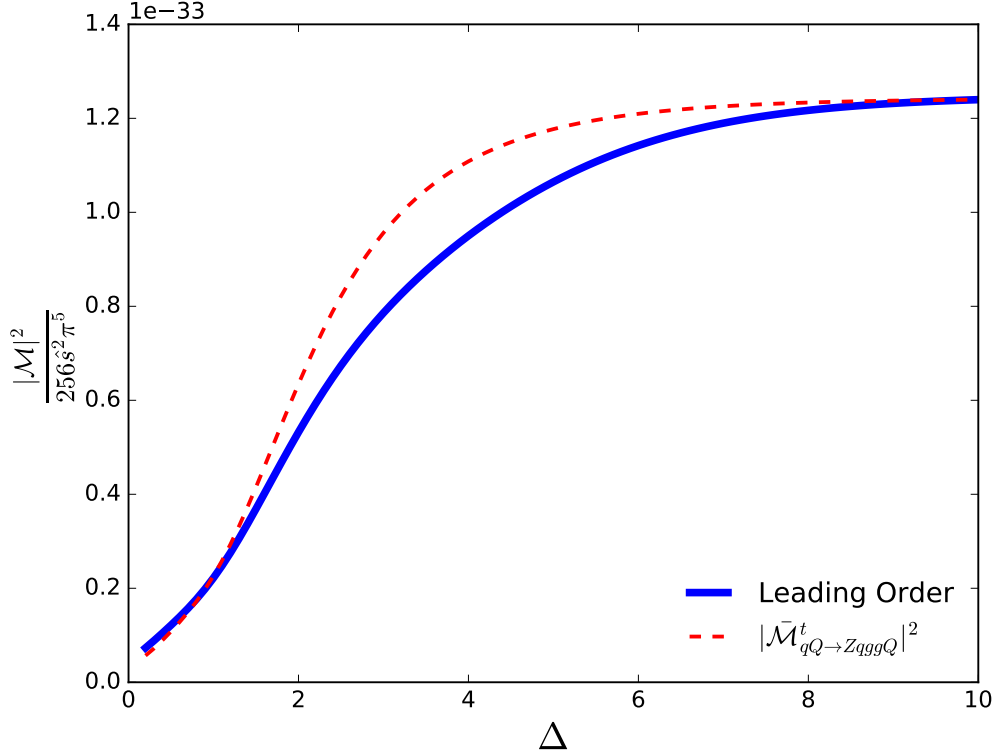


Figure 4.6: A slice through phase space for the $Z/\gamma^* + 3$ jet final state. The slice defined is akin to that described for the 2 and 3 jet case shown in fig. (4.2) and fig. (4.5) respectively.

We start by looking at a $2 \rightarrow n$ process and take the limit of one final state parton momentum, p_i , becoming small. Because of the form of eqn. (4.9) this amounts to looking at the effect of an external gluon becoming soft on our expression for the effective vertex for real emissions.

We can immediately see that for p_i going soft the gluon ‘chain’ momenta going into, and coming out of, the j^{th} emission site will coincide: $q_{j+1} \sim q_j$, therefore:

$$V^\rho(q_j, q_{j+1}) = -2q_j^\rho - 2 \left(\frac{s_{aj}}{s_{ab}} - \frac{q_j^2}{s_{bj}} \right) p_b^\rho + 2 \left(\frac{s_{bj}}{s_{ab}} + \frac{q_j^2}{s_{aj}} \right) p_a^\rho \quad (4.11)$$

Furthermore we can see that the two final terms from the bracketed expressions will dominate as $p_j \rightarrow 0$ and so we can approximate the full vertex by:

$$V^\rho(q_j, q_{j+1}) \sim -2 \frac{q_j^2}{s_{bj}} p_b^\rho + 2 \frac{q_j^2}{s_{aj}} p_a^\rho. \quad (4.12)$$

In eqn. (4.9) we have three terms involving the effective vertex; quadratic terms like $V^2(q_{tj}, q_{t(j+1)})$ and $V^2(q_{bj}, q_{b(j+1)})$ and interference terms like $V(q_{tj}, q_{t(j+1)}) \cdot V(q_{bj}, q_{b(j+1)})$. The procedure for the V^2 terms follows similarly for both the quadratic top-line emission and bottom-line emission terms and so only the calculation for top-line emission is shown here.

$V^2(q_{tj}, q_{t(j+1)})$ Terms

Upon squaring eqn. (4.12) and imposing the on-shell conditions for p_a and p_b we have:

$$V^2(q_{ti}, q_{ti}) = -\frac{4s_{ab}}{s_{bi}s_{ai}} q_i^4 \quad (4.13)$$

We must now explicitly calculate the invariant mass terms. Since we are in the High Energy regime we have that $p_a^+ \gg p_a^-, p_{a\perp}$ and $p_b^+ \gg p_b^-, p_{b\perp}$ therefore we may take:

$$s_{ab} = 2p_a \cdot p_b \sim 2p_a^+ p_b^-, s_{bi} = 2p_b \cdot p_i \sim 2p_b^- p_i^+, \quad (4.14)$$

and,

$$s_{ai} = 2p_a \cdot p_i \sim 2p_a^+ p_i^-, \quad (4.15)$$

but since $E^2 - \vec{p}_1^2 = 0$ for the on-shell external parton this can be written as:

$$V^2(q_{ti}, q_{ti}) = -\frac{4}{|\vec{p}_{1\perp}|^2} q_{ti}^4, \quad (4.16)$$

Now looking back to eqn. (4.9) we see that each vertex is associated with factors of $q_{ti}^{-2} q_{t(i+1)}^{-2}$ but since the emission is soft $q_{ti} = q_{t(i+1)}$ and this becomes q_{ti}^{-4} . That factor conspires to cancel with the corresponding factor of q_{ti}^4 in eqn. (4.16). Including the additional factors of C_A and g_s the finite factor remaining is given by:

$$\frac{4C_A g_s^2}{|\vec{p}_{\perp}|^2}, \quad (4.17)$$

$V(q_{ti}, q_{t(i+1)}) \cdot V(q_{bi}, q_{b(i+1)})$ Terms

Taking the mixed dot-product of the two vertex terms we have:

$$V(q_{ti}, q_{ti}) \cdot V(q_{bi}, q_{bi}) = -\frac{s_{ab}}{s_{ai}s_{bi}} t_{ti}t_{bi} \quad (4.18)$$

having simplified the expression using $p_a^2 = 0$ and $p_b^2 = 0$ once again. The invariant mass terms here are identical to those we saw in the V^2 terms and the products of $t_{ti}t_{bi}$ also appear in the denominator of the interference term in eqn. (4.9). After this cancellation we are left with exactly what we had before in eqn. (4.17). Since exactly the same factor comes from all three terms at the amplitude squared level we may factor them out and express the amplitude squared for an n -parton final state with one soft emission in terms of an $(n-1)$ -parton final state amplitude squared multiplied by a common factor:

$$\lim_{p_i \rightarrow 0} |\mathcal{A}_{Z/\gamma}^{2 \rightarrow n}|^2 = \left(\frac{4C_A g_s^2}{|\vec{p}_{i\perp}|^2} \right) |\mathcal{A}_{Z/\gamma}^{2 \rightarrow (n-1)}|^2 \quad (4.19)$$

Integration of Soft Divergences

As discussed above the divergences contained in eqn. (4.19) only become apparent after we have attempted to integrate over phase space. The Lorentz invariant phase space integral associated with p_i is given by:

$$\int \frac{d^3 \vec{p}_i}{(2\pi)^3 2E_i} \frac{4C_A g_s^2}{|\vec{p}_{i\perp}|^2}. \quad (4.20)$$

It is convenient to replace the integral over the z -component of momentum with one over rapidity, y_2 . Rapidity and transverse momentum are related through the definition of rapidity given in eqn. (3.2). The Jacobian of this transformation is given by:

$$\begin{aligned}
 \frac{dy}{dp_z} &= \frac{1}{2(E+p_z)} \frac{\partial}{\partial p_z}(E+p_z) - \frac{1}{2(E-p_z)} \frac{\partial}{\partial p_z}(E-p_z), \\
 &= \frac{E}{E^2 - p_z^2} - \frac{p_z}{E^2 - p_z^2} \frac{\partial E}{\partial p_z}, \\
 &= \frac{E}{E^2 - p_z^2} - \frac{p_z}{E^2 - p_z^2} \frac{p_z}{E}, \\
 &= \frac{1}{E},
 \end{aligned}$$

and therefore the rewritten phase space integral then reads:

$$\int_{\text{soft}} \frac{d^{2+2\epsilon} \vec{p}_\perp}{(2\pi)^{2+2\epsilon}} \int_{y_{i-1}}^{y_{i+1}} \frac{dy}{4\pi} \frac{4C_A g_s^2}{|\vec{p}_\perp|^2} \mu^{-2\epsilon} = \frac{4C_A g_s^2 \mu^{-2\epsilon}}{(2\pi)^{2+2\epsilon} 4\pi} \Delta_{i-1,i+1} \int_0^{\lambda_{\text{cut}}} \frac{d^{2+2\epsilon} \vec{p}_\perp}{|\vec{p}_\perp|^2}, \quad (4.21)$$

where we have analytically continued the integral to $2 + 2\epsilon$ dimensions to regulate the anticipated divergences and introduced the parameter μ to keep the coupling dimensionless in the process. We have also introduced an upper bound on the transverse momentum integration of λ_{cut} - this parameter will be discussed in more detail later. Converting to polar coordinates and using the result for the volume of a unit hypersphere gives the integrated soft contribution:

$$\frac{4C_A g_s^2}{(2\pi)^{2+2\epsilon} 4\pi} \Delta_{i-1,i+1} \frac{1}{\epsilon} \frac{\pi^{1+\epsilon}}{\Gamma(\epsilon+1)} \left(\frac{\lambda_{\text{cut}}^2}{\mu^2} \right)^\epsilon. \quad (4.22)$$

As promised eqn. (4.22) is clearly divergent in the limit where $\epsilon \rightarrow 0$.

4.3.2 Virtual Emissions

As discussed in chapter 3 the virtual emission diagrams are included using the Lipatov ansatz for the gluon propagator:

$$\frac{1}{q_i^2} \longrightarrow \frac{1}{q_i^2} e^{\hat{\alpha}(q_i) \Delta_{i,i-1}}, \quad (4.23)$$

where:

$$\hat{\alpha}(q_i) = \alpha_s C_A q_i^2 \int \frac{d^{2+2\epsilon} k_\perp}{(2\pi)^{2+2\epsilon}} \frac{1}{k_\perp^2 (k_\perp - q_{i\perp})^2} \mu^{-2\epsilon}. \quad (4.24)$$

To see the cancellation of the infrared ϵ poles we must perform the integral explicitly using dimensional regularisation. Using Feynman parameters to re-express eqn. (4.24):

$$\hat{\alpha}(q_i) = \alpha_s C_A q_i^2 \int \frac{d^{2+2\epsilon} \hat{k}_\perp}{(2\pi)^{2+2\epsilon}} \int_0^1 \frac{dx}{[\hat{k}_\perp^2 + q_{i\perp}^2 (1-x)]^2} \mu^{-2\epsilon}, \quad (4.25)$$

where we have performed a change of variables to $\hat{k}_\perp = k_\perp - x q_{i\perp}$. Changing the order of integration we can perform the \hat{k}_\perp integral using the following result:

$$\int \frac{d^d k}{(2\pi)^d} \frac{1}{(k^2 - C)^\alpha} = \frac{1}{(4\pi)^{\frac{d}{2}}} \frac{\Gamma(\alpha - \frac{d}{2})}{\Gamma(\alpha)} \frac{(-1)^\alpha}{C^{\alpha - \frac{d}{2}}}, \quad (4.26)$$

to give:

$$\hat{\alpha}(q_i) = -\frac{2g_s^2 C_A}{(4\pi)^{2+\epsilon}} \frac{\Gamma(1-\epsilon)}{\epsilon} \left(\frac{q_{i\perp}^2}{\mu^2} \right)^\epsilon, \quad (4.27)$$

having completed the x integral and used the definition $\alpha_s = \frac{g_s^2}{4\pi}$.

4.3.3 Cancellation of Infrared Divergences

We now have all the necessary ingredients to show how the infrared contributions from soft real emissions and virtual emissions cancel leaving our integrated matrix element finite. The only subtlety being that we must sum two diagrams with different multiplicity final states to see the cancellation. This is because they are experimentally indistinguishable; the $2 \rightarrow (n-1)$ virtual diagram has $(n-1)$ resolvable partons in the final state and we only ‘see’ $(n-1)$ of the final states partons from $2 \rightarrow n$ process because we consider one of the emissions too soft to resolve.

The matrix element squared for the real emission diagram with one soft parton will look like:

$$\begin{aligned}
 |\mathcal{A}_{Z/\gamma}^{2 \rightarrow n}|^2 = & \left(\frac{4g_s^2 C_a}{|p_{i\perp}|^2} \right) \left[\left| \mathcal{K}_a j_1^{Z/\gamma} \cdot j_2 \right|^2 \frac{\prod_{i \neq j}^{n-2} V^2(q_{ti}, q_{t(i+1)})}{\prod_{i \neq j}^{n-1} q_{ti}^2} + \right. \\
 & \left| \mathcal{K}_b j_2^{Z/\gamma} \cdot j_1 \right|^2 \frac{\prod_{i \neq j}^{n-2} V^2(q_{bi}, q_{b(i+1)})}{\prod_{i \neq j}^{n-1} q_{bi}^2} + \\
 & 2\Re\{\mathcal{K}_a \overline{\mathcal{K}_b} \times (j_1^{Z/\gamma} \cdot j_2)(\overline{j_2^{Z/\gamma} \cdot j_1})\} \\
 & \left. \times \frac{\prod_{i \neq j}^{n-2} V(q_{ti}, q_{t(i+1)}) \cdot V(q_{bi}, q_{b(i+1)})}{\prod_{i \neq j}^{n-1} q_{ti} q_{bi}} \right], \tag{4.28}
 \end{aligned}$$

where we have taken the i^{th} gluon to be soft. After including the virtual corrections via the insertion of the Lipatov ansatz the $2 \rightarrow (n-1)$ matrix element squared is:

$$\begin{aligned}
 |\mathcal{A}_{Z/\gamma}^{2 \rightarrow (n-1)}|^2 = & \left| \mathcal{K}_a j_1^{Z/\gamma} \cdot j_2 \right|^2 \frac{\prod_i^{n-3} V^2(q_{ti}, q_{t(i+1)})}{\prod_i^{n-2} q_{ti}^2} e^{2\hat{\alpha}(q_{ti})\Delta_{i-1,i+1}} + \\
 & \left| \mathcal{K}_b j_2^{Z/\gamma} \cdot j_1 \right|^2 \frac{\prod_i^{n-3} V^2(q_{bi}, q_{b(i+1)})}{\prod_i^{n-2} q_{bi}^2} e^{2\hat{\alpha}(q_{bi})\Delta_{i-1,i+1}} + \\
 & 2\Re\{\mathcal{K}_a \overline{\mathcal{K}_b} \times (j_1^{Z/\gamma} \cdot j_2)(\overline{j_2^{Z/\gamma} \cdot j_1})\} \\
 & \times \frac{\prod_i^{n-3} V(q_{ti}, q_{t(i+1)}) \cdot V(q_{bi}, q_{b(i+1)})}{\prod_i^{n-2} q_{ti} q_{bi}} e^{(\hat{\alpha}(q_{bi}) + \hat{\alpha}(q_{ti}))\Delta_{i-1,i+1}}, \tag{4.29}
 \end{aligned}$$

We can now go through term-by-term to show the divergences cancel and find the finite contribution to the matrix element squared. Similarly to when we calculated the soft terms the arguments for the pure top- and bottom-line emissions follow similarly and so here we will only state the procedure for the top emission.

For the top line emission we identify the following terms that will appear in the sum of the $2 \rightarrow (n-1)$ virtual and $2 \rightarrow n$ real matrix elements. The finite contribution, \mathcal{F}_{top} , to the matrix element is given by:

$$\mathcal{F}_{\text{top}} = \frac{4C_A g_s^2}{(2\pi)^{2+2\epsilon} 4\pi} \Delta_{i-1,i+1} \frac{1}{\epsilon} \frac{\pi^{1+\epsilon}}{\Gamma(\epsilon+1)} \left(\frac{\lambda_{\text{cut}}^2}{\mu^2} \right)^\epsilon + e^{2\hat{\alpha}(q_{ti})\Delta_{i-1,i+1}}. \tag{4.30}$$

Extracting the relevant power of the strong coupling from the exponential and substituting for $\hat{\alpha}(q_i)$ gives:

$$\begin{aligned}\mathcal{F}_{\text{top}} &= \frac{4C_A g_s^2}{(2\pi)^{2+2\epsilon} 4\pi} \Delta_{i-1,i+1} \frac{1}{\epsilon} \frac{\pi^{1+\epsilon}}{\Gamma(\epsilon+1)} \left(\frac{\lambda_{\text{cut}}^2}{\mu^2} \right)^\epsilon - \frac{2g_s^2 C_A}{(4\pi)^{2+\epsilon}} \frac{\Gamma(1-\epsilon)}{\epsilon} \left(\frac{q_{ti\perp}^2}{\mu^2} \right)^\epsilon, \\ &= \frac{g_s^2 C_A}{4^{1+\epsilon} \pi^{2+\epsilon}} \Delta_{i-1,i+1} \left(\frac{1}{\epsilon \Gamma(1+\epsilon)} \left(\frac{\lambda_{\text{cut}}^2}{\mu^2} \right)^\epsilon - \frac{\Gamma(1-\epsilon)}{\epsilon} \left(\frac{q_{ti\perp}^2}{\mu^2} \right)^\epsilon \right).\end{aligned}\quad (4.31)$$

Expanding the terms involving the regularisation parameter for small values, $\epsilon \rightarrow 0$, yields:

$$\mathcal{F}_{\text{top}} = \frac{\alpha_s C_A \Delta_{i-1,i+1}}{\pi} \ln \left(\frac{\lambda_{\text{cut}}^2}{q_{ti\perp}^2} \right) + \mathcal{O}(\epsilon), \quad (4.32)$$

where we have used:

$$\begin{aligned}\frac{1}{\Gamma(1+\epsilon)} &= 1 + \gamma_E \epsilon + \mathcal{O}(\epsilon^2), \quad \Gamma(1-\epsilon) = 1 + \gamma_E \epsilon + \mathcal{O}(\epsilon^2), \\ \left(\frac{x}{y} \right)^\epsilon &= 1 + \epsilon \ln \left(\frac{x}{y} \right) + \mathcal{O}(\epsilon^2).\end{aligned}\quad (4.33)$$

Similarly, for the terms arising from the bottom quark-line emission we have:

$$\mathcal{F}_{\text{bottom}} = \frac{\alpha_s C_A \Delta_{i-1,i+1}}{\pi} \ln \left(\frac{\lambda_{\text{cut}}^2}{q_{bi\perp}^2} \right), \quad (4.34)$$

Lastly, for the interference terms we expand the exponential with both top-line emission, q_{ti} , momenta and bottom-line emission, q_{bi} , momenta to get:

$$\begin{aligned}\mathcal{F}_{\text{interf.}} &= \frac{g_s^2 C_A \Delta_{i-1,i+1}}{4^{1+\epsilon} \pi^{2+\epsilon}} \left(\left(\frac{1}{\epsilon} + \gamma_E + \ln \left(\frac{\lambda_{\text{cut}}^2}{\mu^2} \right) \right) + \mathcal{O}(\epsilon) \right) - \\ &\quad \frac{1}{2} \left[\frac{2}{\epsilon} + 2\gamma_E + \ln \left(\frac{q_{ti\perp}^2}{\mu^2} \right) - \ln \left(\frac{q_{bi\perp}^2}{\mu^2} \right) + \mathcal{O}(\epsilon) \right] \\ &= \frac{\alpha_s C_A \Delta_{i-1,i+1}}{\pi} \ln \left(\frac{\lambda_{\text{cut}}^2}{\sqrt{q_{ti\perp}^2 q_{bi\perp}^2}} \right).\end{aligned}\quad (4.35)$$

Eqn. (4.35) is a new result which allows the inclusion of the interference terms shown to be important in previous discussion. We can now express the regulated $qQ \rightarrow Z/\gamma^* q(n-2)gQ$ matrix element as follows:

$$\begin{aligned}
 |\mathcal{M}_{qQ \rightarrow Z/\gamma^* q(n-2)gQ}^{HEJ-\text{reg}}|^2 = & g_s^2 \frac{C_F}{8N_c} (g_s^2 C_A)^{n-2} \\
 & \times \left(\frac{|j_a^{Z/\gamma^*} \cdot j_b|^2}{t_{a1} t_{a(n-1)}} \exp(\omega^0(q_{a(n-1)\perp}) \Delta y_{n-1}) \prod_{i=1}^{n-2} \frac{-V^2(q_{ai}, q_{a(i+1)})}{t_{ait} t_{a(i+1)}} \exp(\omega^0(q_{ai\perp}) \Delta y_i) \right. \\
 & + \frac{|j_a \cdot j_b^{Z/\gamma^*}|^2}{t_{b1} t_{b(n-1)}} \exp(\omega^0(q_{b(n-1)\perp}) \Delta y_{n-1}) \prod_{i=1}^{n-2} \frac{-V^2(q_{bi}, q_{b(i+1)})}{t_{bit} t_{b(i+1)}} \exp(\omega^0(q_{bi\perp}) \Delta y_i) \\
 & - \frac{2\Re\{(j_a^{Z/\gamma^*} \cdot j_b)(\overline{j_a \cdot j_b^{Z/\gamma^*}})\}}{\sqrt{t_{a1} t_{b1}} \sqrt{t_{a(n-1)} t_{b(n-1)}}} \exp(\omega^0(\sqrt{q_{a(n-1)\perp} q_{b(n-1)\perp}}) \Delta y_{n-1}) \\
 & \left. \prod_{i=1}^{n-2} \frac{V(q_{ai}, q_{a(i+1)}) \cdot V(q_{bi}, q_{b(i+1)})}{\sqrt{t_{ait} t_{bi}} \sqrt{t_{a(i+1)} t_{b(i+1)}}} \exp(\omega^0(\sqrt{q_{ai\perp} q_{bi\perp}}) \Delta y_i) \right), \tag{4.36}
 \end{aligned}$$

where we have defined

$$\omega^0(q_\perp^2) = -\frac{g_s^2 C_A}{4\pi^2} \ln\left(\frac{q_\perp^2}{\lambda_{cut}^2}\right). \tag{4.37}$$

There is one final improvement we can make to eqn. (4.36). The expressions we obtain upon taking the soft limit of the three effective vertex terms, V_t^2 , V_b^2 and $V_t \cdot V_b$, are not exact and there are sub-leading terms which we can account for. We therefore have to account for the difference between, e.g $-V^2(q_{i-1}, q_i)/(t_{i-1} t_i)$, and its strict limit of $4/p_{i\perp}^2$ for values of $p_{i\perp}$ below λ_{cut} . In practice, we include this correction for $c_{cut} < |p_{i\perp}| < \lambda_{cut}$ with $c_{cut} = 0.2$ GeV and find stable results around this value (see section 4.4).

We are, at last, in a position to move forward and form an expression for an all-orders gauge invariant *finite* matrix element for Z/γ^* plus jets. Before pressing on we now discuss an example calculation showing explicitly the finite nature of matrix element expression.

4.3.4 An Explicit Check: $2 \rightarrow 3$ Scattering

Consider the case of $2 \rightarrow 3$ scattering where one of the final state momenta, p_2 , has become soft. A contributing soft diagram is shown in fig. (4.7a) and one example of a contributing virtual diagram of the same order is shown in fig. (4.7b). When p_2 goes

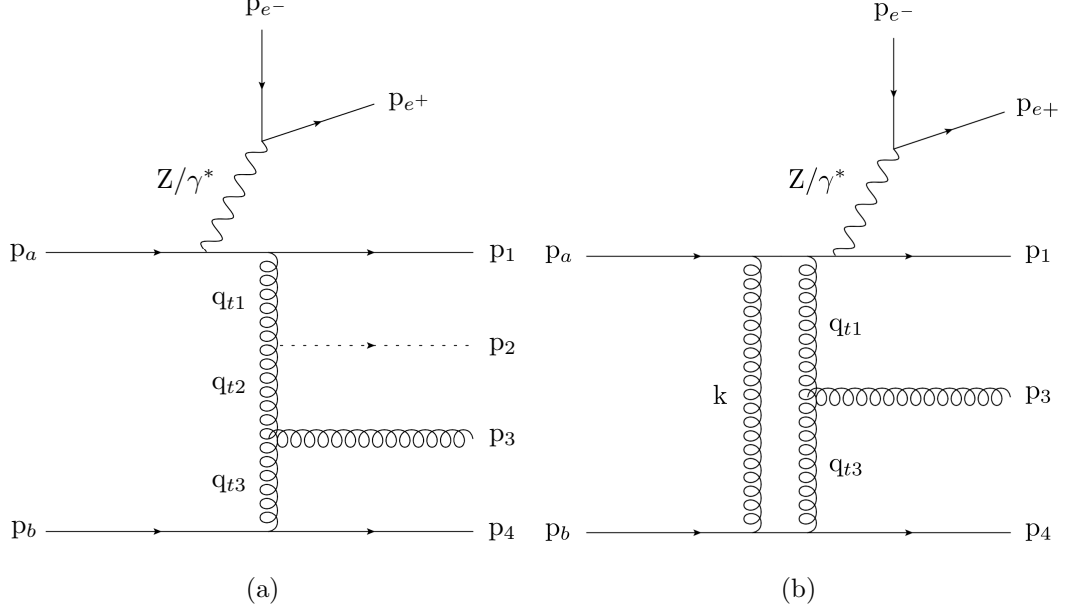


Figure 4.7: Examples of both real and virtual diagrams contributing to $2 \rightarrow 3$ scattering. In fig. (4.7a) the p_2 has been drawn with a dashed line to denote it is not resolvable. In fig. (4.7b) the final state momenta have been labelled in a seemingly strange way - this was done to make clear the cancellation when working through the algebra.

soft we have the following form for the $2 \rightarrow 3$ integrated amplitude squared (N.B.: The integration is only schematic and doesn't represent the full Lorentz invariant phase space):

$$\begin{aligned} \int dPS |\mathcal{A}_{soft}^{2 \rightarrow 3}|^2 = & \frac{4C_A g_s^2 \Delta_{1,3}}{(2\pi)^{2+2\epsilon} 4\pi} \frac{\pi^{\epsilon+1}}{\epsilon \Gamma(\epsilon+1)} \left(\frac{\lambda_{cut}^2}{\mu^2} \right)^\epsilon \left[|\mathcal{K}_a j_1^Z \cdot j_2|^2 \frac{V^2(q_{t1}, q_{t3})}{q_{t1}^2 q_{t3}^2} \right. \\ & + |\mathcal{K}_b j_1 \cdot j_2^Z|^2 \frac{V^2(q_{b1}, q_{b3})}{q_{b1}^2 q_{b3}^2} + 2\Re \left\{ \mathcal{K}_a \overline{\mathcal{K}_b} (j_1^Z \cdot j_2)(\overline{j_1 \cdot j_2^Z}) \right\} \frac{V(q_{t1}, q_{t3}) \cdot V(q_{b1}, q_{b3})}{q_{t1} q_{t3} q_{b1} q_{b3}} \left. \right], \end{aligned} \quad (4.38)$$

and the virtual contributions for the $2 \rightarrow 3$ amplitude are:

$$\begin{aligned} \int dPS |\mathcal{A}_{\text{virtual}}^{2 \rightarrow 3}|^2 &= |\mathcal{K}_b j_1 \cdot j_2^Z|^2 \frac{V^2(q_{t1}, q_{t3})}{q_{t1}^2} e^{2\hat{\alpha}(q_{t1})\Delta_{1,3}} + \\ &|\mathcal{K}_t j_1^Z \cdot j_2|^2 \frac{V^2(q_{b1}, q_{b3})}{q_{b1}^2} e^{2\hat{\alpha}(q_{b1})\Delta_{1,3}} + \\ &2\Re \left\{ \mathcal{K}_a \overline{\mathcal{K}_b} (j_1^Z \cdot j_2) \overline{(j_1 \cdot j_2^Z)} \right\} \frac{V(q_{t1}, q_{t3}) \cdot V(q_{b1}, q_{b3})}{q_{t1} q_{t3} q_{b1} q_{b3}} e^{(\hat{\alpha}(q_{t1}) + \hat{\alpha}(q_{b1}))\Delta_{1,3}}. \end{aligned} \quad (4.39)$$

Once we expand the exponential to the correct order in g_s^2 , the sum of these matrix elements squared over the region of phase space when p_2 is soft is:

$$\begin{aligned} \int dPS (|\mathcal{A}_{\text{soft}}^{2 \rightarrow 3}|^2 + |\mathcal{A}_{\text{virtual}}^{2 \rightarrow 3}|^2) &= \\ &|\mathcal{K}_a j_1^Z \cdot j_2|^2 \frac{V^2(q_{t1}, q_{t3})}{q_{t1}^2} \left(\frac{4C_A g_s^2 \Delta_{1,3}}{(2\pi)^{2+2\epsilon} 4\pi} \frac{\pi^{\epsilon+1}}{\epsilon \Gamma(\epsilon+1)} - 2\hat{\alpha}(q_{t1})\Delta_{1,3} \right) + \\ &|\mathcal{K}_b j_1 \cdot j_2^Z|^2 \frac{V^2(q_{b1}, q_{b3})}{q_{b1}^2} \left(\frac{4C_A g_s^2 \Delta_{1,3}}{(2\pi)^{2+2\epsilon} 4\pi} \frac{\pi^{\epsilon+1}}{\epsilon \Gamma(\epsilon+1)} - 2\hat{\alpha}(q_{b1})\Delta_{1,3} \right) + \\ &2\Re \left\{ \mathcal{K}_a \overline{\mathcal{K}_b} (j_1^Z \cdot j_2) \overline{(j_1 \cdot j_2^Z)} \right\} \frac{V(q_{t1}, q_{t3}) \cdot V(q_{b1}, q_{b3})}{q_{t1} q_{t3} q_{b1} q_{b3}} \\ &\left(\frac{4C_A g_s^2 \Delta_{1,3}}{(2\pi)^{2+2\epsilon} 4\pi} \frac{\pi^{\epsilon+1}}{\epsilon \Gamma(\epsilon+1)} - (\hat{\alpha}(q_{t1}) + \hat{\alpha}(q_{b1}))\Delta_{1,3} \right) + \mathcal{O}(g_s^4), \end{aligned} \quad (4.40)$$

The bracketed terms in eqn. (4.40) are exactly the cancellations calculated in section 4 above and therefore:

$$\begin{aligned} \int dPS (|\mathcal{A}_{\text{soft}}^{2 \rightarrow 3}|^2 + |\mathcal{A}_{\text{virtual}}^{2 \rightarrow 3}|^2) &= \frac{\alpha_s C_A \Delta_{1,3}}{\pi} \left(|\mathcal{K}_a j_1^Z \cdot j_2|^2 \frac{V^2(q_{t1}, q_{t3})}{q_{t1}^2} \ln \left(\frac{\lambda_{\text{cut}}^2}{|q_{1t\perp}|^2} \right) + \right. \\ &|\mathcal{K}_b j_1 \cdot j_2^Z|^2 \frac{V^2(q_{b1}, q_{b3})}{q_{b1}^2} \ln \left(\frac{\lambda_{\text{cut}}^2}{|q_{1b\perp}|^2} \right) + \\ &2\Re \left\{ \mathcal{K}_a \overline{\mathcal{K}_b} (j_1^Z \cdot j_2) \overline{(j_1 \cdot j_2^Z)} \right\} \frac{V(q_{t1}, q_{t3}) \cdot V(q_{b1}, q_{b3})}{q_{t1} q_{t3} q_{b1} q_{b3}} \\ &\left. \ln \left(\frac{\lambda_{\text{cut}}^2}{\sqrt{|q_{1t\perp}|^2 |q_{1b\perp}|^2}} \right) \right) + \mathcal{O}(\alpha_s^2), \end{aligned} \quad (4.41)$$

which is manifestly finite.

4.4 Subtractions and the λ_{cut} scale

We now show the stability of the High Energy Jets predictions with respect to the λ_{cut} scale described above.

We increase our sensitivity to the parameter by showing results for FKL momentum configurations only. The non-FKL samples which are added to give the total cross sections have no dependence on λ_{cut} and would therefore dilute any dependence in the full sample. We begin with tab. (4.1) where we show the value of the cross section for different values of λ_{cut} for exclusive 2-, 3- and 4-jet samples. The cuts applied are the same as in section 4.7.1. It is clear that the cross section does not display a large dependence on the value of λ_{cut} .

λ_{cut} (GeV)	$\sigma(2j)$ (pb)	$\sigma(3j)$ (pb)	$\sigma(4j)$ (pb)
0.2	5.03 ± 0.02	0.70 ± 0.02	0.13 ± 0.03
0.5	5.05 ± 0.01	0.70 ± 0.01	0.13 ± 0.01
1.0	5.09 ± 0.01	0.71 ± 0.01	0.13 ± 0.01
2.0	5.16 ± 0.04	0.72 ± 0.01	0.13 ± 0.01

Table 4.1: The FKL-only cross sections for the 2-, 3- and 4-jet exclusive rates with associated statistical errors shown for different values of the regularisation parameter λ_{cut} . The scale choice was half the sum over all transverse scales in the event, $H_T/2$.

Fig. (4.8) shows the effect of the same variation in λ_{cut} on the differential distribution in both the rapidity gap between the two leading jets in p_\perp , $\Delta y_{j1,j2}$, (a)–(c), and the rapidity gap between the two extremal jets in rapidity, $\Delta y_{jf,jb}$, (d)–(f). Results are shown for exclusive 2-, 3- and 4-jet samples in each case. The distributions also show a very weak dependence on the choice of λ_{cut} . In practice, our default chosen value for λ_{cut} is 0.2.

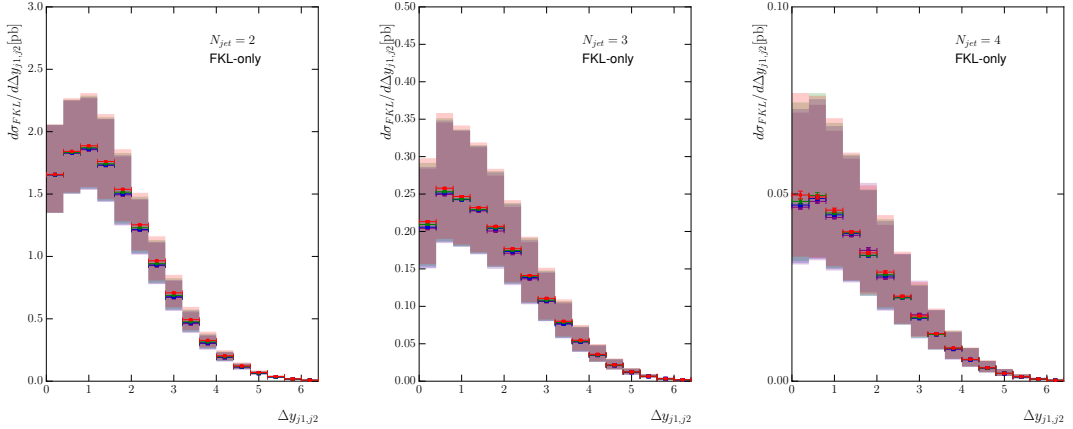


Figure 4.8: The effect of varying λ_{cut} on the differential distribution in the rapidity gap between the two leading jets in p_\perp , $\Delta y_{j1,j2}$, with the $N_{jet} = 2, 3, 4$ exclusive selections shown from left to right. $\lambda_{cut} = 0.2$ (red), 0.5 (blue), 1.0 (green), 2.0 (purple). The bands represent the scale variation described in the text.

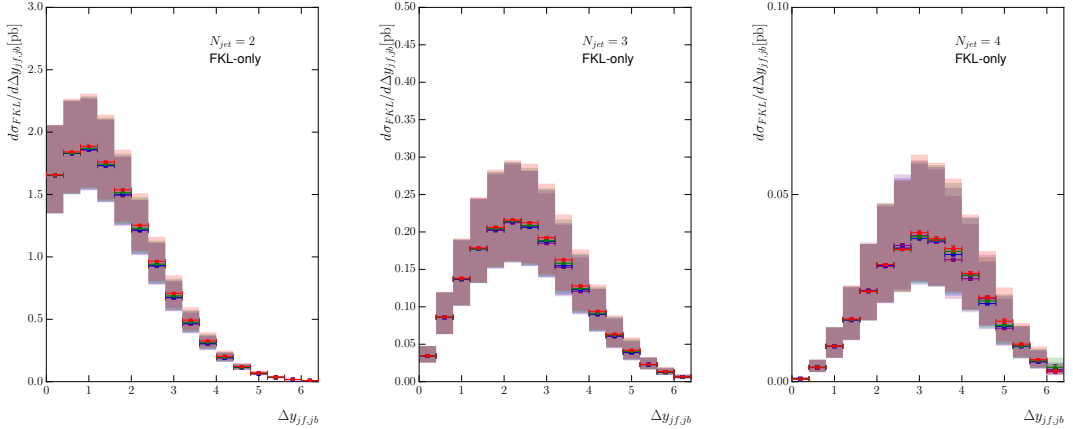


Figure 4.9: The effect of varying λ_{cut} on the differential distribution in the rapidity gap between the two extremal jets in rapidity, $\Delta y_{jf,jb}$, with the $N_{jet} = 2, 3, 4$ exclusive selections shown from left to right. $\lambda_{cut} = 0.2$ (red), 0.5 (blue), 1.0 (green), 2.0 (purple). The bands represent the scale variation described in the text.

4.5 The Differential Z/γ Cross-Section

Starting from eqn. (4.36) we can write down a total (differential) cross section obtained by summing over all values of the number of final state partons, n , and integrating over the full n -particle phase space using an efficient Monte Carlo sampling algorithm [17,23]:

$$\begin{aligned}
 \sigma = & \sum_{f_a, f_b} \sum_{n=2}^{\infty} \int \frac{d^3 p_a}{(2\pi)^3 2E_a} \int \frac{d^3 p_b}{(2\pi)^3 2E_b} \left(\prod_{i=1}^n \int \frac{d^3 p_i}{(2\pi)^3 2E_i} \right) \int \frac{d^3 p_{e^-}}{(2\pi)^3 2E_{e^-}} \int \frac{d^3 p_{e^+}}{(2\pi)^3 2E_{e^+}} \\
 & \times (2\pi)^4 \delta^{(4)} \left(p_a + p_b - \sum_i p_i - p_{e^-} - p_{e^+} \right) \\
 & \times |\mathcal{M}_{f_a f_b \rightarrow Z/\gamma^* f_a(n-2) g f_b}^{HEJ-\text{reg}}(p_a, p_b, \{p_i\})|^2 \frac{x_a f_{f_a}(x_a, Q_a) x_b f_{f_b}(x_b, Q_b)}{\hat{s}^2} \Theta_{\text{cut}},
 \end{aligned} \tag{4.42}$$

where $x_{a,b}$ are the momentum fractions of the incoming partons and $f_{f_k}(x_k, Q_k)$ are the corresponding parton density functions for beam, k , and flavour f_k . The function Θ_{cut} imposes any desired cuts on the final state. The minimum requirement is that the final state momenta cluster into at least two jets for the desired jet clustering algorithm.

In the regions of phase space where all final state particles are well separated in rapidity, this gives the dominant terms in QCD at all orders in α_s (the leading logarithmic terms in s/t). However, in other areas of phase space, the differences due to the approximations used in $|\mathcal{M}_{qQ \rightarrow Z/\gamma^* q(n-2) g Q}^{HEJ-\text{reg}}|^2$ will become more significant as we saw in figs. (4.2), (4.5) and (4.6). We can therefore further improve upon eqn. (4.42) by matching our results to fixed order results. Here, we match to high-multiplicity tree-level results obtained from `MadGraph_aMC@NLO` [13] in two different ways. This amounts to merging tree-level samples of different orders according to the logarithmic prescription of HEJ.

1. Matching for FKL configurations:

As described in chapter 3, these are the particle assignments and momentum configurations which contain the dominant leading-logarithmic terms in s/t . The first step of the HEJ description was to develop an approximation to the matrix element for these processes which was later supplemented with the finite correction which remained after cancelling the real and virtual divergences: $|\mathcal{M}_{qg \rightarrow Zqg}^{HE}|^2$ (eqn. (4.4)) or $|\mathcal{M}_{qQ \rightarrow ZqQ}^{HE}|^2$ (eqn. (4.9)). The approximation is necessary to allow us to describe the matrix element for any (and in particular, large) n and for including both the leading real and virtual corrections. However, if the parton momenta cluster into four or fewer jets (these may have arisen from many more partons), the full tree-level matrix element remains calculable. In these cases, we perform the matching multiplicatively, so we multiply the integrand of eqn. (4.42) by the ratio:

$$|\mathcal{M}_{qQ \rightarrow Z/\gamma^* q(k-2)gQ}^{\text{full}}(p_a, p_b, \{j'_i\})|^2 / |\mathcal{M}_{qQ \rightarrow Z/\gamma^* q(k-2)gQ}^{\text{HEJ}}(p_a, p_b, \{j'_i\})|^2. \quad (4.43)$$

Here, $\{j'_i\}$ are the jet momenta after a small amount of reshuffling. This is necessary because the evaluation of the tree-level matrix elements assumes that the jet momenta are both on-shell and have transverse momenta which sum to zero, neither of which is true in general for our events due to the presence of extra emissions. Our reshuffling algorithm [22] redistributes this extra transverse momentum in proportion to the size of the transverse momentum of each jet. The plus and minus light-cone components are then adjusted such that the jet is put on-shell and the rapidity remains unaltered. This last feature ensures that after reshuffling the event is still in an FKL configuration.

2. Matching for non-FKL configurations:

Away from regions in phase space where the quarks and gluons are well-separated, the non-FKL configurations will play a more significant rôle. These have so far not been accounted for at all, and hence we add three exclusive samples of leading-order two-jet, three-jet and four-jet leading-order events to our resummed events.

These two matching schemes complete our description of the production of Z/γ^* with at least two jets, including the leading high-energy logarithms at all orders in α_s . Tabs (4.2) and (4.3) show the effect of the matching to leading order on the total cross sections of various FKL configurations for 2 and 3-4 jet processes respectively. We see that although the resummation-only result often gives a good approximation to the exact leading order result it sometimes differs but that this difference is corrected for by our matching. Tab. (4.4) shows the total cross sections generated by HEJ for 2-, 3- and 4-jet processes which contain non-FKL configurations. Once again we see that after the inclusion of the extra exclusive sums we are in good agreement with the leading order result.

In the next sections, we discuss the computational aspects of the work presented here and compare the resulting predictions from this formalism to LHC data from recent ATLAS and CMS analyses.

Table 4.2: The effect of matching on the total cross-section of the 2 jet final state FKL configurations.

Incoming	Resum.	Resum.+FKL	Leading Order
(1, 1)	0.6550 ± 0.0172	0.6742 ± 0.0170	0.6742 ± 0.0170
(1, 2)	1.1030 ± 0.0581	1.1030 ± 0.0581	1.1029 ± 0.0581
(1, 3)	0.2667 ± 0.0077	0.2667 ± 0.0077	0.2667 ± 0.0077
(1, 4)	0.1991 ± 0.0113	0.1992 ± 0.0113	0.1992 ± 0.0113
(1, 5)	0.1085 ± 0.0036	0.1085 ± 0.0036	0.1085 ± 0.0036
(2, 2)	1.3672 ± 0.0980	1.3910 ± 0.0935	1.3910 ± 0.0935
(2, 3)	0.4832 ± 0.0174	0.4832 ± 0.0174	0.4832 ± 0.0174
(2, 4)	0.2744 ± 0.0203	0.2744 ± 0.0203	0.2744 ± 0.0203
(2, 5)	0.2033 ± 0.0082	0.2033 ± 0.0082	0.2033 ± 0.0082
(3, 3)	0.0837 ± 0.0021	0.0880 ± 0.0022	0.0880 ± 0.0022
(3, 4)	0.0630 ± 0.0034	0.0630 ± 0.0034	0.0630 ± 0.0034
(3, 5)	0.0313 ± 0.0008	0.0313 ± 0.0008	0.0313 ± 0.0008
(4, 4)	0.0310 ± 0.0018	0.0326 ± 0.0017	0.0326 ± 0.0017
(4, 5)	0.0236 ± 0.0016	0.0236 ± 0.0016	0.0236 ± 0.0016
(5, 5)	0.0114 ± 0.0003	0.0121 ± 0.0003	0.0121 ± 0.0003
(1, 21)	4.3680 ± 0.1600	2.7868 ± 0.0909	2.7868 ± 0.0909
(2, 21)	5.6100 ± 0.3344	3.6284 ± 0.1957	3.6284 ± 0.1957
(3, 21)	1.8842 ± 0.0732	1.1718 ± 0.0353	1.1718 ± 0.0353
(4, 21)	1.2172 ± 0.1449	0.7136 ± 0.0405	0.7136 ± 0.0405
(5, 21)	0.7480 ± 0.0335	0.4697 ± 0.0153	0.4697 ± 0.0153

4.6 $Z/\gamma^* + \text{Jets}$: Computational Aspects

The physics presented in the preceding sections is a significant departure from work previously done by the High Energy Jets collaboration. As such developing the Monte Carlo for Z/γ^* plus jets was a serious undertaking; the inclusion of the aforementioned interference terms required that two t -channel ‘chains’ of momenta and vertices be computed and carried throughout the evaluation. Furthermore to correctly calculate at the amplitude level the way the High Energy Jets currents are constructed in the codebase needed to be modified. Since the virtual corrections are scale dependent it was necessary to change large sections of code to work with multiple copies of t -chains and multiple scales.

In previous HEJ releases the matching mentioned above was performed using `MadGraph` version 4. However, due to increases in speed and efficiency we chose to match the $Z/\gamma^* + \text{jets}$ HEJ matrix elements to `MadGraph_aMC@NLO` version 5. While this might seem like a trivial change the underlying computational work was anything but simple; since the latest version of `MadGraph` outputs matrix elements in C++ (as well as

Table 4.3: The effect of matching on the total cross-section of the 3 and 4 jet final state FKL configurations.

Incoming	Resum.+FKL	Leading Order
3-jet		
(1, 1)	0.3467 ± 0.0202	0.3467 ± 0.0202
(1, 2)	0.6851 ± 0.0589	0.6851 ± 0.0589
(1, 3)	0.1065 ± 0.0073	0.1065 ± 0.0073
(1, 4)	0.0684 ± 0.0059	0.0684 ± 0.0059
(1, 5)	0.0431 ± 0.0032	0.0431 ± 0.0032
4-jet		
(3, 1)	0.0011 ± 0.0001	0.0011 ± 0.0001
(3, 5)	0.0097 ± 0.0006	0.0097 ± 0.0006

Fortran 90) a completely new approach to incorporating matching was required. A novel ‘abstract factory’ design pattern was employed to efficiently construct and call the relevant leading order matrix element. In this way we avoided the necessity of having extremely large matching files containing $\mathcal{O}(18,000)$ lines of code which was very difficult to debug and improve; instead this new structure allowed the matching code to be reduced to only a few thousand lines since the abstract factory class presents a uniform interface and therefore almost all of the process specific lines became unnecessary (some process specific content remains due to the distinction made between FKL and non-FKL configurations).

Throughout the course of this work it became apparent that the High Energy Jets codebase as it was at the time needed to be restructured. Each physics process (pure jets, $W^\pm + \text{jets}$, Higgs+jets and $Z/\gamma^* + \text{jets}$) was structured individually as a stand-alone piece of code. This became a problem when testing and modifying HEJ since there are large sections of code which are the same regardless of what electroweak boson emission (if any) we are concerned with, for example the parton distribution function calls are almost entirely the same no matter which code is run. To improve upon this situation a unified HEJ package was created. This was a complete restructuring of the code into a form in which a general `HejGen` polymorphic base class can be constructed abstractly and then made concrete depending on user input. The unified version of the code is an improvement in that it is much more user friendly, and significantly easier to test and extend. This work entailed being one of the primary authors of the new design for High Energy Jets and will soon be released as HEJ (v2).

Lastly a word about the generation of High Energy Jets predictions for comparisons to data. The sections and chapters which follow contain theoretical predictions to experimental analyses. These predictions were generated using distributed computing

Table 4.4: The effect of matching on the total cross-section of the 2-, 3- and 4-jet final state non-FKL configurations.

Incoming	Resum.+FKL	Non-FKL	Leading Order	HEJ/Leading Order
2-jet				
(1, 2)	1.0985 ± 0.1048	0.1047 ± 0.0072	1.2260 ± 0.0037	0.9814 ± 0.0857
(3, 4)	0.0706 ± 0.0107	0.0086 ± 0.0001	0.0804 ± 0.0001	0.98587 ± 0.1334
(21, 21)	0.0000 ± 0.0000	0.4002 ± 0.9090	0.3612 ± 0.0357	1.00389 ± 0.0878
(1, -1)	0.4262 ± 0.0107	1.8962 ± 0.0586	2.3460 ± 0.0064	0.98991 ± 0.0255
(2, -2)	0.6151 ± 0.0640	2.0954 ± 0.0742	2.6770 ± 0.0079	1.01254 ± 0.0367
(3, -3)	0.1250 ± 0.0154	0.6116 ± 0.0078	0.7576 ± 0.0023	0.97232 ± 0.0230
(4, -4)	0.0733 ± 0.0319	0.2308 ± 0.0040	0.3096 ± 0.0010	0.98228 ± 0.1037
(5, -5)	0.0186 ± 0.0003	0.1211 ± 0.0036	0.1447 ± 0.0005	0.96592 ± 0.0254
3-jet				
(1, -1)	0.1713 ± 0.0026	0.4848 ± 0.0104	0.6112 ± 0.0031	1.0354 ± 0.0183
(21, 21)	0.0000 ± 0.0000	6.8566 ± 0.2022	6.7920 ± 0.0220	1.0095 ± 0.0299
(3, 1)	0.0008 ± 0.0000	0.1615 ± 0.0041	0.1633 ± 0.0005	0.9937 ± 0.9937
(2, -5)	0.0724 ± 0.0053	0.0627 ± 0.0046	0.1300 ± 0.0005	1.0392 ± 0.0544
(1, 21)	0.5804 ± 0.0930	3.4127 ± 0.2900	4.1498 ± 0.0149	0.9624 ± 0.0735
4-jet				
(1, 2)	0.2308 ± 0.0230	0.3199 ± 0.0447	0.5491 ± 0.0032	1.0030 ± 0.0917
(4, 21)	0.0133 ± 0.0007	0.2728 ± 0.0370	0.2780 ± 0.0509	1.0292 ± 0.1334
(1, -1)	0.0545 ± 0.0030	0.1544 ± 0.0111	0.1965 ± 0.0011	1.0631 ± 0.0588
(3, -3)	0.0002 ± 0.0000	0.0366 ± 0.0042	0.0333 ± 0.0001	1.1059 ± 0.1251

both locally in Edinburgh and using the CERN **GRID** system. The former required the development of a set-up to distribute, execute and finalise jobs across a large network of machines standard desktop machines (i.e. not actual computing nodes) distributed through Edinburgh University. This was a time-consuming process however without this system it would not have been possible to produce the interesting results of chapter 5 (which also contains a discussion of the computational challenges of generating **HEJ+ARIADNE** predictions). The **GRID** distributed computing work was available only in the final stages of this work because it became clear it was necessary (had it been available sooner the aforementioned local distributed computing set-up could have been avoided completely). This involved a good deal of learning to work with distributed systems and working with the **Ganga** batch submission system which was, again, time-consuming.

4.7 $Z/\gamma^* + \text{Jets}$ at the LHC

4.7.1 $Z/\gamma^* + \text{Jets}$ at the ATLAS Experiment

We now compare the results of the formalism described in the previous sections to data. We begin with a recent ATLAS analysis of Z^0 -plus-jets events from 7 TeV collisions [2]. We summarise the cuts in tab. (4.5).

Any jet which failed the final isolation cut was removed from the event, but the event itself is kept provided there are a sufficient number of other jets present. Throughout the central value of the **HEJ** predictions has been calculated with factorisation and renormalisation scales set to $\mu_F = \mu_R = H_T/2$, and the theoretical uncertainty band has been determined by varying these independently by up to a factor of 2 in each direction (removing the corners where the relative ratio is greater than two). Also shown in the plots taken from the ATLAS paper are theory predictions from **Alpgen** [65], **Sherpa** [52, 56], **MC@NLO** [50] and **BlackHat+Sherpa** [28, 58]. We will also comment on the recent theory description of Ref. [47].

In Fig. (4.10), we begin this set of comparisons with predictions and measurements of the inclusive jet rates. **HEJ** and most of the other theory descriptions give a reasonable description of these rates. The **MC@NLO** prediction drops below the data because it only contains the hard-scattering matrix element for Z/γ^* production and relies on a parton shower for additional emissions. The **HEJ** predictions have a larger uncertainty band which largely arises from the use of leading-order results in the matching procedures.

The first differential distribution we consider here is the distribution of the invariant mass between the two hardest jets, Fig. (4.11). The region of large invariant mass is particularly important because this is a critical region for studies of vector boson fusion (VBF) processes in Higgs-plus-dijets. Radiation patterns are largely universal between these processes, so one can test the quality of theoretical descriptions in Z/γ^* -plus-dijets and use these to inform the VBF analyses. It is also a distribution which will be studied to try to detect subtle signs of new physics. In this study, **HEJ** and the other theory descriptions all give a good description of this variable out to 1 TeV, with **HEJ** being closest throughout the range. The merged sample of Ref. [47] (Fig. 9 in that paper) combined with the **Pythia8** parton shower performs reasonably well throughout the range with a few deviations of more than 20%, while that combined with **Herwig++** deviates badly. Fig. (3.9) shows the equivalent distribution from a recent ATLAS analysis of $W^\pm + \text{dijet}$ events [5], that distribution was extended out to an invariant mass of 2 TeV and, as discussed in section 3.9, almost all of the theoretical

predictions deviated significantly while the `HEJ` prediction remained flat. This is one region where the high-energy logarithms which are only included in `HEJ` are expected to become large.

In Fig. (4.12), we show the comparison of various theoretical predictions to the distribution of the absolute rapidity difference between the two leading jets. It is clear in the left plot that `HEJ` gives an excellent description of this distribution. This is to some extent expected as high-energy logarithms are associated with rapidity separations. However, this variable is only the rapidity separation between the two hardest jets which is often not representative of the event as harder jets tend to be more central. Nonetheless, the `HEJ` description performs well in this restricted scenario. The next-to-leading order (NLO) calculation of `Blackhat+Sherpa` also describes the distribution quite well while the other merged, fixed-order samples deviate from the data at larger values. The merged samples of Ref. [47] (Fig. 8 in that paper) describe this distribution well for small values of this variable up to about 3 units when combined with `Herwig++` and for most of the range when combined with the `Pythia8` parton shower, only deviating above 5 units.

The final distribution in this section is that of the ratio of the transverse momentum of the second hardest jet to the hardest jet. The perturbative description of `HEJ` does not contain any systematic evolution of transverse momentum and this can be seen where its prediction undershoots the data at low values of p_{T2}/p_{T1} . However, for values of $p_{T2} \gtrsim 0.5p_{T1}$, the ratio of the `HEJ` prediction to data is extremely close to 1. The fixed-order based predictions shown in Fig. (4.10) are all fairly flat above about 0.2, but the ratio of the data differs by about 10%.

We have seen that in all of the figures presented in this section `HEJ` has scale uncertainty bands significantly larger than other theoretical descriptions, including `Alpgen` who also have only leading order accuracy. From fig. (4.10) we see that we describe the experimentally observed inclusive two jet rate very well and, as such, do not require normalisation to agree with the data. However, applying a normalisation procedure which consistently applies scale variation simultaneously in numerator and denominator significantly reduces the size of the scale uncertainty bands for High Energy Jets (or any theoretical prediction). In figs. (4.14a), (4.14b) and (4.14c) we show the results from figs. (4.13a), (4.12a) and (4.11a). We see that, as expected, the central value of `HEJ` still describes the data well in the regions discussed above and now the size of the theoretical uncertainty band is significantly reduced (by a factor of around 250 for example in the last bin of the $p_{\perp 2}/p_{\perp 1}$ -distribution. This illustrates that varying μ_R and μ_F leads to a change in overall normalisation but not to any significant change in

shape. Therefore, it is still valuable to discuss the quality of agreement of the central line, despite their apparently large accompanying uncertainty bands.

Lepton Cuts	$p_{T\ell} > 20 \text{ GeV}, \eta_\ell < 2.5$ $\Delta R^{\ell^+\ell^-} > 0.2, 66 \text{ GeV} \leq m^{\ell^+\ell^-} \leq 116 \text{ GeV}$
Jet Cuts (anti- k_T , 0.4)	$p_{Tj} > 30 \text{ GeV}, y_j < 4.4$ $\Delta R^{j\ell} > 0.5$

Table 4.5: Cuts applied to theory simulations in the ATLAS Z^0 -plus-jets analysis results shown in Figs. (4.10)–(4.13).

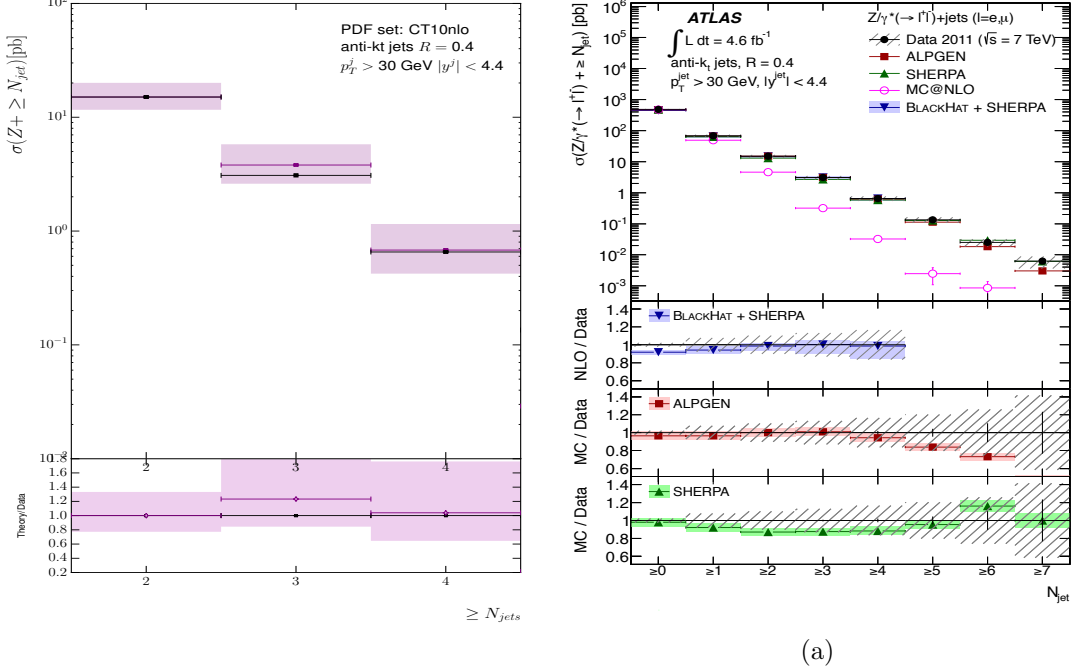


Figure 4.10: These plots show the inclusive jet rates from (a) HEJ and (b) other theory descriptions and data [2]. HEJ events all contain at least two jets and do not contain matching for 5 jets and above, so these bins are not shown.

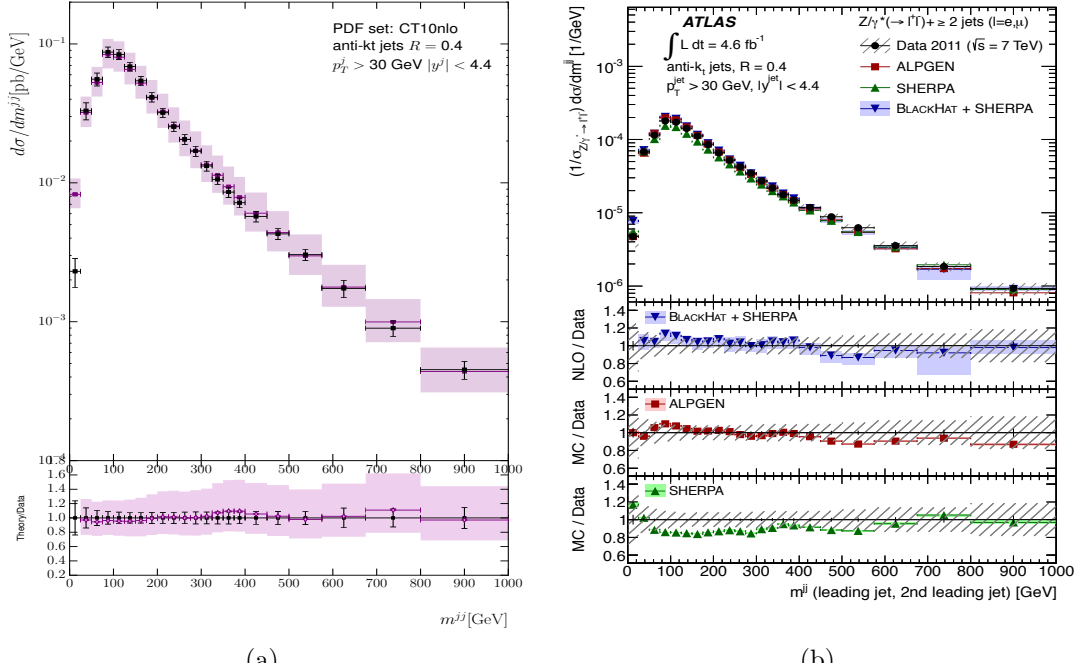


Figure 4.11: These plots show the invariant mass between the leading and second-leading jet in p_T . As in Fig. (4.10), predictions are shown from (a) HEJ and (b) other theory descriptions and data [2]. These studies will inform Higgs plus dijets analyses, where cuts are usually applied to select events with large m_{12} .

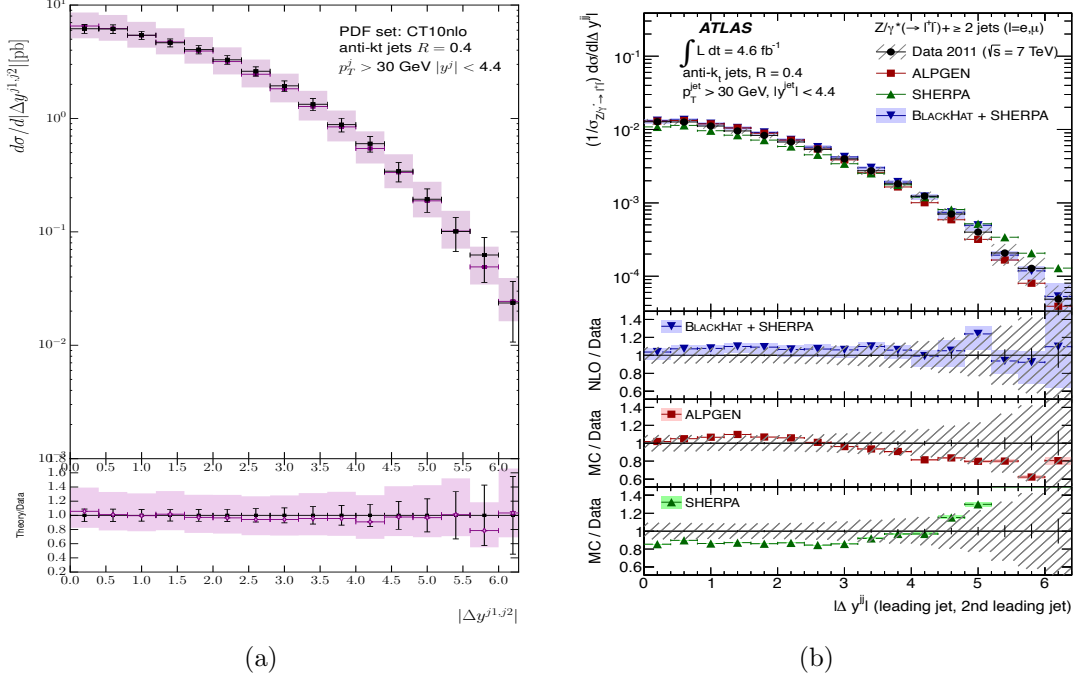


Figure 4.12: The comparison of (a) HEJ and (b) other theoretical descriptions and data [2] to the distribution of the absolute rapidity different between the two leading jets. HEJ and Blackhat+Sherpa give the best description.

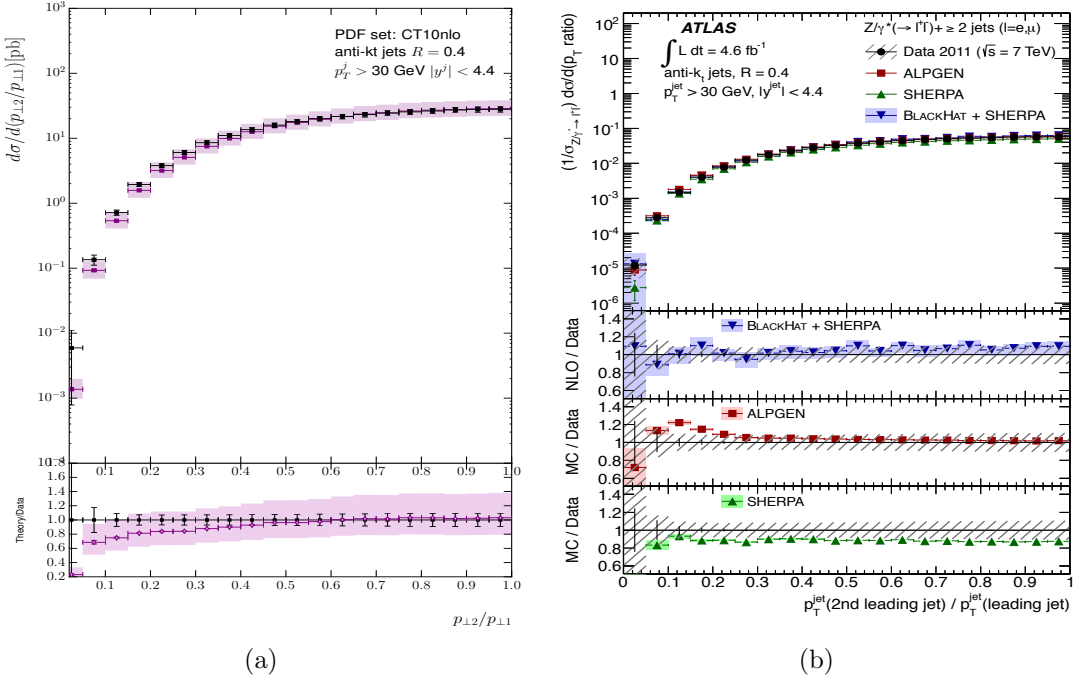


Figure 4.13: These plots show the differential cross section in the ratio of the leading and second leading jet in p_T from (a) HEJ and (b) other theory descriptions and data [2].

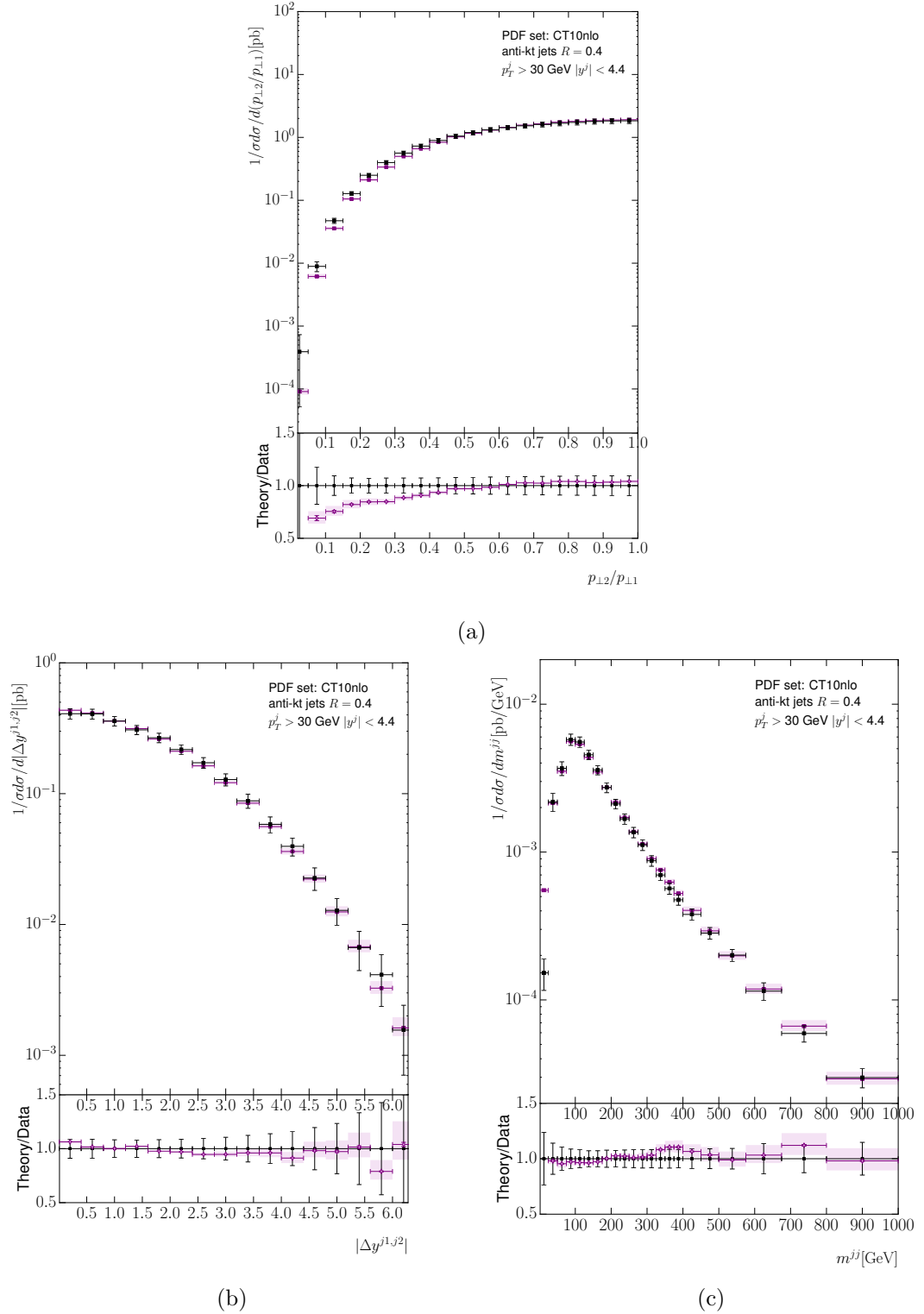


Figure 4.14: The predictions of figs. (4.13a), (4.12a) and (4.11a) normalised to the total cross-section, with scale variation consistently applied to numerator and denominator.

4.7.2 The $W^\pm + \text{Jets}$ to $Z/\gamma^* + \text{Jets}$ Ratio at the ATLAS Experiment

In this section we present predictions for the ratio of $Z/\gamma^* + \text{Jets}$ to $W^\pm + \text{Jets}$ at all orders in α_s . We compare to the recent study undertaken by the ATLAS collaboration [3]. While W^\pm plus jets and Z/γ^* plus jets are both relevant separately for Standard Model physics and beyond the ratio of the two processes is particularly interesting as a precision test since many of the systematic errors which limit the $W^\pm, Z/\gamma^*$ -plus-jets measurements cancel in the ratio. The cuts for both final states are summarised in tab. (4.6).

Lepton Cuts	$p_{T\ell} > 25 \text{ GeV}, \eta_\ell < 2.5$ $\Delta R^{\ell^+\ell^-} > 0.2$
Reconstructed Z Cuts	$66 \text{ GeV} < m^{\ell^+\ell^-} < 116 \text{ GeV}$
Reconstructed W^\pm Cuts	$m_{TW} > 40 \text{ GeV}$ $\cancel{E}_T > 25 \text{ GeV}$
Jet Cuts (anti- k_T , 0.4)	$p_{Tj} > 30 \text{ GeV}, y_j < 4.4$ $\Delta R^{j\ell} > 0.5$

Table 4.6: Cuts applied to theory simulations in the analysis of the ATLAS $W^\pm + \text{jets}/Z + \text{jets}$ ratio predictions shown in tabs. (4.7)–(4.8).

N_{jets}	Data ($\pm \text{stat.} \pm \text{syst.}$)	HEJ ($\pm \text{stat.} \pm \text{s.v.}$)	HEJ/Data ($\pm \text{stat.} \pm \text{s.v.}$)
≥ 2	$8.64 \pm 0.04 \pm 0.33$	$8.66 \pm 0.12^{+0.14}_{-0.16}$	$1.00 \pm 0.01^{+0.02}_{-0.01}$
≥ 3	$8.18 \pm 0.08 \pm 0.52$	$7.96 \pm 0.25^{+0.01}_{-0.01}$	$0.97 \pm 0.03^{+0.01}_{-0.00}$
≥ 4	$7.62 \pm 0.20 \pm 0.95$	$8.55 \pm 0.69^{+0.02}_{-0.02}$	$1.12 \pm 0.09^{+0.00}_{-0.00}$

Table 4.7: The HEJ prediction for inclusive R_{jet} rates at 2, 3 and 4 jets compared with ATLAS data.

N_{jets}	Data ($\pm \text{stat.} \pm \text{syst.}$)	HEJ ($\pm \text{stat.} \pm \text{s.v.}$)	HEJ/Data ($\pm \text{stat.} \pm \text{s.v.}$)
2	$8.76 \pm 0.05 \pm 0.31$	$8.88 \pm 0.135^{+0.15}_{-0.18}$	$1.01 \pm 0.02^{+0.021}_{-0.02}$
3	$8.33 \pm 0.10 \pm 0.45$	$7.85 \pm 0.265^{+0.01}_{-0.01}$	$0.94 \pm 0.01^{+0.001}_{-0.03}$
4	$7.69 \pm 0.21 \pm 0.71$	$8.44 \pm 0.684^{+0.04}_{-0.04}$	$1.10 \pm 0.01^{+0.005}_{-0.09}$

Table 4.8: The HEJ prediction for exclusive R_{jet} rates at 2, 3 and 4 jets compared with ATLAS data.

4.7.3 $Z/\gamma^* + \text{Jets}$ at the CMS Experiment

We now compare to data from a CMS analysis of events with a Z/γ^* boson produced in association with jets [60]. We show, for comparison, the plots from that analysis which contain theoretical predictions from Sherpa [52, 56], Powheg [11] and MadGraph_aMC@NLO [13]. The cuts used for this analysis are summarised in tab. (4.9).

Lepton Cuts	$p_{T\ell} > 20 \text{ GeV}, \eta_\ell < 2.4$ $71 \text{ GeV} \leq m^{\ell^+\ell^-} \leq 111 \text{ GeV}$
Jet Cuts (anti- k_T , 0.5)	$p_{Tj} > 30 \text{ GeV}, y_j < 2.4$ $\Delta R^{j\ell} > 0.5$

Table 4.9: Cuts applied to theory simulations in the CMS Z^0 -plus-jets analysis results shown in Figs. (4.15)–(4.17)

As in the previous section, any jet which failed the final isolation cut was removed from the event, but the event itself is kept provided there are a sufficient number of other jets present. The main difference to these cuts and those of ATLAS in the previous section is that the jets are required to be more central; $|\eta| < 2.4$ as opposed to $|y| < 4.4$. This allows less room for evolution in rapidity; however, HEJ predictions are still relevant in this scenario. Once again, the central values are given by $\mu_F = \mu_R = H_T/2$ with theoretical uncertainty bands determined by varying these independently by factors of two around this value. HEJ events always contain a minimum of two jets and therefore here we only compare to the distributions for an event sample with at least two jets or above.

We begin in Fig. (4.15) by showing the inclusive jet rates for these cuts. The HEJ predictions give a good description, especially for the 2- and 3-jet inclusive rates in this narrower phase space. The uncertainty bands are larger for HEJ than for the **Sherpa** and **Powheg** predictions due to our LO matching prescription (those for **MadGraph_aMC@NLO** are not shown).

In Figs. (4.16)–(4.17), we show the transverse momentum distributions for the second and third jet respectively (the leading jet distribution was not given for inclusive dijet events). Beginning with the second jet in Fig. (4.16), we see that the HEJ predictions overshoot the data at large transverse momentum. In this region, the non-FKL matched components of the HEJ description become more important and these are not controlled by the high-energy resummation. The HEJ predictions are broadly similar to Powheg’s Z^0 -plus-one-jet NLO calculation matched with the Pythia parton shower. In contrast, **Sherpa**’s prediction significantly undershoots the data at large transverse momentum. Here the **MadGraph_aMC@NLO** prediction gives the best description of the data.

Fig. (4.17) shows the transverse momentum distribution of the third jet in this data sample. Here, the ratio of the HEJ prediction to data shows a linear increase with transverse momentum (until the last bin where all the theory predictions show the same dip). Both the **Sherpa** and **Powheg** predictions show similar deviations for this variable while the **MadGraph_aMC@NLO** prediction again performs very well.

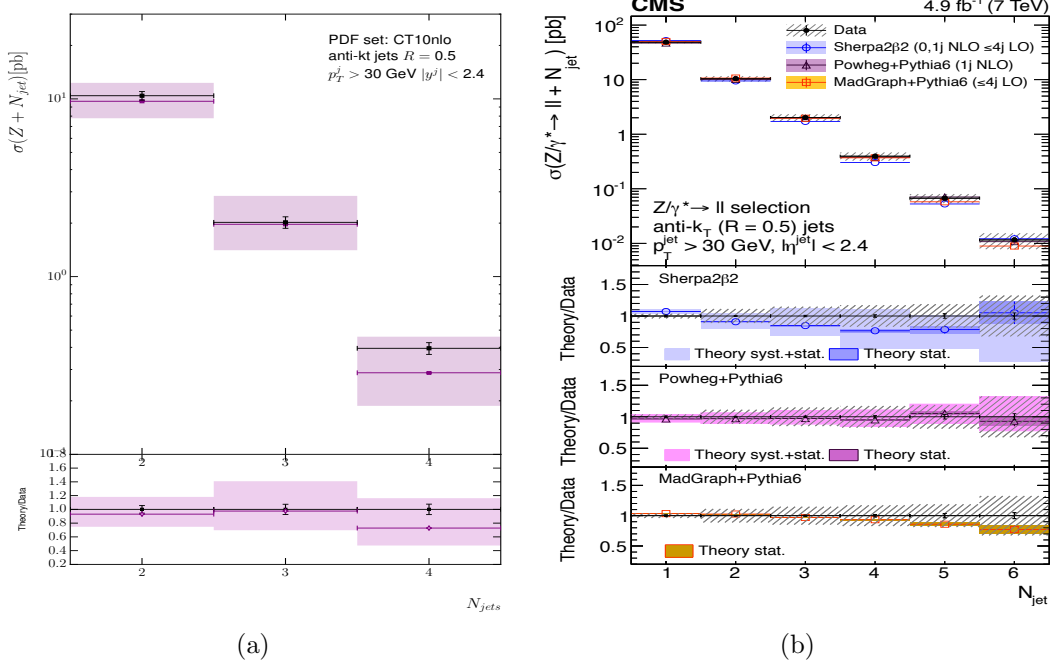


Figure 4.15: The inclusive jet rates as given by (a) the HEJ description and (b) by other theoretical descriptions, both plots compared to the CMS data in [60].

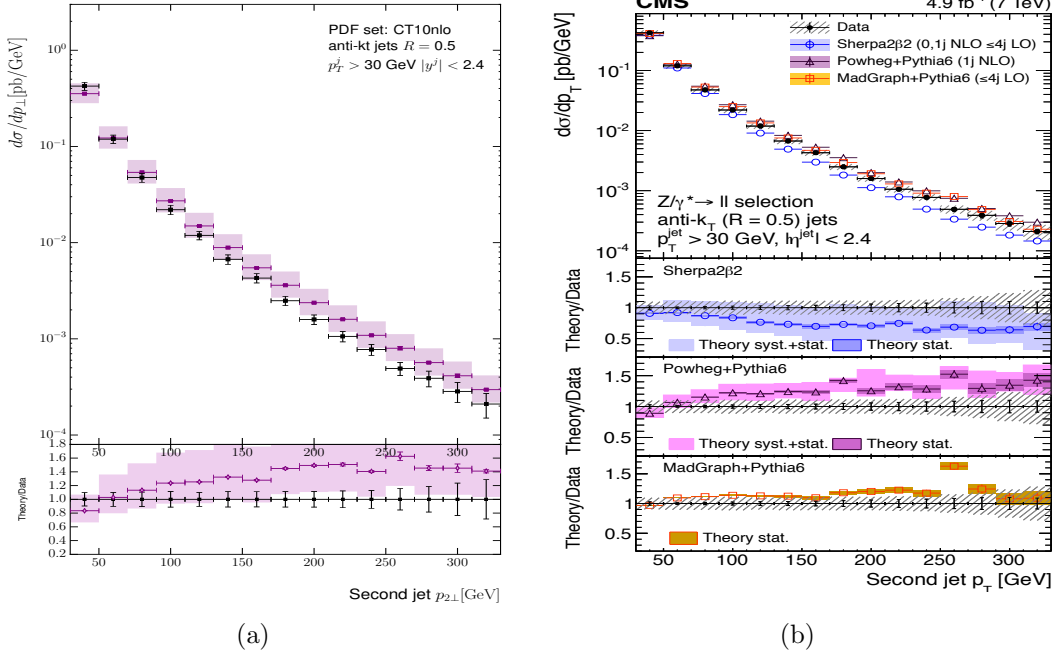


Figure 4.16: The transverse momentum distribution of the second hardest jet in inclusive dijet events in [60], compared to (a) the predictions from HEJ and (b) the predictions from other theory descriptions.

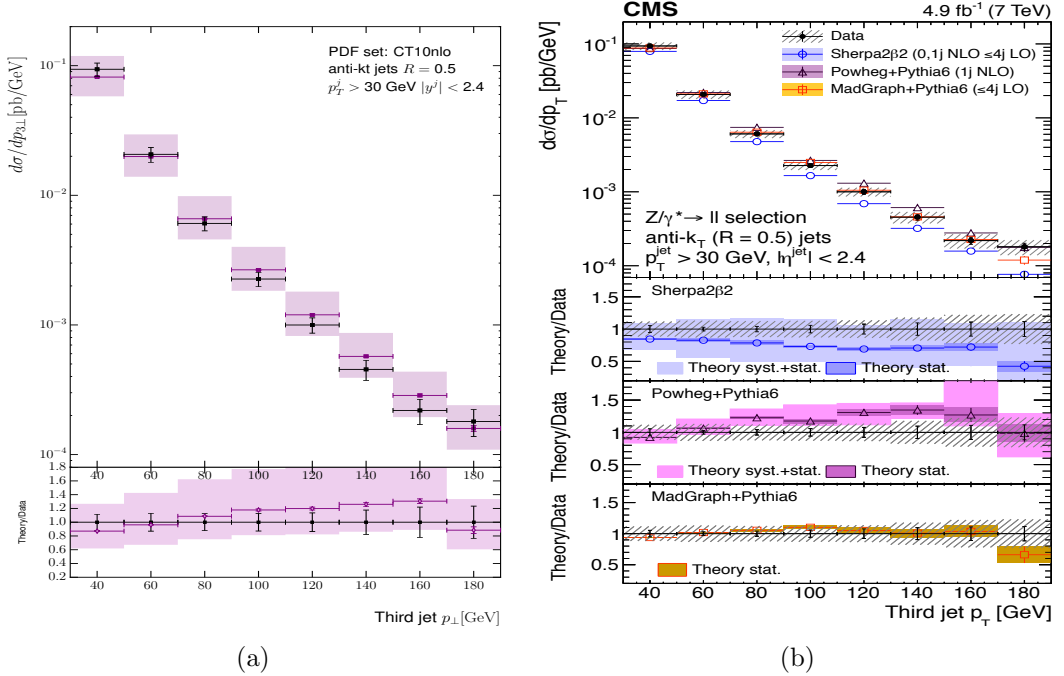


Figure 4.17: The transverse momentum distribution of the third hardest jet in inclusive dijet events in [60], compared to (a) the predictions from HEJ and (b) the predictions from other theory descriptions.

4.7.4 Differential Drell-Yan at the CMS Experiment

Throughout the course of this work many analyses were used to compare High Energy Jets to experimental data. Though we usually only take part in studies illuminating for a discussion of higher order logarithmic corrections of QCD processes at hadronic colliders the High Energy Jets collaboration was asked to generate numbers discuss a Drell-Yan study undertaken by the CMS experiment [39].

In particular, we consider the Drell-Yan cross-section differential in both the pseudo-rapidity gap between the reconstructed Z/γ^* boson and the leading jet in p_T and in the invariant mass of the di-lepton decay products. This is *not* a region of phase space where resummation is expected to reign supreme and we therefore anticipate that the matching of our High Energy Jets amplitudes to exact leading order results obtained using `MadGraph_aMC@NLO` will be significant.

The study focussed on 0-, 1- and 2-jet events in addition to a di-muon pair; since we can only describe final states with at least two jets we only consider the later final state. The final state cuts applied in this analysis are shown in tab. (4.10).

Lepton Cuts	$p_{\mu 1\perp} > 20 \text{ GeV}, p_{\mu 2\perp} > 10 \text{ GeV},$ $ \eta_\mu < 2.1, \eta_{Z/\gamma^*} < 2.5$
Jet Cuts (anti- k_T , 0.5)	$p_{Tj} > 30 \text{ GeV}, \eta_j < 4.5$

Table 4.10: Cuts applied to theory simulations in the CMS Drell-Yan analysis results shown in Figs. (4.18a)–(4.18e)

Fig. (4.18a) shows the distribution in the absolute rapidity gap between the reconstructed Z/γ^* and the leading jet in p_\perp for a reconstructed di-muon mass in the Z^0 peak range (defined as 60–120 GeV). We see that both the leading order exact and HEJ give a good description of data in this range. Figs. (4.18c) and (4.18e) show the same distribution but for a reconstructed Z/γ^* mass of between 30–60 GeV and 120–1500 GeV respectively. Here we see that both `MadGraph_aMC@NLO` and HEJ give a poor description of the data but agree well with one another. This is exactly because the HEJ predictions are being driven by the leading order matching in the regions considered. This is a good consistency check of both the High Energy Jets matching scheme and the implementation of the importance sampling in HEJ.

In HEJ the production of the Drell-Yan decay products via a Z^0 boson or an off-shell photon is implemented by using exactly the importance sampling scheme shown in chapter 2, eqn. (2.89) and fig. (2.7) - that is we focus our matrix element evaluations predominantly around the Z^0 mass peak. Fig. (4.18b) was generated using the standard importance sampling (which is *not* designed for this range of invariant masses) while fig. (4.18c) was generated using a modified importance sampling approach which was better suited for probing the low mass end of the Breit-Wigner distribution. Clearly using an intelligently chosen importance sampling scheme makes a big difference to the results - since, although the integrals are formally equal, when we come to perform the Monte Carlo integration we must use what computational resources we have to focus on the regions which contribute most to the integral. Figs. (4.18d) and (4.18e) show the same distribution now for an invariant mass of between 120 and 1500 GeV, once again fig. (4.18d) was calculated with the default importance sampling whereas fig. (4.18e) used a modified scheme: the same behaviour can be seen with the default sampling describing the data poorly and being statistically limited.

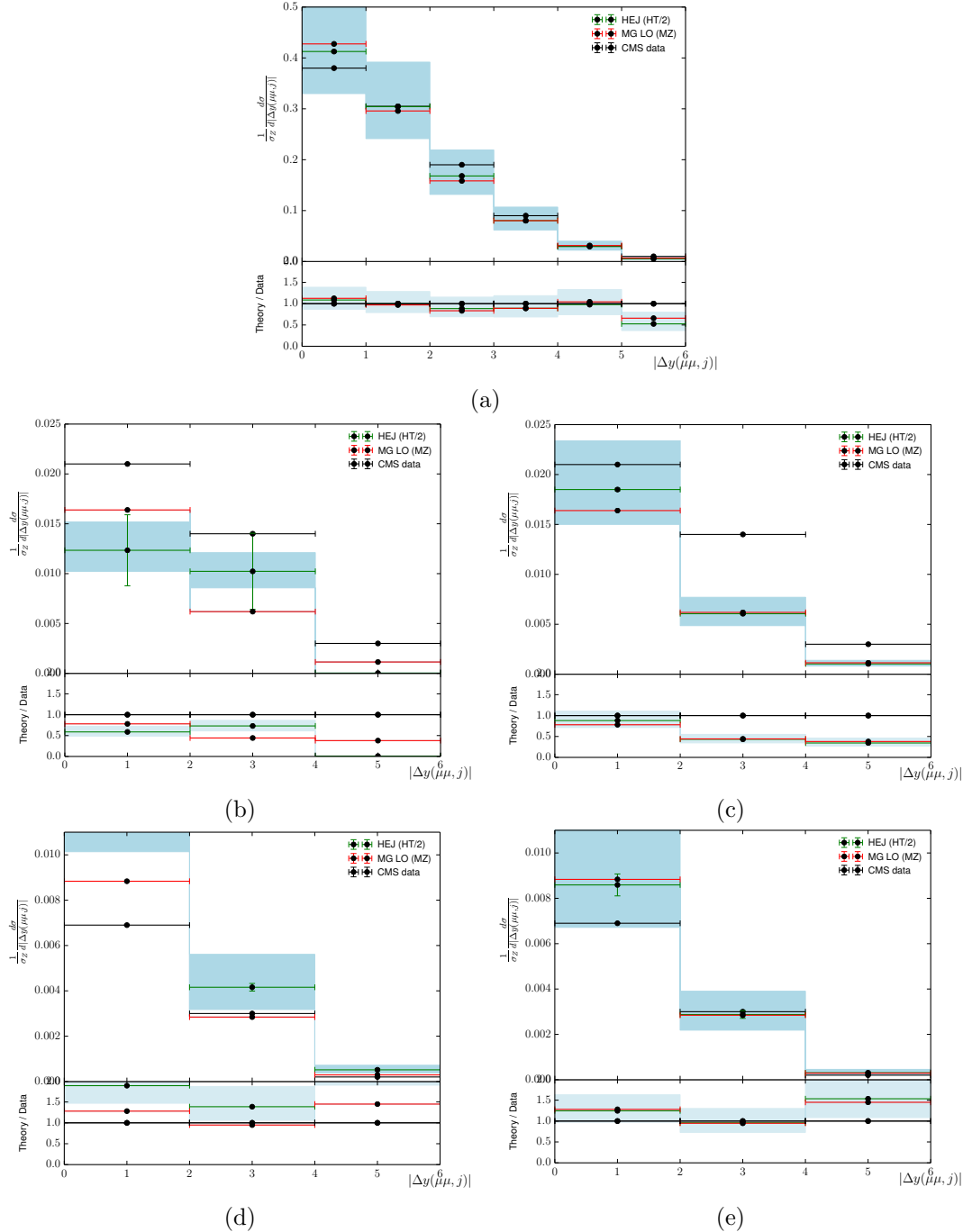


Figure 4.18: Comparisons of HEJ and `MadGraph-aMC@NLO` to data from a CMS study of double-differential Drell-Yan production. Fig. (4.18a) shows the mass range focussed on the Z^0 peak (60-120 GeV), figs. (4.18b) and (4.18c) show the di-lepton invariant mass range from 30-60 GeV and lastly figs. (4.18d) and (4.18e) show the mass range from 120-1500 GeV. For figs. (2.9b-e) which probe regions away from the Breit-Wigner peak two HEJ lines are shown - figs. (4.18b) and (4.18d) use the naïve Breit-Wigner sampling while figs. (4.18b) and (4.18d) use a modified importance sampling scheme.

4.8 $Z/\gamma^* + \text{Jets}$ Conclusions

In this chapter we have discussed augmenting the theoretical description of inclusive Z/γ^* -plus-dijets processes with the dominant logarithms in the High Energy limit at all orders in α_s . In particular, the description constructed here is accurate to leading logarithm in s/t . This is achieved within the High Energy Jets framework. We began in chapter 3 by motivating and describing the construction of an approximation to the hard-scattering matrix element for an arbitrary number of gluons in the final state. This uses factorised currents for electroweak boson emission and outer jet production combined with a series of (gauge-invariant) effective vertices for extra QCD real emissions.

In contrast to previous HEJ constructions (for pure jets, W -plus-jets and Higgs boson-plus-jets), the complete description of the interference contributions between Z and γ^* processes *and* between forward and backward emissions required a new regularisation procedure. This is described in section 4.3 where we showed explicitly the cancellation of real and virtual divergences by using the Lipatov ansatz to include the dominant contributions in the High Energy limit of the all-order virtual contributions. The method by which we match our matrix element to the leading order matrix elements was also outlined here. In this way we achieve the formal accuracy of our Monte Carlo predictions to Leading Logarithmic in s/t and merge Leading Order predictions in α_s for the production of two, three or four jets.

In sections 4.7.1 and 4.7.3 we compared the predictions of our construction to Z/γ^* -plus-jets data collected at the ATLAS and CMS experiments during Run I. We see excellent agreement for a wide range of observables and can be seen to describe regions of phase space well where some other fixed-order-based predictions do not fare as well. Discrepancies between HEJ and data which occur only do so in regions where we do not expect this description to perform as well, for example where there is a large ratio between p_{T1} and p_{T2} . We also discuss properties of other available theoretical descriptions.

This all-order description of Z/γ^* -plus-dijets allows predictions for the ratio of $W^\pm + \text{dijets}$ to $Z/\gamma^* + \text{dijets}$ at all-orders in α_s for the first time. This is an extremely important analysis as many theoretical and experimental uncertainties cancel in this ratio and in section 4.7.2, we show that we correctly reproduce the ratios of the total cross sections.

Just as for previous analyses of LHC data, it is found that the high-energy logarithms contained in HEJ are necessary for a satisfactory description of data in key regions of

phases space, e.g. at large values of jet invariant mass. Such regions of phase space are crucial for the analysis of Higgs boson production in association with dijets for example. The impact of the high-energy logarithms will only be more pronounced at the larger centre-of-mass energy of LHC Run II, and beyond at a possible future circular collider. The HEJ framework and Monte Carlo is the unique flexible event generator to contain these corrections and will provide important theoretical input for the study of important processes at LHC Run II and beyond.

Chapter 5

Dijets and Gap Jets at ATLAS

Here we present the results of a complex experimental study of the effects of jet vetoes and azimuthal decorrelations in dijet events [4]. High Energy Jets is compared to both data and state-of-the-art fixed-order perturbative QCD predictions supplemented with radiation by merging with a parton shower from **POWHEG+PYTHIA8** and **POWHEG+HERWIG** (both implemented through the **POWHEG BOX** package [68]).

The data are taken from 7 TeV proton-proton collisions as observed by the ATLAS experiment in two distinct data sets referred to as 2010 data and 2011 data. The experimental cuts applied to these data sets differs and both are outlined in tab. (5.1).

2010 Jets (anti- k_T , 0.6)	$p_{Tj} > 20 \text{ GeV}, y_j < 4.4$ $p_{T1} > 60.0 \text{ GeV}, p_{T2} > 50.0 \text{ GeV},$ $Q_0 = 20 \text{ GeV}$
2011 Jets (anti- k_T , 0.6)	$p_{Tj} > 30 \text{ GeV}, y_j < 2.4$ $p_{T1} > 60.0 \text{ GeV}, p_{T2} > 50.0 \text{ GeV}$ $Q_0 = 30 \text{ GeV}, \Delta y_{jj} > 1.0$

Table 5.1: Cuts applied to theory simulations in the ATLAS dijets analyses. Q_0 is the gap jet veto scale. The results are shown in figs. (5.1)–(5.6).

This study focused on additional jet activity in dijet events where the dijet system is constructed using the two leading jets in p_T - this, is in stark contrast to defining dijets by the most forward and most backward jets: naturally the p_\perp choice favours high transverse momentum dijets in the central region (and hence with relatively small rapidity gaps) while the forward-backward dijet system definition typically lead to softer systems with bigger rapidity spans [7]. These two jets are required to be significantly harder than any additional jets with extra cuts on the leading and sub-leading jets of 60 GeV and 50 GeV respectively. After tagging the two leading jets in the event

and additional jet radiation is only considered in the rapidity interval bounded by the dijets as a QCD correction. Within the two data sets defined in tab. (5.1) a further subdivision was made. For both the 2010 and 2011 data a subset of events was defined by vetoing events with extra QCD radiation in the rapidity interval bounded by the dijet system above some veto scale Q_0 . It should also be noted that the 2011 data set required a minimum rapidity gap of 1.0 between the leading jets (for both cases with and without the gap jet veto) in order to encourage a large rapidity span into which extra radiation may arise. In summary, the full breakdown of this analysis then is into four event categories; 2010 data with and without a veto applied to gap jets and the 2011 data with and without a veto applied to gap jets.

I generated the predictions for these analyses on behalf of the High Energy Jets collaboration at the request of the ATLAS collaboration. Predictions for both the partonic **HEJ** calculation (shown in green in this chapter) and the **HEJ+ARIADNE** calculation (shown in orange) were calculated. As discussed in chapter 3 **ARIADNE** is a parton shower package based on the Lund colour cascade dipole model. As per the algorithm outlined in section 3.9, the steps necessary to remove the double counting in this interfaced package (which arises from **HEJ** and **ARIADNE** both generating soft radiation) make generating large data samples which can be used to give statistically significant predictions for the challenging regions of phase space considered here is *extremely* computationally demanding. The generation of these predictions was so demanding several changes were made to the **HEJ** codebase; the size of event files generated meant that the analysis framework for High Energy Jets required rewriting so that binning to histograms could occur on-the-fly. As discussed in section 4.6, this analysis was initially run using local computing resources however it quickly became apparent that this would not be sufficient, at which point it was necessary to switch to running **HEJ** on the CERN grid computing cluster - this was the first time this was done.

A central scale was chosen based on previously agreement with data seen in a previous ATLAS comparison to gap jets [1]; this set of 19 scale combination form an ‘envelope’ of predictions for each bin in each plot - this spread is then represented by the green bands shown in the figs. (5.1)–(5.6). Due to the structure of the matrix element evaluations within **HEJ+ARIADNE** we can only afford one scale choice per event and, as such, we cannot provide scale variation uncertainty bands with our showered numbers. To be clear this is not a limitation of the physics since it is entirely possible to evaluate each matrix element multiple times - it is only a computational consideration. As seen in chapter 4, the renormalisation scale appears in a non-trivial way in the High Energy Jets matrix element. It is contained implicitly in the strong coupling constant which is

contained within the virtual corrections exponential. As such we cannot simply generate predictions at a single scale and then re-weight events at the post-analysis level. This is further complicated in **HEJ+ARIADNE** because of the additional scale dependencies in the parton shower description.

The orange bands shown with the **HEJ+ARIADNE** predictions throughout this chapter are the statistical bands shown at the 68% confidence level. The calculation of these statistical bands had to be completed manually - that is to say, not using the out-of-the-box result provided by **ROOT** since many of the individual distributions required calculating ratios of distributions for which the statistical errors in the numerator and denominator are highly correlated. It was seen that the naïve statistical uncertainty bands were not representative of the actual uncertainty. The bands presented were calculated using a statistical bootstrapping approach: given a Monte Carlo sample comprising N events we repeatedly form ‘bootstrap samples’ each of which also with N events by randomly selecting subsets of the full sample (allowing for repetition). Once a sufficient number of these have been generated we have a distribution of results for each bin in each histogram and we can easily form a statistical uncertainty band which contains 68% of the bootstrapped samples in each bin.

Here observables were studied as a function of two properties of a dijet system. The rapidity gap between the dijets, Δy , and the mean traverse momenta of the dijet system, $\overline{p_T}$.

For small Δy we expect to see fewer gap jets since there is a limited region in which extra jets may be clustered before they are clustered in to the dijet system itself. Conversely, as we pull the dijets apart in rapidity we expect to see an increase in additional QCD radiation (since there is a larger phase space in which to radiate). Similarly for $\overline{p_T}$, we expect that events with harder dijet systems will have higher gap activity simply because they can cheaply add extra radiation.

Throughout the remainder of this chapter the left hand figures, (a), show data and predictions for the 2010 data set with respect to the rapidity span of the dijet system, Δy , while the right hand figures, (b), show data and predictions from the 2011 data set with respect to the mean transverse momenta of the dijet system, $\overline{p_T}$.

We begin by discussing the gap fraction, $f(Q_0)$, defined as:

$$f(Q_0) = \frac{\sigma_{jj}(Q_0)}{\sigma_{jj}}, \quad (5.1)$$

where σ_{jj} is the total dijet cross section passing the cuts in tab. (5.1) and $\sigma_{jj}(Q_0)$ is

the dijet cross section passing the cuts plus the extra veto on additional gap scales for a scale choice Q_0 .

Fig. (5.1) shows the gap fraction with a veto scale of 20 GeV in fig. (5.1a) and a veto scale of 30 GeV in fig. (5.1b). The data are shown in black with the inner bars representing the statistical uncertainty while the outer lines are the total uncertainty arising from statistical and systematic effects. The behaviour observed is in line with our expectation discussed previously since the gap fraction decreases at both large Δy and large $\overline{p_T}$. We can see the best description of both data sets is given by **HEJ+ARIADNE** (excluding two very high $\overline{p_T}$ bins where the predictions from **HEJ+ARIADNE** are visibly statistically limited). The partonic **HEJ** prediction overshoots both data sets meaning that we underestimate the jet activity in the gap region while the predictions from **POWHEG** plus parton showers overestimate the QCD radiation here. The big difference between the partonic and showered **HEJ** lines in fig. (5.1) indicates clearly that in this region of phase space it is not sufficient to only describe the wide-angle logarithmically enhanced terms resummed within the High Energy Jets framework and that the soft and collinear logarithms added by interfacing to **ARIADNE** play a very important rôle - equally it is clear from the differences between **HEJ** and the other theory descriptions that we cannot completely describe data without resumming the High Energy logarithms. It is visible from fig. (5.1) that the scale variations shown in *partonic* **HEJ** (since the **HEJ+ARIADNE** bands are statistical only) are quite significantly bigger than that shown by the other predictions. This is expected since we only include matching up to leading-order whereas **POWHEG** is formally NLO accurate. In pure fixed-order calculations it is well observed that as higher order terms are included a better control of the scale uncertainties is achieved.

Similarly, when we study the mean number of jets in the rapidity interval shown for in fig. (5.2) we see that **HEJ+ARIADNE** and **POWHEG+PYTHIA8** give the best description of the data. Once again the partonic **HEJ** prediction undershoots the data significantly when describing both of the dijet characteristics while **POWHEG+HERWIG** overestimates the jet activity.

We now turn to look at the azimuthal decorrelations of dijet systems. These are defined as $\langle \cos(n(\pi - \Delta\phi)) \rangle$ with $n = 1, 2, \dots$ and $\Delta\phi$ is the azimuthal separation between the leading dijets. Here we only consider the first and second moments. We follow the notation of [4] and rewrite the second moment as $\langle \cos(2\Delta\phi) \rangle$. Clearly for a final state with two partons momentum conservation will enforce that the jets be in a back-to-back configuration i.e. they will have $\Delta\phi = \pi$ and both $\langle \cos(\pi - \Delta\phi) \rangle$ and $\langle \cos(2\Delta\phi) \rangle$ will simply be constant at 1.0. As additional partons are emitted the moments will

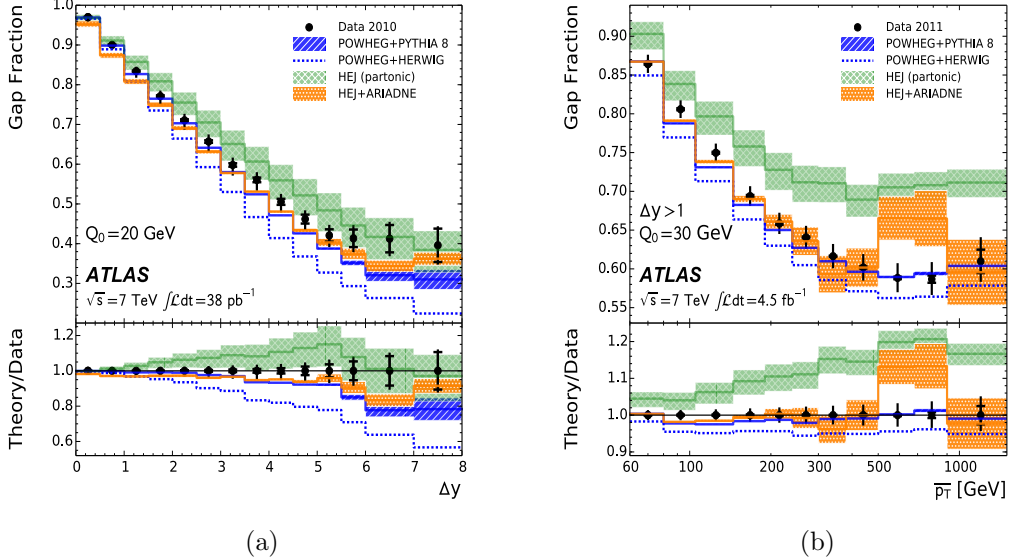


Figure 5.1: The gap fraction, $f(Q_0)$, as a function of (a) the rapidity gap, Δy in the 2010 data, and (b) the average p_T , $\overline{p_T}$, of the dijet system in the 2011 data.

depart from the straight line as the constraint softens and the extra radiation allows for $\Delta\phi < \pi$. These moments have long been seen as an excellent test of the difference between DGLAP QCD parton showers and BFKL-like resummations [43]. Indeed it is in these figures where we see the biggest difference between HEJ and the POWHEG plus parton shower results.

Fig. (5.3) shows the first azimuthal moment for the inclusive selection. We see that in the 2010 study HEJ+ARIADNE and both POWHEG descriptions slightly underestimate $\langle \cos(\pi - \Delta\phi) \rangle$ while the partonic HEJ result slightly overestimates. However, the evolution of the first azimuthal moment with respect to $\overline{p_T}$ shows a clear difference between the two formalisms. Partonic HEJ does not radiate sufficiently to predict the correct decorrelation at low mean transverse momentum (which is understood since it does not include the parton shower effects) while both POWHEG descriptions cause too much decorrelation at low $\overline{p_T}$. The best description of the data is given by HEJ+ARIADNE since it adds extra emissions to High Energy Jets which improves our description of the decorrelation. Once again it is clear that the low p_\perp region of fig. (5.3) is extremely sensitive to shower effects - not only because there is a large difference between HEJ and HEJ+ARIADNE but also because the two POWHEG plus shower results differ significantly.

Another variable thought to be a good test of DGLAP vs. BFKL physics is the ratio of the second moment to the first moment, this is shown in fig. (5.4). Once again we do see a sizeable difference in the predictions given by the two resummations. Similarly

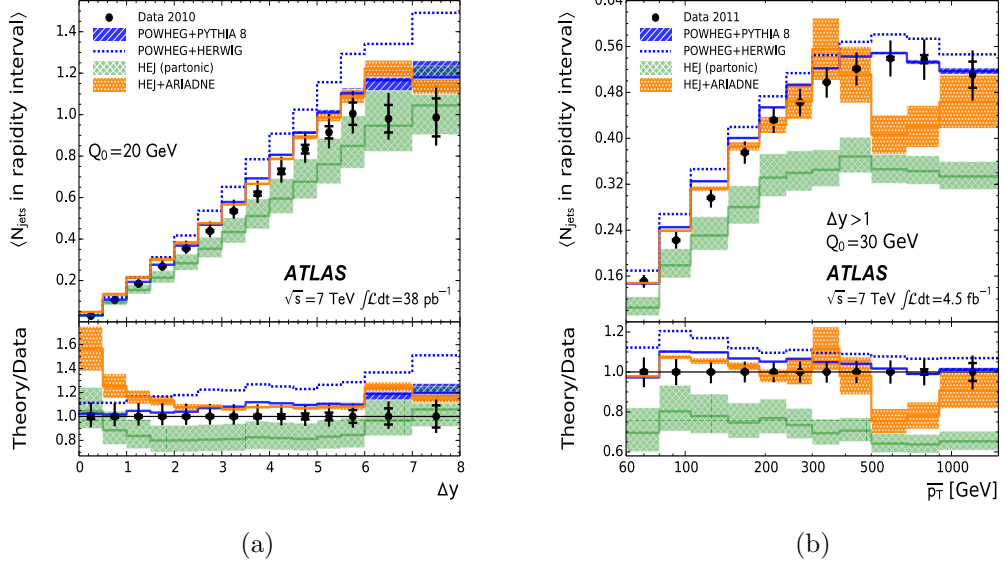


Figure 5.2: The average number of jets, $\langle N_{\text{jets}} \text{ in the rapidity interval} \rangle$, in the rapidity gap bounded by the dijet system, as a function of (a) the rapidity gap, Δy , and (b) the average p_T , $\overline{p_T}$, of the dijet system.

to fig. (5.3) we see that interfacing to the **ARIADNE** package brings the partonic **HEJ** prediction into much better agreement with the data and that the parton showers alone does not give a good description of data. We remark on the similarity of the **POWHEG** prediction that that of **HEJ+ARIADNE** here, given the stark contrast of the underlying physics in these two descriptions it is not at all expected. This similarity has also been observed in previous studies and has been discussed in [10].

The two remaining figures are similar to figs. (5.3) and (5.4) but with the addition of the jet veto applied to events. Similarly to the inclusive case we see that the partonic **HEJ** predictions overestimates the correlation for the 2010 and the 2011 data sets while the NLO plus shower predictions, once again, undershoot the decorrelation. Given the statistical limited data available (especially for the 2010 gap jet vetoed data set) it is more difficult to draw clear conclusions here but certainly the inclusion of the **ARIADNE** shower improves the High Energy Jets results.

Lastly we have the ratio of the second azimuthal moment to the first azimuthal moment for the events which pass the additional jet veto. **HEJ+ARIADNE** and **POWHEG+PYTHIA8** come closest to describing the data however there is some disagreement; in particular no one gives a good description of the evolution of this ratio at low $\overline{p_T}$.

In summary, the best description of the data overall is given by **HEJ+ARIADNE** and **POWHEG+PYTHIA8** while parton level **HEJ** overestimates (underestimate) the gap fraction

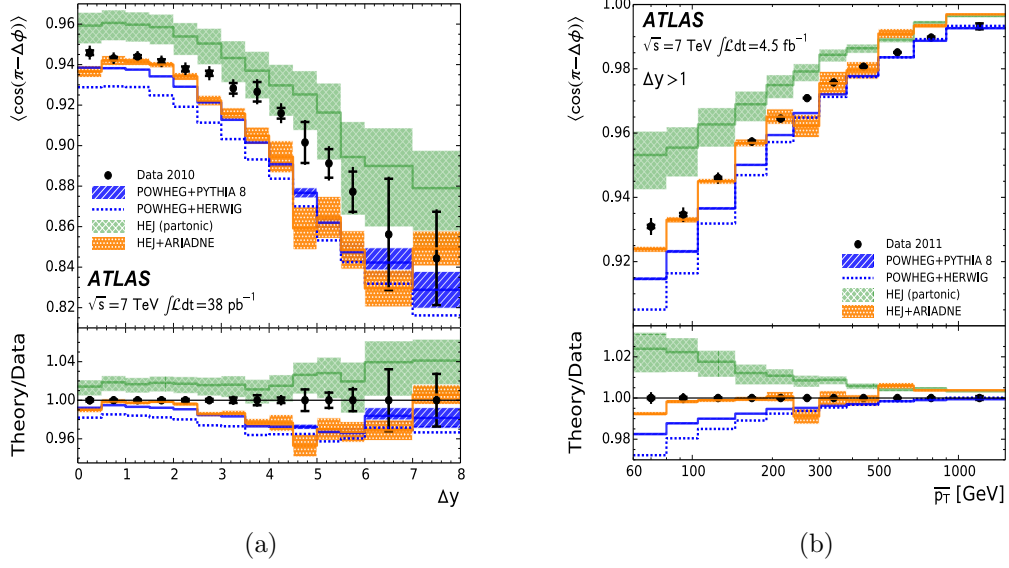


Figure 5.3: The first azimuthal angular moment, $\langle \cos(\pi - \Delta\phi) \rangle$, as a function of (a) the rapidity gap, Δy and (b) the average p_T , $\overline{p_T}$, of the dijet system.

(the mean number of jets in the rapidity gap) and overshoots both the first azimuthal moment and the ratio of the second to the first azimuthal moment. POWHEG+HERWIG describes the data poorly for the gap fraction, the mean number of gap jets and the azimuthal decorrelations. From this it is clear that while the logarithmically enhanced resummed in the High Energy Jets framework are important in regions of phase space where we have large rapidity gaps (such as the analyses described here) there are equally important contributions arising from the logarithms given to us by the interface with a parton shower. It is clear that no one package describes all of the data presented and therefore the LHC is probing challenging reasons of phase space and thus more attention is needed. This study also strongly motivates further development of High Energy Jets with other parton shower descriptions.

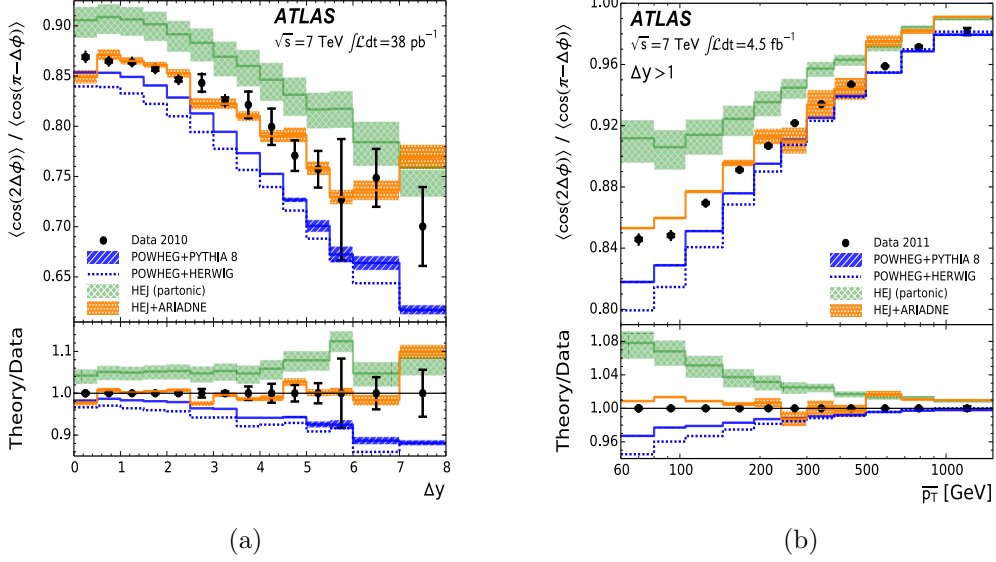


Figure 5.4: The ratio of the second azimuthal angular moment, $\langle \cos(2\Delta\phi) \rangle$, to the first azimuthal angular moment, $\langle \cos(\pi - \Delta\phi) \rangle$, as a function of (a) the rapidity gap, Δy , and (b) the average p_T , \bar{p}_T , of the dijet system.

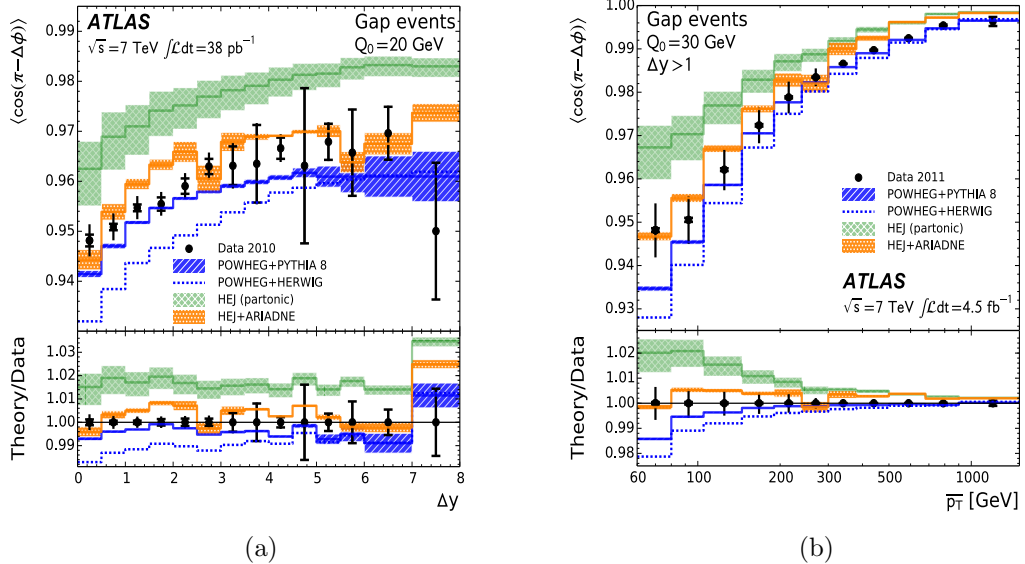


Figure 5.5: The first azimuthal angular moment, $\langle \cos(\pi - \Delta\phi) \rangle$, for events passing the veto on gap activity above $Q_0 = 20 \text{ GeV}$ as a function of (a) the rapidity gap, Δy , and (b) the average transverse momentum, \bar{p}_T , of the dijet system.

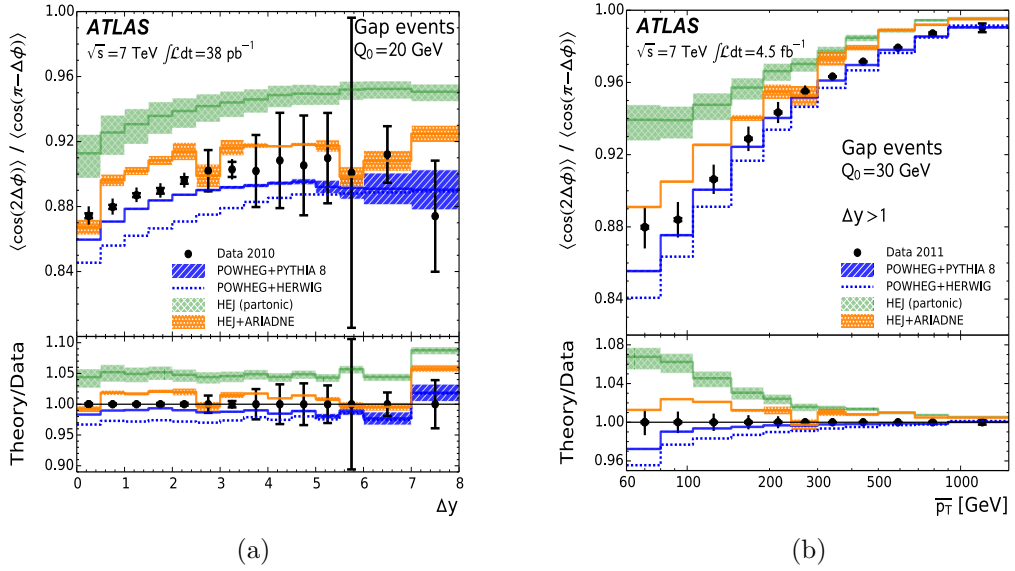


Figure 5.6: The ratio of the second azimuthal angular moment, $\langle \cos(2\Delta\phi) \rangle$, to the first azimuthal angular moment, $\langle \cos(\pi - \Delta\phi) \rangle$, as a function of (a) the rapidity gap, Δy , and (b) the average p_T , \bar{p}_T , of the dijet system. A veto of $Q_0 = 20 \text{ GeV}$, for (a), and $Q_0 = 30 \text{ GeV}$, for (b), is applied on activity in the rapidity gap is applied.

Chapter 6

$Z/\gamma^* + \text{Jets}$ at 100TeV

Even though the Large Hadron Collider has only just begun run II, there is an ever growing effort to discuss where we go next as a high energy collider physics community. A wide range of options have been put forward including the Compact Linear Collider (CLIC) experiment [8] and the International Linear Collider (ILC) experiment [32]. While both of these machines are designed to be precision electron-positron linear colliders they have very different designs; CLIC would operate at around a centre-of-mass energy of 3 TeV and use cutting edge accelerating technology whereas the ILC would collide at 0.5 TeV (with a possible upgrade to 1 TeV to follow).

There are, however, other suggestions on the table. Of particular interest for this work is the prospect of a hadronic Future Circular Collider (FCC-hh). There are other possible initial states such as hadron-lepton or a lepton-lepton being discussed but we will focus on the FCC-hh here since the resummation developed in chapters 3 and 4 is most relevant here.

One particularly exciting scenario is that of a 100 TeV hadronic collider housed in an extended tunnel approximately 100 km in circumference at the CERN site in Geneva. Such a machine would make an excellent ‘discovery machine’ since it would cover a vast range in partonic centre-of-mass energies. The energies probed here would be orders of magnitude higher than ever seen at a hadronic collider and so this would be an invaluable test of high scale QCD. Similarly to physics at the current LHC the dominant background would be QCD in nature and so in order for us to be able to extract useful information about potential new physics we would need to be able to model this QCD background with incredible precision. Current state-of-the-art for many QCD processes is still limited to next-to-leading order in α_s although progress is being made towards improving this to next-to-next-to-leading order in some key

physics processes. For example, Higgs production via gluon fusion is already known at N³LO [15]. However, as in the preceding chapters we will instead investigate the effects of the higher-order logarithmically enhanced contributions to the perturbative series. As discussed in chapter 2 these terms are not all captured by any fixed-order scheme

The results of chapters 4 and 5 clearly show that these effects are already important at a the 7 TeV for both dijets and Z/γ^* +dijets respectively. We therefore expect that at a 100 TeV FCC-hh we would see a greater effect from the terms enhanced in the High Energy limit.

Here we present a study of Z/γ^* +dijets at a centre-of-mass energy of 100 TeV. The final state cuts are outlined in tab. (6.1). For each figure we show the equivalent result calculated at 7 TeV with a jet p_T cut of 30 GeV (which was found to be in excellent agreement with data in chapter 4) as well as the 100 TeV predictions for jet cuts of 30 GeV, 60 GeV and 100 GeV. The choice of jet cut is an interesting problem since it is the best variable for weeding out physics other than the hard perturbative scatter. For example, even at the 7 TeV LHC a QCD study with a jet cut of, say, 10 GeV would be a test of multiple parton interactions and underlying event and not so much of a test of the hard scatter. While this is a perfectly valid analysis to do it is *not* the best choice if our aim is to test and improve our understanding of perturbative QCD. The same argument applies for a 100 TeV collider only more so! As we go to increasingly higher centre-of-mass energies we need to raise our jet cuts so as to ensure the data we hope to describe is as unpolluted as possible. We may also need to narrow our jet radius to keep the jet multiplicities to an experimentally manageable level. Each figure shows the ratio of the 100 TeV prediction to the 7 TeV prediction to emphasise any features which may otherwise be hard to see - such as changes in shape at different energies and with different cut criteria. The 7 TeV results are shown in

Lepton Cuts	$p_{T\ell} > 20 \text{ GeV}, \eta_\ell < 2.5$ $\Delta R^{\ell^+\ell^-} > 0.2, 66 \text{ GeV} \leq m^{\ell^+\ell^-} \leq 116 \text{ GeV}$
7 TeV Jet Cuts (anti- k_T , 0.4)	$p_{Tj} > 30 \text{ GeV}$ $ y_j < 4.4, \Delta R^{j\ell} > 0.5,$
100 TeV Jet Cuts (anti- k_T , 0.4)	$p_{Tj} > 30 \text{ GeV}, 60 \text{ GeV}, 100 \text{ GeV}$ $ y_j < 4.4, \Delta R^{j\ell} > 0.5,$

Table 6.1: Cuts applied to theory simulations for the 100 TeV Z -plus-jets analysis results shown in Figs. (6.1a)–(6.4c). We apply only one jet cut of 30 GeV to the jets in the 7 TeV analysis, shown in purple in the figures, but separately study the 100 TeV jets with cuts of 30 GeV, 60 GeV and 100 GeV shown in the figures in red, green and blue respectively.

We begin by discussing what is by far the most uninteresting figure in this thesis (at

least at first glance!); fig. (6.1a) shows the differential distribution in the azimuthal separation of the two leading jets in p_T , $\Delta\phi_{j1,j2}$. It is clear that although the cross-section of the 100 TeV study with 100 GeV jets is significantly greater than that of the 7 TeV result the increase in cross-section is uniform throughout the range of $\Delta\phi_{j1,j2}$ - this is clear from the ratio. What makes the uninteresting fig. (6.1a) so interesting is that if QCD behaved exactly the same at 100 TeV as it did at 7 TeV we would expect all of the plots in this chapter to have a ratio line which was a perfectly straight line which would merely reflect the increase in cross-section we would expect to see. However, this turns out not to be the case. We can also see that as we increase the minimum p_\perp requirements in the 100 TeV study we see the cross-section decreases, as we would expect it to do, and we induce a more interesting behaviour in the ratio of the predictions to the 7 TeV line. This can be easily understood since as we force the jets to higher values of transverse momenta the back-to-back topology becomes more favourable and hence more of the total cross-section is found at $|\Delta\phi^{j1,j2}| \approx \pi$.

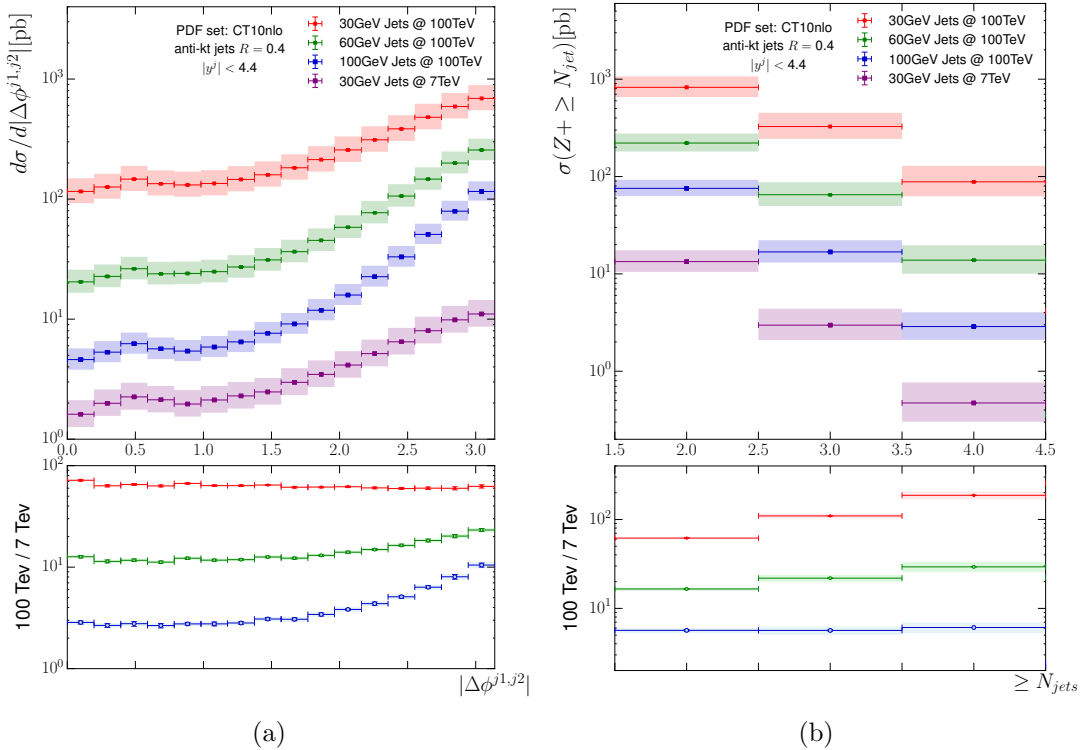


Figure 6.1: Fig. (6.1a) - The differential cross-section for Z/γ^* plus inclusive dijets as a function of the azimuthal separation of the dijet system. Fig. (6.1b) - The cross-section for Z/γ^* plus inclusive dijets as a function of the number of jets, N_{jet} .

Fig. (6.1b) shows the breakdown of the $Z/\gamma^* + \text{dijets}$ cross-section in terms of the inclusive number of jets, N_{jet} . Once again we see that the total integrated cross-section

grows as we go to higher energy but we also see, at least for the 30 GeV jets, that the relative contribution to the cross-section increases as we go to higher jet multiplicity. This is direct evidence that the convergence of the QCD perturbative expansion worsens as we go to higher centre-of-mass energies. Clearly then resummation effects such as those described by High Energy Jets become more important at a prospective FCC-hh machine and will need to be included not only in order to understand the QCD background well enough to extract and study new physics but also in order for precision tests of QCD. As we increase the jet cut to 60 GeV we see that the ratio with respect to the 7 TeV prediction becomes a little flatter and at a cut of 100 GeV the prediction is identical to that at 7 TeV save for an extra order of magnitude in the total cross-section. We can understand this by considering the effect of requiring high transverse momenta on rapidity and therefore rapidity gaps; it is energetically very expensive to emit high p_{\perp} radiation outside of the $y_j \approx 0$ region and therefore we can suppress the effects of the logarithmic corrections by limiting the access to phase-space where they are most important. It should be noted that although increasing our jet cuts to 100 GeV at a future machine will help suppress higher-order corrections and therefore improve the convergence of our α_s expansion it would *not* solve the problem - i.e. although the physics of 100 GeV jets at 100 TeV would be closer to that at 7 TeV (modulo an increased cross-section) that simply means we would be left with the *same problems*, detailed in previous chapters, as we have at our current generation of colliders. We also need to see the effect of the increased cut criteria on the distributions before selecting a value to actually propose. Fig (6.1a) and fig (6.1b) stand in stark contrast to one another - forgetting for a moment the added question of the correct choice of jet cut and just focussing on the comparison of 30 GeV jets at centre-of-mass energies of 7 TeV and 100 TeV - we see how important the issue of the convergence of the perturbative series is at an FCC; at this energy even sophisticated fixed-order schemes may not be able to describe data.

Fig (6.2a) shows the differential distribution in the absolute value of the rapidity span between the two leading jets in p_T , $\Delta y^{j1,j2}$. We see that as we go to large rapidity gaps between the dijets the relative increase in the cross-section grows by almost a factor of 10 as we pull the hardest two jets apart in rapidity. This is precisely the effect of the logarithmic corrections as we saw in chapters 3 and 4. Therefore to correctly describe QCD radiation patterns with large rapidity separations at an FCC we must capture at least these leading logarithms. As discussed above we see that requiring harder jets puts a limitation on the rapidity ranges available to radiation and therefore suppresses these effects - however, even when we consider only extremely hard jets above 100 GeV the enhancement is still visible and still leads to a two-fold increase in cross-section in

dijet events with a large rapidity span.

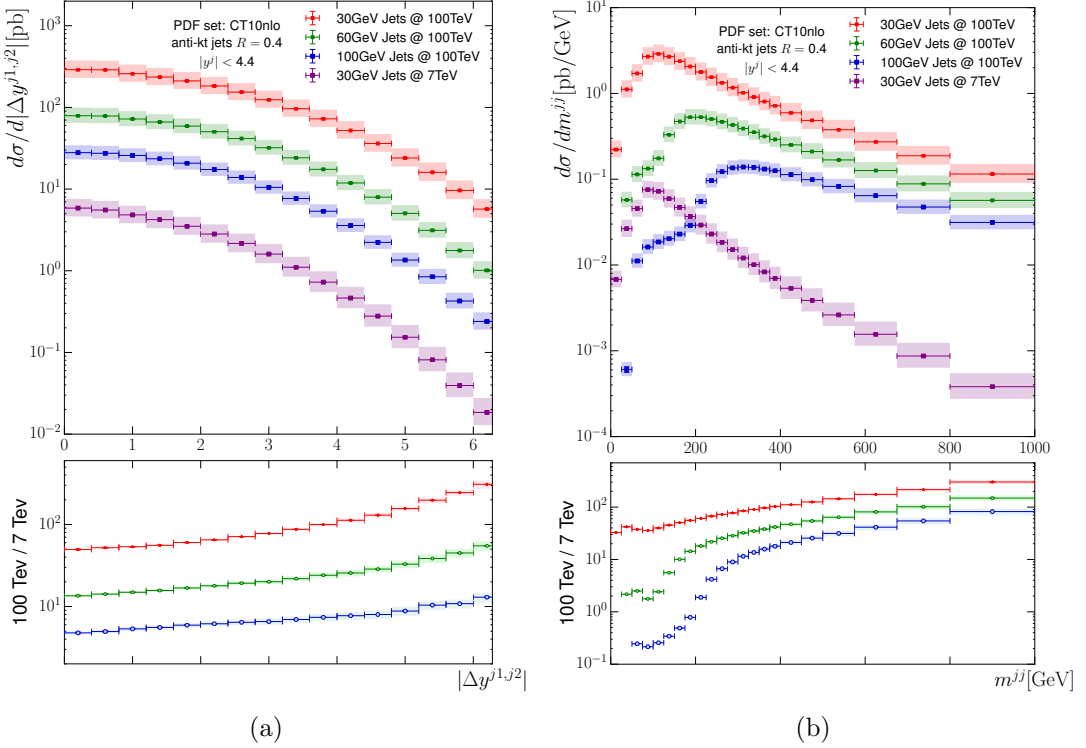


Figure 6.2: Fig. (6.2a) - The differential cross-section for Z/γ^* plus inclusive dijets as a function of the absolute value of the rapidity gap between the dijets, $\Delta y^{j1,j2}$. Fig. (6.2b) - The differential cross-section for Z/γ^* plus inclusive dijets as a function of the invariant mass of the dijets, m^{jj} .

In fig. (6.2b) we show the differential cross-section in the invariant mass of the two leading jets in p_T . Similarly to the discussion of fig. (6.2a) regions of large dijet invariant mass, m^{jj} , are exactly the regions we expect to have significant higher-order perturbative corrections at play. Indeed, at large invariant mass there is a factor $\mathcal{O}(10)$ increase compared to systems with small reconstructed mass when compared to the 7 TeV prediction. As we make the p_\perp jet cut more stringent we induce a large suppression at values of m^{jj} equal to or below the transverse momentum cut, this also shifts the invariant mass peak to higher values. But more importantly, we see the same behaviour at very large dijet mass as for the softer cut of 30 GeV.

Figs. (6.3a), (6.3b) and (6.3c) show the transverse momentum distributions for the second, third and fourth leading jet in p_\perp respectively. We observe that for all three variables there is a significant increase in the high p_\perp region at 100 TeV though here this can be understood not just in terms of an enhancement caused by logarithmic corrections but also simply because at a prospective FCC there would be extra energy

available to radiate jets with large transverse momentum. We see that as we move to 60 and even 100 GeV cuts there is a small effect in the cross-section but that the shape of the ratios with respect to the 7 TeV remains approximately unchanged. Note that the 100 GeV prediction is not present in fig. (6.3c) since all the events have been cut from the region in question.

Figs. (6.4a), (6.4b) and (6.4c) show the distributions in terms of the absolute value of the rapidity of the second, third and fourth leading jet in p_{\perp} . Once again we observe the expected behaviour with an increase in QCD radiation at large values for rapidity at 100 TeV relative to at 7 TeV clearly visible. In fig. (6.4a) we see that an increase in the jet p_{\perp} cut has little effect on the shape of the ratio lines since there is still ample energy to access those rarefied regions of very forward and backward phase-space. By contrast for figs. (6.4b) and (6.4c) we see that the higher jet cuts begin to take a toll on the jet activity at high values of $|y^j|$ and we see that the relative rates are suppressed in these regions.

In summary, we see that the theoretical ideas discussed in chapters 3, 4 and 5 and shown to be present in 7 and 8 TeV LHC data would be even more pervasive at a prospective high energy hadronic future circular collider. The regions of phase space, such as those with very high invariant mass or large rapidity gaps, which are poorly described by fixed-order schemes at the (relatively) moderate energy ranges of the LHC would be impossible to describe correctly upon raising the energy to 100 TeV. We see that it is possible to somewhat protect the convergence of the QCD perturbative expansion by enforcing stringent jet transverse momentum cuts and that doing so would still lead to a significant increase in the measured total cross-section in Z/γ^* plus dijet events. However, even minimum jet p_{\perp} cuts of 100 GeV are not sufficient to completely negate the effect of the large logarithmic corrections described in previous chapters.

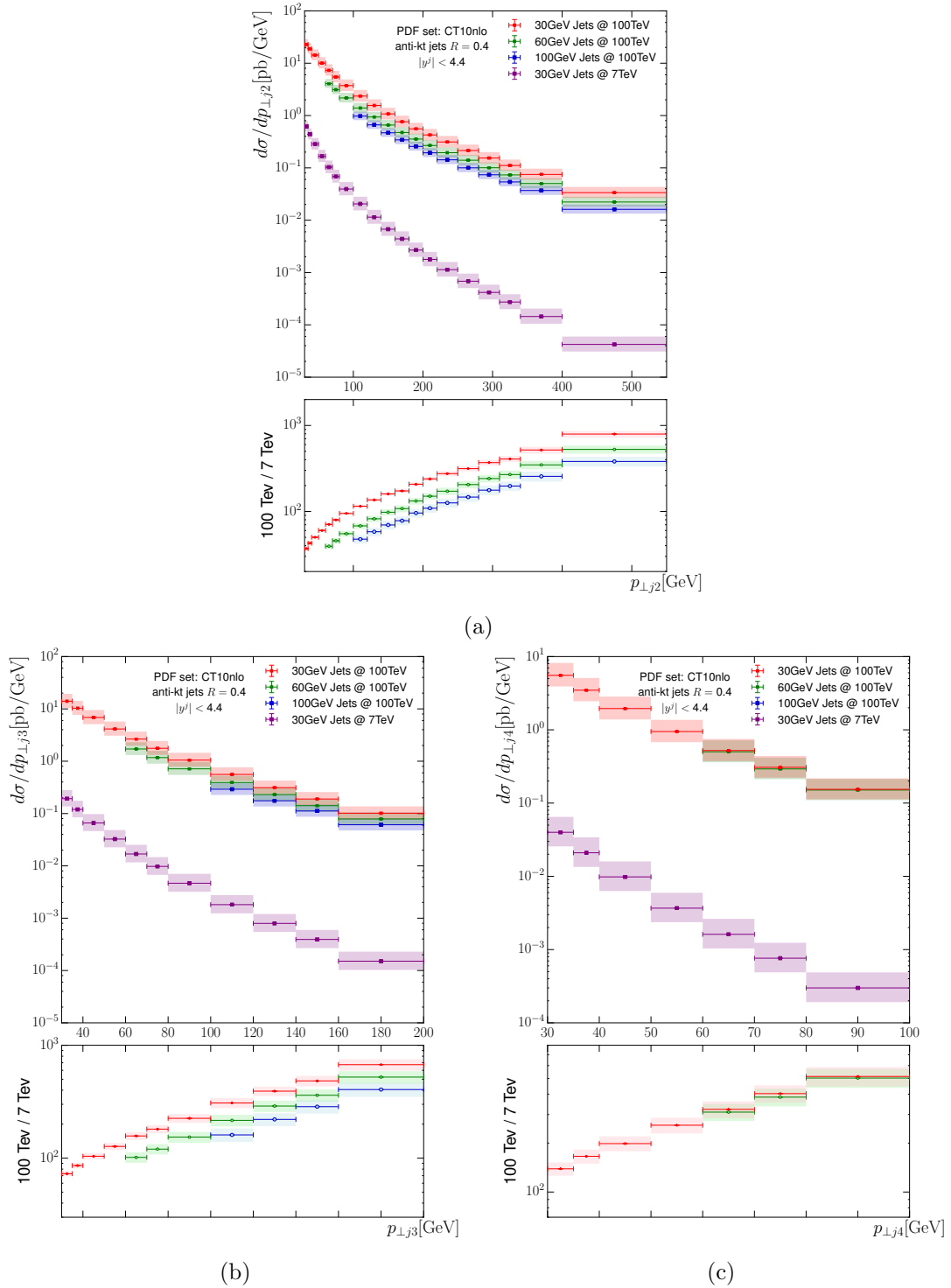


Figure 6.3: The differential cross-section for Z/γ^* plus inclusive dijets as a function of the transverse momentum of the first, second and third leading jets in p_T shown in fig. (6.3a), (6.3b) and (6.3c) respectively.

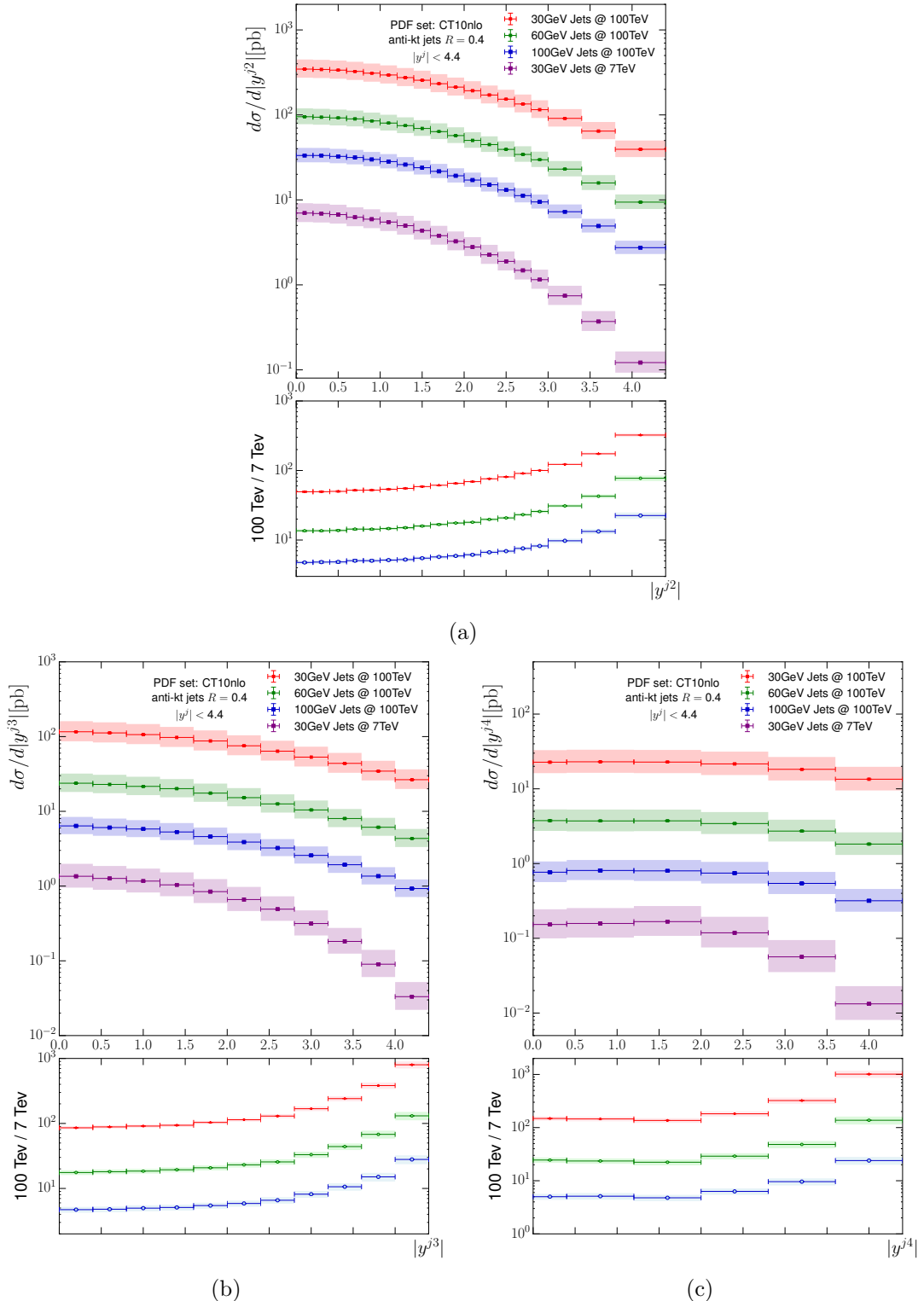


Figure 6.4: The differential cross-section for Z/γ^* plus inclusive dijets as a function of the absolute value of the rapidity of the first, second and third leading jets in rapidity shown in fig. (6.4a), (6.4b) and (6.4c) respectively.

Chapter 7

Conclusions and Outlook

In this thesis we have studied the perturbative description of Quantum Chromodynamics at colliders including the current Large Hadron Collider and a possible hadronic Future Circular Collider. In chapter 2 we gave an overview of a few key components required to perform the calculations seen in later sections. In particular, the question of the validity of truncating this expansion was raised since the presence of large logarithm corrections could mean that the convergence of any such truncated series would be in doubt.

In chapter 3 we specifically discussed the High Energy limit of QCD processes and how, in this limit, simple $2 \rightarrow 2$ scattering processes can be expressed as a contraction of currents over a pole in the momentum transfer variable, t . We saw that the next-to-leading order corrections to these simple processes contained an unexpected enhancement in exactly the form discussed earlier; a logarithm of s/t which would be large in the limit in question. The idea of t -channel dominance was generalised to more complicated processes using ideas from Regge theory. We were able to include extra real and virtual corrections by way of an effective vertex term and the Lipatov ansatz respectively. We concluded with a discussion of the High Energy Jets framework for describing all-order corrections to dijet events at hadronic colliders built upon these results; in particular we saw that in the High Energy limit we can describe processes in terms of contractions of ‘current’ and discussed the software set-up of High Energy Jets in the form of the publicly available HEJ package.

In chapter 4 we focussed on dijet events in the presence of a di-lepton pair produced by the decay of a Z^0 electroweak boson and an off-shell photon, γ^* . We were able to derive a current describing the Z^0 emission and saw that, for the two jet case, this agreed exactly with the leading order result. This was extended to include emission of a photon as well

as the resulting Z/γ^* interference. We saw that the interference term arising from the multiple possible boson emission sites neglected in previous work by the High Energy Jets collaboration was no longer small and, therefore, developed the tools to be able to include all possible emission sites for a boson *and* the interference terms. This result was then extended to arbitrarily high multiplicity final states through the aforementioned effective vertex. Due to the inclusion of the interference term it was necessary to develop a new regularisation for the Z/γ^* plus jets matrix elements - this was done and the resulting scheme was explicitly shown to be finite upon performing the phase space integration. The resulting regularised matrix element was shown to be independent of our phase-space regularising parameter, λ_{cut} . The procedure by which the HEJ matrix elements are matched to the leading-order exact matrix elements (provided by `MadGraph_aMC@NLO`) was then detailed and a summary of the computational challenges encountered throughout this work was presented. We concluded by comparing the HEJ Z/γ^* plus jets package to several recent experimental comparisons from both the ATLAS and CMS experiments. HEJ was seen to be in excellent agreement with the data in the regions where the logarithms we capture are significant. Any deviations are well understood.

In chapter 5 a study of dijet and gap events was presented. Four separate final states were considered in which the HEJ package interfaced with the parton shower `ARIADNE`, `HEJ+ARIADNE`, gave an excellent description of data throughout. We saw that partonic HEJ alone was not able to correctly describe the data highlighting the importance of the collinear logarithms added by the parton shower resummation. The fixed-order plus parton shower schemes also struggled to give good agreement with data indicating that, already at centre-of-mass energies of 7 TeV, it is necessary to resum the higher order logarithmic corrections included within the High Energy Jets framework.

In chapter 6 we presented an analysis of inclusive dijets in association with a Z/γ^* decaying to a di-lepton pair at 100 TeV. Three possible final state cuts were shown with possible minimum transverse momentum jet cuts of 30, 60 and 100 GeV. We saw that at 100 TeV the convergence of the fixed-order QCD perturbative series could be seriously undermined by the logarithmic corrections discussed in this thesis; this was somewhat neutralised by enforcing a jet cut of 100 GeV and even here we are only able to reduce the problems at 100 TeV to something comparable to those observed at 7 TeV. The regions of phase space where there were dijets spanning large rapidity intervals or with high invariant mass were seen to be most effected by the increased centre-of-mass energy.

To conclude, the effect of large logarithmic corrections on inclusive dijet events in

association with a Z/γ^* boson is seen to be large. Certainly a good description of data throughout the entire phase-space would not be possible without an attempt to capture at least the leading logarithmic term. More generally correctly describing QCD events at hadronic colliders is not possible without resumming the logarithms significant in the High Energy limit but this, alone, is not the full picture. We have seen throughout this work that, although the leading logarithmic terms are undoubtedly important, it is also necessary to contain as much of the terms described by current fixed-order approaches as possible. In the experimental studies of chapters 4 and 5 `HEJ`'s predictions have scale variation bands which are significantly larger than the fixed-order descriptions. This is well understood to be linked to our leading order matching - therefore the highest priority for High Energy Jets is to modify the matching scheme within the High Energy Jets framework must be improved to allow matching the next-to-leading order in α_s matrix elements. Unfortunately this is not as simple as just replacing our current `MadGraph_aMC@NLO` interface to instead call an NLO matrix element since this would cause us to double count contributions. Furthermore the collinear terms neglected by High Energy Jets's wide angle approximation must also be considered. We saw in chapter 5 that there are regions of phase space where the logarithms contributed by `ARIADNE` are necessary for us to describe data and that, once included, we gave the best description of data. To that end it would be excellent to interface `HEJ` with more of the current state-of-the-art parton showers such as `HERWIG` and `PYTHIA`.

Armed with next-to-leading order accuracy and a range of possible parton showers the description of data at 7, 8, 13 or even 100 TeV would be, I believe, excellent in many final states and troublesome regions of phase space currently of interest to experimental and theoretical physicists alike.

Appendix A

Next-to-leading order corrections for $\gamma^* \rightarrow q\bar{q}$

Here we present the full calculation for the next-to-leading order corrections (in α_s) to $\gamma^* \rightarrow q\bar{q}$ which was summarised in chapter 2. The diagrams contributing at NLO were depicted previously in fig (2.3).

The Leading Order Process

If we let the pair-produced quarks have charge $\pm Qe$ then we have:

$$\mathcal{A}_0 = -ieQ\bar{u}^{\lambda_2}(k_2)\gamma^\mu v^{\lambda_1}(k_1)\epsilon_\mu^r(p), \quad (\text{A.1})$$

where we have used the QED Feynman rule for a quark-antiquark-photon vertex: $iQe\gamma^\mu$, the λ_i 's are the spins of the quarks, r is the polarisation of the incoming photon and $p = k_1 + k_2$ is the momentum carried by the incoming photon. To proceed we can square and since we are typically interested in unpolarised calculations we perform a sum over all polarisations, spins and colours:

$$|\overline{\mathcal{A}_0}|^2 = 3 \sum_{\forall \lambda, r} e^2 Q^2 [\bar{u}^{\lambda_2}(k_2)\gamma^\mu v^{\lambda_1}(k_1)][\bar{v}^{\lambda_1}(k_1)\gamma^\nu v^{\lambda_2}(k_1)]\epsilon_\mu^r(p)\epsilon_{*\mu}^r(p). \quad (\text{A.2})$$

We now use Casimir's trick [54] to convert this spinor string into a trace, using the replacements $\sum_r \epsilon_\mu^r \epsilon_{*\nu}^r = -g_{\mu\nu}$ and the completeness conditions for spinors:

$$|\overline{\mathcal{A}_0}|^2 = -e^2 Q^2 \text{Tr}[\not{k}_2 \gamma^\mu \not{k}_1 \gamma_\mu], \quad (\text{A.3})$$

where we have used the high energy limit to discard the quark mass terms. This trace can be evaluated in arbitrary dimensions to give, in the high energy limit:

$$|\overline{\mathcal{A}_0}|^2 = 6e_d^2 Q^2 s(d-2), \quad (\text{A.4})$$

where we have defined the usual Mandelstam variable $s = (k_1 + k_2)^2 = 2k_1 \cdot k_2$ and define $e_d^2 = e^2 \mu^{4-d}$ where μ has units of mass in order to make the coupling e dimensionless. To find the leading order cross-section we divide by the particle flux and multiply by the two particle phase space which is given by:

$$\int d^{2d-2} R_2 = 2^{1-d} \pi^{\frac{d}{2}-1} \frac{\Gamma(\frac{d}{2}-1)}{\Gamma(d-2)} s^{\frac{d-4}{2}}, \quad (\text{A.5})$$

where R_2 is the two particle phase space in d dimensions. Combining these factors and defining $\alpha_e = \frac{e^2}{4\pi}$:

$$\begin{aligned} \sigma_0 &= 3 \cdot 2^{2-d} \pi^{1-\frac{d}{2}} \frac{\Gamma(\frac{d}{2}-1)}{\Gamma(d-2)} s^{\frac{d-4}{2}} 4\pi \alpha \mu^{d-4} Q^2 s(d-2) \frac{1}{2s} \\ &= 3\alpha Q^2 \left(\frac{s}{4\pi \mu^2} \right)^{\frac{d}{2}-2} \left(\frac{d}{2}-1 \right) \frac{\Gamma(\frac{d}{2}-1)}{\Gamma(d-2)}. \end{aligned} \quad (\text{A.6})$$

and finally using $x\Gamma(x) = \Gamma(x+1)$ we get:

$$\sigma_0 = 3\alpha Q^2 \frac{\Gamma(\frac{d}{2})}{\Gamma(d-2)} \left(\frac{s}{4\pi \mu^2} \right)^{\frac{d}{2}-2}. \quad (\text{A.7})$$

It is important to note that in the limit $\epsilon \rightarrow 0$ (i.e. $d \rightarrow 4$) the Born cross-section remains finite.

The Virtual $\mathcal{O}(\alpha_s)$ Corrections

The virtual correction graphs are shown in figs. (2.3b), (2.3c) and (2.3d). We will begin by calculating the second term in eqn. (2.44). Using the Feynman rules we have:

$$\mathcal{A}_v = \int \frac{d^d k}{(2\pi)^d} \bar{u}^{\lambda_2}(k_2) (-ig_s \mu^\epsilon \gamma^\alpha T_{ij}^a) \frac{i(\not{k}_1 + \not{k})}{(k_1 + k)^2} (-ieQ \gamma^\mu) \frac{i(\not{k}_2 - \not{k})}{(k_2 - k)^2} (-g_s \mu^\epsilon \gamma^\beta T_{ij}^a) \epsilon_\mu^r(p) \frac{-i}{k^2} \left(g_{\alpha\beta} + (1 - \xi) \frac{k^\alpha k^\beta}{k^2} \right) v^{\lambda_1}(k_1).$$

$$\mathcal{A}_v = -ig_s^2 e Q \mu^{2\epsilon} \text{Tr}(T^a T^a) \bar{u}^{\lambda_2}(k_2) \int \frac{d^d k}{(2\pi)^d} \frac{\mathcal{N}_1(k_1, k_2, k)}{k^2 (k_1 + k)^2 (k_2 - k)^2} v^{\lambda_2}(k_2),$$

where the numerator of the fraction is given by:

$$\mathcal{N}_1(k_1, k_2, k) = \gamma^\alpha(\not{k}_1 + \not{k}) \gamma^\mu(\not{k}_2 - \not{k}) \gamma_\beta \left(g^{\alpha\beta} + (1 - \xi) \frac{k^\alpha k^\beta}{k^2} \right). \quad (\text{A.9})$$

From eqn. (2.44) we see we need $\mathcal{A}_0^* \mathcal{A}_v$:

$$\mathcal{A}_0^* \mathcal{A}_v = g_s^2 e^2 Q^2 \text{Tr}(T^a T^a) [\bar{v}^{\lambda_1}(k_1) \gamma^\nu u(k_2)] \quad (\text{A.10})$$

$$\left[\bar{u}^{\lambda_2}(k_2) \int \frac{d^d k}{(2\pi)^d} \frac{\mathcal{N}_1(k_1, k_2, k)}{k^2 (k_1 + k)^2 (k_2 - k)^2} v^{\lambda_1}(k_1) \right] \epsilon_\mu^r(p) \epsilon_{*\nu}^r(p). \quad (\text{A.11})$$

Now performing the spin/polarisation/colour sum and average gives:

$$\overline{\mathcal{A}_0^* \mathcal{A}_v} = -\frac{g_s^2 e^2 Q^2}{2} \int \frac{d^d k}{(2\pi)^d} \frac{\mathcal{N}_2(k_1, k_2, k)}{k^2 (k_1 + k)^2 (k_2 - k)^2}, \quad (\text{A.12})$$

where:

$$\mathcal{N}_2(k_1, k_2, k) = \text{Tr}[\not{k}_1 \gamma_\alpha(\not{k}_1 + \not{k}) \gamma_\mu(\not{k}_2 - \not{k}) \gamma_\beta \not{k}_2 \gamma^\mu] \left(g^{\alpha\beta} + (1 - \xi) \frac{k^\alpha k^\beta}{k^2} \right). \quad (\text{A.13})$$

Before we can proceed any further we must evaluate the trace term in eqn. (A.13). As mentioned briefly in section 2.3.3 this is not as easy as it seems because, although the Dirac matrices still satisfy the Clifford algebra, the various identities for their

contractions and traces change when we are in d dimensions. Two useful examples are shown below:

$$g_{\mu\nu}g^{\mu\nu} = d \quad (\text{A.14a})$$

$$\gamma^\mu\gamma_\nu\gamma_\mu = (d-2)\gamma_n u \quad (\text{A.14b})$$

Using the FORM package [62] to perform the two trace terms present gives:

$$\begin{aligned} \text{Tr}[\not{k}_1\gamma_\alpha(\not{k}_1 + \not{k})\gamma_\mu(\not{k}_2 - \not{k})\gamma^\alpha\not{k}_2\gamma^\mu] &= s[s(8-4d) + \frac{(k_1 \cdot k)(k_2 \cdot k)}{s}(32-16d) \\ &\quad - (16-8d)(k_1 \cdot k - k_2 \cdot k) + k^2(16-12d+2d^2)], \end{aligned} \quad (\text{A.15})$$

and,

$$\begin{aligned} \text{Tr}[\not{k}_1\gamma_\alpha(\not{k}_1 + \not{k})\gamma_\mu(\not{k}_2 - \not{k})\gamma_\beta\not{k}_2\gamma^\mu]k^\alpha k^\beta &= s[(k_1 \cdot k)(k_2 \cdot k)(16-8d) \\ &\quad + k^2(8-4d)(k_2 \cdot k - k_1 \cdot k) - k^4(4-2d)], \end{aligned} \quad (\text{A.16})$$

where $s = 2k_1 \cdot k_2$ and we have used the on-shell relations. After factorising the terms quadratic in d and combining the two trace terms we arrive at:

$$\overline{\mathcal{A}_0^*\mathcal{A}_v} = -4s \left(\frac{d}{2} - 1 \right) \frac{g_s^2 e^2 Q^2}{2} \int \frac{d^d k}{(2\pi)^d} \frac{\mathcal{N}_3(k_1, k_2, k)}{k^2(k_1 + k)^2(k_2 - k)^2}, \quad (\text{A.17})$$

where:

$$\begin{aligned} \mathcal{N}_3(k_1, k_2, k) &= -2s + \frac{8k \cdot k_1 k \cdot k_2}{s} + (6+2\xi)(k \cdot k_1 - k \cdot k_2) + k^2(d-4) \\ &\quad - 4(1-\xi) \frac{k \cdot k_1 k \cdot k_2}{k^2} - (1-\xi)k^2. \end{aligned} \quad (\text{A.18})$$

Combining this with the particle flux and the two particle phase space we can write an expression for the vertex corrected cross-section. Once again we scale the couplings

such that they remain dimensionless by defining $g_d^2 = g_s^2 \mu^{2-\frac{d}{2}}$:

$$\begin{aligned}\sigma_v &= -4s \left(\frac{d}{2} - 1 \right) \frac{g_d^2 \mu^{2-\frac{d}{2}} e^2 Q^2}{4s} 2^{1-d} \pi^{\frac{d}{2}-1} \frac{\Gamma(\frac{d}{2}-1)}{\Gamma(d-2)} s^{\frac{d-4}{2}} \int \frac{d^d k}{(2\pi)^d} \frac{\mathcal{N}_3(k_1, k_2, k)}{k^2(k_1+k)^2(k_2-k)^2}, \\ \Rightarrow \sigma_v &= -g_d^2 \mu^{2-\frac{d}{2}} Q^2 4\pi \alpha \mu^{4-d} 2^{1-d} \pi^{\frac{d}{2}-1} \frac{\Gamma(\frac{d}{2})}{\Gamma(d-2)} s^{\frac{d-4}{2}} \int \frac{d^d k}{(2\pi)^d} \frac{\mathcal{N}_3(k_1, k_2, k)}{k^2(k_1+k)^2(k_2-k)^2}, \\ \Rightarrow \sigma_v &= -\frac{4\sigma_0}{3} g_d^2 \mu^{2-\frac{d}{2}} \int \frac{d^d k}{(2\pi)^d} \frac{\mathcal{N}_3(k_1, k_2, k)}{k^2(k_1+k)^2(k_2-k)^2},\end{aligned}$$

where we have expressed the virtual rate as a multiplicative correction to the Born level rate. We must now use the Feynman parametrisation to re-express the product of propagators as a sum by introducing new integration variables. Using:

$$\frac{1}{ab} = \int_0^1 dy \frac{1}{(ay + b(1-y))^2}, \quad (\text{A.20})$$

we have:

$$\sigma_v = -\frac{4\sigma_0}{3} g_d^2 \mu^{2-\frac{d}{2}} \int \frac{d^d k}{(2\pi)^d} \int_0^1 dy \frac{\mathcal{N}_3(k_1, k_2, k)}{(k^2 - 2k \cdot k_y)^2 k^2}, \quad (\text{A.21})$$

where $k_y = yk_1 - (1-y)k_2$. Examining now the integrand we see there are two different k dependences and so we partition the terms as follows:

$$\sigma_v = -\frac{4\sigma_0}{3} g_d^2 \mu^{2-\frac{d}{2}} \int \frac{d^d k}{(2\pi)^d} \int_0^1 dy \left(\frac{\mathcal{N}_3^{(1)}(k_1, k_2, k)}{(k^2 - 2k \cdot k_y)^2 k^2} + \frac{\mathcal{N}_3^{(2)}(k_1, k_2, k)}{(k^2 - 2k \cdot k_y)^2 k^4} \right), \quad (\text{A.22})$$

where,

$$\mathcal{N}_3^{(1)}(k_1, k_2, k) = -2s + \frac{8k \cdot k_1 k \cdot k_2}{s} + (6+2\xi)(k \cdot k_1 - k \cdot k_2) + k^2(d-4) - (1-\xi)k^2, \quad (\text{A.23})$$

and

$$\mathcal{N}_3^{(2)}(k_1, k_2, k) = -4(1-\xi)k \cdot k_1 k \cdot k_2. \quad (\text{A.24})$$

Differentiating eqn. (A.20) with respect to a and b we get the following useful

parametrisations:

$$\begin{aligned}\frac{1}{a^2 b} &= \int_0^1 dx \frac{2x}{(ax + b(1-x))^3}, \\ \frac{1}{a^2 b^2} &= \int_0^1 dx \frac{6x(1-x)}{(ax + b(1-x))^4}.\end{aligned}\tag{A.25}$$

and taking $a = k^2 - 2k \cdot k_y$ and $b = k^2$, simplifying the denominators and performing a change of variables $K = k - xp_y$ yields:

$$\sigma_v = -\frac{4\sigma_0}{3} g_d^2 \mu^{2-\frac{d}{2}} \int \frac{d^d K}{(2\pi)^d} \int_0^1 dy \int_0^1 dx \left(\frac{2x \mathcal{N}_3^{(1)}(k_1, k_2, K + xk_y)}{(K^2 - C)^3} + \frac{6x(1-x) \mathcal{N}_3^{(2)}(k_1, k_2, K + xk_y)}{(K^2 - C)^4} \right),\tag{A.26}$$

where $C = x^2 p_y^2$. The change of variables modifies the numerator terms to:

$$\begin{aligned}\mathcal{N}_3^{(1)}(k_1, k_2, K + xk_y) &= -2s + K^2 \left(\frac{4}{d} + d - 5 + \xi \right) \\ &\quad - (3 + \xi)xs + x^2 ys(1-y)(3-d-\xi),\end{aligned}\tag{A.27a}$$

$$\mathcal{N}_3^{(2)}(k_1, k_2, K + xk_y) = (1 - \xi) \left(x^2 ys^2(1-y) - \frac{2s}{d} K^2 \right).\tag{A.27b}$$

We can now perform the integrations over K with the aid of the following result:

$$\int \frac{d^d K}{(2\pi)^d} \frac{(K^2)^m}{(K^2 - C)^n} = \frac{i(-1)^{m-n}}{(4\pi)^{\frac{d}{2}}} C^{m-n+\frac{d}{2}} \frac{\Gamma(m + \frac{d}{2}) \Gamma(n - m - \frac{d}{2})}{\Gamma(\frac{d}{2}) \Gamma(n)}.\tag{A.28}$$

Looking at the K structure of eqs. (A.27) we can see that there are going to be four forms of eqn. (A.28) needed in this calculation. I will not show the calculation for every integral but will show one as an example of how the calculations can proceed. Consider the contribution of the first term of eqn. (A.27a):

$$\begin{aligned} I &= -4s \int_0^1 dy \int_0^1 dxx \int \frac{d^d K}{(2\pi)^d} \frac{1}{(K^2 - C)^3} \\ &= 4si \int_0^1 dy \int_0^1 dxx (4\pi)^{-\frac{d}{2}} C^{-3+\frac{d}{2}} \frac{\Gamma(\frac{d}{2})\Gamma(3-\frac{d}{2})}{\Gamma(\frac{d}{2})\Gamma(3)}. \end{aligned} \quad (\text{A.29})$$

From above we see that $C = x^2 k_y = -x^2 y(1-y)s$ and so:

$$I = 4si(4\pi)^{-\frac{d}{2}} \Gamma(3 - \frac{d}{2})(-s)^{-3+\frac{d}{2}} \int_0^1 dy \int_0^1 dxx^{-5+d} y^{(-2+\frac{d}{2})-1} (1-y)^{(-2+\frac{d}{2})-1}, \quad (\text{A.30})$$

Therefore:

$$I = 4si(4\pi)^{-\frac{d}{2}} \Gamma\left(3 - \frac{d}{2}\right) (-s)^{-3+\frac{d}{2}} \frac{1}{d-4} \frac{\Gamma^2(\frac{d}{2}-2)}{\Gamma(d-4)}. \quad (\text{A.31})$$

Choosing $d = 4 + \epsilon$ (with the intention of taking the limit $\epsilon \rightarrow 0$ once it is safe to do so), and manipulating the gamma functions to expose the pole structure gives:

$$-4 \int_0^1 dy \int_0^1 dxx \int \frac{d^d K}{(2\pi)^d} \frac{1}{(K^2 - C)^3} = 4(-s)^{\frac{\epsilon}{2}} i(4\pi)^{-2-\frac{\epsilon}{2}} \frac{4}{\epsilon^2} \frac{\Gamma(1-\frac{\epsilon}{2})\Gamma^2(1+\frac{\epsilon}{2})}{\Gamma(1+\epsilon)}, \quad (\text{A.32})$$

which is clearly divergent in the limit $\epsilon \rightarrow 0$. The other integrals follow similarly and the combined result can be expressed as:

$$\sigma_v = \frac{2\alpha_s}{3\pi} \sigma_0 \left(\frac{s}{4\pi\mu^2} \right)^{\frac{\epsilon}{2}} \frac{\Gamma(1-\frac{\epsilon}{2})\Gamma^2(1+\frac{\epsilon}{2})}{\Gamma(1+\epsilon)} \left(-\frac{8}{\epsilon^2} + \frac{6}{\epsilon} - \frac{8+4\epsilon}{1+\epsilon} \right), \quad (\text{A.33})$$

where we have used $\alpha_s = \frac{g_a^2}{4\pi}$. Expanding the product of gamma matrices for $\epsilon \rightarrow 0$ gives:

$$\frac{\Gamma(1-\frac{\epsilon}{2})\Gamma^2(1+\frac{\epsilon}{2})}{\Gamma(1+\epsilon)} = \frac{\gamma_E}{2}\epsilon + \left(\frac{\gamma_E^2}{8} - \frac{\pi^2}{48} \right) \epsilon^2 + \mathcal{O}(\epsilon^3), \quad (\text{A.34a})$$

$$\left(\frac{s}{4\pi\mu^2} \right)^{\frac{\epsilon}{2}} = e^{\ln\left(\frac{s}{4\pi\mu^2}\right)^{\frac{\epsilon}{2}}} = e^{\frac{\epsilon}{2}\ln\left(\frac{s}{4\pi\mu^2}\right)} = 1 + \frac{\epsilon}{2}\ln\left(\frac{s}{4\pi\mu^2}\right) + \mathcal{O}(\epsilon^2), \quad (\text{A.34b})$$

where γ_E is Euler's constant. Finally then we have:

$$\sigma_v = \frac{2\alpha_s}{3\pi} \sigma_0 \left[-\frac{8}{\epsilon^2} + \frac{1}{\epsilon} (6 - 4\gamma_E - 4L) + \gamma_E(3 - \gamma_E) - 8 + \frac{\pi^2}{6} + \pi^2 - L^2 - (2\gamma_E - 3)L \right], \quad (\text{A.35})$$

where $L = \ln\left(\frac{s}{4\pi\mu^2}\right)$. We can now see that the result for the vertex correction is gauge independent as the ξ dependence has completely cancelled. We also see that the parameter introduced to fix the coupling to be dimensionless appears in the final result; this is often the case when using dimensional regularisation and the modified minimal subtraction renormalisation scheme.

The Real $\mathcal{O}(\alpha_s)$ Corrections

The real gluon emission diagrams which contribute to the $\mathcal{O}(\alpha_s)$ corrections are figs. (2.3e) and (2.3f). These diagrams have an indistinguishable final state and so the real contribution, \mathcal{A}_r , will be of the form:

$$|\mathcal{A}_r|^2 = |\mathcal{A}_{left} + \mathcal{A}_{right}|^2 = |\mathcal{A}_{left}|^2 + |\mathcal{A}_{right}|^2 + 2\mathcal{A}_{left}\mathcal{A}_{right}^*, \quad (\text{A.36})$$

where \mathcal{A}_{left} and \mathcal{A}_{right} refer to figs. (2.3e) and (2.3f) respectively and are given by:

$$\mathcal{A}_{left} = -Q e i g_s T_{ij}^a \bar{u}(k_2) \gamma^\mu \frac{\not{k}_1 + \not{k}}{(k_1 + k)^2} \gamma^\nu v(k_1) \epsilon_\nu \eta_\mu, \quad (\text{A.37a})$$

$$\mathcal{A}_{right} = -Q e i g_s T_{ij}^a \bar{u}(k_2) \gamma^\nu \frac{\not{k}_2 + \not{k}}{(k_2 + k)^2} \gamma^\mu v(k_1) \epsilon_\nu \eta_\mu. \quad (\text{A.37b})$$

In the calculation of the terms of eqn. (2.44) it will be useful to write the energy fractions for each particle as $x_i = \frac{2E_i}{\sqrt{s}}$ (where $i = 1$ is the external antiquark, $i = 2$ is the antiquark and $i = 3$ is the external gluon). In terms of these invariants the contraction of any two external particles simplifies to $p_i \cdot p_j = \frac{1}{2}s(1 - x_k)$ which (since we are still assuming our quarks can be taken to be massless) gives a simple expression for the Mandelstam variables. Evaluating the modulus squared terms gives:

$$|\mathcal{A}_{left}|^2 = \frac{Q^2 e^2 g_s^2}{(k_1 + k)^4} \text{Tr}(T^a T^a) \text{Tr}(\not{k}_2 \gamma^\mu (\not{k}_1 + \not{k}) \gamma^\nu \not{k}_1 \gamma_\nu (\not{k}_1 + \not{k}) \gamma_\mu), \quad (\text{A.38a})$$

$$|\mathcal{A}_{right}|^2 = \frac{Q^2 e^2 g_s^2}{(k_2 + k)^4} \text{Tr}(T^a T^a) \text{Tr}(\not{k}_2 \gamma^\nu (\not{k}_2 + \not{k}) \gamma^\mu \not{k}_2 \gamma_\mu (\not{k}_2 + \not{k}) \gamma_\nu), \quad (\text{A.38b})$$

$$\mathcal{A}_{left} \mathcal{A}_{right}^* = \frac{Q^2 e^2 g_s^2}{(k_2 + k)^2 (k_1 + k)^2} \text{Tr}(T^a T^a) \text{Tr}(\not{k}_2 \gamma^\mu (\not{k}_1 + \not{k}) \gamma^\nu \not{k}_1 \gamma_\mu (\not{k}_2 + \not{k}) \gamma_\nu). \quad (\text{A.38c})$$

Evaluating the trace terms and rearranging in terms of the energy fractions gives:

$$|\mathcal{A}_{left}|^2 = 32 Q^2 e^2 g_s^2 \left(1 + \frac{\epsilon}{2}\right)^2 \frac{1 - x_1}{1 - x_2}, \quad (\text{A.39a})$$

$$|\mathcal{A}_{right}|^2 = 32 Q^2 e^2 g_s^2 \left(1 + \frac{\epsilon}{2}\right)^2 \frac{1 - x_2}{1 - x_1}, \quad (\text{A.39b})$$

$$2\mathcal{A}_{left} \mathcal{A}_{right}^* = 64 Q^2 e^2 g_s^2 \left(1 + \frac{\epsilon}{2}\right) \left(-\frac{\epsilon}{2} - 2 \frac{1 - x_3}{(1 - x_1)(1 - x_2)}\right). \quad (\text{A.39c})$$

Summing these expressions gives:

$$|\mathcal{A}_r|^2 = 32 Q^2 e^2 g_s^2 \left[\left(1 + \frac{\epsilon}{2}\right)^2 \frac{x_1^2 + x_2^2}{(1 - x_2)(1 - x_1)} + \epsilon \left(1 + \frac{\epsilon}{2}\right) \frac{2 - 2x_1 - 2x_2 + x_1 x_2}{(1 - x_2)(1 - x_1)} \right]. \quad (\text{A.40})$$

As with the virtual contributions, we are interested in the observable cross-section and so we must include the phase space factor for a three particle final state. Unlike the two particle phase space calculation the three particle phase space, $\int d^{3d-3}R_3$, cannot be integrated completely and we are left with a differential in terms of the energy fractions defined above:

$$\frac{d^2 R_3}{dx_1 dx_2} = \frac{s}{16(2\pi)^3} \left(\frac{s}{4\pi}\right)^\epsilon \frac{1}{\Gamma(2+\epsilon)} \left(\frac{1-z^2}{4}\right)^{\frac{\epsilon}{2}} x_1^\epsilon x_2^\epsilon, \quad (\text{A.41})$$

where $z = 1 - 2 \frac{1-x_1-x_2}{x_1 x_2}$. Combining eqs. (A.40) and (A.41) with a flux factor gives:

$$\frac{d^2 \sigma_r}{dx_1 dx_2} = \frac{2 Q^2 e^2 g_s^2 F(x_1, x_2; \epsilon)}{\pi} \left(\frac{s}{4\pi}\right)^\epsilon \frac{1}{\Gamma(2+\epsilon)} \left(\frac{1-z^2}{4}\right)^{\frac{\epsilon}{2}} x_1^\epsilon x_2^\epsilon, \quad (\text{A.42})$$

where we define $F(x_1, x_2; \epsilon)$ as the algebraic factor in square brackets from eqn. (A.40). Switching to a dimensionless coupling and introducing α_s as above comparing with the Born cross-section in eqn. (A.7) this can be written as:

$$\frac{d^2\sigma_r}{dx_1 dx_2} = \frac{2\alpha_s \sigma_0}{3\pi} F(x_1, x_2; \epsilon) \left(\frac{s}{4\pi\mu^2} \right)^{\frac{\epsilon}{2}} \frac{1}{\Gamma(2 + \frac{\epsilon}{2})} \left(\frac{1 - z^2}{4} \right)^{\frac{\epsilon}{2}} x_1^\epsilon x_2^\epsilon. \quad (\text{A.43})$$

Integrating over the allowed region of x_1 and x_2 gives:

$$\sigma_r = \frac{2\alpha_s \sigma_0}{3\pi} \left(\frac{s}{4\pi\mu^2} \right)^{\frac{\epsilon}{2}} \frac{1}{\Gamma(2 + \frac{\epsilon}{2})} \int_0^1 dx_1 x_1^\epsilon \int_{1-x_1}^1 x_2^\epsilon \left(\frac{1 - z^2}{4} \right)^{\frac{\epsilon}{2}} F(x_1, x_2; \epsilon). \quad (\text{A.44})$$

We can define a change of variables $x_2 = 1 - vx_1$ to decouple these integrals and therefore:

$$\sigma_r = \frac{2\alpha_s \sigma_0}{3\pi} \left(\frac{s}{4\pi\mu^2} \right)^{\frac{\epsilon}{2}} \frac{\Gamma^2(1 + \frac{\epsilon}{2})}{\Gamma(1 + \frac{3\epsilon}{2})} \left[\frac{8}{\epsilon^2} - \frac{6}{\epsilon} + \frac{19}{2} \right]. \quad (\text{A.45})$$

Further expanding the Gamma functions gives:

$$\sigma_r = \frac{2\alpha_s}{3\pi} \sigma_0 \left[\frac{8}{\epsilon^2} + \frac{1}{\epsilon} (-6 + 4\gamma_E + 4L) - \gamma_E(3 - \gamma_E) - \frac{57}{6} + \frac{7\pi^2}{6} + L^2 + (2\gamma_E - 3)L \right].$$

As in the case of the virtual corrections this is divergent in the limit $\epsilon \rightarrow 0$ and exhibits a residual dependence on μ .

Cancellation of divergences

Having now found the vertex corrections and the real corrections up to $\mathcal{O}(\epsilon^2)$ we can write the next-to-leading order cross-section by simply summing the two:

$$\sigma_{NLO} = \sigma_r + \sigma_v = \frac{\alpha_s}{\pi} \sigma_0. \quad (\text{A.46})$$

So the total cross-section to next-to-leading order accuracy is:

$$\sigma = \sigma_0 \left(1 + \frac{\alpha_s}{\pi} \right) + \mathcal{O}(\alpha_s^2). \quad (\text{A.47})$$

The fact that the infrared divergences in both the real and virtual emission NLO diagrams cancel is an example of the KLN theorem [61] which states that the Standard Model is completely free of infrared divergences at all orders.

Bibliography

- [1] AAD, G., ET AL. Measurement of dijet production with a veto on additional central jet activity in pp collisions at $\sqrt{s} = 7$ TeV using the ATLAS detector. *JHEP* 09 (2011), 053.
- [2] AAD, G., ET AL. Measurement of the production cross section of jets in association with a Z boson in pp collisions at $\sqrt{s} = 7$ TeV with the ATLAS detector. *JHEP* 1307 (2013), 032.
- [3] AAD, G., ET AL. A measurement of the ratio of the production cross sections for W and Z bosons in association with jets with the ATLAS detector. *Eur. Phys. J. C74*, 12 (2014), 3168.
- [4] AAD, G., ET AL. Measurements of jet vetoes and azimuthal decorrelations in dijet events produced in pp collisions at $\sqrt{s} = 7$ TeV using the ATLAS detector. *Eur. Phys. J. C74*, 11 (2014), 3117.
- [5] AAD, G., ET AL. Measurements of the W production cross sections in association with jets with the ATLAS detector. *Eur. Phys. J. C75*, 2 (2015), 82.
- [6] AAD, G., ET AL. Search for high-mass diboson resonances with boson-tagged jets in proton-proton collisions at $\sqrt{s} = 8$ TeV with the ATLAS detector. *JHEP* 12 (2015), 055.
- [7] ABAZOV, V. M., ET AL. Studies of W boson plus jets production in $p\bar{p}$ collisions at $\sqrt{s} = 1.96$ TeV. *Phys. Rev. D88*, 9 (2013), 092001.
- [8] ABRAMOWICZ, H., ET AL. Physics at the CLIC e+e- Linear Collider – Input to the Snowmass process 2013. In *Community Summer Study 2013: Snowmass on the Mississippi (CSS2013) Minneapolis, MN, USA, July 29-August 6, 2013* (2013).
- [9] ALIOLI, S. Matching NLO QCD to Monte Carlo showers and POWHEG. *PoS LL2012* (2012), 056.
- [10] ALIOLI, S., ANDERSEN, J. R., OLEARI, C., RE, E., AND SMILLIE, J. M. Probing higher-order corrections in dijet production at the LHC. *Phys. Rev. D85* (2012), 114034.
- [11] ALIOLI, S., NASON, P., OLEARI, C., AND RE, E. Vector boson plus one jet production in POWHEG. *JHEP* 01 (2011), 095.
- [12] ALWALL, J., ET AL. Comparative study of various algorithms for the merging of parton showers and matrix elements in hadronic collisions. *Eur. Phys. J. C53* (2008), 473–500.
- [13] ALWALL, J., FREDERIX, R., FRIXIONE, S., HIRSCHI, V., MALTONI, F., MATTELAER, O., SHAO, H. S., STELZER, T., TORRIELLI, P., AND ZARO, M. The automated computation of tree-level and next-to-leading order differential cross sections, and their matching to parton shower simulations. *JHEP* 07 (2014), 079.
- [14] ALWALL, J., HERQUET, M., MALTONI, F., MATTELAER, O., AND STELZER, T. MadGraph 5 : Going Beyond. *JHEP* 06 (2011), 128.

- [15] ANASTASIOU, C., DUHR, C., DULAT, F., HERZOG, F., AND MISTLBERGER, B. Higgs Boson Gluon-Fusion Production in QCD at Three Loops. *Phys. Rev. Lett.* **114** (2015), 212001.
- [16] ANDERSEN, J. A. Qcd at high energy. <https://conference.ippp.dur.ac.uk/event/514/contribution/6/material/slides/0.pdf>, 2016. [Online; accessed 10-03-2016].
- [17] ANDERSEN, J. R., DEL DUCA, V., AND WHITE, C. D. Higgs Boson Production in Association with Multiple Hard Jets. *JHEP* **0902** (2009), 015.
- [18] ANDERSEN, J. R., HAPOLA, T., AND SMILLIE, J. M. W Plus Multiple Jets at the LHC with High Energy Jets. *JHEP* **1209** (2012), 047.
- [19] ANDERSEN, J. R., LONNBLAD, L., AND SMILLIE, J. M. A Parton Shower for High Energy Jets. *JHEP* **07** (2011), 110.
- [20] ANDERSEN, J. R., AND SMILLIE, J. M. Constructing All-Order Corrections to Multi-Jet Rates. *JHEP* **1001** (2010), 039.
- [21] ANDERSEN, J. R., AND SMILLIE, J. M. The Factorisation of the t-channel Pole in Quark-Gluon Scattering. *Phys.Rev. D81* (2010), 114021.
- [22] ANDERSEN, J. R., AND SMILLIE, J. M. Multiple Jets at the LHC with High Energy Jets. *JHEP* **1106** (2011), 010.
- [23] ANDERSEN, J. R., AND WHITE, C. D. A New Framework for Multijet Predictions and its application to Higgs Boson production at the LHC. *Phys. Rev. D78* (2008), 051501.
- [24] ANDERSSON, B., MOHANTY, S., AND SODERBERG, F. Recent developments in the Lund model. In *36th Annual Winter School on Nuclear and Particle Physics (PINP 2002) and 8th St. Petersburg School on Theoretical Physics St. Petersburg, Russia, February 25-March 3, 2002* (2002).
- [25] B. L. IOFFE, V. S. FADIN, L. N. L. *Quantum Chromodynamics: Perturbative and Nonperturbative Aspects*. Cambridge University Press.
- [26] BADGER, S., BIEDERMANN, B., UWER, P., AND YUNDIN, V. Numerical evaluation of virtual corrections to multi-jet production in massless QCD. *Comput. Phys. Commun.* **184** (2013), 1981–1998.
- [27] BALITSKY, I., AND LIPATOV, L. The Pomeranchuk Singularity in Quantum Chromodynamics. *Sov.J.Nucl.Phys.* **28** (1978), 822–829.
- [28] BERGER, C. F., BERN, Z., DIXON, L. J., FEBRES CORDERO, F., FORDE, D., GLEISBERG, T., ITA, H., KOSOWER, D. A., AND MAITRE, D. Next-to-Leading Order QCD Predictions for $Z, \gamma^* + 3$ -Jet Distributions at the Tevatron. *Phys. Rev. D82* (2010), 074002.
- [29] BINGER, J., ET AL. Review of Particle Physics (RPP). *Phys. Rev. D86* (2012), 010001.
- [30] BERN, Z., OZEREN, K., DIXON, L. J., HOECHE, S., FEBRES CORDERO, F., ITA, H., KOSOWER, D., AND MAITRE, D. High multiplicity processes at NLO with BlackHat and Sherpa. *PoS LL2012* (2012), 018.
- [31] BLECHMAN, A. E. Spin correlations in top production and decay e^+e^- colliders, 2001.
- [32] BRAU, J., OKADA, Y., WALKER, N., DABROWSKI, W., GAJEWSKI, J., IDZIK, M., KISIELEWSKA, D., KULIS, S., SUSZYCKI, L., SWIENTEK, K., ET AL. ILC Reference Design Report: ILC Global Design Effort and World Wide Study.

- [33] BUTTERWORTH, J. M., DAVISON, A. R., RUBIN, M., AND SALAM, G. P. Jet substructure as a new Higgs search channel at the LHC. *Phys. Rev. Lett.* **100** (2008), 242001.
- [34] CACCIARI, M., DREYER, F. A., KARLBERG, A., SALAM, G. P., AND ZANDERIGHI, G. Fully Differential Vector-Boson-Fusion Higgs Production at Next-to-Next-to-Leading Order. *Phys. Rev. Lett.* **115**, 8 (2015), 082002.
- [35] CACCIARI, M., SALAM, G. P., AND SOYEZ, G. The Anti-k(t) jet clustering algorithm. *JHEP* **0804** (2008), 063.
- [36] CAMPBELL, J. M., HARTANTO, H. B., AND WILLIAMS, C. Next-to-leading order predictions for $Z\gamma + \text{jet}$ and $Z\gamma\gamma$ final states at the LHC. *JHEP* **11** (2012), 162.
- [37] CHATRCHYAN, S., ET AL. Measurement of the inclusive production cross sections for forward jets and for dijet events with one forward and one central jet in pp collisions at $\sqrt{s} = 7$ TeV. *JHEP* **06** (2012), 036.
- [38] CHATRCHYAN, S., ET AL. Measurement of the ratio of the inclusive 3-jet cross section to the inclusive 2-jet cross section in pp collisions at $\sqrt{s} = 7$ TeV and first determination of the strong coupling constant in the TeV range. *Eur. Phys. J. C* **73**, 10 (2013), 2604.
- [39] COLLABORATION, C. Measurement of the double differential Drell-Yan cross section at low and high masses of the di-muon system at $\sqrt{s} = 7$ TeV.
- [40] CORCELLA, G., KNOWLES, I. G., MARCHEGINI, G., MORETTI, S., ODAGIRI, K., RICHARDSON, P., SEYMOUR, M. H., AND WEBBER, B. R. HERWIG 6: An Event generator for hadron emission reactions with interfering gluons (including supersymmetric processes). *JHEP* **01** (2001), 010.
- [41] DEL DUCA, V. An introduction to the perturbative QCD pomeron and to jet physics at large rapidities, hep-ph/9503226.
- [42] DIXON, L. J. Calculating scattering amplitudes efficiently. In *QCD and beyond. Proceedings, Theoretical Advanced Study Institute in Elementary Particle Physics, TASI-95, Boulder, USA, June 4-30, 1995* (1996).
- [43] DUCLOUE, B., SZYMANOWSKI, L., AND WALLON, S. Mueller-Navelet jets at LHC: the first complete NLL BFKL study. *PoS QNP2012* (2012), 165.
- [44] ELVANG, H., AND TIN HUANG, Y. *Frontmatter*. Cambridge University Press, 2015. Cambridge Books Online.
- [45] FIELD, R. *Applications of Perturbative Quantum Chromodynamics*. Addison Wesley Longman Publishing Co., 1989.
- [46] FORSHAW, J. R., AND ROSS, D. A. *Quantum Chromodynamics and the Pomeron*. Cambridge University Press, 1997. Cambridge Books Online.
- [47] FREDERIX, R., FRIXIONE, S., PAPAEFSTATHIOU, A., PRESTEL, S., AND TORRIELLI, P. A study of multi-jet production in association with an electroweak vector boson.
- [48] FRIXIONE, S., NASON, P., AND OLEARI, C. Matching NLO QCD computations with Parton Shower simulations: the POWHEG method. *JHEP* **11** (2007), 070.
- [49] FRIXIONE, S., STOECKLI, F., TORRIELLI, P., WEBBER, B. R., AND WHITE, C. D. The MCaNLO 4.0 Event Generator.
- [50] FRIXIONE, S., AND WEBBER, B. R. Matching NLO QCD computations and parton shower simulations. *JHEP* **06** (2002), 029.

- [51] GEHRMANN, T., GRAZZINI, M., KALLWEIT, S., MAIERHFER, P., VON MANTEUFFEL, A., POZZORINI, S., RATHLEV, D., AND TANCREDI, L. W^+W^- Production at Hadron Colliders in Next to Next to Leading Order QCD. *Phys. Rev. Lett.* **113**, 21 (2014), 212001.
- [52] GLEISBERG, T., HOECHE, S., KRAUSS, F., SCHONHERR, M., SCHUMANN, S., SIEGERT, F., AND WINTER, J. Event generation with SHERPA 1.1. *JHEP* **02** (2009), 007.
- [53] GRAZZINI, M., KALLWEIT, S., AND RATHLEV, D. W and Z production at the LHC in NNLO QCD. *JHEP* **07** (2015), 085.
- [54] GRIFFITHS, D. *Introduction to Elementary Particles*. Physics Textbook. Wiley, 2008.
- [55] GUSTAFSON, G., AND PETTERSSON, U. Dipole formulation of QCD cascades. Tech. Rep. LU-TP-87-19. LU-TP-87-9. LUTP-87-9, Leipzig Univ., Leipzig, Jun 1987.
- [56] HOECHE, S., KRAUSS, F., SCHONHERR, M., AND SIEGERT, F. QCD matrix elements + parton showers: The NLO case. *JHEP* **04** (2013), 027.
- [57] HCHE, S., KUTTIMALAI, S., SCHUMANN, S., AND SIEGERT, F. Beyond Standard Model calculations with Sherpa. *Eur. Phys. J. C* **75**, 3 (2015), 135.
- [58] ITA, H., BERN, Z., DIXON, L. J., FEBRES CORDERO, F., KOSOWER, D. A., AND MAITRE, D. Precise Predictions for Z + 4 Jets at Hadron Colliders. *Phys. Rev. D* **85** (2012), 031501.
- [59] J. ANDERSEN, J.MEDLEY, J. Z/gamma* plus Multiple Hard Jets in High Energy Collisions.
- [60] KHACHATRYAN, V., ET AL. Measurements of jet multiplicity and differential production cross sections of Z+ jets events in proton-proton collisions at $\sqrt{s} = 7$ TeV. *Phys. Rev. D* **91**, 5 (2015), 052008.
- [61] KINOSHITA, T. Mass singularities of feynman amplitudes. *Journal of Mathematical Physics* **3**, 4 (1962).
- [62] KUIPERS, J., UEDA, T., VERMASEREN, J. A. M., AND VOLINGA, J. Form version 4.0. *CoRR abs/1203.6543* (2012).
- [63] KURAEV, E. A., LIPATOV, L. N., AND FADIN, V. S. Multi - Reggeon processes in the Yang-Mills theory. *Sov. Phys. JETP* **44** (1976), 443–450.
- [64] LONNBLAD, L. ARIADNE version 4: A Program for simulation of QCD cascades implementing the color dipole model. *Comput. Phys. Commun.* **71** (1992), 15–31.
- [65] MANGANO, M. L., MORETTI, M., PICCININI, F., PITTAU, R., AND POLOSA, A. D. ALPGEN, a generator for hard multiparton processes in hadronic collisions. *JHEP* **07** (2003), 001.
- [66] MANGANO, M. L., MORETTI, M., AND PITTAU, R. Multijet matrix elements and shower evolution in hadronic collisions: $Wb\bar{b} + n$ jets as a case study. *Nucl. Phys. B* **632** (2002), 343–362.
- [67] MUTA, T. *Foundations Of Quantum Chromodynamics: An Introduction to Perturbative Methods in Gauge Theories*. World Scientific lecture notes in physics. World Scientific Publishing Company Incorporated, 2010.
- [68] NASON, P. A new method for combining nlo qcd with shower monte carlo algorithms. *Journal of High Energy Physics* **2004**, 11 (2004), 040.
- [69] PAULI, W., AND VILLARS, F. On the invariant regularization in relativistic quantum theory. *Rev. Mod. Phys.* **21** (Jul 1949), 434–444.

- [70] R. K. ELLIS, W. J. STERLING, B. R. W. *QCD and Collider Physics*. Cambridge Monographs on Particle Physics, 2010.
- [71] SALAM, G. P., AND SOYEZ, G. A Practical Seedless Infrared-Safe Cone jet algorithm. *JHEP* 05 (2007), 086.
- [72] SJOSTRAND, T., EDEN, P., FRIBERG, C., LONNBLAD, L., MIU, G., MRENNA, S., AND NORRBIN, E. High-energy physics event generation with PYTHIA 6.1. *Comput. Phys. Commun.* 135 (2001), 238–259.
- [73] SJOSTRAND, T., MRENNA, S., AND SKANDS, P. Z. A Brief Introduction to PYTHIA 8.1. *Comput. Phys. Commun.* 178 (2008), 852–867.
- [74] STERMAN, G. F. Partons, factorization and resummation, TASI 95. In *QCD and beyond. Proceedings, Theoretical Advanced Study Institute in Elementary Particle Physics, TASI-95, Boulder, USA, June 4-30, 1995* (1995).
- [75] VERA, A. S. High energy scattering in quantum chromodynamics, www.hep.man.ac.uk/u/forshaw/sabio.ps.gz, 2000.